Structural variation of size-selected metal clusters in chemical reactions

by

Kuo-Juei Hu

Nanoscale Physics Research Laboratory

School of Physics and Astronomy

The University of Birmingham

December 2015

UNIVERSITY OF BIRMINGHAM

University of Birmingham Research Archive

e-theses repository

Abstract

This thesis is comprised of studies in the characterisation of monolayer-protected and metal cluster of the structural response of size-selected (bare) clusters to chemical reactions. The technique employed is high-angle annular dark field (HAADF) aberration-corrected scanning transmission electron microscopy (AC-STEM).

Monolayer-protected Au_{40} clusters were characterised for their structure and their dynamical behaviour under an electron beam. Nuclearity atom counting and aspect ratio measurements of chemically synthesised MP-Au_{40} clusters was obtained. The aspect ratio measurement offers a statistical proof of the elongated shape of MP-Au40 clusters. These ultrasmall clusters were found to be unstable against prolong irradiation and underwent serious electron beam damage.

In a second strand of the Thesis, the effect of chemical reactions on size-selected metal clusters was investigated. The clusters under investigation were imaged with AC-STEM and their structure was assigned by comparing the atomic resolution images with a set of multi-slice STEM image simulation atlases.

The effect of vapour-phase 1-pentyne hydrogenation on size-selected Au_x (x=923 and 2057) cluster was studied and it was found that the gold nanoclusters demonstrate high stability in both size distribution and structure under the reaction. On the contrary, size-selected Pd_x (x=923 and 2057) clusters tended to transform from amorphous to high symmetry structures under the same reaction condition.

The gas-phase CO oxidation reaction on size-selected Au_x (x=561, 923 and 2057) cluster was studied with regard to cluster size distribution and atomic structure. It was found that under the same conditions of the CO oxidation reaction, two different kind of ripening modes could be identified depended on the cluster size. Smoluchowski ripening, in which clusters diffuse intact and coalescence, is found to occur for Au_{2057} in the CO oxidation reaction. Ostwald ripening, in which larger clusters grow at the expense of smaller ones, was found to occur for Au_{561} and Au_{923} clusters, due to the extra energy generated from catalytic CO oxidation reaction.

ACKNOWLEDGEMENTS

I would like to thank my parents, who have integrity, for setting up a model for me to follow, who made me a human being before I can be anything else.

Also I would like to thank my supervisor Prof. Richard E. Palmer, who granted me the chance to study in his group and arrange financial support for me (together with Johnson Matthey) over these four years, who has been educated us about science during everyday of our time here.

"You should completely ignore the theory and give our results and conclusions in a completely objective, scientific way with full disclosure. It is utterly irrelevant whether it agrees with theory, the truth and nothing but the experimental truth is the only thing that counts." –Richard E. Palmer 2012.09.30

I am grateful for the education I have received here, in all of its aspects. I am very lucky that during my time here, I have had the chance to witness, step by step, how to bring a great idea on paper to become an instrument that is actually working. This is an experience I have never had, and probably would have never had, if I were not here.

In addition, along the way in these four years, guidance was provided by my co-supervisors Dr. Simon R. Plant and Dr. Zhi-Wei Wang, who made a task, that would have been impossible for my to achieve by myself, become possible. If it was not for them, I would not have came this far.

Finally, I would like to thank part of myself. The confliction within myself has never stopped, I am thankful that the other half of myself, that I do not have control of, did not fail me, and did not collapse.

I think people who choose to be here are all, in a way, idealists who are looking for a practical way to survive in this world. I would like to quote Sir Humphry Davy's words:

"Nothing is so dangerous to the progress of the human mind than to assume
that our views of science are ultimate,
that there are no mysteries in nature,
that our triumphs are complete and that there are no new worlds to conquer."

Keep advancing.

Author's Publications

(1) Malola, S.; Lehtovaara, L.; Knoppe, S.; Hu, K. J.; Palmer, R. E.; Brgi, T.; Hkkinen, H. *$Au_{40}(SR)_{24}$ Cluster as a Chiral Dimer of 8-Electron Superatoms: Structure and Optical Properties. J. Am. Chem. Soc. 2012, 134 (48), 19560*

(2) Hu, K.-J.; Plant, S. R.; Ellis, P. R.; Brown, C. M.; Bishop, P. T.; Palmer, R. E. *Atomic Resolution Observation of a Size-Dependent Change in the Ripening Modes of Mass-Selected Au Nanoclusters Involved in CO Oxidation J. Am. Chem. Soc. 2015, jacs.5b08720*

(3) Hu, K.-J.; Plant, S. R.; Ellis, P. R.; Brown, C. M.; Bishop, P. T.; Palmer, R. E. *The Effects of 1-Pentyne Hydrogenation on the Atomic Structures of Size-Selected Au N and Pd N (N = 923 and 2057) Nanoclusters Phys. Chem. Chem. Phys. 2014, 16 (48), 26631*

CONTENTS

CHAPTER 1

INTRODUCTION AND BACKGROUND

1.1 Magic Clusters

The size-dependent properties of metal clusters were widely used when the colour of glass was seen to change when it contained clusters. When the metal nanoparticles are made ultrafine, they show drastically different properties from their original properties under bulk conditions.[1]

Bare metal nanoclusters produced by the supersonic seeded method are more likely to be several specific sizes than others. At first glance, experiments conducted on Group IA: (alkali-metal), abundance spectra show that clusters tend to be formed of specific sizes, see Fig.1.1. For Sodium, the cluster size of 8, 20, 40 and 58 are observed more frequently than other sizes.[2] A similar trend is seen for Potassium, although the effect is less pronounced. The peaks in the spectra are the sizes of 14, 26, 30, 34 and 54. This phenomena is highly reproducible across a range of materials, the cluster sizes corresponding to the peaks are know as magic numbers.
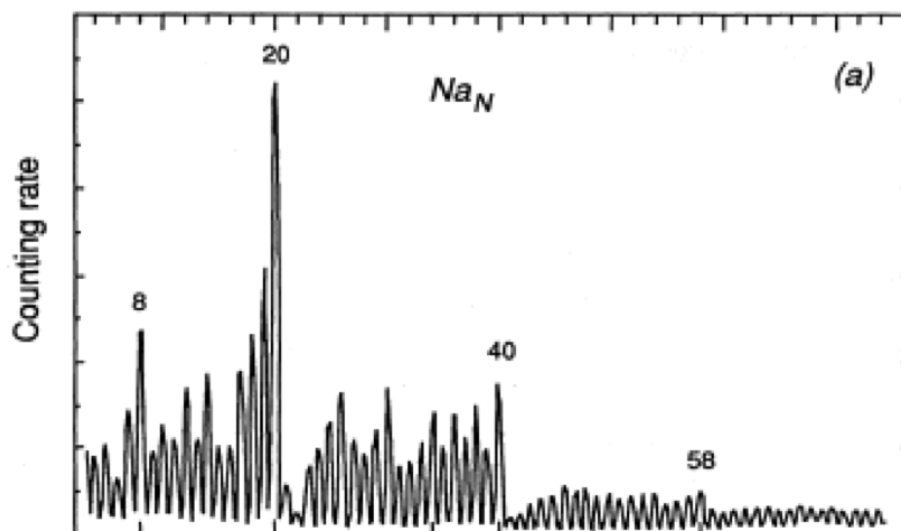
Figure 1.1: Experimental sodium cluster abundance spectrum. The number of sodium atoms N for selected clusters is shown and the value where the counting rate reached peaks is labelled above.[3]

Clusters have also been produced from Copper, Silver and Gold.[3] Although a slightly different technique for generating clusters is involved for experiments of noble-metals. A 20kV krypton ion beam is used for sputtering the metal source needed. The trend that more clusters are formed at specific sizes is again observed, but also the abundance spectra of Copper and Silver are similar to each other. In Fig.1.2 the special sizes measured by mass spectrometer where the clusters tend to form become 9, 21, 41 and 57, instead of 8, 20, 40 and 58 for Alkali group elements and we see a trend in the fine structure of the spectra of Cu and Ag that oscillates from even to odd numbers of atoms per cluster.[3]

Finally the mass abundance spectra of gold show a quasi-logarithmic decay with other defining features. One is the ion intensities appear to be alternating between odd and even number of atoms per cluster. Another is some of the clusters with peculiar sizes are more likely to be formed. The mass abundance spectra of gold clusters peak at n=3, 9, 21, 35, 41, 59, 93 and 139. However, in successive experiments conducted by the same group using negative ion mass spectroscopy, a different series of sizes are observed. For instance for silver, the magic number set is 1, 3, 9, 19, 21, 35, 41, 59, and 137. Similarly, all the magic numbers observed for gold and copper in positive IMS have 2 atoms fewer than the

negative ion counterparts compared with the results in positive ion mass spectroscopy. The reason for this is positive charged means the cluster of interest loses one electron when entering the mass spectroscope.[3] If negative, then the clusters gain an extra electron. Let us assume that this magic number phenomena is electronic shell related, then the extra and insufficient electron would result in a shift of $\Delta n=1$. Therefore, we can interpret that the magic numbers for IB group noble-metals to be still similar to the set of numbers for alkali-group elements.[3]
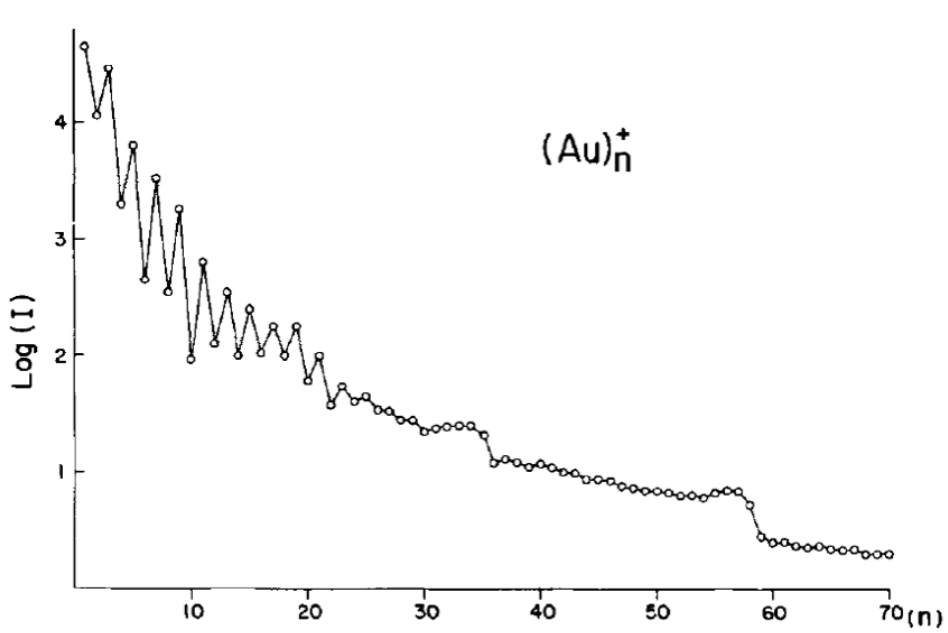
Figure 1.2: Mass distribution of gold clusters (Au)n+. up to clusters size n=100. Plotted in logarithmic scale. Clear odd-even alternation below size 20 is seen and the overall trend of the plot is decreasing when the clusters size increases. The mass abundance spectra of gold clusters peak at n=3, 9, 21, 35, 41, 59, 93 and 139.[3]

1.1.1 The Electronic Shell Structure of Clusters

The phenomena of magic numbers in cluster formation must have something to do with the electronic structures of atoms. This judgment is not too hard to make since sets of magic numbers for different materials follow the category of different atomic groups on the periodic table.[1] The electronic structure of atoms can affect aggregation and the formation of metal nanoclusters.

8

To explain the preferable sizes along the mass abundance spectra observed, models are proposed.[1] Self-consistent jellium models can predict main features on spectra quite well,[4, 5, 6, 7, 8, 9] though the contents and assumptions of this model are simply treating electrons in the valence band as a free electron gas and the positively charged ions as a spherical and uniform field that contains those valence electrons. A critical hypothesis of the jellium model is to regard the whole cluster as an atom. So the phenomena that an atom gains extraordinary stability from getting enough electrons to a closed-electron shell may explain the phenomena of magic numbers. That is, for example for the alkali-group elements formed clusters, when these clusters have enough electrons to form a complete shell (determined by radial quantum number n and the angular momentum l), the next electron brought by an addition atom would have to be filled into the next, higher energy band. This makes the configuration energy of the joining of an additional atom significantly higher. Higher configuration energy means lower stability and therefore the number of clusters not forming full shells falls.[4]
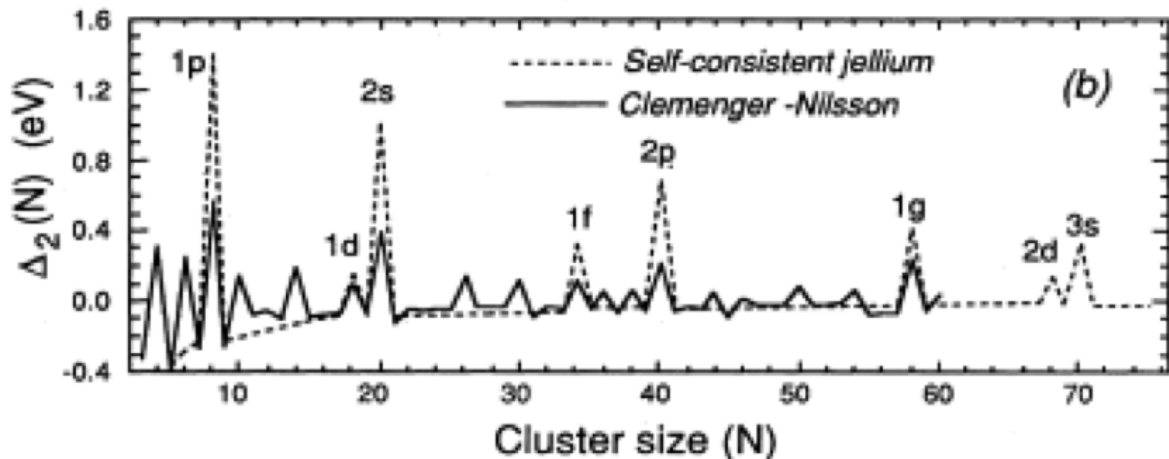
Figure 1.3: Dashed line, using Wood-Saxon potential (after Knight et (1984)); Solid line, using ellipsoidal shell (Clemenger-Nilsson) model. (after de Beer, Knight, Chou, and Cohen, (1987))[1]

Though the most spherical shell clusters can be predicted by the conventional jellium model quite well, minor peaks between the closed-shell sizes are unresolved through this spherical model. According to the Jahn-Teller theorem, clusters that cannot form close-

9

shell tend to be ellipsoidal. This contradicts the assumption in the jellium model that positive charged backgrounds in the calculations are all spherical. Thus, the Clemenger-Nilsson model is employed. This model utilizes a shell theory for axially symmetric distortions which was previous developed and used for nuclei. Fine structure in abundance spectra related to subshell closing can also be reproduced using this model.[10, 11]

1.1.2 Geometric Shell Effect and Comparison

Electronic shell completion explains the magic numbers observed in small clusters (<20 shells). However, later research indicates that when reaching a certain size, the influence of the electronic shell start weakening and the significance of the affect of completing a geometric shell rises. Fig.1.4 shows that for sodium clusters, the electronic effects govern the magic number series until n~1500. A different period of shell oscillation in mass abundance spectra replaced the formal one in the size region of 1500 to 22000.[12, 13] In the following study conducted on Magnesium, stable Mg clusters are found to follow the geometric magic numbers, forming icosahedra clusters.[13] Intriguingly, whether geometric or electronic magic numbers of clusters is in fact formed dependent on temperature according to Martin et al.[14] Mass abundance spectra of sodium clusters that clearly show the existence of geometric shell structure at 193K, starting to melt down with the increasing temperature. When the temperature is increased to 307K, all geometric shell features up to 10000 atoms per cluster disappear from the mass spectra. Extended studies have been made about the atomic shells of clusters.[15]
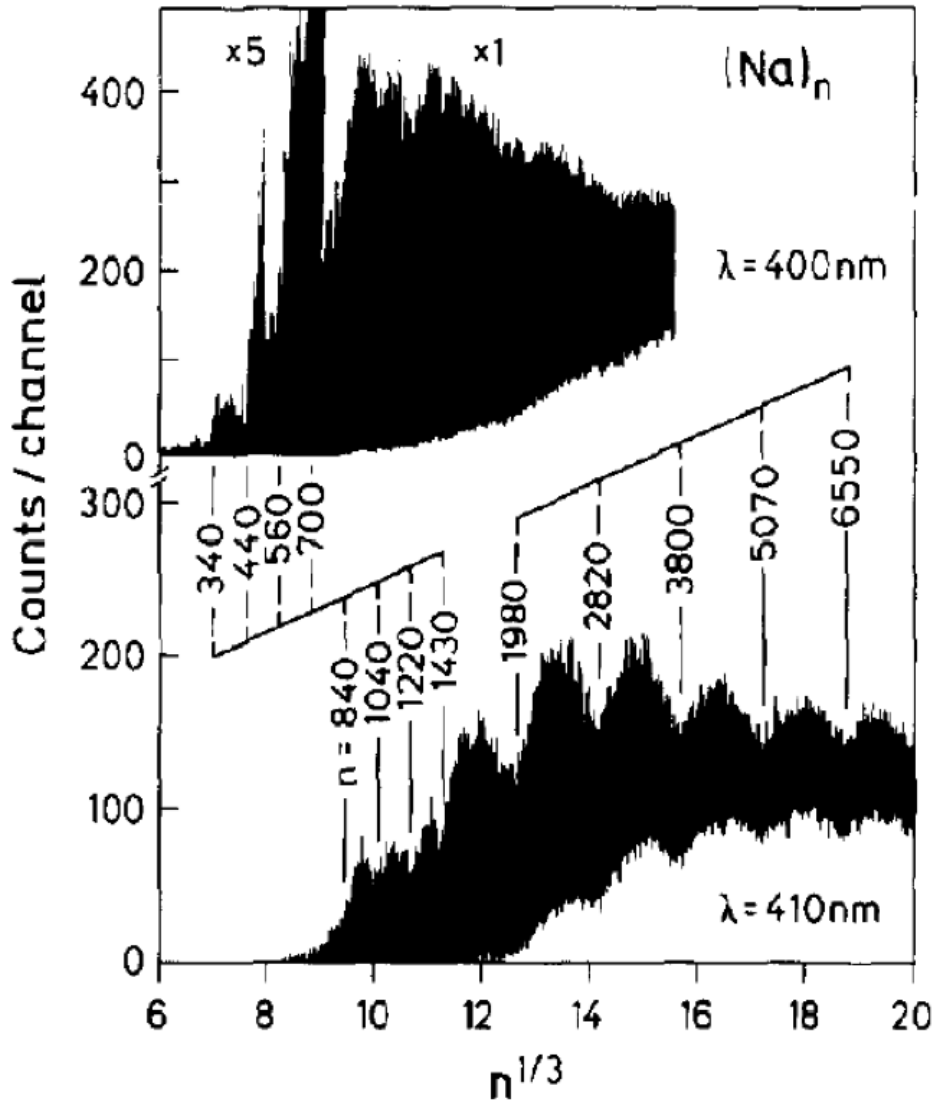
Figure 1.4: Mass spectra of Na$_n$ clusters. The y axis denotes the total number of counts accumulated in a 40 ns time channel. Two sequence of structures are observed at equally spaced intervals on the n$^{1/3}$ scale.[1]

Competition between electronic and geometric shell effects appear to be governed by the temperature and size of the cluster.[14, 16, 17] The bigger the size of clusters, the stronger the geometric effect is,[12] unless the temperature is high enough to cause the melting of the cluster.[14] One possible reason could be that the steps between electronic shells become indistinct when the clusters grow bigger. The experiment of mass abundance of large sodium clusters show the magic numbers transfer from electronic to geometric ones which fit the Mackay icosahedra shell structure when the size of clusters is bigger

than 2000 atoms.[14] Further research conducted by Martin and Bergmann also suggests that atoms in small clusters in fact act like molecules in liquid. That is, they considered the clusters like atom droplets contained in spherical jellium.[12]

1.1.3   Monolayer-Protected clusters

After the $Au_{55}(PPh_3)_{12}Cl_6$ cluster was discovered in 1981, another idea of forming rigid nano-sized gold clusters is demonstrated. $Au_{55}(PPh_3)_{12}Cl_6$ is special because of its monodispersity, structural integrity, small size and unusual electronic properties. The process of synthesis of ligand-protected Au_{55} is not controllable, they are found by chance to have high selectivity after a certain set of chemical method. Though the conclusive atomic structure is still unclear, it is believed that they are three-layered full-shell icosahedral gold core with ligands attached to them.[18]

The real breakthrough of structural determination of ligand-protected clusters was the structure of Au_{102}(p-MBA, para-mercaptobenzoic acid, $SC_7O_2H_5$)$_{44}$. They manage to first prepare sufficient monodispersed clusters, and then crystallize these clusters into large single crystals. The structure is determined through X-ray diffraction studies. Consisting of an Au_{79} core of D_5h symmetry and another 23 Au atoms forming Au-ligand complexes, monolayer-protected 102-atom gold clusters are found to have an unexpected structure as shown in Fig.1.5. Interestingly, the 23 Au atoms outside the core do not have direct contact with the main Au core instead, they bind to the surface of it as -RS-Au-RS- or RS-(AuRS)$_2$- oligomers instead. According to theoretical calculations, 19 short staples and 2 long staples bond to 42 anchoring points provided by the Au_{79} core, effectively forming a layer of protecting motif around it.[19]
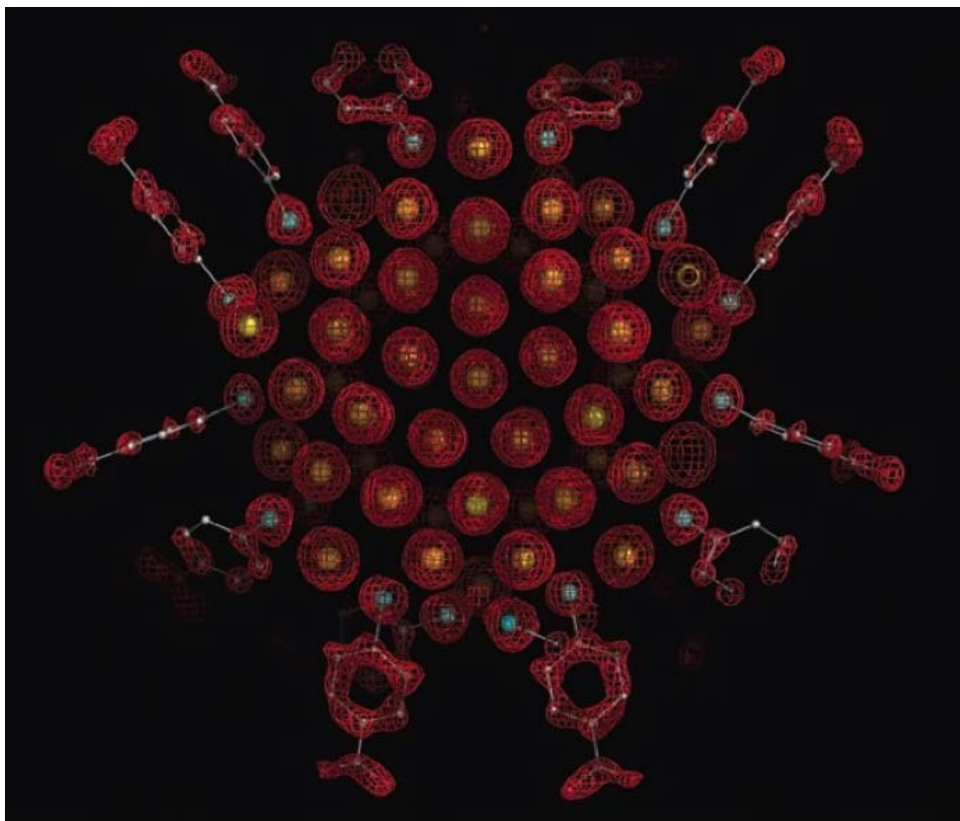
Figure 1.5: X-ray crystal structure determination of the Au102(p-MBA)44 nanoparticles. Electron density map (red mesh) and atomic structure. (Gold atoms as yellow spheres, and p-MBA shown as framework and with small spheres (sulphur in cyan, carbon in gray, and oxygen in red)).[19]

There are two possible explanations for the extraordinary stability of $Au_{102}(p\text{-}MBA)_{44}$. Firstly, each gold atom could provide a certain amount of valence electrons (N, number of atoms, vA, number of valence band electron provided), in this case, one. If so the attached ligands will delocalise a certain amount of the valence charge from Au atoms (M), given that the charge on the complex is z. We can then estimate whether the remaining charge on the cluster meets the shell-closing electron count (n*) or not. For $Au_{102}(p\text{-}MBA)_{44}$, the n*=NvA-M-z calculated is n*=58. This happens to complete the 1G shell and form a rigid cluster. The alternative explanation uses a DOS (density of states) argument to explain the enhanced stability of MP-Au_{102}. As we can see in the Fig.1.6, there is region in the diagram that is free of density of states (labelled 58 electrons). This vacant area is between the 1G and 3S+1H+2D bands. For Au_{79} bare cluster, 21 excessive electrons are force to fill in the 3S+1H+2D band which lead to a no HOMO-LUMO gap situation for

13

Au$_{79}$ core. On the contrary, ligands in Au$_{102}$(p-MBA)$_{44}$ cluster successfully deplete that 21 electrons and make the Fermi level locate right at the middle of the 0.5 eV HOMO-LUMO gap.[20]
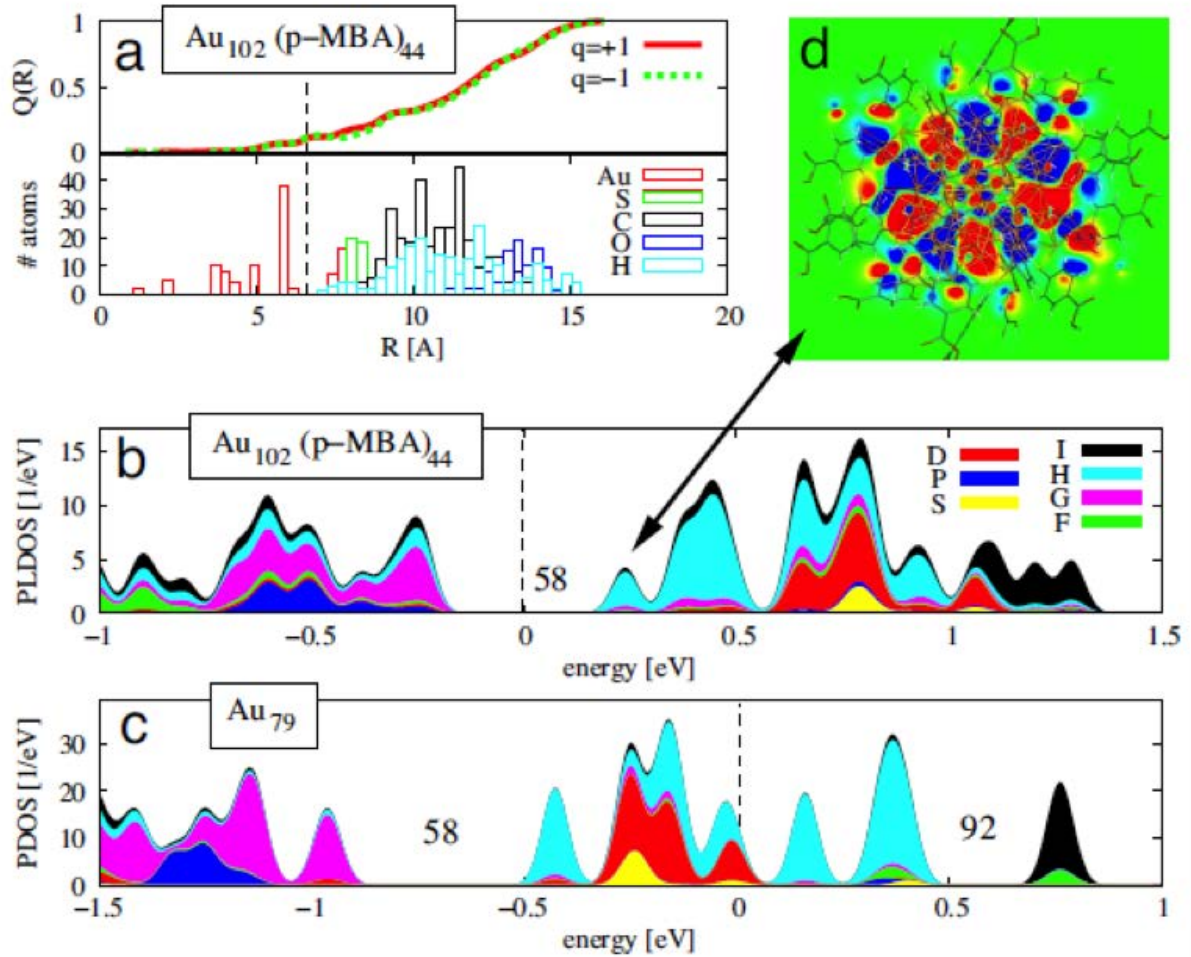
Figure 1.6: Electronic structure analysis of the Au$_{102}$(p-MBA)44 cluster. (a) The radial dependence of the integrated induced charge Q(R). The dashed line indicates a midpoint between the surface of Au$_{79}$ core and the Au-thiolate layer. (b) The angular-momentum-projected local electron density of states (PLDOS) (projection up to the I symmetry, for the Au$_{79}$ core in Au$_{102}$(p-MBA)$_{44}$. (c) The angular-momentum-projected electron density of states (PDOS) for the bare Au$_{79}$ without the Au-thiolate layer. (d) A cut-plane visualization of the LUMO state of the Au$_{102}$(p-MBA)$_{44}$ cluster.[20]

A Scanning Transmission Electron Microscope (STEM) equipped with a spherical aberration corrector can provide sub-Ångstroms resolution and therefore it is a powerful tool for cluster research.[21] Electron tomography can be employed to obtain high resolution three-dimensional atomic images. In a previous study, Van Tenderloo et al. used

HAADF-STEM as electron tomography to determine the three-dimensional structure of Ag nanoparticle.[22] However, tomography requires an indication as to the orientation of specimen in the images.[23] Purposely added fiducial markers are usually used or it may require the substrate to be periodical structure that can provide the information of sample orientation. To successfully perform tomography using STEM, a series of images from different orientation have to be taken. That makes this approach not suitable for smaller clusters because the strong interaction between electron beam and clusters causes structural instability of the specimen. However, we can still take advantage of the Z-dependent high-resolution HAADF-STEM images and images simulation techniques to determine the structure of clusters.[23]
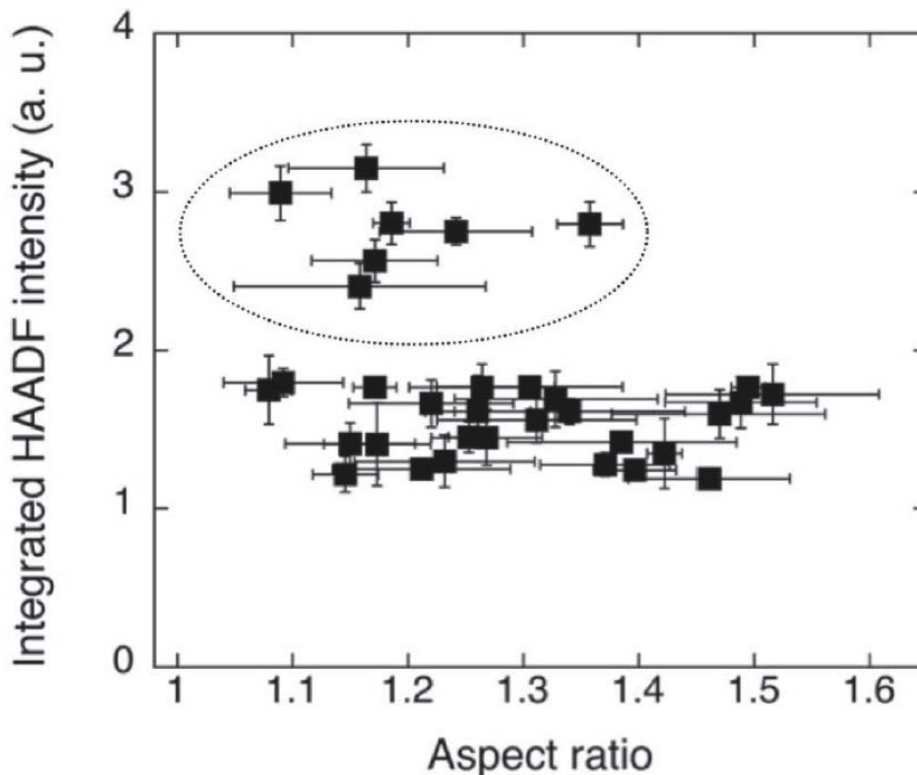
Figure 1.7: Statistical distribution of integrated HAADF intensities as a function of aspect ratio for deposited MP-Au$_{38}$ clusters. The dotted ellipse shows the signal from aggregated non-monomeric clusters.[24]

Previous studies that investigated the structure of monolayer-protected Au$_{38}$ cluster have used STEM. The MP-Au$_{38}$ clusters used are Au$_{38}$(SR)$_{24}$ (SR: 2-phenylethanethiol),

prepared by chemical synthesizing of Tetrachloroauric acid followed by core etching.[25] The ability to resolve the structural information directly through electron microscopy is limited by the strong effect of the electron beam on clusters as small as MP-Au$_{38}$ causing continuous morphological changes. However, though the morphologies are changing, the shape of clusters is generally preserved over scanning if we optimise parameters of experiments. Therefore, we aim to determine the structure by the distinct the shape of clusters. Experimental observations show the aspect ratio of clusters is 1.6. From several theoretical atomic models predicted, a bi-icosahedral Au$_{23}$ core model which has an aspect ratio of 1.58 has a good agreement with experimental result.[24]
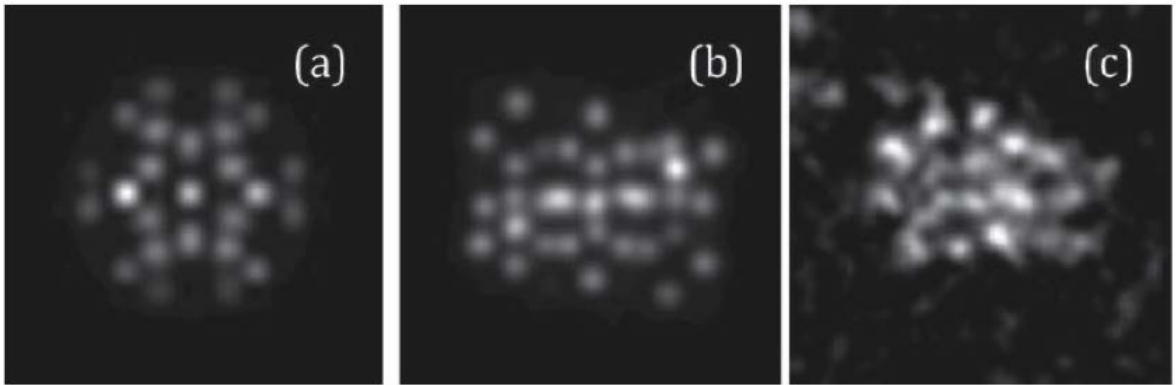
Figure 1.8: Comparison of simulated HAADF-STEM images (a) and (b). (a) central Au$_{14}$ core. (b) a bi-icosahedral Au$_{23}$ core. (c) Representative experimental image of MP-Au$_{38}$.[24]

While imaging with the transmission electron microscope, small cluster often suffer from serious fluctuations due to the intense electron beam. This makes the intention of understanding the atomic structure of small nanoparticles through direct imaging with STEM challenging. In a previous study, the three dimensional structure of monolayer-protected Au$_{102}$ was successfully resolved using X-ray diffraction combined with data reconstruction; these monodispersed MP-Au$_{102}$ clusters were crystallised before X-ray diffraction. However, other gold nanoparticles produced with wet methods can not be resolved with the same technique. A study combining aberration-corrected transmission electron microscopy, data reconstruction, and confirmed with density functional theory

has been performed on the nanoparticles and aimed at solving the structure of the MP-Au_{68} cluster[26]. Due to the perturbation by the electron beam, several measures were taken by the author to reduce its effect; a cryogenic stage was used to reduce thermal fluctuation and a lower electron dose as is generally used for biological samples was chosen. Instead of employing typical tomography that records the relative tilting angle to the image, images of 939 particles were captured, and through use of the software package EMAN2, an electron density map was reconstructed. The resulting electron map was then sent for DFT calculation to find the optimal configuration. The result showed that the position of gold atoms in MP-Au_{68} nanoparticles were largely unchanged from the reconstructed experimental result; the atomic structure of MP-Au_{68} nanoparticles was found to be closely based on the FCC structure.
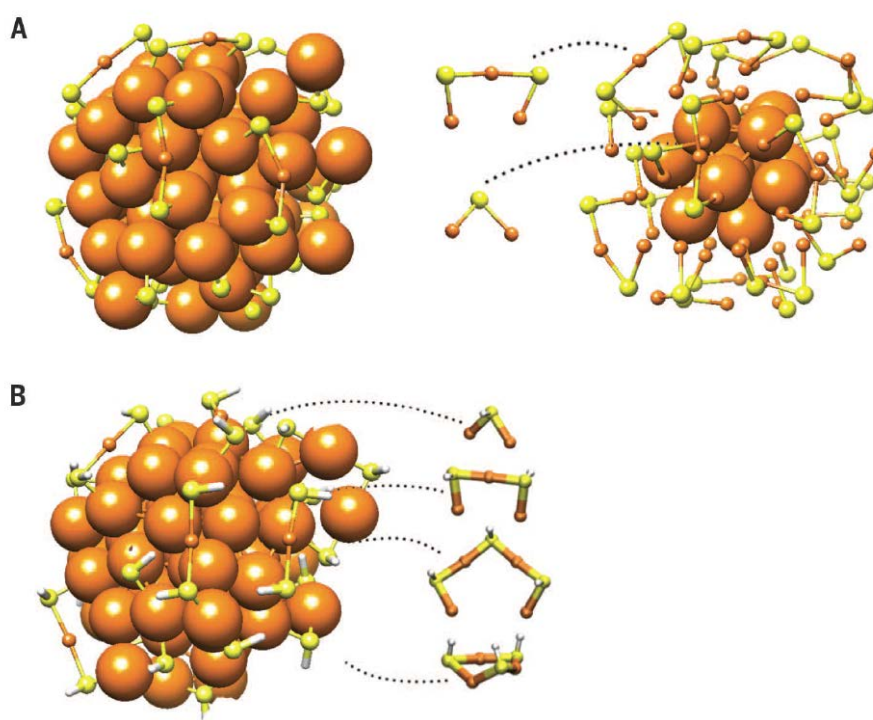
Figure 1.9: (a) The reconstructed structure from experimental electron density map data extracted from 939 nanoparticles. (Right) The same atomic structure with reduced visual size of atoms to display the structure of the core. (b) Atomic model relaxed from the DFT calculation. [26]

1.1.4 Dynamical behaviour of clusters induced by Electron Irradiation

Structural changes of small nanoparticles were reported as early as 1985 by Wallenberg and Bovin.[27, 28] They suggest the cause of the observed dynamical effects is the incident electron microscope beam. These dynamical behaviours of nanoparticles included surface atom hopping and structural transform of the whole cluster are observed in the following experiments. On the other hand, structural changes driven by the thermal fluctuation are also seen in the experiments.[29, 30] The relation of incident electron beam intensity and equivalent temperature of nanoparticles was connected and explain principally by Belov et al, in 1991[31] and also linked experimentally in the previous work from our group.[32]

In Wallenberg's experiments, behaviour of atom column by atom column growth on specific facet of metal nanoparticles was observed for chemical prepared Platinum and Gold. Their experiments show that the spontaneous coalescence of Au_{55} clusters is common. They also observe crystal growth of Au_{55} clusters induced by electron beam. Recently, research indicates that electron beam can cause geometric transformations of clusters.[28, 33] Among these studies, an experiment conducted by Jose-Yacaman works on comparing structural instability of bare and passivated gold clusters with sizes between 2-5 nm observed with high resolution electron microscopy.[34] In their experiments, the n-Alkyl thiol protected gold clusters appear to be less likely to undergo structural changes than bare gold clusters.
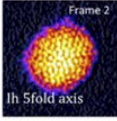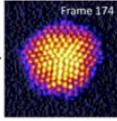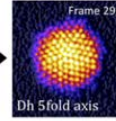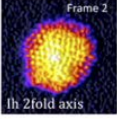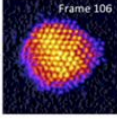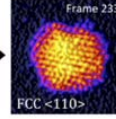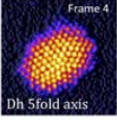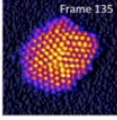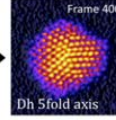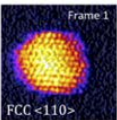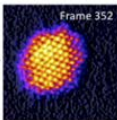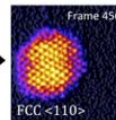
Initial state	After irradiation	Examples		
Ih: 42	Dh: 29 FCC: 12 Ih: 1	Ih->Dh		
		Ih->FCC		
Dh: 18	Dh: 18	Dh unchanged		
FCC: 19	FCC: 18 Dh: 1	FCC unchanged		

Figure 1.10: The table shows the number of clusters from different initial structure and how many of them would transform into other structures after prolong irradiation under STEM[35].

A study was conducted by the structural transformation on the size-selected bare $Au_{923\pm23}$ clusters under electron beam irradiation[35]. In this work, unambiguous evidence was given about the structural change induced by the electron beam. Gold clusters were soft-landed on the amorphous carbon film so that they maintain their shape after impact. The converged electron beam of STEM continuously scan the cluster that was under observation. This high energy electron beam of 200 keV was imaging and irradiating the cluster at the same time. Sequential images were taken on each of the clusters at 0.8 s/frame for up to 500 images per cluster. At this imaging rate, the electron dose on clusters being imaged was 2.4×10^4 e$^-$Å^{-2}/frame. When clusters that were initially icosahedron were imaged, and irradiated under the electron beam, 29 out of 42 transformed to decahedron, 12 clusters became FCC in structure, and only 1 remained icosahedron. However, for clusters with an initial structure of either D_h or FCC, almost all retain their original structure. This result revealed that the icosahedron is not the most sta-

ble structure. When icosahedron clusters gained energy from electron beam, they were more likely to transform to decahedral than FCC structure, indicating D_h might be more structurally accessible from I_h than FCC at size 923. Nevertheless, even though the D_h structure may have the lowest configuration energy, when FCC clusters were irradiated, only 1 FCC cluster transformed to D_h, meaning that the energy barrier between D_h and FCC structures is too high for the energy provided by irradiation to overcome.

Fluctuating dynamic behaviour is observed for Au_{55} clusters throughout STEM imaging[32]. During the imaging of size-selected (bare) Au_{55} clusters, produced with a magnetron cluster beam source, it was found that it is hard to capture an image of a cluster under direct irradiation with the electron beam (200 kV accelerating voltage and electron dose of $\sim 6.9 \times 10^3$ electrons $\mathring{A}^{-2}$). As a result, a time-lapse image sequence was taken and each of these individual images were compared with theoretical simulated STEM images. The result was that no high symmetry structures (FCC, icosahedron, or decahedron) were found in Au_{55} clusters. Instead, repeatedly matches between experimental images and chiral-Au_{55} simulated STEM images were found. Similar fluctuating dynamic behaviour was observed for the Au_{20} cluster[36]. Direct imaging of small cluster under intense electron beam irradiation (200kV, $\sim 8.8 \times 10^3$ electrons $\mathring{A}^{-2}$) at high magnification (13.3×13.3 nm) was significantly disturbing small clusters during imaging. Investigations have shown that the incident electron beam can induce crystal growth and crystal structural change of clusters[28]. The effect of the electron beam can largely be regarded as similar to a thermal fluctuation[31].

1.2 Incoherent Z-contrast imaging and atom counting

Using HAADF AC-STEM for high resolution imaging, quantitative analysis of HAADF STEM images was performed by Li et al[23]. The major discovery was the strong dependency of integrated HAADF intensity of an atomic column on the atomic number,

Z, and the number of atoms in a column. This principle was expanded and applied to clusters imaged. The integrated HAADF intensity over all the pixels of a cluster in a image is proportional to the atomic number and to the number of atoms in the cluster. In this study, size-selected gold clusters were used as an example and a linear increase of integrated HAADF intensity with increasing cluster size was found for clusters in size range between 55 to 1500 atoms, as shown in Fig.1.11.
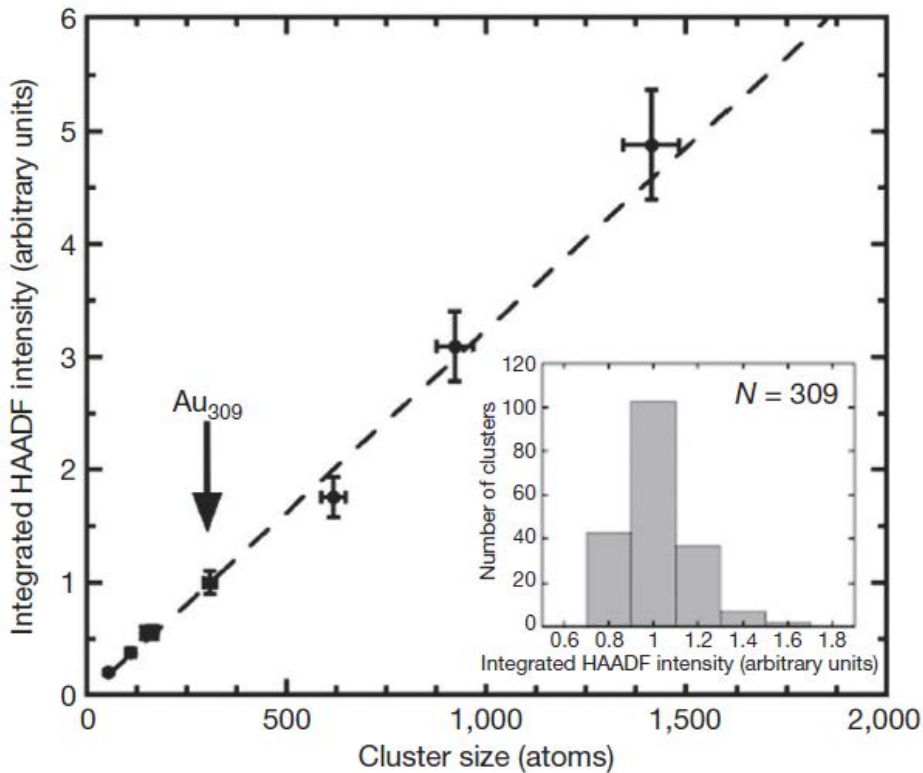
Figure 1.11: Graph showing integrated HAADF intensity of size-selected gold nanoclusters between sizes 55 and 1500. The integrated HAADF intensity is found to be proportional to the number of atoms contained in a gold nanocluster[23].

The principle discovered in the previous study[23] was used in a quantitative investigation of monolayer-protected gold clusters[37]. In this study the size-selected Au_{38} and Au_{25} nanoclusters were used as atomic mass standards. These size-selected clusters were deposited on separated regions of the same TEM grid alongside MP-Au_{38} nanoclusters. The integrated HAADF intensity of the two different kinds of clusters were acquired in the same imaging session (the same imaging conditions) and thus their HAADF intensity is directly comparable to each other. A statistical analysis of integrated HAADF inten-

sity of clusters imaged was shown in Fig.1.12 (d) and (e). Size-distributions of MP-Au_{38} clusters and size-selected Au_{38} clusters that were used as a mass standard were presented in Fig.1.12 (d). The relation between integrated HAADF intensity, number of clusters, and atomic number can be described as

$$\frac{I_A}{I_B} = \frac{N_A}{N_B}(\frac{Z_A}{Z_B})^n.$$

(1.1)

The composition of the monolayer-protected gold cluster is $Au_{38}(SC_2Ph)_{24}$. It contains 24 sulphur atoms, 166 carbon atoms, and 312 hydrogen atoms. The equivalent HAADF intensity contributed by the ligands is the equivalent intensity for 8.7±2.6 gold atoms. The number of gold atoms in MP-Au_{38} nanoclusters was 38±2 with the contribution from the ligands estimated. This new method, named atom counting, of measuring mass of clusters with HAADF STEM imaging relies on comparing the integrated intensity acquired from a cluster to that of another cluster that serves as a mass standard.
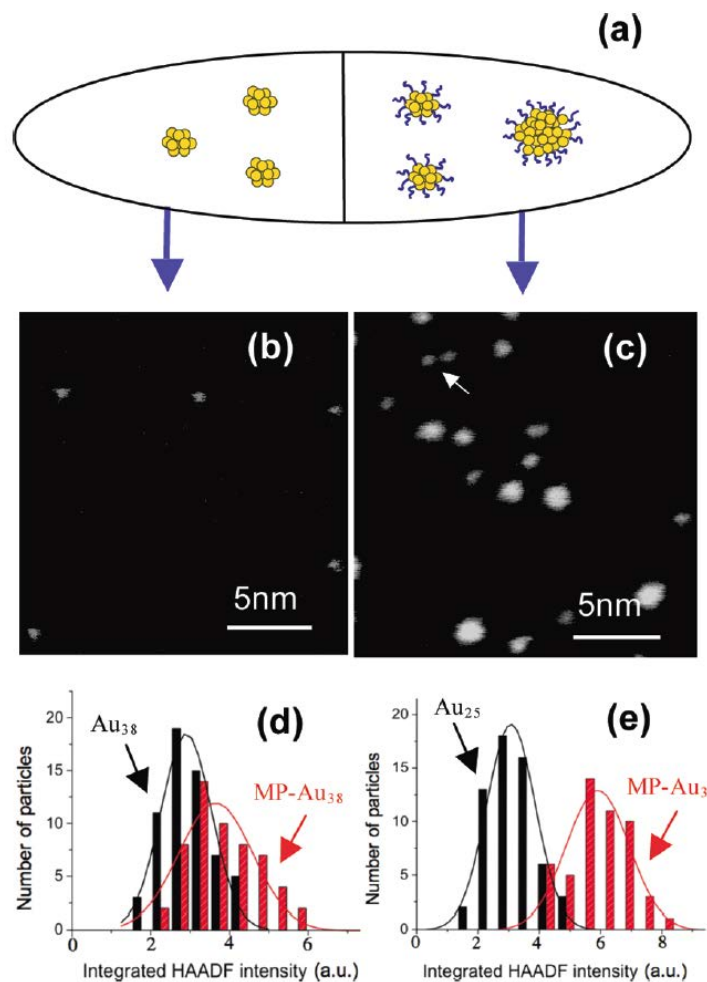
Figure 1.12: Diagram showed (a) co-deposition of synthesised gold nanoclusters of interest and size-selected gold nanoclusters served as mass balance. (b, c) The representative images of Au_{55} (b) and MP-Au_{40} (c). Size distribution of Au_{38} (d) and Au_{25} (e), compared with mass balance. [37]

1.3 Structural transformation of gold and palladium nanoclusters

Atoms in nanocrystals can be packed in a different manner to the atomic structure of their bulk form. Examples of this are icosahedron, and decahedron structures formed by Au nanocluster compared to its normal bulk FCC structure.[38] An icosahedron is created by twenty tetrahedrons with each of the tetrahedron sharing three faces with another tetrahedron. A decahedron is formed by five tetrahedrons each of which share two

faces with another tetrahedron. Nanocrystals of these structure have five-fold symmetry, which is higher symmetry than the FCC structure. However, tetrahedrons join to form decahedron or icosahedron, the geometric structure does not fit perfectly and leaves gaps between tetrahedrons which requires each tetrahedron to expand slightly to fill the gap. The further away from the centre, the more expansion needed to form complete polyhedron. Furthermore, the decahedron is not energetically favourable because of its high surface area. These structures are not seen when crystals have grown above a certain size, due to the internal strain and high surface-volume ratio.
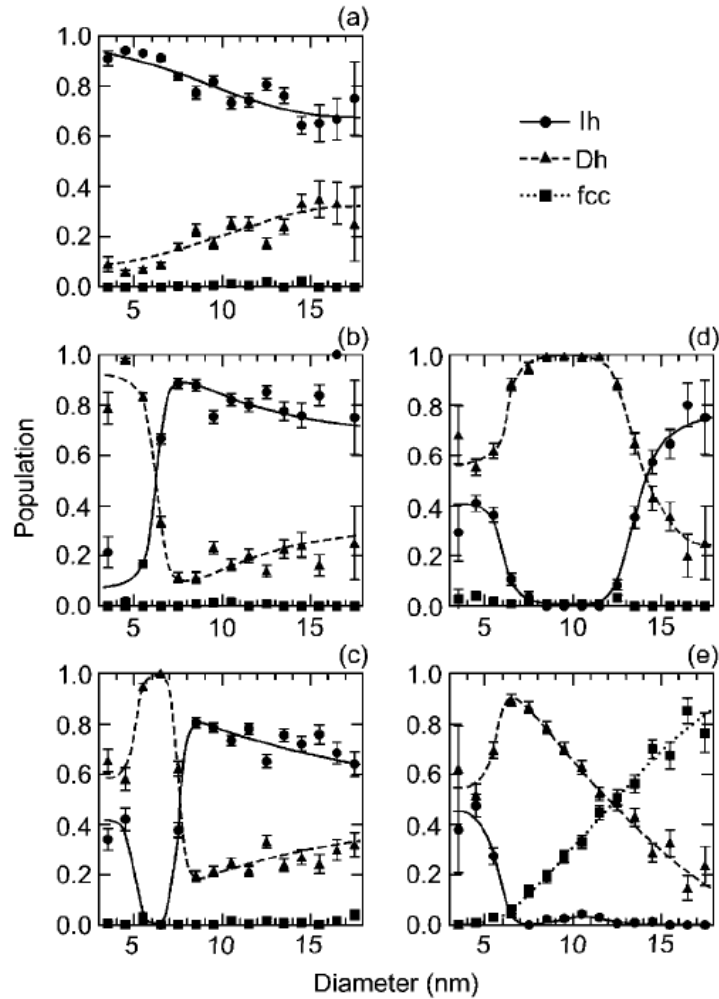
Figure 1.13: Graphs show the relative proportion of different structures (-●- I_h, -▲- D_h, and -■- fcc) as a function of cluster size (a) as prepared, or after annealing to different temperature (b) 1173 K, (c) 1223 K, (d) 1273 K, and (e) 1373K.[39, 40]

Structure of nanoclusters are observed in experiments for both gold[39, 40] and palla-

dium. [41] The existence of FCC, icosahedron, and decahedron structure were confirmed when the size of cluster is smaller than 7 nm. In both studies, nanocluster were prepared on amorphous carbon TEM grids. Some interaction from unpaired bonding from the amorphous carbon is sufficient to Immobilise the nanoclusters but the effect on the structure of nanocluster from the orderliness of carbon film was kept to minimum[42]. The proportion of each structure maybe affected by many different factors. If the preparation parameters are not carefully controlled then the initial proportion of different structures might not Not reflect the process of generation accurately. Experiments leading to structural change through heating have been conducted. On Gold clusters[39], the metastable icosahedron structure was eliminated and transformed to the more energetically favourable decahedron and FCC structures. (temperatures near the cluster's melting point were used)[43] The nanoclusters would again have the chance to enter less energy favourable icosahedron structure when later the temperature goes beyond the melting temperature of a specific size.

1.3.1 Amorphisation of metal nanocluster
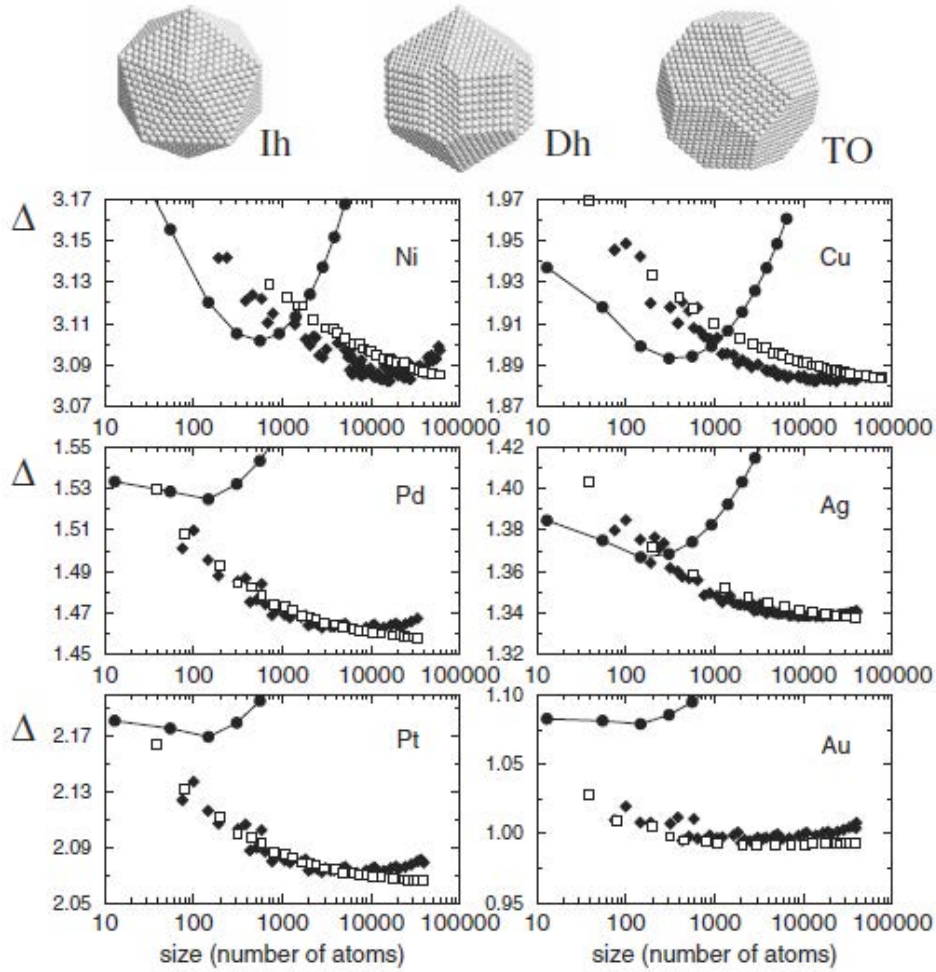
Figure 1.14: The relative energy as function of number of atoms in the cluster for Ni, Cu, Pd, Ag, Pt, and Au clusters. Three morphologies are taken into account. (Icosahedron ●, truncated octahedron ▢, and decahedron ◆)[44, 45]

The co-existence of different structure from clusters of similar size indicates the configuration energy of forming different structure are close, so when clusters were formed, thermodynamically there was a considerable proportion of clusters in each structure. The structural transformation, on the other hand, is following the trend of configuration energy difference between structures.[44, 45] Atomic structure of free metallic nanoclusters with their size up to 3×10^4 atoms is investigated with tight-bonding semiempirical potentials. Six elements are calculated, group 10 and 11 in d-block, period 4 to 6 (Ni, Cu, Pd, Ag, Pt, and Au). It is found that the energetically most favourable structure between FCC,

I_h, or D_h is size dependent. For Ni and Cu, the cost of configuration energy raised rapidly when the size is larger than 600 atoms, but the configuration energy of I_h structure can still be more favourable than other structures under ~1000 atoms. Decahedron, another five-fold symmetry structure, constantly has lower energy cost than FCC when the size of cluster is smaller than 12000 atoms in this study. At the highest mass investigated for all six elements in this study, FCC is the lowest energy structure which agrees with the fact that the crystal structure for these elements in bulk is FCC. On period 5 and 6 elements investigated, I_h structure keeps having higher configuration energy than FCC and D_h structure which makes I_h less accessible. This is also confirmed with detection of icosahedron and decahedron structure for free Cu, Ni, and Ag clusters within a limited size range.[46, 47, 48, 49]

Cluster that lack of long-range order are considered as amorphous, which is rarely tackled due to the difficulty in defining them. However, small Pd nanoclusters with amorphous structure are observed in experiments.[41, 50] Amorphous structure could be the most stable structure for small gold clusters (38, 55, 75 atoms, size between 1 and 1.5 nm) in calculations.[51] Direct imaging with electron microscopy on Au_{55} clusters is conducted to provide more information on the structure of small gold clusters. In this study, size-selected Au_{55} clusters are soft-landed onto an amorphous carbon film. Au_{55} clusters are observed with both a chiral and amorphous-like structure.[32] The chiral structure is investigated in calculation to approach their actual structure.[52] It is found that the chiral structure is a slightly twisting structure that adopts five-fold (I_h cap) and six-fold symmetry (FCC packing) at two ends. In other studies, they were also trying to tackle similar problem of amorphisation.[53, 54, 55, 56] In this study the amorphous structure of Pt_{55} is found to be more favourable than the I_h structure (while under 600 K). Furthermore, the key step of symmetry breaking from I_h structure to amorphous "rosette" structure in calculation is to squeeze one more atom to join those five atoms surrounding the five-fold axis apex.

1.3.2 Structural transformation and melting point depression
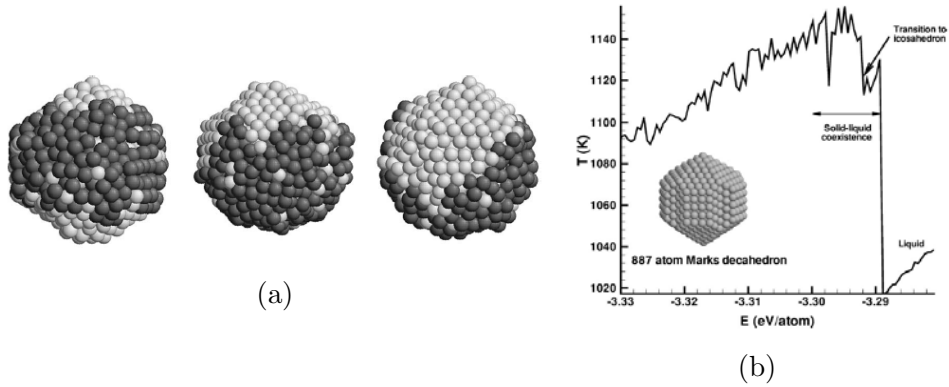
Figure 1.15: (a) Atomic model snapshot from molecule dynamics calculation if coexisting state of decahedral structure (left), the nearly complete molten condition (centre), and icosahedral coexisting state (right). (b) The caloric curve of an marks-decahedral Pd nanoclusters that contains 887 atoms. Graph represented as temperature as a function of energy per atom. coexisting state and melted liquid state are labelled.[57]

The structural transformation is closely related to the melting point of the nanocluster.[39, 40] Various reasons have been proposed for the phenomenon that affects melting point on nanoclusters were proposed. Firstly, when the size of material is reduced to the nanometer range, the melting point would start to lower from their bulk melting point. Take gold for example, when the particle size drops below 10 nm, the melting point starts to reduced significantly (~1200 K at 10 nm) from their bulk melting point at 1337 K.[43] The melting temperature is strongly related to particle size, but clusters of similar size could shift to higher value by attaching to periodic support.[44] Studies also showed that melting temperature can be significantly lowered by incorporating hydrogen into the metal nanoclusters.[58, 59, 60] The measurement of melting point of nanoclusters is obscured by structure transformation. As the result, to pinpoint melting point under microscopic conditions, molecular-dynamic simulation were employed to study that the temperature a nanocluster starts to lose their long range order. High symmetry crystal structures were put into calculations of different simulated temperature to observe the process from solid to molten states.[61, 57] In these studies it is found that structural transformation could also take place through a partially melted state where liquid and solid (which maintains

their initial clusters structure) coexist. This coexisting state was observed on palladium and gold, it requires less energy than full melting. Simulations show that during the transition temperature drops by 70 K and the molten fraction of 887-atom decahedron cluster jumped from 0.3 to 0.5, and this finally stabilised at 0.4 for the rest of the process.

1.4 Ripening and the catalytic reactivity of gold nanoclusters in CO combustion

Since mankind has had the need for energy and materials, research into chemical reactions has never stopped. These reactions could be triggered spontaneously or may require an energy barrier to be overcome according to the reactants and the specific product that is aimed for. In the case where the chemical reaction is slow or non-spontaneous, a catalyst can be added into the system to increase the speed of reactions, or lead to the production of a desired product. The progress of research into chemical physics is such that chemical reactions have been studied at the atomic level where they are understand to only involve a few reaction sites, consisting of only a small number of atoms on the catalyst surface. This microscopic aspect also come from the discovery of the unusual properties of ultrasmall nanoclusters. Take gold for instance, gold has long been considered as inert material that does not react with other chemicals nor catalyse other reactions. However, these are properties of gold in its bulk form. Ultrasmall gold clusters have unusual chemical and physical properties that are worth to investigate in order to understand the origin of catalytic ability. The idea of catalyst ageing can also be studied in microscopic viewpoint in clusters. When nanoclusters are introduced to chemicals or simply heated during annealing, they can easily undergo disintegration, diffusion, and aggregation due to their lower coordinating number. The quantity and condition of reaction sites will be significantly modified as a result of the changing cluster morphologies.

1.4.1 Catalytic ability of gold nanoclusters
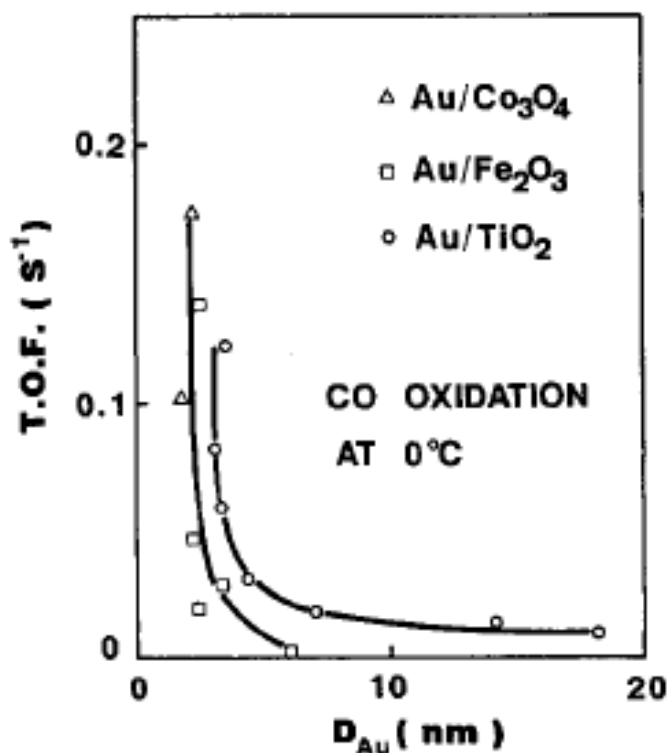
Figure 1.16: Reactivity of gold supported on different substrates. Turnover frequency is calculated for CO oxidation rate at $0\,^{\circ}C$, based on the number of atoms on the surface under given average diameter gold particle.[62]

Ultradispersed metal clusters were found to have unusual catalytic reactivity in the pioneering research conducted by M. Haruta.[62] Clusters investigated in this research were prepared in deposition-precipitation method and supported on TiO_2, α-Fe_2O_3 and Co_3O_4 non-crystalline oxides. The morphology of gold nanoparticles attached to the oxides is hemispherical. Nanoparticles of various sizes were tested for their catalytic activity, which increase sharply with decreasing size, when the average diameter of nanoparticles is smaller than 5 nm. At $0\,^{\circ}C$ gold nanoparticles can already oxidise CO with high efficiency is also another main discovery of this research. Since gold was always considered as very inert material that does not participate or assist in most chemical reactions, the mechanism of catalytic activity on nanoparticles is particularly interesting. Different annealing temperature also affects the reactivity of gold nanoparticles. It was proposed in

this study that the edge between cluster and oxide accounts for most of the catalytic activity. It also come to Haruta's notice that the different annealing temperature the nanoparticles reached in preparation would change their catalytic ability.
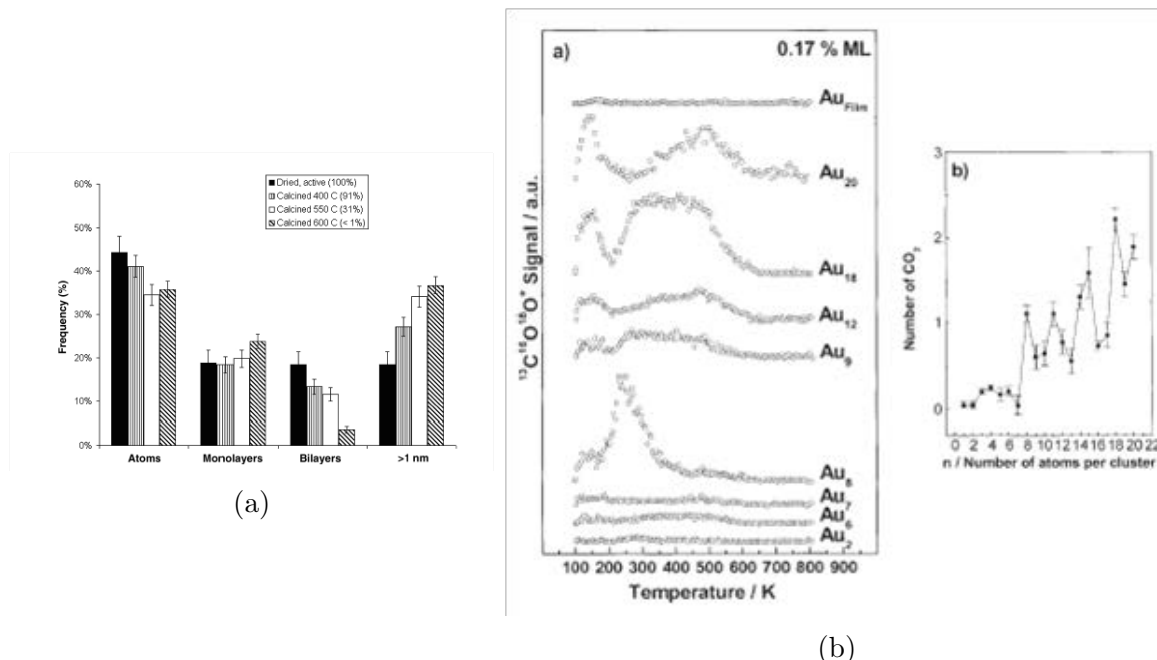
Figure 1.17: (a) Population of gold nanoclusters supported on iron oxide that undergoes different calcined temperature(Bar marked as different pattern). Gold particles are divided into four groups in statistic. (i) Single atoms. (ii) Monolayer Gold clusters with diameter of 0.2 to 0.3 nm. (iii) Bilayer gold particles with 0.5 nm diameter. (iv) Gold nanoparticle with diameter larger than 1 nm.[63] (b) Temperature programmed reaction of CO oxidation on small Gold nanoparticles ranging from 2 to 20 atoms. ^{13}CO and $^{18}O_2$ were saturate condensed on gold nanoclusters at 90 K. Temperature programmed start recording between 100 K and 800 K with $^{13}C^{16}O^{18}O_2$ signal recorded.[64]

Since the unusual reactivity of gold nanoparticles is related to the fact that they are ultrasmall in size, different synthesis techniques and substrate material were used is an attempt to control the size and structure of these nanoparticles. Microscopy was applied to characterise nanoparticles subsequent to preparation and the sample were sent to chemical reactors to test their catalytic ability afterwards. This set of procedures comprise a general approach of catalytic research. In this research they were trying to answer the question of which size of nanoparticle is the most reactive. Since nanoparticles in the research are not freely suspended in gaseous reactants, how the substrate affects the reactivity was also investigated. In Fig.1.17 (a) was shown a study of active gold nanoclusters

supported on iron oxide. Samples were tested for their catalytic ability in standard condition with 0.5 % by volume of CO at 25 °C , the same sample was also characterised with aberration-corrected HAADF-STEM to the reactivity to the cluster size distribution. The size distribution was varied by different temperature samples reached during calcination. The sample that has the highest conversion rate of reactant to product ($\sim$100%) is the as prepared sample which has the highest relative population of bilayer nanoclusters of 0.5 nm in diameter. After calcination that reached 600 °C , bilayer nanocluster diminished coinciding with a drop of conversion rate to less than one percent. Although there were still monolayer (0.2 to 0.3 nm) or larger ($>$1 nm) nanocluster, they were not considered to account for the reactivity attained by the uncalcined sample.[63] In Fig.1.17 (b), another investigation with atomic precision gold nanoclusters, this time supported on an MgO(110) film showed that only specific size of gold clusters, were able to catalyse CO. In this study, size-selected laser vaporised gold clusters were deposited on a defect-rich MgO(110) surface with kinetic energy in the soft landing range ($<$0.2 eV/atom). Temperature programmed reaction experiments with ^{13}CO and $^{18}O_2$ as isotopic marker were conducted on Au_n (n$<$20). The signal $^{13}C^{16}O^{18}O^+$ was monitored over the temperature range between 100 to 900 K. Au_3 to Au_7 was almost completely inert with a steep increase in reactivity on Au_8 was observed. Further increasing in size, Au_9 and Au_{12} became relatively inert again. For Au_{18} and Au_{20}, intense bifurcating peaks separated at 250 K were observed which indicates strong catalytic reactions. Finally a gold film was tested and found to be inert as expected.[64]
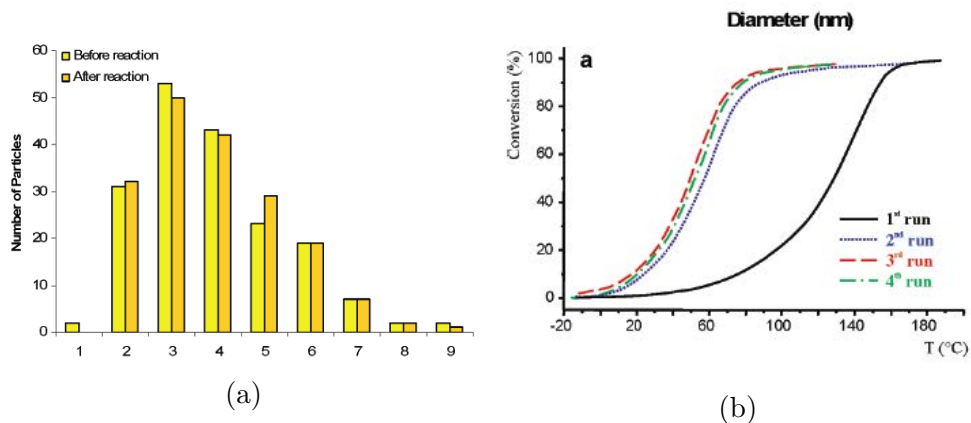
Figure 1.18: (a) Size distribution of glucose protected Au/TiO$_2$ catalyst before and after chemical reaction. (b) Activity result recorded as CO oxidation conversion rate over four runs of temperature cycles.[65]

A separate study aimed at different aspects was conducted.[65] Firstly, the difference between reactivity of similar size of gold nanoclusters on different substrates. Secondly, the effect of calcination nanocluster size. Shown in Fig.1.18, catalyst under investigation was prepared through colloidal deposition onto different substrates. Imaging with transmission electron microscopy was carried out to characterise the size of nanoclusters before and after chemical reactions. The result were that the size of nanoclusters were stable in temperature cycles. The reactivity of the first cycle is the lowest across all substrates due to the removal of protecting agents. In the subsequent cycles the nanoclusters became reactive and there reactivity remained constant through four temperature cycles. Due to the focus on the effect of support, size of nanocluster on different support were made similar with average size of 2.8±1.1 (Au/ZnO), 3.0±1.3 (Au/TiO$_2$), 3.1±1.3 (Au/γ-Al$_2$O$_3$), and 2.8±1.2 nm (Au/ZrO$_2$). The size distribution after temperature reaction cycles was characterised to be almost unchanged. However, under these conditions, gold nanoclusters of similar size on different supports demonstrated different catalytic ability. T$_{1/2}$ (temperature where the given catalyst has 50% conversion rate to the specific reactant) on Au/ZnO, Au/TiO$_2$, Au/γ-Al$_2$O$_3$, and Au/ZrO$_2$ were 50 °C , -13 °C , -11.6 °C , and 74 °C , respectively. Among them, gold on a γ-Al$_2$O$_3$ support, which is poorly reducible, demonstrated unexpectedly high reactivity that approached the reactivity achieved by

33

Au/TiO$_2$. This contradicted the conclusion in the previous studies and might suggest that the reducibility of a substrate is not the only factor influencing the reactivity of gold nanoparticles supported on it.[65] In this study, it was also pointed out that the geometry of the attached metal nanoparticles may differ significantly from that in the colloidal state, with the degree of structural variation depending on the substrate used. This might be the reason for the different demonstrated reactivity between substrates. It is found through investigation of catalytic ability of nanoparticles after calcination that subsequent to preparation the reactivity drops (T$_{1/2}$ increases) with increasing calcination temperature. The calcination temperatures were chosen to be between 330 °C to 550 °C , which is higher than the highest temperature reached in the temperature programmed reaction cycles. Aggregation leading to larger clusters was observed in the TEM images.

In summary, reactivity of gold nanoclusters is size dependent and nanoparticles become very active when they are dispersed to a few nanometer in diameter. However, the reactivity of gold nanoparticles of a single size is greatly affected by the material of oxide substrate used. The relationship between reactivity and type of substrate is not monotonically dependent on the reducibility of oxide support.
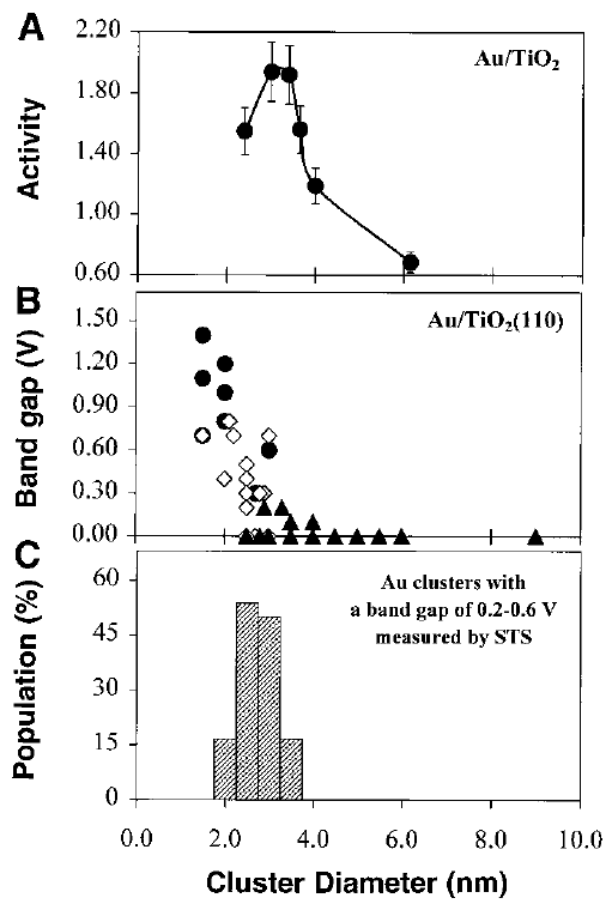
Figure 1.19: Activities and its corresponding measurements of gold nanoparticles as a function of particle size. (a) CO oxidation reaction activity at 350 K on TiO_2-(1×1). (b) Band gap measurement with STS. (c) Size distribution of gold nanoparticles.[66]

In order to understand the origin of the activation of nanoparticles' reactivity, single crystal Titania(110) supported gold nanoclusters were investigated, by scanning tunnelling microscopy. The height and diameter were precisely measured with scanning tunnelling microscopy. In addition, scanning tunnelling spectra were recorded. Turnover frequencies (number of CO molecular oxidation react per second) of these supported gold nanoparticles for oxidising carbon monoxide were presented as a function of the average size of the Au clusters measured by TEM. The relationship between reactivity and band gap measurements were connected with particle size measurement from STS. Gold clusters appear to be the most catalytically capable when their band gap is between 0.2 and 0.6 eV. The thickness of clusters with band gaps of this range were two Au atomic layers, with a diameter distribution peaking between 2.5 to 3.0 nm. This research showed that

35

clusters that are most reactive have a very specific diameter and thickness. Scanning tunnelling spectroscopy also shows a similarity to the band gap for these active clusters. This suggests the activation of reactivity is depending on the interplay between geometric and electronic structure.[66]

Further evidence for this trend is revealed in an experimental and theoretical study of the small Au clusters (size smaller than 20 atoms) supported on defect-rich magnesia.[67] In this study, temperature programmed reactions were conducted and $^{13}C^{16}O^{18}O^+$ was monitored, in order to distinguish carbon dioxide catalytically produced by the substrate from that produced by gold nanoclusters. Firstly, no $^{13}C^{16}O^{18}O^+$ signal was found in TPR of CO oxidation on defect-rich or defect-poor magnesia without gold nanoclusters. Subsequently, similar TPR experiments on Au_8 clusters supported on a magnesia substrate showed the production of no $^{13}C^{16}O^{18}O^+$. Moreover, defect-rich magnesia supported Au_8 is found to be more active than defect-poor magnesia supported ones. This indicates that the effect of the substrate was not simply disperse the metal nanoclusters, but also plays a more important role in affecting the catalytic ability of nanoclusters. Further investigations of this system were conducted with ab-initio simulation wich was used to determine the optimal structure geometric and electronic structure of Au_8 clusters, and the energy barrier of a possible reaction pathway. In the optimisation of gold octamer clusters, charge transfer of ∼0.5 e into the clusters was confirmed using DFT calculations. This charge transfer provides a binding energy of 5.56 eV for the gold octamer on the defect-rich magnesia surface. The binding energy of Au_8 to defect-free magnesia was reduced by 2.2 eV and structural deformation is less than on the defect-rich surface. It is also found in earlier investigations that reactivity exhibits size-depedent pattern. Only anionic gold nanoclusters formed of an even number of atoms (size between 4 and 20 atoms) can react with gaseous oxygen.[68, 69]

Being able to chemically adsorb reactants is crucial to initialising catalytic reactions. For Au_8 in this study, nanoclusters formed a deformed two layer structure with 5 atoms in the first layer and 3 atoms in the second layer. the second layer of the cluster is triangular

in shape which provides two binding position for molecular oxygen on top of the facet. Except for the top facet, oxygen can also be adsorbed at the interface of Au/MgO in the ab-initio calculation. Calculations of the binding energy where preferred for vacancy adsorption sites. As well as providing an adsorption energy of 0.80 to 1.85 eV, the bond between oxygen atoms is also stretched from 1.24 (oxygen in gas phase) Å to 1.41 to 1.46 Å at adsorption. The adsorption of CO takes place on an Au atom on the top facet of the Au_8 cluster with a small stretch from 1.13 Å to 1.14 Å. Following the co-adsorption of CO and molecular oxygen on gold nanoclusters, the oxidation reaction proceeds spontaneously to carbon monoxide and releases 4.8 eV of energy. This study reveals the initiating and limiting factor for catalytic reactions on gold nanoclusters. The surface of nanoclusters, high proportion of surface atoms with low coordination number, the charge transfer to or from the substrate which varies electronic structure of the clusters, allows it to become feasible for all reactant involved in the reaction to adsorb on the cluster. Geometrically the reaction site of the two reactants have to be within reach to each other. When the adsorbed reactants react or during the adsorption, there will be energy barriers for these reactants to overcome. This implies an activation temperature and also limit the rate atomically the reaction can proceed. If the desorption temperature is lower than the activating temperature, or the nanoclusters are not stable at elevated temperature, the catalytic reaction would not be able to take place.
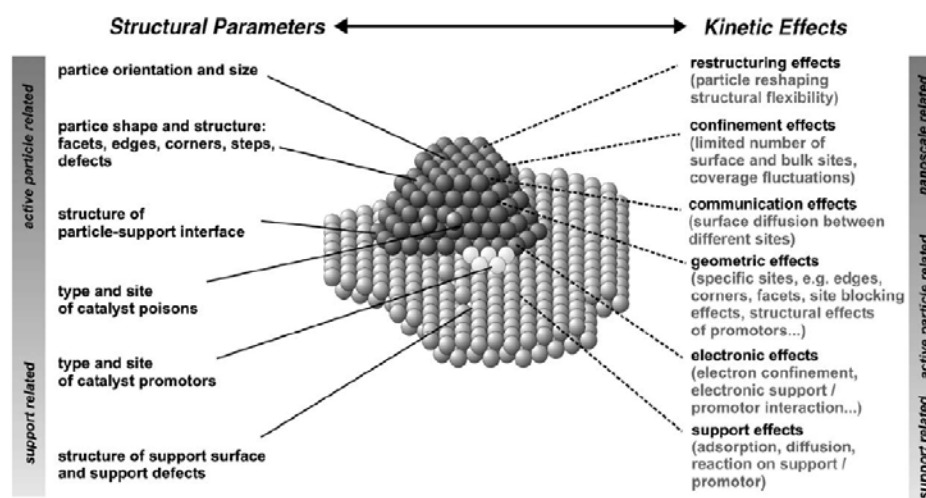
Figure 1.20: Summarising the factors that affects catalytic ability of supported metal nanoclusters.[70]

When discussing the catalytic ability of nanoclusters, it is often convoluted of several factors which determines the final behaviours of the cluster. Libuda et al provide a detailed summary of these factors affect catalytic activity.[70] Because clusters are in the nanometer size range, a high proportion of atoms become exposed as surface atoms. The basic concept behind microscopic catalytic reactions is that adsorption and the following reactions occur on reaction sites that involves 1 surface atom (on-top site), 2 surface atoms (bridge site), or 3 surface atoms (three-fold hollow site). Additionally, facets of different Miller index would have different reaction properties because they expose different types of reaction site. On the joining part of facets and interface atoms would have low co-ordination number on edge, vertices, which would also provide reaction sites of different electronic structures. When the size of clusters is small, the proportion of atoms with low coordination number increases so the effect of these minority reaction sites become significant. Moreover, the distance between two different reaction sites or two different facets becomes small when the size of clusters is small, the combined effect multiple of active sites and facets should also be considered. Impurities and defects could also play a role in catalytic reactions. For instance, incomplete chemical reactions might leave residual atoms like atomic carbon on the surface, that forms strong bonds and occupies reaction

sites. This eventually disable the catalytic ability. Impurities could also be added to the substrate or onto the clusters deliberately, as a promoter to alter the electronic structure.

1.4.2 Catalytic ability of non-supported gold nanoclusters

The strong interactions between clusters and the metal oxide substrate would affect the size and distribution of clusters by affecting diffusion and coalescence processes. The interaction between substrate and cluster could also cause the cluster to deform and make the clusters become island-like in shape. Interactions between cluster and substrate also change the electronic structure through charge transfer from or to the cluster. As a result, the catalytic ability of free clusters might be different from supported clusters. Furthermore, at specific sizes, electronic or geometrically closed shell structures formed on these standalone clusters requires reinvestigation because they would have a different structure from supported clusters.

In [71], oxidation resistance is found in Au_{55} magic size clusters. Reasonably well size-controlled gold nanoparticles with size range from 1 to 8 nm were deposited on silicon wafers. X-ray photoelectron spectroscopy was then employed to measure the oxidation resistance of clusters'. Au_{55} magic clusters were stabilised by $(PPh_3)_{12}Cl_6$ and clusters of other sizes were prepared by macromolecules self-organising in a micelle. After deposition onto the silicon wafer, oxygen plasma was used to remove the polymer matrix. The Au-4f spectrum was measured in order to monitor the degree of oxidation of gold atoms. It is shown, after extensive radio frequency (rf) oxygen plasma oxidising, that all sizes of gold clusters (both bigger and smaller than Au_{55} clusters) underwent different degrees of oxidation but that Au_{55} clusters only exhibit metallic peaks. This extraordinary oxidation resistance cannot be attributed to size dependent energy gap opening at Fermi level, because Au_{55} clusters still appear to have metallic electronic behaviour.
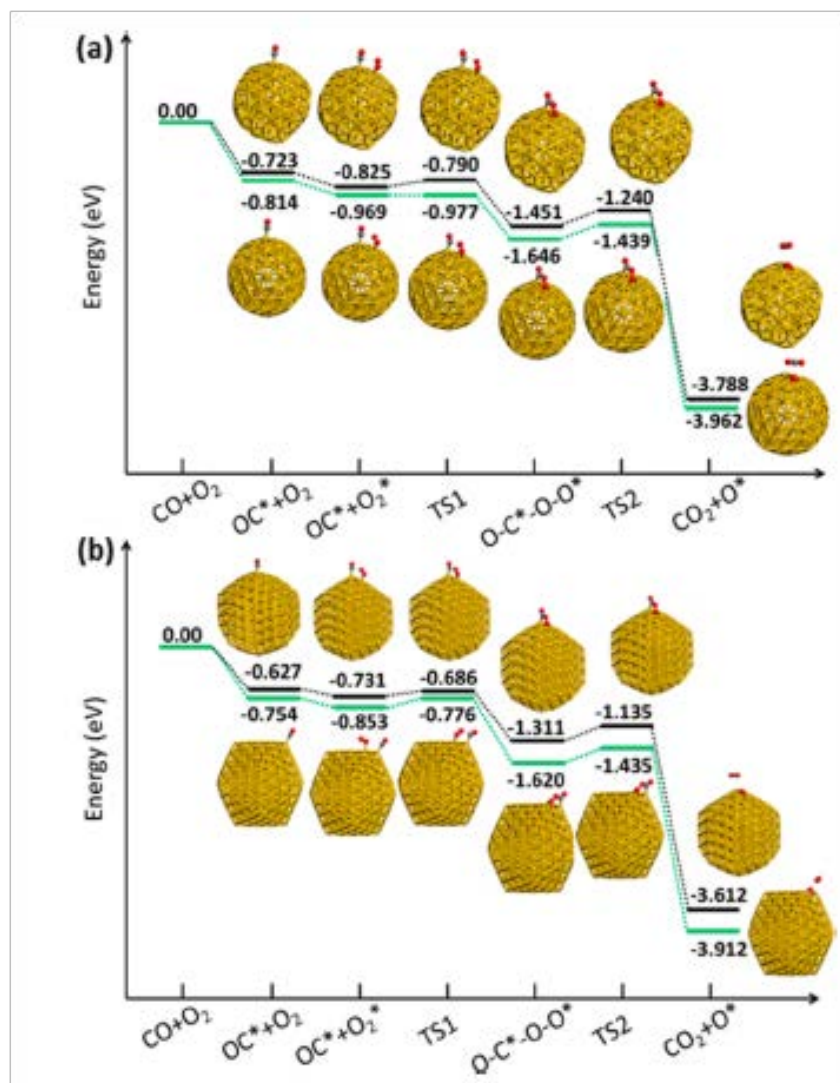
Figure 1.21: Reaction pathway of CO oxidation and energy corresponding to each steps on (a) Au_{147} and (b) Au_{309} I_h clusters. Green pathway stands for I_h structure and black pathway the reconstruct I_h structure. Star symbol superscripting by the CO and O_2 indicates molecule adsorbing on the gold cluster.[72]

Recently, a comprehensive study using density functional theory to investigate the stability and catalytic ability for CO oxidation reaction of magic-number Au clusters ranging from 1 to 3.5 nm was conducted.[72] In the three high symmetry structures considered, (icosahedron, decahedron and cuboctahedron), the trend of stability is $I_h > D_h > O$. However, the energy difference between structures is reduced to less than 4 meV/atom at the largest size calculated Au_{923}. This suggest that, since the stability is similar between different structures, the population of different structures could be similar for this size.

In addition to calculation toward the optimised structure of different magic-number sizes, CO oxidation reactions were conducted on the optimal structures previously calculated for I_h-Au_{147}, I_h-Au_{309}, and reconstructed atomic models for these two magic-numbers I_h clusters. Firstly, when investigating CO adsorption, CO is found to bind strongly on vertex sites than on edge site for I_h-Au_{147}. On larger I_h-Au_{309} clusters the trend is similar but the energy difference between vertex and edge adsorption sites is reduced. On the contrary, the more energetically favourable reconstructed I_h models showed weaker adsorption when compared with their higher symmetry counterparts. Secondly, it is found in DFT calculations that molecular oxygen is weakly bond to the surface of Au_{147} and Au_{549} clusters, but this adsorption could be assisted by CO molecular binding on the neighbouring site and thus the adsorption energy reduced. To complete the CO oxidation reaction, two molecules have to overcome two energy barriers. The first one is to form a OCOO bridge-like intermediate compound where CO is bond on a vertex and molecular oxygen is attracted by the carbon atom from its binding position on an edge site. The second barrier is for the CO molecule to acquire an O atom and form CO_2. Following the formation of carbon dioxide, the final process in the calculation is the desorption of CO_2, leaving an oxygen atom on the surface. In summary, through DFT calculation of the optimal structure of magic-number gold clusters from 147 to 923 atoms and the investigation of the complete reaction pathway for CO oxidation following that, it is demonstrated that magic-number clusters around 2 nm have the capability to serve as effective catalyst for CO oxidation reaction under the condition that no substrate is involved.

The relation between chemisorption and electronic shell structure in Au clusters, including geometric reconstruction, was studied with DFT and effective medium theory[73, 74]. In this study, magic-number gold clusters were found to open up large band gaps. Clusters with a number of atoms near a magic-number would have the tendency to deform significantly in order to compensate the band structure energy extra electrons have to fill in. Further, in terms of chemisorption of an oxygen atom, electronic magic number clusters were found to make up to 1 eV of adsorption energy difference compared

to non-magic number clusters. Magic number clusters behave like inert gases due to the electronic closed-shell structure and are not reactive with oxygen. Clusters with a number of atoms close to magic numbers were halogen-like and alkali-metal-like.[75]

1.4.3   Nanoclusters ripening

Ripening of gold nanoclusters in vacuum

Properties of nanocluster are highly dependent on their structure[76]. As a result, ripening of nanoclusters is just as important. In the early studies, observation focused on the collective behaviour or distribution of supported nanoparticles due to the challenging of the nature of microscopic control or imaging at that time. The mechanism of nanoclusters ripening is the topic that those studies that were trying to resolve.[77, 78, 79, 80, 81] In these studies, metal was evaporated onto the surface and allowed to freely diffuse on the surface. By the means of which surface metal atoms aggregate, ripening processes can generally be divided into two mechanisms: (i) Ostwald ripening - particles formed can undergo disintegration under the conditions provided, single atoms leaving the particles can transfer through diffusion on the surface join another particle; (ii) Smoluchowski ripening - particles formed were not undergoing disintegration under the conditions provided, particles on the surface can only diffuse and coalescence to another particle as a whole particle. Through different ripening mechanism, the size distribution of particles could be different shapes. For coalescence growth, a statistical model was established under the assumption that only two particles can coalesce in one collision incident.[77, 78] An asymptotic model that is basically an asymmetry gaussian distribution tailing to the larger size direction is predicted base on these assumptions. On the other hand, for the Ostwald ripening mechanism, an asymmetry distribution is also predicted but tailing to the direction of smaller particle size. (Fig.1.22)
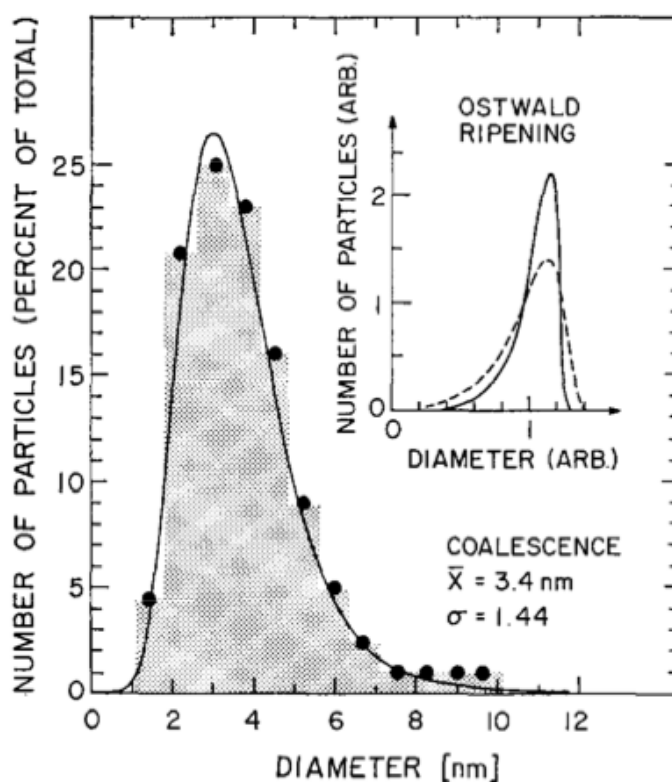
Figure 1.22: Figure is showing the number of particle as a function of diameter of the clusters for Smoluchowski ripening and Ostwald ripening(inset).[78]

A microscopic viewpoint was provided by observing evaporated Ag atom onto highly oriented pyrolytic graphite (HOPG) with scanning electron microscope (SEM).[82, 83, 84] Evaporation was performed at 20 °C and nanoclusters formed on the surface subsequent to that were observed with SEM at initial and elevated temperature. Clusters of various size from 1 to 10 nm were formed both on terraces and on steps of the HOPG. A denuded zone about the step and the irregular size of clusters on the steps indicate that cluster diffusion can happen at room temperature. Following a raise in the temperature to 120 °C , clusters were found to be able to diffuse along the steps at 50 °C to 90 °C . At 120 °C , there was some evidence that showed clusters previously fixed on the steps could escape to diffuse on the surface. This suggests the steps were providing a high constraint in fixing clusters. Clusters that were freely diffusing across the surface at room temperature were trapped by the steps and it was not until the whole system was brought to higher temperature, that these clusters that were previously trapped by steps could start to diffuse along or,

break free from the steps. This has been further proven in subsequent studies[85, 86], if Ag clusters that were formed in gas condensation prior to deposition were deposited with high kinetic energy, clusters are found to deform when colliding with the HOPG surface and when the impact energy is higher than a critical value proportional to the size of the cluster, they would create a point defect at the place where they impact on the surface. This would lead to the elimination of diffusion of clusters deposited at room temperature. In short, coalescence growth is significantly affected by the interaction between clusters and the substrate. Clusters can freely diffuse on the graphite surface unless encountering steps at which they become trapped. In addition, point defects created by the energetic collision of metal clusters can fix them at the position of collision and prevent them from diffusing.

Means of ripening other than coalescence growth are observed for kinetically pinned Au_{70} clusters on HOPG.[87] Au_{70} is accelerated before depositing on HOPG with energy up to 1700 eV (24 eV/atom). Similarly to pinned Ag clusters, surface diffusion was not observed from room temperature to 413 K. When the annealing temperature went above 413 K, some clusters on the surface start to grow while other clusters shrink in size. However, cluster diffusion were not observed at this stage. A further increase in annealing temperature to 873 K, the results in clusters leaving their trapped site and diffusing to regroup to surface steps. In summary these studies show that the stability of metal clusters on the HOPG surface can be increased by energetic pinning, thus leading to eliminated surface diffusion at room temperatures or higher. In ultrahigh vacuum conditions, through annealing alone, clusters can be driven from the line defect at HOPG steps, or collision-created point-defects eventually. Nevertheless, if the defect sites trapped the clusters strongly before the cluster can diffuse, they may experience other ripening processes: for example, some clusters could lose atoms while other more stable clusters absorbing them and grow larger.

(a) Graphene/Rh(111)

(b) Hexagonal boron-nitride covered Rh(111)
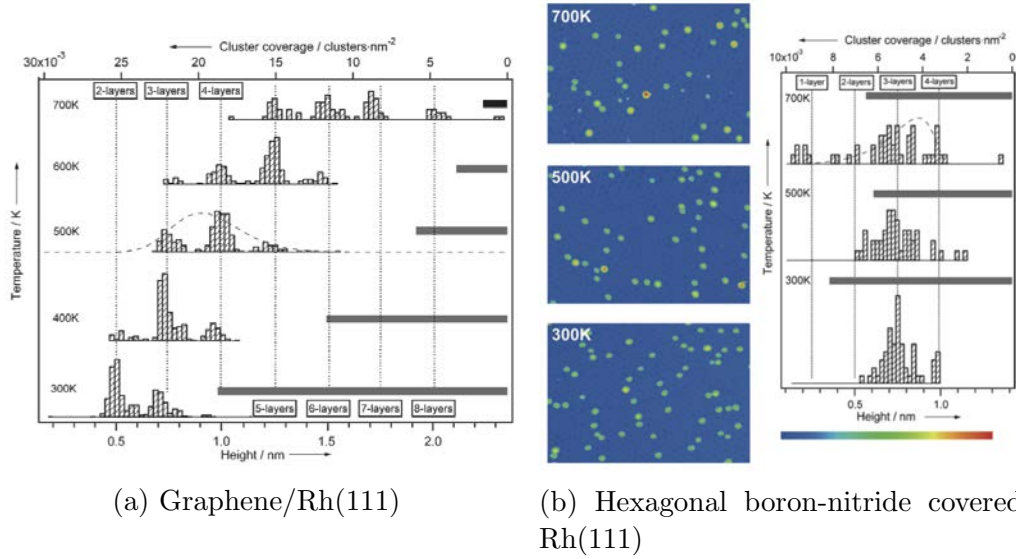
Figure 1.23: Figure is showing the stepwise ripening results for Pd_{19} clusters on (a)graphene/Rh(111) substrate and (b)hexagonal boron-nitride film covered Rh(111). In each figures the size distribution of clusters is presented as the number of clusters as a function of the height of cluster. Distribution of clusters that underwent different temperature in annealing are listed horizontally. Vertical dash lines label the height of different number of layers.[88]

A comprehensive study with regard to both modes of ripening was done on Pd_{19} clusters deposit on the graphene-moiré covered Rh(111) and hexagonal boron-nitride film covered Rh(111) surface.[88] This study utilises different surface materials to observe substrate-dependent ripening mode changes under elevated temperature in ultra-high vacuum conditions. To begin with, palladium clusters were deposited onto the graphene/Rh(111) surface with soft landing energy at 300 K, followed by STM imaging at the same temperature. The height of the Pd_{19} clusters was measured to be two to three atomic layers, which means no flattening during deposition. The height of the clusters was statistically analysed and plotted to give a distribution of the number of clusters with each height. In Fig.1.23, cluster statistics at 300 K, which was the sample as prepared. They show a bi-modal distribution, with peaks centred at 0.5 and 0.7 nm. These correspond to clusters with two or three layers. The sample was then annealed at higher temperature for 5 minutes before being imaged after cooling with STM. Anneals were performed in 100 K increment between 300 K and 700 K. The results of annealing

45

were that the height of the clusters increased monotonically. This clearly indicates the ripening process. In addition, the peaks in the histograms remain distributed in a discreet manner with peaks centres located at the height of every integral number of layers of Pd atoms with a shift in the distribution to clusters with greater height.

On the other hand, when identical Pd_{19} clusters are deposited on boron-nitride-Moiré covered Rh(111) and heated to a range of temperature between 300 K and 700 K, another ripening mode is observed. Under heating, clusters that began with a distribution centred at three atomic layers, did not grow higher as on graphene/Rh(111). Nevertheless, the distribution gradually flattened out under elevated temperature. After annealing to 700 K, some very small particles appeared on the surface as shown in Fig.1.23, indicating cluster disintegration. Due to the strong binding between the Pd_{19} clusters and h-BN/Rh(111), Pd clusters underwent Ostwald ripening. On the contrary, identical Pd_{19} clusters on graphene/Rh(111) would go through Smoluchowski ripening and merely start to experience Ostwald ripening at 600 K or higher temperature. Summary, the energy barrier for cluster diffusion or disintegration is affected by the size of the clusters, and the material and structure of the substrate. The ripening mode changing is an result of a competition of energy barriers, with whichever mode of ripening that has the lowest energy barrier being selected. However, under higher annealing temperatures, both modes of ripening can occur simultaneously.

To compare the cluster-substrate interaction, structure of Au nanoclusters deposited on amorphous carbon and MgO crystalline were investigated using HREM.[42] On a commonly used amorphous covered copper TEM grid, Au nanoclusters generated from a laser-evaporation cluster beam source were deposited with about 0.5 eV/atom (low-energy cluster beam deposition) after MgO crystallines were first placed on the same grid. Gold clusters could be free standing on amorphous carbon or MgO crystal, and the interaction between substrate and clusters could be investigated by observing how the structure and orientation of the clusters was affected by each substrate. On graphite, due to all available bonds being saturated, the interaction between clusters and substrate is

weak enough for the clusters to diffuse at room temperature.[89] On the contrary, on the amorphous carbon films, more unoccupied bonds would be available from the disordered carbon structure, thus the interaction is strong enough to immobilise clusters at room temperature. Finally, when Au clusters were deposited on the (100) surface of an MgO microcrystal, clusters formed octahedral structures and exclusively aligned with the MgO lattice in the $[111]_{MgO}//[100]_{Au}$ direction. Au clusters was also found to dilate or contract in order to compensate the lattice distance difference between gold and MgO. Compared with the MgO substrate, Au clusters on amorphous carbon were randomly oriented and both cuboctahedron and decahedron structures were observed.

A few studies about cluster ripening or diffusion on amorphous carbon are worthy of notice[90, 91]. In these studies, gold clusters were soft landed on the surface at room temperature in a ultrahigh vacuum and heated after deposition to 150 °C , 300 °C , and 450 °C . With an average size of 1.5 nm as prepared, gold clusters gradually increase their size to ~3 nm as the annealing temperature increases to 300 °C . However, when the annealing temperature reaches 450 °C , the average size of the clusters decrease while the cluster density increases. This suggests that the Ostwald ripening mechanism occurs for the given size of gold clusters on the amorphous carbon surface.

Ripening of gold nanoclusters in gaseous and reaction conditions

The simplest practical environment for observing how clusters could sustain ripening processes when not in UHV is in atmosphere.[92] Small gold clusters (number of atom <20) were deposited onto an amorphous carbon substrate with low deposition energy. Subsequent to the deposition, the clusters were stored at room temperature in ambient condition for 32 months and the coarsening process was imaging with TEM regularly during the time it was preserved. Au_n (10≤n≤20) had an initial average diameter of 0.5 nm. The ripening process was seen to occur most quickly in the first 8 months leading to an average diameter of 1.4 nm. From 8 to 32 months, the ripening saturated and slowly approached the final size of 1.6 nm. This provided evidence that an ambient environment

is sufficient to support Ostwald ripening of small gold clusters on amorphous carbon. However, it takes a prolong period of time for the aggregation process to be visible.

It is interesting to see how sintering occurs in air for slightly more complex systems and to extensively study the process in real-time. Pt nanoparticles ripening on amorphous Al_2O_3[93] and SiO_2[94] in synthetic air were studies with *in situ* TEM at 650 °C . Both systems were exposed to 10 mbar of synthetic air and quickly (at 30 °C /min) brought to 650 °C and left there for several hours. During the time of heating, TEM images were taken and the size distribution of the Pt nanoparticles was the main aim of observation. In both systems, sintering of the Pt nanoparticles occurs and, in parallel with an increase in the average size, the size distribution histogram appears transformed from the initial Gaussian distribution to a Lifshitz-Slyozov-Wagner (LSW) distribution[81], This suggests Ostwald ripening is the dominate ripening process. Comparing the two studies, the LSW distribution is more pronounced on alumina than on the silica substrate. Further, the idea of a critical radius was tested in the Pt/SiO_2 study[95, 96]. The idea of a critical radius assume that, during the ripening process, particles reach an size at which it becomes easier to keep an atom than lose it and thus this particle would become stable. It was also proposed in this study that Pt nanoparticle ripening could proceed through the formation of Pt-oxide volatile species.[79, 97]

To study the sintering process in CO, a graphene moiré was epitaxially grown on the Ir(111) single crystal surface and Pt atoms were evaporated onto the surface in the ultrahigh vacuum. These evaporated Pt would spontaneously form nanoclusters on the graphene/Ir(111) moiré. Graphene/Ir(111) was grown to form a hexagonal packing template that allows the Pt nanoclusters to sit on the graphene surface in an array-like, ordered manner. Each of the Pt clusters was confined within an identical site that the graphene moiré provided, but the height of the clusters could be different. The smallest one layer Pt clusters contained less than 10 atoms. When the system was subjected to CO exposure, at 300 K, these small Pt nanoclusters could either hop to a neighbouring vacant site or merge with neighbouring occupied clusters. In addition to that, clusters

larger than 10 atoms were not affected by CO exposure and cluster motion for clusters of such size takes considerably higher temperature in the absence of CO.[98] This behaviour of cluster diffusing as a whole suggests Smoulchowski ripening, which recalls the Smoluchowski ripening behaviour of Pt_{19} clusters on a graphene/Rh(111) moiré at higher annealing temperature and without the involvement of CO.[88]

TiO_2(110) supported Au nanoparticles are observed with STM while being introduced to reactants: O_2, CO, or the mixture of both. The result reveals an accelerated sintering effect in CO/O_2. At 300 K Au nanoparticles have neither mobility nor do they transform under UHV conditions for more than 4h. However in the presence of 0.1 torr of CO/O_2 at 300 K, an Ostwald ripening process is launched. Smaller clusters start to disappear, with clusters around 2.3 Å being eliminated in 28 minutes and clusters around 4.6 Å being eliminated in 2h. The number density of clusters was decreased also. A sample is also introduced to the same pressure of reactant at elevated temperature. At 410 K, most of the Au particles with a height less than 4.6 Å disappeared within 1h and the particle density decreased by 60% to 6.9×10^{11}/cm^2 in the same amount of time. This showed the process of Ostwald ripening is more rapid at elevated temperature. When supported Au clusters of the same initial conditions were exposed to 0.1 torr of oxygen at 300 K for 1.5 hour, little variation was seen. Clusters of 2.3 Å in height remain and the density of nanoparticles is 1.5×10^{12}/cm^2, twice the density after the carbon monoxide oxidation. Previous studies showed the mechanism of the disintegration of some of the metal clusters occurs through the formation of a volatile metal-adsorbate complex. In this study, the gold particles are nearly stable and undergoes a much slower rate of sintering in pure CO than in O_2. Both O_2 and CO would form a metal-adsorbate complex, but only clusters in the CO oxidation reaction have obvious Ostwald ripening behaviour. Furthermore, initialisation of Ostwald ripening could depend on generating enough energy. In a DFT calculation, it is found that each CO_2 production could release 2.9 eV. It is also demonstrated that hot electrons can be generated in a system that comprise a metal film on top of TiO_2 during CO oxidation. The energy released is larger when compared with the Schottky barrier at

the metal-oxide interface which is 0.7 to 1.2 eV.[99]

1.5 Principal of Z-contrast property of HAADF STEM

In order to further explain the Z contrast property of HAADF imaging, the Rutherford scattering model can be used to interpret high-angle, electron-nucleus interaction. Scattering with regard to a nucleus is showed in Fig.1.24.
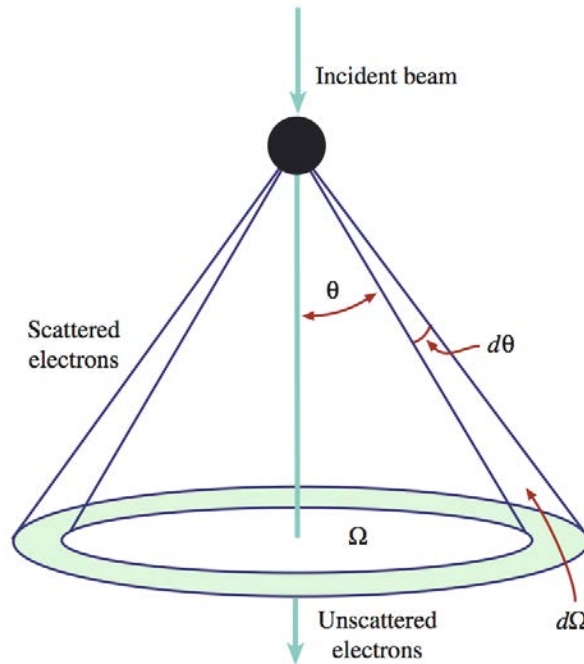
Figure 1.24: Rutherford scattering parameters.[100]

The differential cross section in this high angle scattering scenario is

$$\sigma_R(\theta) = \frac{e^4 Z^2}{16(4\pi\varepsilon_0 E_0)} \frac{d\Omega}{\sin^4 \frac{\theta}{2}}, \tag{1.2}$$

where e is the electron charge, Z is the atomic number of the given element, θ is the direction of the solid angle Ω, ε_0 is the permittivity in the free space and E_0 is the energy of the electrons. However, this result cannot be applied directly without taking into consideration of screening effect from the electron cloud and relativistic modification to the formula. The screening effect is more pronounced for electrons scattered shallowly

near to the edge of the atomic electron cloud. That is to say, small scattering angle electrons. To correct for the screening effect in the Rutherford scattering cross section equation,

$$[\sin^2 \frac{\theta}{2}] \; would \; be \; replaced \; by \; [\sin^2(\frac{\theta}{2}) + (\frac{\theta_0}{2})^2], \; with \; \theta_0 = \frac{0.117Z^{1/3}}{E_0^{1/2}}. \tag{1.3}$$

Also, electrons that are so fast relativistic effects cannot be ignored, (Table 1.25) must be accounted for.

TABLE 1.2 Electron Properties as a Function of Accelerating Voltage				
Accelerating voltage (kV)	Non-relativistic wavelength (nm)	Relativistic wavelength (nm)	Mass ($\times m_0$)	Velocity ($\times 10^8$ m/s)
100	0.00386	0.00370	1.196	1.644
120	0.00352	0.00335	1.235	1.759
200	0.00273	0.00251	1.391	2.086
300	0.00223	0.00197	1.587	2.330
400	0.00193	0.00164	1.783	2.484
1000	0.00122	0.00087	2.957	2.823

Figure 1.25: Table for electron properties at different acceleration voltage.[100]

To modify relativistically correction with wavelength λ_R and Bohr radius a_0 of the scattering atom:

$$\lambda_R = \frac{h}{[2m_0 eV(1 + \frac{eV}{2m_0 c^2})]^2} \; and \; a_0 = \frac{h^2 \varepsilon_0}{\pi m_0 e^2}, \tag{1.4}$$

the screened, relativistically corrected, differential Rutherford cross section would be

$$\sigma_R(\theta) = \frac{Z^2 \lambda_R^4}{64\pi^4 a_0^2} \frac{d\Omega}{[\sin^2(\frac{\theta}{2}) + \frac{\theta_0^2}{4}]^2}. \tag{1.5}$$

The definition of Rutherford cross section is

$$\sigma(\Omega)d\Omega = \frac{number \; of \; particles \; scattered \; into \; solid \; angle \; d\Omega \; per \; unit \; time}{incident \; intensity}. \tag{1.6}$$

This is describing, at a given incident intensity (defined as number of particles incoming per unit time) how many electrons would be scattered into solid angle $d\Omega$, per unit time. It can also be written in a differential form by itself: $\sigma(\theta)$, then it represents the number

of all particles scattered into angle θ, under a certain incident intensity, per unit time, per unit solid angle. Therefore, 1.5 is

$$\sigma_{nucleus}(\theta) = 1.62 \times 10^{-24} (\frac{Z}{E_0})^2 \cot^2 \frac{\theta}{2}. \tag{1.7}$$

To conclude, in the scenario of electrons being scattered by the nucleus, at a given angle θ, and accelerating voltage E_0, the higher the atomic number Z is, the higher the probability of particles being scattered into this direction is.

As we have discussed, the electrons that contribute to HAADF imaging are incoherent, though they are elastically scattered. The phase of elastically scattered electrons is dependent on the scattering angle as in Fig.2.12. The reason why electrons become incoherent is that when electrons interact with matter, their velocity changes. The electron-optical refractive index, that works similar to in light optics, n can be defined as n = $c/c_{in\ material}$ = $\lambda/\lambda_{in\ material}$. The velocity of electrons in matter is affected by the Coulomb potential V(r) it experiences.

$$V(r) = -\frac{e^2 Z_{eff}(r)}{4\pi\varepsilon_0 r} \tag{1.8}$$

The Z_{eff} is the effective positive charge carried by the nucleus, taking the screening effect of the atomic electron cloud into account. The refractive index is

$$n(r) = \frac{\lambda}{\lambda_m} = \frac{p_m}{p}\ with\ p = \frac{1}{c}\sqrt{2EE_0 + E^2}. \tag{1.9}$$

E is the kinetic energy eU, E_0 is the rest energy (511 keV for electron). As the result, the refractive index for an electron in the atomic Coulomb potential generated by the positive charge of the nucleus would be

$$n(r) = [\frac{2(E-V)E_0 + (E-V)^2}{2EE_0 + E^2}]^{1/2} \approx 1 - \frac{V(r)}{E}\frac{E_0 + E}{2E_0 + E} + ..., \tag{1.10}$$

if V(r) $\ll$ E and E_0. n(r)$\geq$1 because when the electron interacts with the positive charge of the nucleus, V(r) is always negative. Furthermore, after electron-optical refractive

index around potential produced by the positive charge of nucleus is defined. The phase shift when an electron passes through the Coulomb potential can be obtained from the optical path difference Δs relative to the planewave wavefront in vacuum,

$$\varphi_s(\mathbf{r}) = \frac{2\pi}{\lambda} \int_{-\infty}^{+\infty} [n(\mathbf{r}) - 1] dz \approx -\frac{2\pi}{\lambda E} \frac{E + E_0}{E + 2E_0} \int_{-\infty}^{+\infty} V(r) dz. \tag{1.11}$$
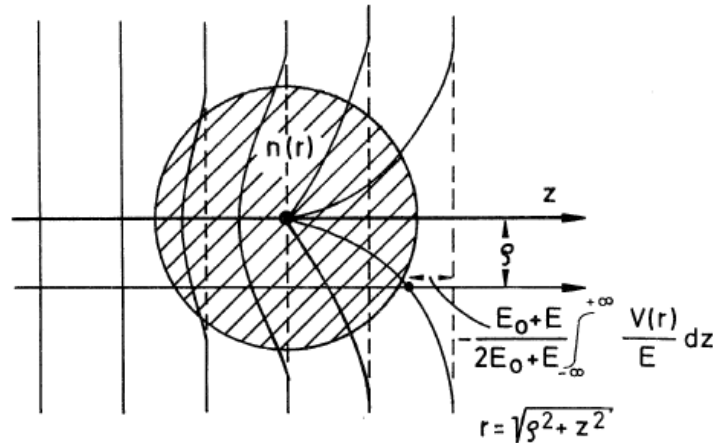
Figure 1.26: Phase shift along the plane wave direction using electron optical refractivity.[101]

A graph that visualises how phase shift, which describes phase delay behind the undistorted planewave that is caused by the nucleus Coulomb potential as shown as Fig.1.26. In the graph, the phase delay can be seen after electrons enter the potential area of the atom. The closer the trajectory of the electron is to the nucleus, the larger the phase shift is. If the trajectory of the electron passes right through the nucleus, the phase shift would never catch up with the planewave wavefront. Due to the phase shift caused by the potential, electrons that are elastically scattered electrons into higher angle would not be in-phase after they are scattered by the nucleus.

CHAPTER 2

EXPERIMENTAL METHODS

This chapter concerns the experimental instruments and techniques used in this research. Well-defined size-selected clusters were generated with a magnetron cluster beam source. The structure of the clusters before and after subjecting them to chemical reactions was probed with the aberration-correction scanning transmission electron microscope (AC-STEM). The structure of the cluster is assigned by comparing experimental images with multi-slice simulated images. In this chapter, I will introduce these techniques in some detail.

2.1 Cluster beam deposition

Producing size-selected clusters, the simplest metal evaporation methods and chemical synthesis are not very trivial to control. In our research, we employ a magnetron-sputtering, gas condensation cluster beam source with inline mass filtration which can achieve rather precise control over the cluster size with a typical mass resolving power reaching M/ΔM $\sim$25[102].
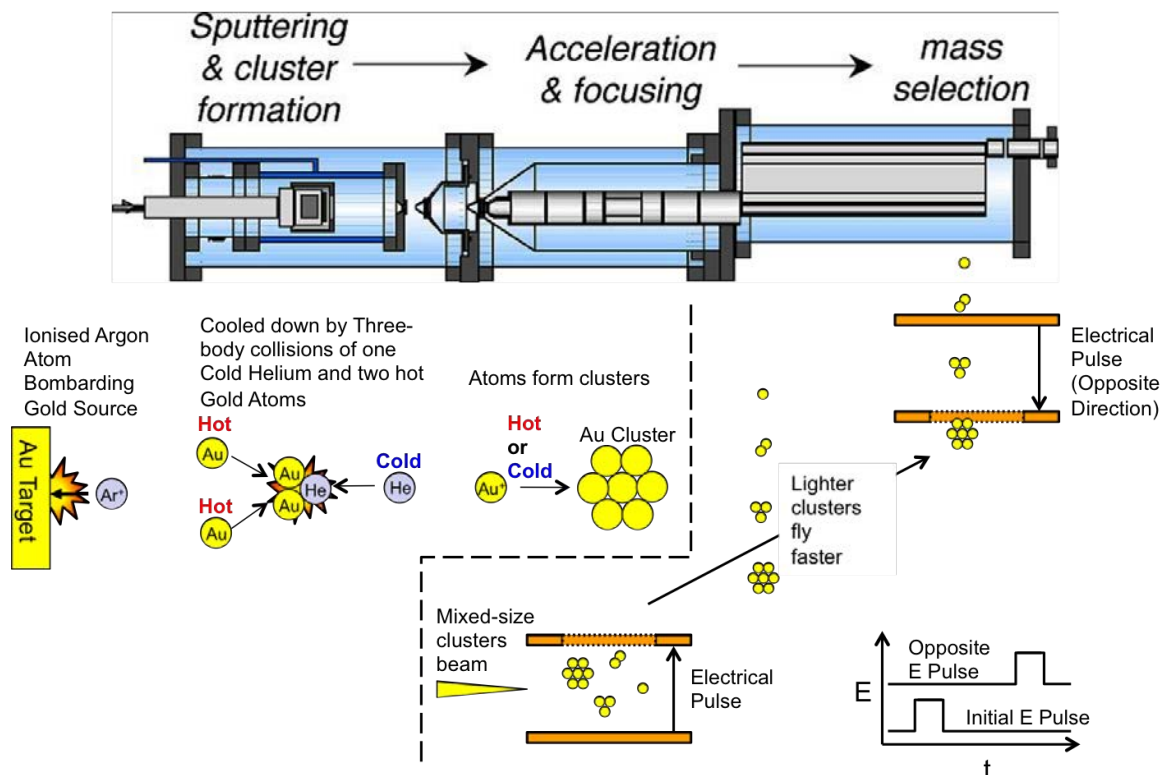
Figure 2.1: Schematic of cluster beam source with inline size-selection. First pumping stage with condensation chamber. Second pumping stage and ion optics. Third pumping stage and mass selector. Diagram at the bottom half showing three-body collision involved in gas condensation and brief introduction to how mass selection works. Diagram and caption after [102]

A schematic of the cluster source is shown in Fig.2.1. The cluster source system consists of three pumping stages. Before entering the first pumping stage, D.C. plasma sputtering is used to evaporate metal atoms from a disk-shaped source. Evaporated atoms aggregate in the condensation chamber, which is cooled by liquid nitrogen, with the help of cooling gas that is a mixture of He and Ar. The exit of the condensation chamber is regulated by an adjustable nozzle. The cluster beam with varied-size of clusters enter the first and second pumping stages through two skimmers which chop the expanding cluster beam into one direction. After the second skimmer, the cluster beam encounters a set of ion optics, which consists of a pair of einzel lens that perform the focusing. The purpose of the ion optics is to form a well-focused beam before the time-of-flight (TOF) mass selector. The entrance and the exit of the TOF chamber are not coaxial. The mass selector comprises two sets of parallel plates, both of which provide a high voltage pulse

perpendicular to the incident direction of the beam. The first pair of parallel plates is put at the entrance of TOF chamber, designed to give the entering beam a lateral pulse. The incident beam with varied-size of clusters would then get lateral speed. While travelling through the field-free region between two pairs of parallel plates. The lighter the cluster is, the greater the speed it travels. After a certain amount of time, clusters would arrive a second pair of parallel plates located on the axis of exit sequentially. A second high voltage pulse that is the same as the first pulse, but in opposite direction, from the first pulse would be applied on the second pair of parallel plates to decelerate the clusters (in vertical direction) of selected mass is focussed through the aperture and resumed to travel in horizontal direction. The resultant cluster beam can then be deposited onto the substrate in the deposition chamber.

2.1.1   The cluster beam source apparatus

Cluster production start with the generation of a beam of mixed-size of metal clusters. Cluster condensation takes place in the first chamber on a three stage differential pumping beam source and it is basically comprised of two elements. A. Magnetron source sputtering on high purity metal target to produce metal vapour into the condensation chamber. B. Injection of helium and argon into a liquid nitrogen cooled chamber, through three body collisions, cooled gases induce seed creation, from which large particles can form by aggregation/condensation.

The condensation chamber has a cylindrical shape with a magnetron mounted on one end and a adjustable nozzle (size from 0.5 mm to 12.5 mm) at the exit of the condensation chamber. The axial position of the magnetron is adjustable, so the distance between the magnetron and the exit nozzle can be from 250 mm to 150 mm. The wall of condensation chamber is hollow and is filled with liquid nitrogen as the coolant. Argon is feed in to the front end of magnetron and helium is feed from the rear end of the condensation chamber. Both gas feeds to the chamber are regulated by mass-flow controllers. By tuning the amount of gas fed into the chamber and the size of the exiting nozzle, the pressure

in the condensation chamber can be controlled, which is crucial for cluster formation. The typical pressure maintained the condensation chamber during cluster formation is $1.4 \times 10^{-1} \sim 3$ mbar. One of the advantage of using magnetron sputtering source is that a considerable amount ($\sim 30\%$) of sputtered atoms and aggregated clusters are ionised in the plasma so they can be mass selected.[102]

The interplay between Ar and He partial pressures and overall pressure on cluster formation has been scrutinised in a previous study.[102] The argon gas, that is used for the magnetron to sputter the metal target, plays a lesser role in condensing atomic vapour into clusters. Some cluster condensation is triggered by Ar. However, cluster condensation is more effectively triggered by He. It is shown in experiment that under argon partial pressure of 0.4 mbar, another 0.2 mbar of helium injection could increase the size of clusters by 1000 times.[102] The growth of clusters is initialised by the formation of a cluster seed which serves as the core of nucleation. The seeds are formed through three-body collisions between two metal atoms and a cooled helium atom. Three-body collisions are more likely to take place in highly dense vapour close to the magnetron. After the seeds have been formed, they may continue to increase their size along the way to the nozzle at the exit of the condensation chamber by one of these two mechanisms: A. merge with another cluster or B. metal atoms condense on the existing cluster. Clusters can be allowed more time to grow by increasing the condensation length, which can be adjusted by the axial position of the magnetron. However, increasing the helium pressure or condensation length does not monotonically increase the size of clusters formed. This is because under the same flow rate of Ar gas and sputtering power, the amount of atomic vapour produced in the condensation chamber is fixed. Therefore, the size and quantity of the clusters would increase with more nucleation seeds formed, until excessive nucleation cores lead to the depletion of the atomic vapour.

The mass selector is comprised of four rectangular plates. They form two pairs of parallel electrodes, the arrangement of these four plates numbered 1 to 4 from top to bottom as their arrangement is shown in Fig.2.2. The mechanism by which of how this

time-of-flight mass selector works is to apply a short electric pulse upward, when the beam of mixed size of clusters enters mass-selection chamber. This electric pulse accelerate the clusters upward. The same potential applied to a different mass of clusters would end up accelerating them to a different speed; lighter clusters travel faster in the vertical direction. As a result, clusters of different sizes arrive at the second pair of electrode sequentially. A second electric pulse that is the same voltage and duration but in the opposite direction from the first one is applied on the second set of electrodes, which are on the axis of the exit, to remove vertial component of velocity of cluster of the size selected and make them head toward the direction of the exit. In this way, the time interval between the first and the second pulse applied can be use to select the size of clusters needed.

(a) Arrangement of electrodes

(b) Time-of-flight pulse graph
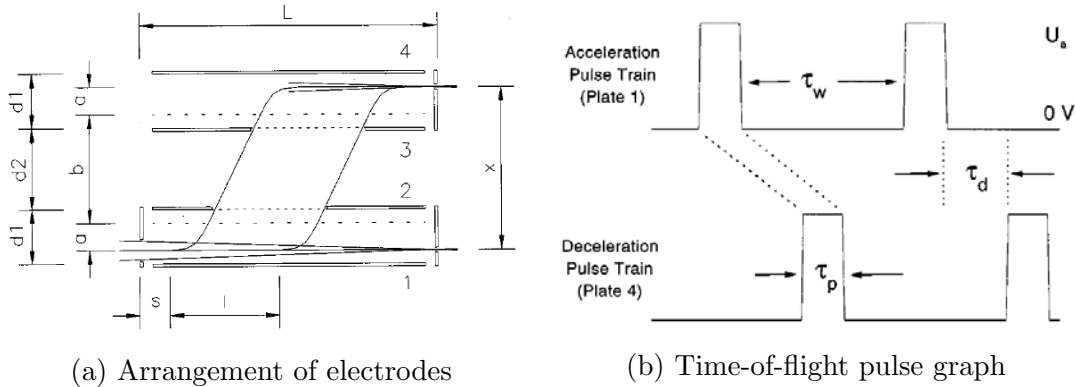
Figure 2.2: The graph of electrode arrangement and parameters used in the mass selector and the diagram of time of flight pulse.[103]

At the exit of the mass selection chamber, a size-variable slit that can open up to 8 mm is placed at the exit. Since the cluster beam is spread in vertical direction according to their size by the electric pulse applied on the parallel electrode, the wider the slit the more accurate the mass resolution will be. In the set-up of mass selector shown in Fig.2.2, the mass resolution is determined by the lateral displacement from entrance to the exit axis, x (180 mm), divided by the size of the exit slit, Δx.[103]

$$R = \frac{m}{\Delta m} = \frac{x}{\Delta x} \tag{2.1}$$

58

2.1.2 Operation of the cluster beam source

In practical operation of the cluster beam source, we would start by feeding the liquid nitrogen to the hollow wall of the condensation chamber. This would bring the condensation chamber to liquid nitrogen temperature. We would choose suitable gas flow of argon to inject to the magnetron according to the target material. After the argon plasma is ignited by magnetron, argon ions and atomic vapour of the target material would start to be generated. With suitable settings for the ion optics in the second pumping stage, ions generated are led into the mass selector in the third pumping stage. These ions would finally reach the deposition chamber. The sample is mounted on a insulated manipulator which is connected to a pico-ammeter that can measure the strength of current generated by the ion beam that hits the sample plate. A high, negative voltage is applied to the sample plate. This applied voltage is accelerating the cluster beam and controlling the impact energy of the clusters on to the sample. The manipulator is also adjustable so that the optimal position for deposition can be found. The mass selector is used to focus on a specific mass but also can be use to scan over a certain range of masses. Under this type of operation, the mass selector and the following beam current measurement can be regarded as a mass spectrometer. The argon ion beam can be used as a preliminary confirmation of working condition of all components and alignment. After this initial check, a suitable amount of helium gas would be injected into the condensation chamber on top of the existing argon gas flow. Typical parameter used in producing Au_{923} clusters is shown in Table 2.1.

The typical parameters used during cluster production is list in Table 2.1. In these parameters, Ar and He gas flow is determining the magnetron sputtering power onto the target and controlling the seeds generating in the cooling process. The pressure in the condensation chamber is maintained under between sub-mbar and 3 mbar, depending on the material and the size of cluster selected. In each of the pumping stage shown in 2.1, a independent turbo molecular pump is was to maintain vacuum. The pressure in deposition chamber is typically 1×10^{-6} to 3×10^{-6} mbar when operating. The ion

Condensation conditions	
Ar gas flow	200 (sccm)
He gas flow	150 (sccm)
Magnetron power	10 (Watt D.C.)
Condensation length	250 (mm)
Condensation pressure	0.99 (mbar)
Ion optic setting	
Lens	Voltage (V)
Skimmer	12
Lens 1	700
Lens 2	500
Lens 3	150
Lens 5, X+	500
Lens 5, X-	500
Lens 6, Y+	1116
Lens 6, Y-	1133
Lens B	200
Lens E	100
Substrate bias	461.5 (0.5 eV/Atom for Au_{923})

Table 2.1: Typical parameters used in producing size-selected metal clusters with the magnetron clusters beam source. Presented here are the parameters for the production of Au_{923}.

optic settings is aiming at focus the cluster beam and deliver the most of the clusters generated into the mass-selector. These voltages would be set differently depend on the size of clusters generated. The substrate bias is used to accelerate the clusters after size selection to make clusters impact with energy or soft landing on the substrates.
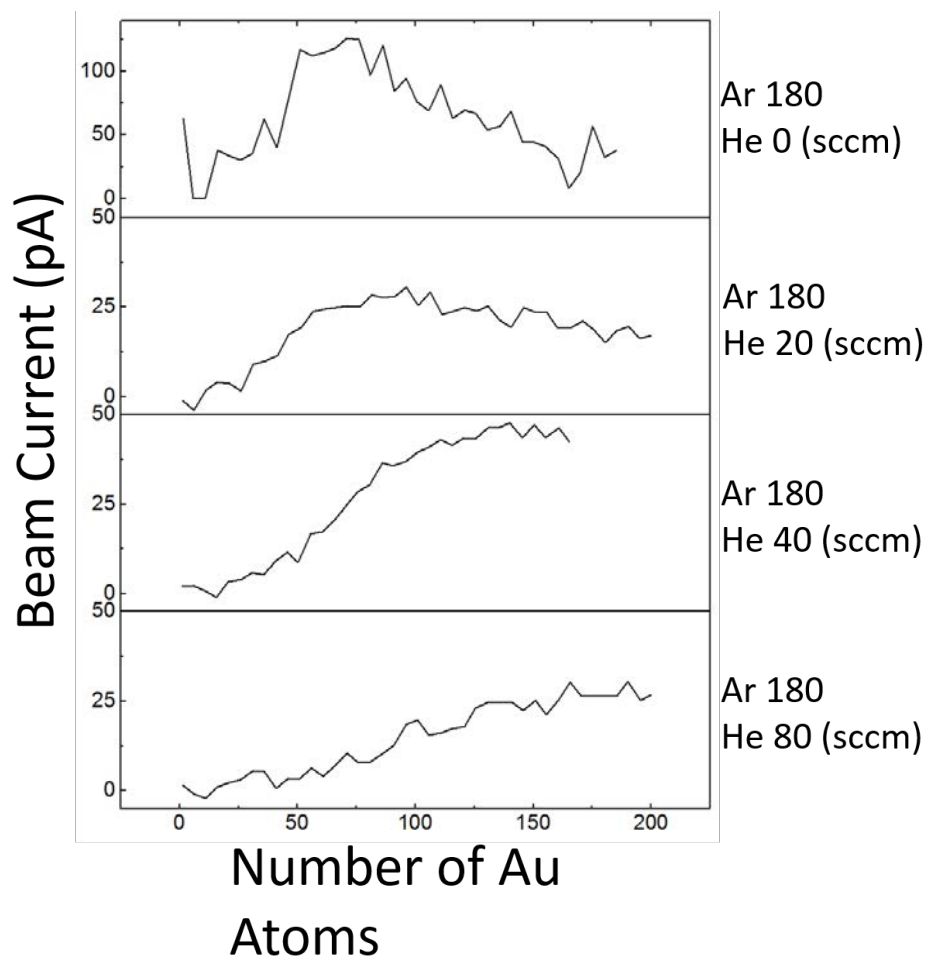
Figure 2.3: Figure summarises a demonstration of how helium gas affects the size distribution of gold clusters produced. In each graph is a mass spectrum, vertical axis is the beam current of charged clusters hitting the sample plate in the condensation chamber and the horizontal axis is mass of clusters (no. of gold atoms) scanning across number of atoms from 1 to 200. In these four curves, the gas flow in the top one is 180 sccm of Ar alone. From the top curve to the bottom one, He flow gradually increases with Ar flow being kept the same.

In Fig.2.3 is a demonstration of how helium gas flow affects the cluster condensation. In this test, the amount of cluster with size between 1 and 200 atoms was monitored with all conditions kept identical. The helium flow was gradually increased from 0 sccm to 80 sccm. With the increment of helium, the intensity of beam current increased and there was a shift to the higher mass clusters. This agrees with the observation previously made by Pratontep et al.[102]

(a) Exit Slit at 8 mm

(b) Exit Slit at 3 mm

(c) Exit Slit at 2 mm
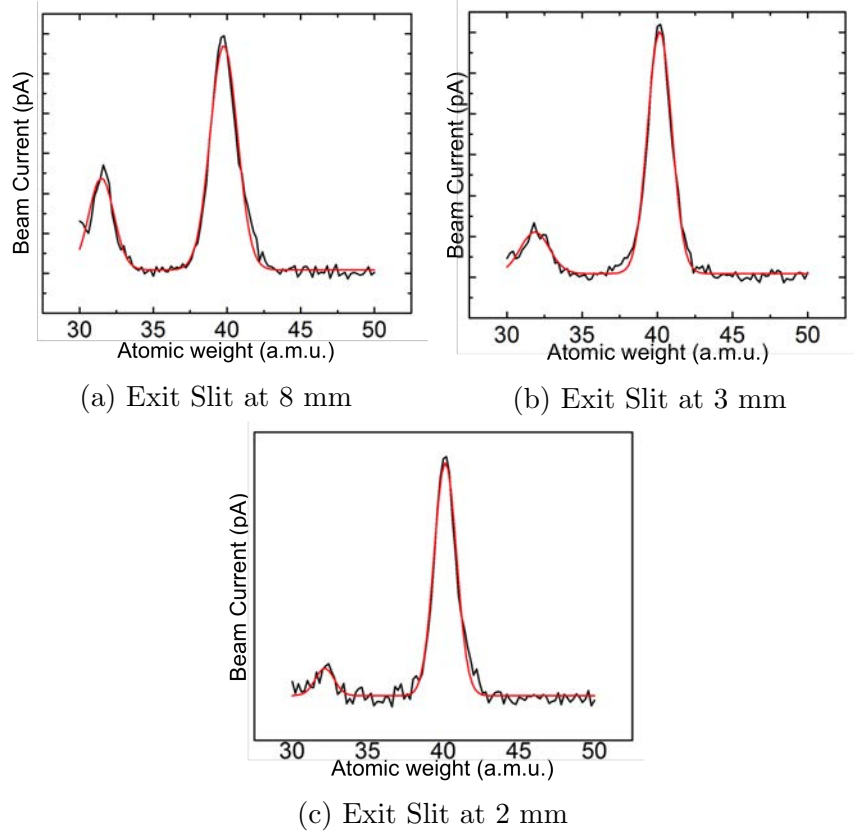
Figure 2.4: Mass resolution test with Ar ions under different size of exiting slits. The peak at mass 32 is the signal from residual oxygen gas inside the chamber.

In order to probe how accurate the mass resolution is, it can be tested by generating single atomic weight ions and making them pass through the cluster beam source. By scanning over the mass around this specific material, with the TOF mass selector and beam current received on the sample, how well the mass selector deals with this single atomic mass can be revealed. Shown in Fig.2.4 is the mass resolution test with ^{40}Ar gas under different exit slit width. $\Delta m/m$ can be derived from the the Gaussian curve fitting to the curve acquired from mass selector scanning over mass 40 (amu). In Fig.2.4 (a) to (c), it can be seen that the size distribution becomes narrower when the width of the exit slit is narrower, which indicates that a more accurate mass can be selected. $\Delta m/m$ derived from (a), (b), and (c) are 18 ($\pm 2.7\%$), 21 ($\pm 2.3\%$), and 23 ($\pm 2.1\%$), respectively. Given that the overall lateral beam displacement is 180 mm, the theoretical $\Delta m/m$ value for exiting slit setting at 8 mm, 3 mm, and 2 mm would be 22.5, 60, and 90, respectively.

2.2 Scanning transmission electron microscope
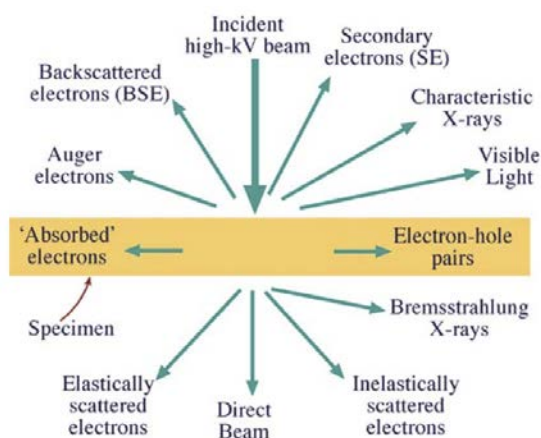
Figure 2.5: Various kind of different signal generated when an ultra high energy electron beam impact on samples.[100]

Transmission Electron Microscopy (TEM) makes acquiring structural information with sub-Ångstroms resolution possible. In scanning transmission electron microscope mode, the electron beam is converged into a probe and rastered over the sample. The size of this probe determines the resolution of imaging. When the electron beam hits the sample, various kinds of interactions take place between electrons and atoms.[100] These different interactions are summarised in Fig.2.5. In my study, high angle annular dark field (HAADF) imaging under STEM mode is the main tool utilised. The HAADF detector is a ring shape electrode that collects elastic, incoherent electrons after the sample. The electrons that are detected by the HAADF detector are those that are deflected by nucleus to a high angle ($> 3°$ or 50 mrad, 1 mrad = $0.0573°$) and the image formed is free of contribution from diffraction. As a result, the intensity of the HAADF image is proportional to the atomic number (amount of positive charge in the nucleus).

The model of the microscope used was a JEOL-2100F, which is equipped with a spherical aberration probe corrector (CEOS GmbH) at a convergence angle of 19 mrad and the collecting angle on HAADF detector was between 62 mrad (inner) and 164 mrad (outer). The electron source is a field-emission gun (FEG). The microscope operates at 200 kV.

(b) Lenses arrangement

(a) JEOL-2100F used in our group.
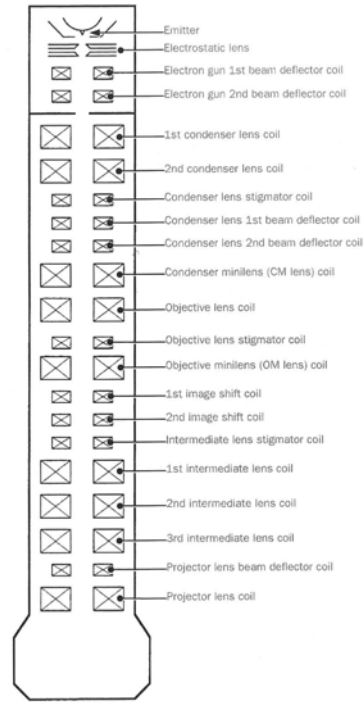
Figure 2.6: Detailed structure sketches of lenses, apertures, deflectors, and other parts used in JEOL-2100F.[104]

2.2.1 Field emission electron source

The field-emission gun (FEG) takes advantage of the fact that an electric field is considerably increased at the sharp point of an object. The electric field E on the tip of a needle with radius r, and voltage V, applied to it is $E = \frac{V}{r}$. It is a superior source compared with the traditional thermionic emission source in several aspects. The FEG has longer lifetime, higher brightness and most importantly much smaller energy spread (0.3 eV at 100 kV) and crossover size. The price that comes with better performance is the higher cost and having to operate under ultrahigh vacuum to keep the emitting tip free of oxide and contamination. Impurities on the surface could change the work function and disturb the emission of electrons. In de Broglie's hypothesis, the energy of the electrons defines the wavelength of the matter wave. Therefore, a small energy spread helps to increase

64

the accuracy for the electrons going through the following lens because the aberration is dependent on the wavelength of the electrons, and also keeps the electron beam coherent. The coherence of wavelength is defined as $\lambda_C = \frac{vh}{\Delta E}$, where v is the electron velocity, ΔE is the energy spread, and h is the Planck's constant.

(a) FEG anodes diagram

(b) FEG tip
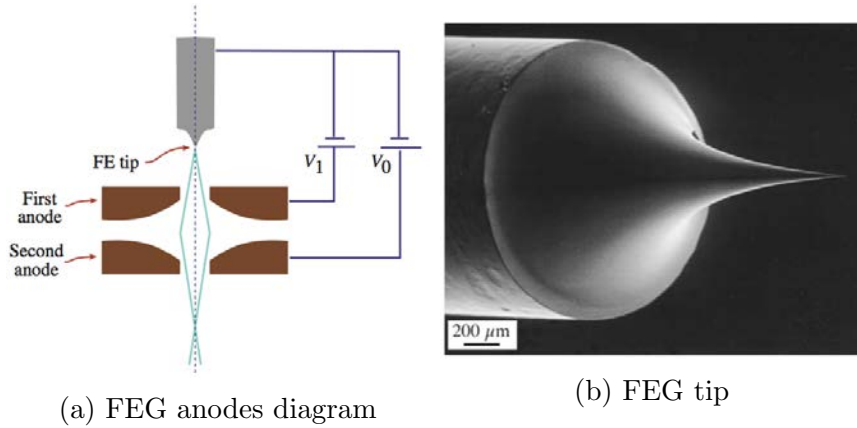
Figure 2.7: Electron gun with field emission source and their accelerating electrodes.[100]

The diagram of a FEG is shown in Fig.2.7. The first anode is set at several kV to extract electrons from the field emission tip and the bias applied between first and second anode would accelerate electrons to the designated operating high voltage (50~400kV). The first crossover point, formed by the electric field of both anodes combined, is effectively determined by the source size. The source size for a tungsten filament can be larger than 10^5 nm, while source size formed by FEG is around 3 nm. Source size affects spatial coherency. The relation between effective source size d_c, electron wavelength λ, and angle subtended by the source at the specimen α can be defined as $d_c = \frac{\lambda}{2\alpha}$. The angle of coherent illumination is limited by effective source size. The larger the source size is, the smaller the coherent illumination angle is, given that the acceleration voltage is kept the same (thus λ is a constant).

2.2.2 Electron lenses and aberration

(a) EM lens diagram.[100]

(b) Diagram of electron beam focussed by magnetic lens.[105]
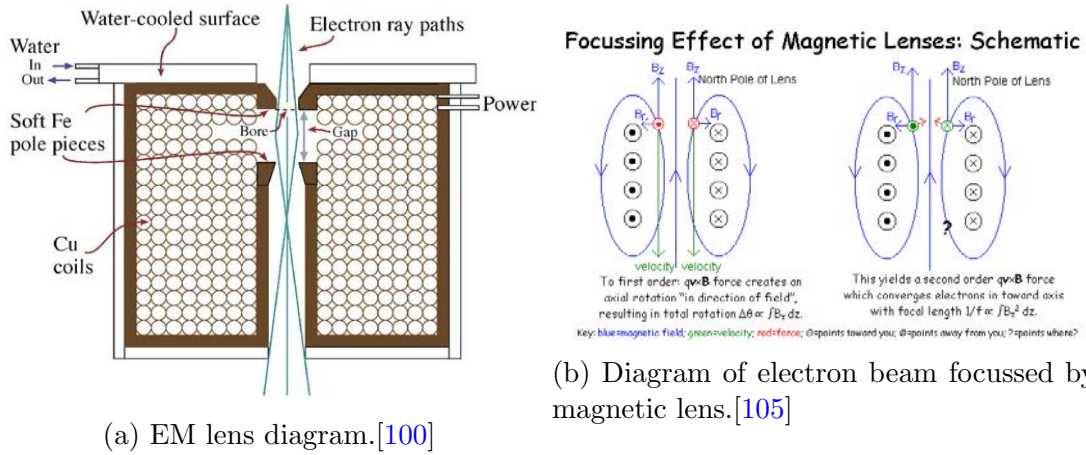
Figure 2.8: (a) structure of a magnetic electron lens used in TEM. (b) Graph showing how magnetic lens bend electrons.

In order to change the direction of the electron beam in the microscope in a controllable way, magnetic electron lenses are used. It is the equivalent of glass lenses in optical microscopes. The typical structure of a magnetic electron lens is shown in Fig.2.8. Magnetic electron lenses are comprised of copper coils contained in a soft iron cylindrical casing. In the centre of the cylinder case, a bore is drilled for the electrons to pass through. In the inner side of the iron casing, there is a gap in the vertical direction which creates a polepiece. This polepiece is used to create a axially symmetry magnetic field but inhomogeneous along the vertical direction. How electrons interact with the magnetic field is visualised in Fig.2.8 (b). Initially, the electrons generated and accelerated by the electron gun are travelling straight downward along the axial direction of the electron lens. Electrons interact with the magnetic field lines that are unparalleled to the axial direction of the lens. The interaction between the magnetic field and the electrons travelling downward induce Lorentz force in the azimuthal direction (in this case, counter-clockwise), yet no force is exerted on the electrons in the radial direction. After electron gains azimuthal acceleration and starts to spiral, the motion in the azimuthal direction interacts with the same magnetic field and induces Lorentz forces in radial direction, pulling the electrons inward. Being able to change the electrons trajectory in the radial direction along the cur-

vature of inhomogeneous magnetic field lines facilitates the polepiece to bend electrons similarly to lens glass in optical systems. Notice that the magnetic electron lens only works if there is a inhomogeneous magnetic field generated by the polepiece structure, otherwise solenoid created parallel magnetic field line would not be able to start the spiral motion, let alone contracting electron beams. All magnetic electron lenses work as convex lenses in electron microscope. Converging effects can be seen before crossover point and diverging imaging is seen after the crossover point.

The magnetic electron lens used in microscopy is always imperfect. In fact, the structure and basic principal of the lens are mostly unchanged from those used 80 years ago. There are several factors that affect focusing, but the three most important ones are chromatic aberration, astigmatism, coma, and spherical aberration.
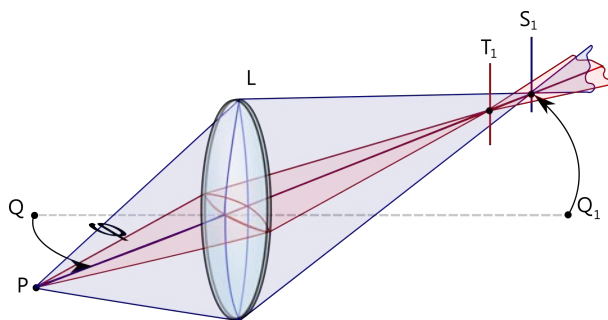
Figure 2.9: Diagram shows different focussing point from rays of different axial direction caused by astigmatism.[106]

Except for chromatic aberration, all other aberration that are usually encountered in STEM have nothing to do with the energy difference between electrons. Astigmatism is a common aberration which appears due to the focusing strength being different in tangential (horizontal) and sagittal (vertical) direction. As a result, the position of the focal point of light in one direction would be different from the focal point of the light in another direction. In the centre of the line between the tangential and sagittal focal point, there is a point where the image of light from both direction are equally defocused, which is called " The circle of least confusion".
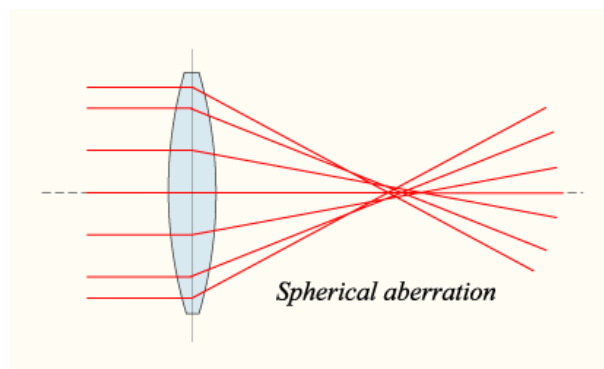
Figure 2.10: Spherical aberration is caused by different focussing strength for on-axis and off-axis rays.[106]

Spherical aberration arises when the electron lens behaves differently for on-axis and off-axis rays. In other words, the focussing strength is not a constant for rays incident at different distance from the optical axis of the electron lens. As a result, incident rays which enter at a different distance from the axis can not focus at the same focal point. Off-axis beams focus closer to the lens and the on-axis beam focus' further away from the lens. This forms a series of focus point for on-axis and off-focus rays. However, in contrast to coma aberration, a series of focal point for spherical aberration distribute along the direction of the optical axis of the lens. Besides, it still exist when incident light is perpendicular to the lens. The resolution of a given transmission electron microscope is usually limited by spherical aberration. Spherical aberration also propagates through the lens system. In other words, the aberration caused by one electromagnetic lens would be magnified by the following lens. All the lenses in STEM are convex lenses. Inhomogeneous magnetic fields are used to bend the electron beam reaching from the edge of the bore that allows electron beam to pass through. The magnetic field for off-axis electrons would always stronger than for on-axis (centre of the bore) electrons. Thus, off-axis rays would always be bent more than on-axis rays, which is called "positive spherical aberration". The method that STEM employs to correct spherical aberration is, in principal, to take a series of multipole lenses and form a equivalent lens that has negative spherical aberration so that the positive spherical aberration generated by all lenses can be compensated. In practice, the correction is done by a set of computer-controlled quadropoles and hexapoles, which

corrects not only spherical aberration but also aberrations of other angular meridional frequencies.

(a) Hexapole Force

(b) Equivalant Effect double hexapole
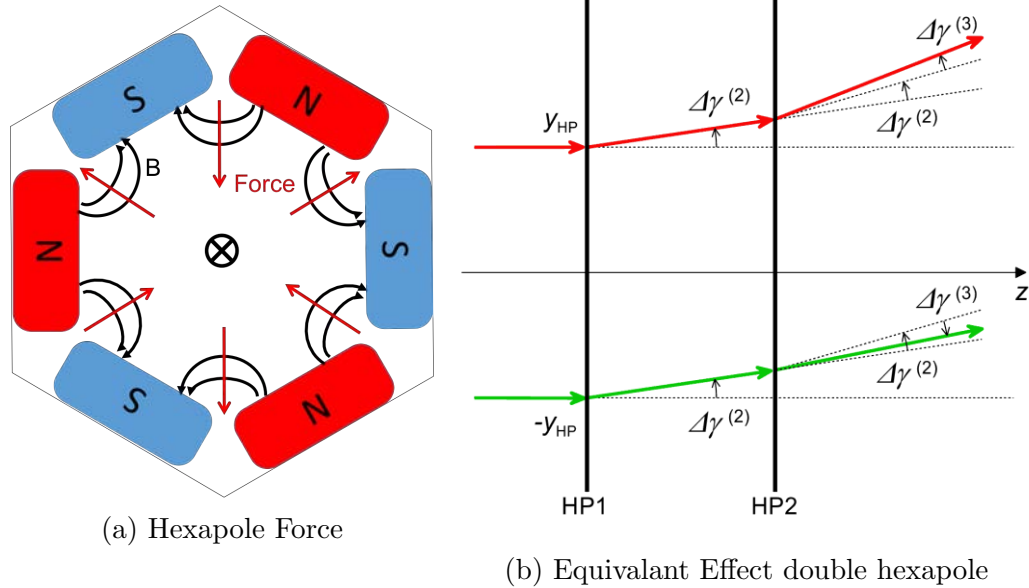
Figure 2.11: (a) Scheme of a hexapole lens, showing it can bend electrons to the same direction on opposite sides of the lens, instead of heading toward the directions away from each other like in other kid of lenses. (b) The combinition of two hexapole lenses can diverge two beams of electrons that enter parallel.[107]

An ordinary magnetic electron lens can only exert force on electron coming through its bore with a force towards the optical axis. The force exerted on electrons in a quadrupole lens can be facing or opposite to each other in pairs with regards to the optical axis. On the contrary, hexapole magnetic lens' can push electrons coming through it towards the same direction on the opposite side of the lens. Also, intrinsically, the structure of the hexapole magnetic lens is useful to correct three-fold symmetry aberrations. (Fig.2.11 (a)) In Fig.2.11 (b) shows the effect of two hexapole magnetic lens' deflecting electrons in sequence and how it achieves negative spherical aberration.[107] As it has been discussed in the previous paragraphs, all magnetic lens' are converging lens' and produce positive spherical aberration. When two electrons enter the combination of two hexapole lenses from position +y and -y (y=0 is the optical axis in z direction), the two electrons will be deflected towards the same direction by the same strength (and being deflected by angle $\Delta\gamma^{(2)}$) because both electrons enter the field at the same radial distance from the

axis. However as shown in Fig.HexapoleForce (b) , when electrons encounter a second hexapole lens, the electron marked with the green trajectory is going to bend less than the one marked wit the trajectory red. this is due to the radial distance for the two electrons becoming different and the closer to the optical axis the weaker the magnetic field will therefore be, the electron marked as red experiences larger deflection at the second hexapole and as a result the two electrons that enter parallel diverge.

2.2.3 High-Angle Annular Dark Field (HAADF) Imaging

When electrons interact with atoms, there are several possibilities that could happen as shown in Fig.2.12. An electron could travel through the sample without interacting with any material and maintain its direction. These unscattered electrons form the direct beam post to the sample and contributes to the bright-field image. Electrons could also interact with the atomic electron cloud and be scattered into a low deflection angle. These electrons are elastically scattered and maintain their coherency. In TEM mode, the low angle scattered electrons contribute to form the diffraction pattern. Finally, an electron with ultrahigh kinetic energy can overcome the Coulomb repulsive force between itself and the atomic electron cloud and can travel close to the nucleus. These high kV electrons experience an attractive interaction with the nucleus and therefore are deflected to a high-angle. Electrons that have been deflected are collected by a ring shape detector (with its optical axis aligned with incident beam) below the sample. HAADF imaging is basically the signal of a sub-angstroms electron beam probe incident on the atoms on the sample. The term in HAADF: "Dark Field" means the image intensity is formed by deflected electrons and "annular" means a ring shape detector is used. The deflected electrons in all angular directions are collected. "High-angle" means the image is formed by electrons for which the scattering angle, θ, is $> 3°$ from the incident direction. What the HAADF signal can tell us about the specimen is basically the distribution of protons. The reason why we can explain it this way is because the HAADF signal is the collective effect of the electrons that are deflected by the nuclei and then hit the detector. As the result,
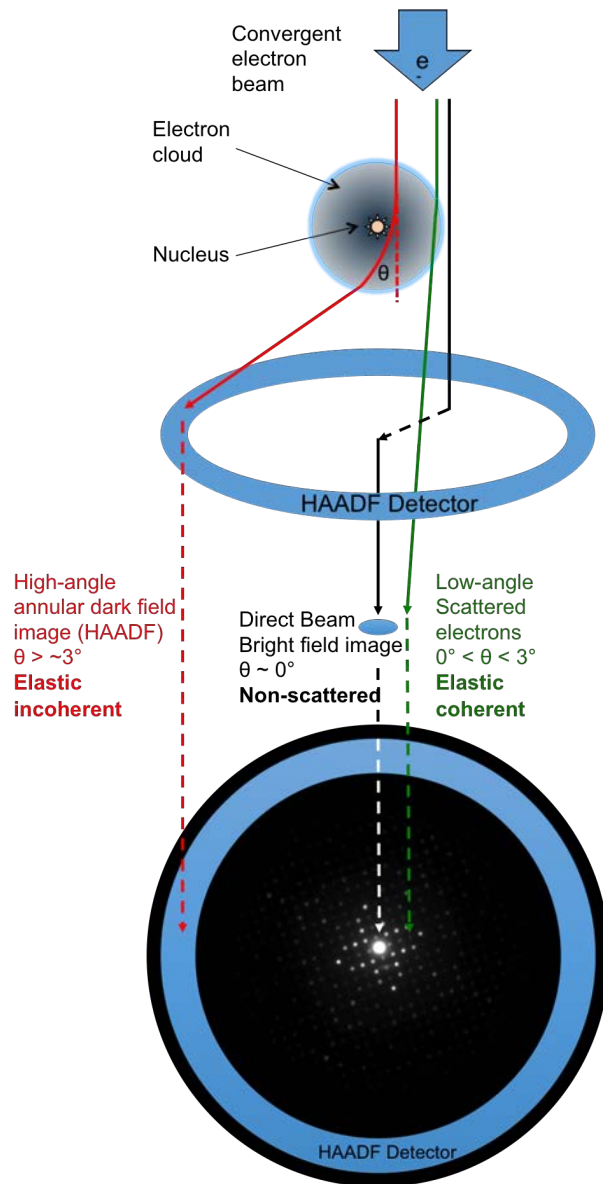
Figure 2.12: Schematic showing how electrons interact with an atom when scattered elastically(or not affected), and where these electrons end up hitting on the detector.

the intensity of HAADF signal is dependent on atomic number (Z), HAADF imaging is also called Z-contrast imaging. Similarly, the more atoms stacking up along the incident direction would cause the same effect, take imaging on a atomic column for example. Not only is the HAADF signal a reflection of the atomic number and quantity of atoms, but also due to the incoherent nature of high-angle signal, HAADF-STEM images carry little information about the crystallite orientation of the specimen. In short, the HAADF signal is formed from incoherent, elastically scattered electrons for which the relation of

intensities between two clusters is as follows:

$$\frac{I_A}{I_B} = \frac{N_A}{N_B}(\frac{Z_A}{Z_B})^n \tag{2.2}$$

I_A and I_B are the intensity of cluster A and B. N_A and N_B are the number of atoms in each of them. Z_A and Z_B are the atomic number of element A and B. Superscript n is an instrument specific parameter which is 1.46±0.18 on our instrument.

2.2.4 Practical operation of scanning transmission electron microscopy
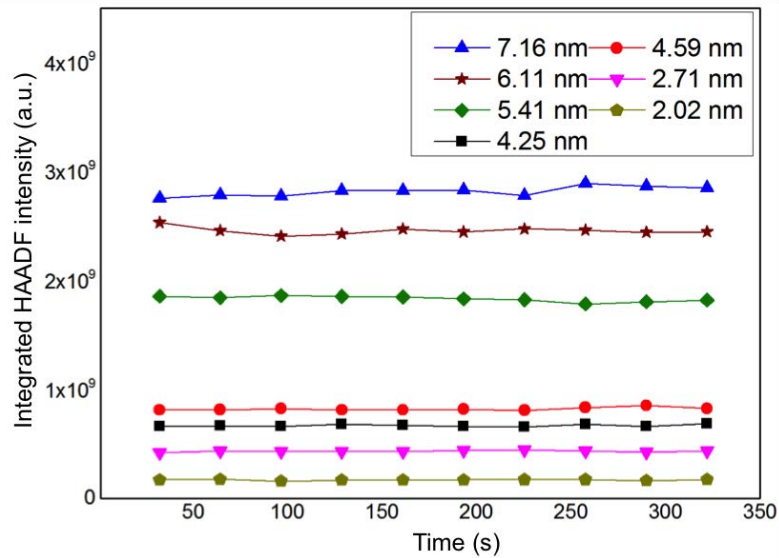
Figure 2.13: Prolonged scanning on clusters with regards to their integrated HAADF intensity change

Fig.2.13 shows the integrated HAADF intensity as a function of time for the prolonged imaging of Au clusters in the size range from 2.02 to 7.16 nm in diameter. Each image is captured over a period of 32.2 s. The integrated HAADF intensity of the clusters is stable for consecutive images taken over a total period of 300 seconds, demonstrating the mass stability of the clusters under the electron beam. Our previous results demonstrate stability of the atomic structure for Au clusters following prolonged exposure to the electron beam.
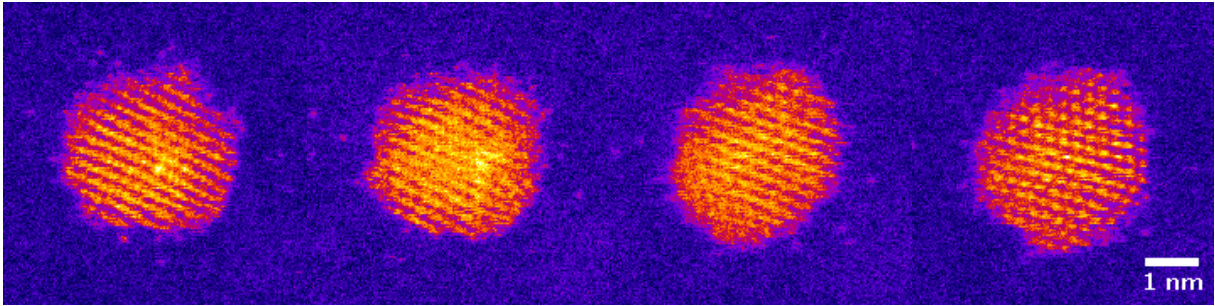
Figure 2.14: A series of HAADF-STEM images, taken consecutively, of a size-selected $Au_{923\pm20}$ nanocluster exhibiting a face-centred cubic (fcc) structure. Each image is captured over a period of 5.49 s.

Fig.2.14 shows a series of images, taken consecutively, revealing the atomic structure (in this case, face-centred cubic) of a size-selected $Au_{923\pm20}$ nanocluster. Each image is captured over a period of 5.49 s. Although the nanoclusters may rotate slightly from one image to the next, the nanocluster remains as face-centred cubic throughout. Hence, this demonstrates that the nanocluster structure maintains its integrity under the electron beam.
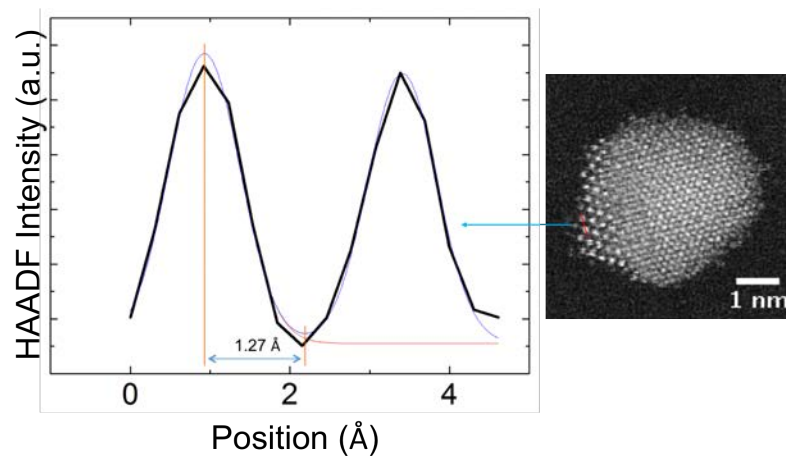
Figure 2.15: A demonstration of typical resolution of aberration-corrected HAADF STEM.

To summarise, we demonstrate the typical resolution achievable with HAADF STEM imaging with C_s corrector on our microscope. In Fig.2.15 is a experimental image of a Au_{2057} cluster. At a well defined area in the image, a profile is made across two atomic columns. The result of the profile is shown in the figure. According to the Rayleigh criterion of resolution, the definition of the resolution limit is from the centre of one of

the peaks to the first zero intensity position (dark ring) at either side of it. When a neighbouring point object sits at this position, the highest intensity between the overlapping area would be 73% of the intensity of the peak and at this distance, these two point objects would be considered as barely resolved, which made this scenario the Rayleigh limit. In the profile we plotted in Fig.2.15, the distance from centre to the first background intensity is 1.27 Å. This is an indication of the typical resolving power of our instrument.

2.3 Image processing

A set of data processing methods that aim to perform "Atom Counting" by measuring integrated HAADF STEM intensity from images and is performed by software package ImageJ and its advanced version Fiji.[108] The complete code used for image processing is in the appendix.

The basic steps written in this script are as follows, (filtering the noise), (locate the position of clusters), (sampling of intensity distribution), (finding contour of cluster by differential intensity), and finally (cropping and saving processed images).

Noise filtering (Fourier transform) - perform Fourier transform on the image and treat the width of the image as the longest period of sin and cos functions.This allows the frequency between a designated range to pass and to form a new, noise-free image. The noise encountered the most is spike noise that randomly appears in images which is usually at extreme high frequency (Very low period, 1 pixel usually). The reason for removing this random noise is to create a image with smoother edge from raw image. Later the contour measuring will benefit from this noise free image processing.

Noise filtering (Median Filter) - the median filter is used to remove very long period background structure or extensive contamination. The way the median filter works is to first set a radius in units of pixels. Any pixel in the image would then be compared with all pixels within this pixel radius. The median number would then be selected to be the intensity of this centre pixel.

Sampling of intensity distribution - A script was written to find out the intensity distribution. This is important due to the reason that when processing the image, a threshold would need to be decided so that the area of substrate and cluster could then be distinguished.

Finding the contour of the cluster by differential intensity - after the initial contour was selected, the script would take a measurement of the overall intensity it encircled which step-wisely expands its size to make new measurements from the enlarged contour. The purpose of this script is for the macro to see whether the contour has reached the edge of the cluster in that image. When the step-wise expanded contour has gone past the high intensity pixels area in the image that indicates the morphology of the clusters, there would be a a steep drop in overall intensity measurement. This is equal to finding the differential edge of the overall intensity measurement.

In work with mono-layer protected clusters, the aim of this method is to acquire a collective signal of the target cluster with the background subtracted. This is done by measuring the total intensity within a circle that we choose to cover the target cluster, the background signal is also measured in a ring shape area that encircles the target cluster, at the same time. Aspect ratio measuring is also conducted with ImageJ with the Fit Ellipse module. The major and minor axes of the results from fit ellipse shape are measured.

In the rest of the work with morphological changes of metal clusters due to chemical reactions, these basic steps introduced above are combined in processing images to find their integrated HAADF intensity or the width of the clusters. A set of images that demonstrates the image processing procedure is shown as follows:

(a) Raw image

(b) Background features filtered

(c) Fourier filtered

(d) Coarse contour

(e) Differential contour edge finding
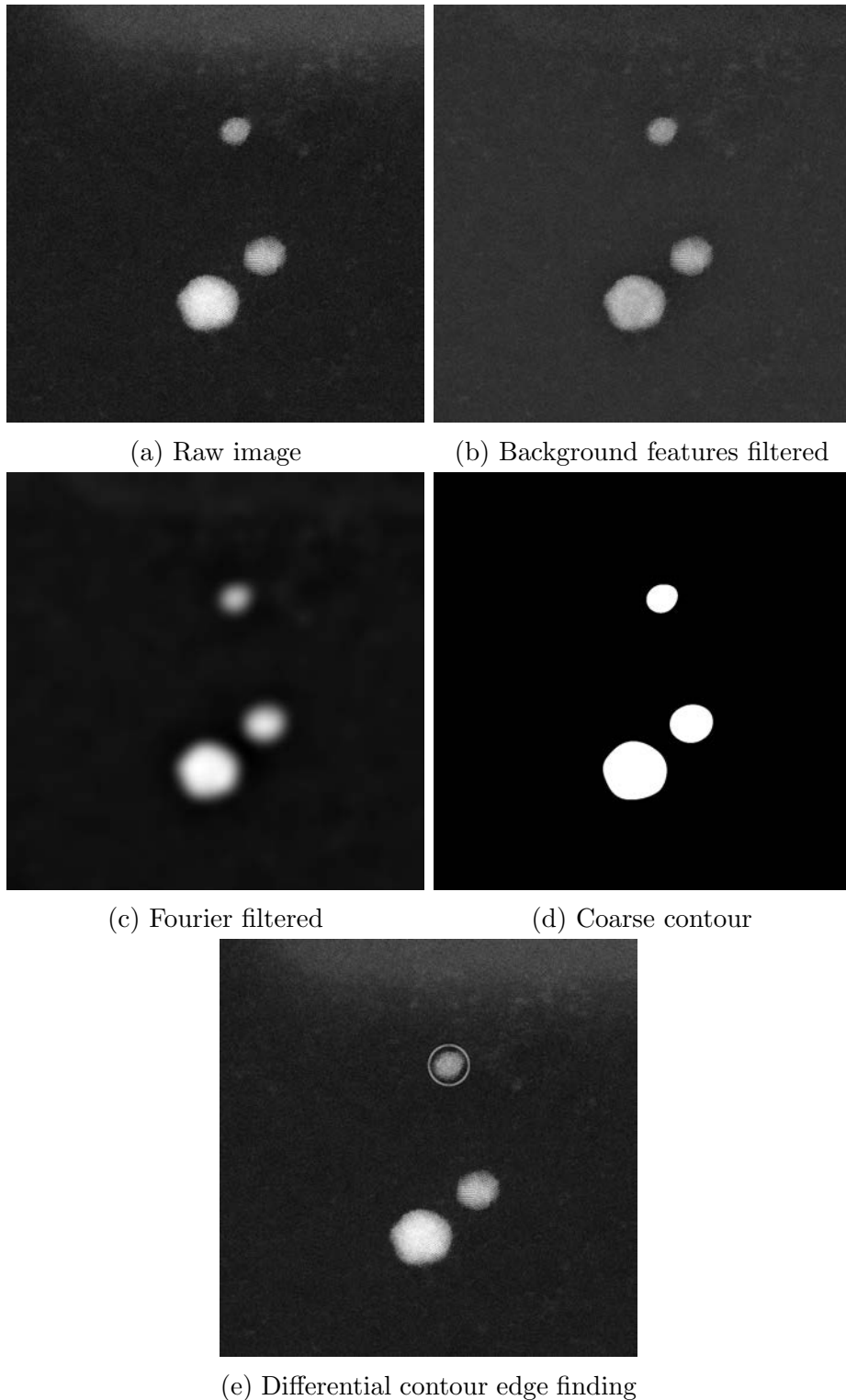
Figure 2.16: **Background features filtered:** We can notice the contamination(strip shape) at the top edge is removed. **Fourier filtered:** the feature of clusters were smoothed so that the coarse contour can be performed more easily. **Coarse contour:** sampling throughout the whole image is taken to generate a intensity distribution of all pixels, contour was selected by setting up a threshold based on the number of standard deviations from the peak centre. **Differential contour edge finding:** by gradually enlarging the circle and measuring the total intensity encircled, the script looks for a steep drop in intensity which indicates the edge of cluster has been reached.

2.3.1 Atom counting
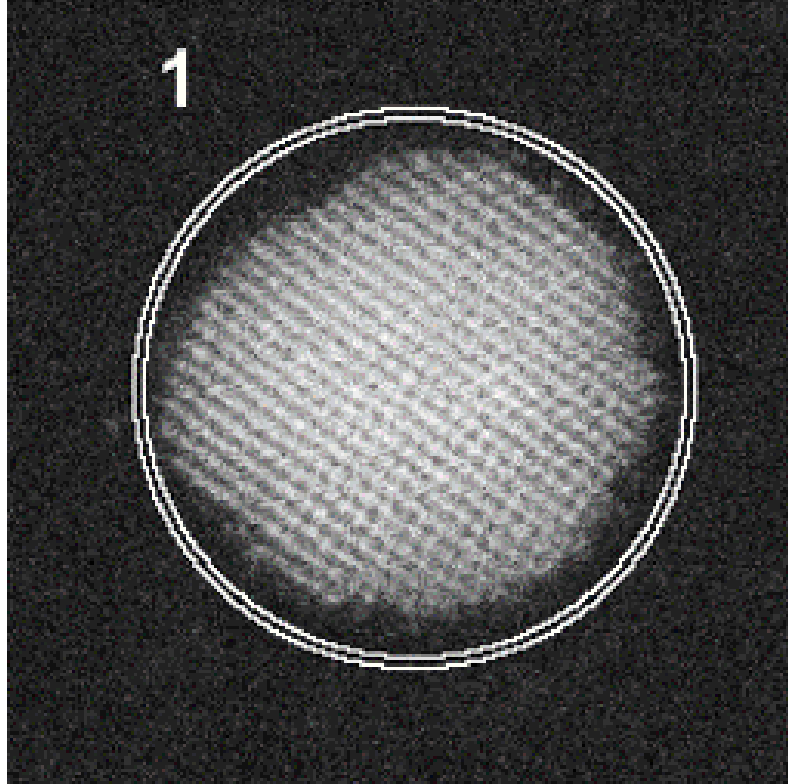
Figure 2.17: Diagram of image processing for atom counting from the AC-STEM images acquired.

In Eq.2.2, it is shown the intensity of the HAADF imaging is dependent on the atomic number of the given element and the number of atoms in the cluster[23]. To utilise the Z-dependent property of HAADF image, a set of two concentric areas were plotted around the area of clusters in the image as shown in Fig.2.17. In the figure, two concentric circles are dividing the areas around this cluster into A. area inside the inner circle and B. area between the inner and outer circle. The integral HAADF intensity within inner circle includes the intensity of atoms from cluster, the intensity from carbon support with possible contamination on it. The integral HAADF intensity in the surrounding ring-shape area is defined between inner and outer circle, from which the average background intensity from support and contamination can be measured. Finally, the intensity within inner circle subtract the average intensity multiples the area encircled by the inner circle from ring-shaped area between two concentric circles can provide us the intensity of the

cluster.

2.3.2 Cluster diameter measurement
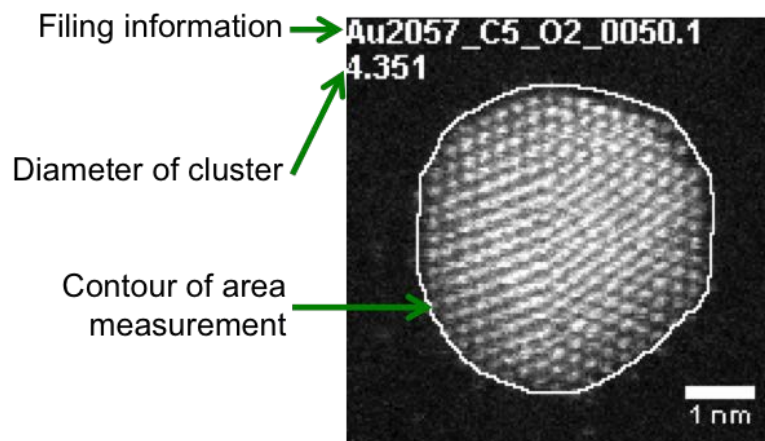
Figure 2.18: A sample image of typical diameter measurement.

The diameter of the cluster is measured from STEM image. The image processing determines an approximate contour for this cluster, then base on the initial contour, stepwisely expanding the contour while measuring the overall intensity encircled to the edge of a suddent drop in intensity as described before. The diameter of cluster is calculated from area measured by assuming the cluster is circular in shape.

2.4 Multislice STEM image simulation

In order to determine the structure of observed cluster, HAADF STEM images are compared against simulated HAADF STEM images generated from several possible high symmetry models. The QSTEM software package is used to perform this function.[109] Theoretical high symmetry atomic models that match the size of the cluster produced and used in the experiment are loaded into this software package to generate the simulated images. Parameters used on our microscope are also input into this package so that the simulated image generated fits the outcome of the actual imaging as well as possible. The

atomic model used for the calculations are also rotated to different orientations according to Eulerian angles, first θ (along the initial Z axis) then α (along rotated X axis, X'). In this way, a full survey of different patterns seen from different orientations of a particular cluster structure can be made.

(a) Sliced Lattice

(b) Diagram for multislice calculation.[109]
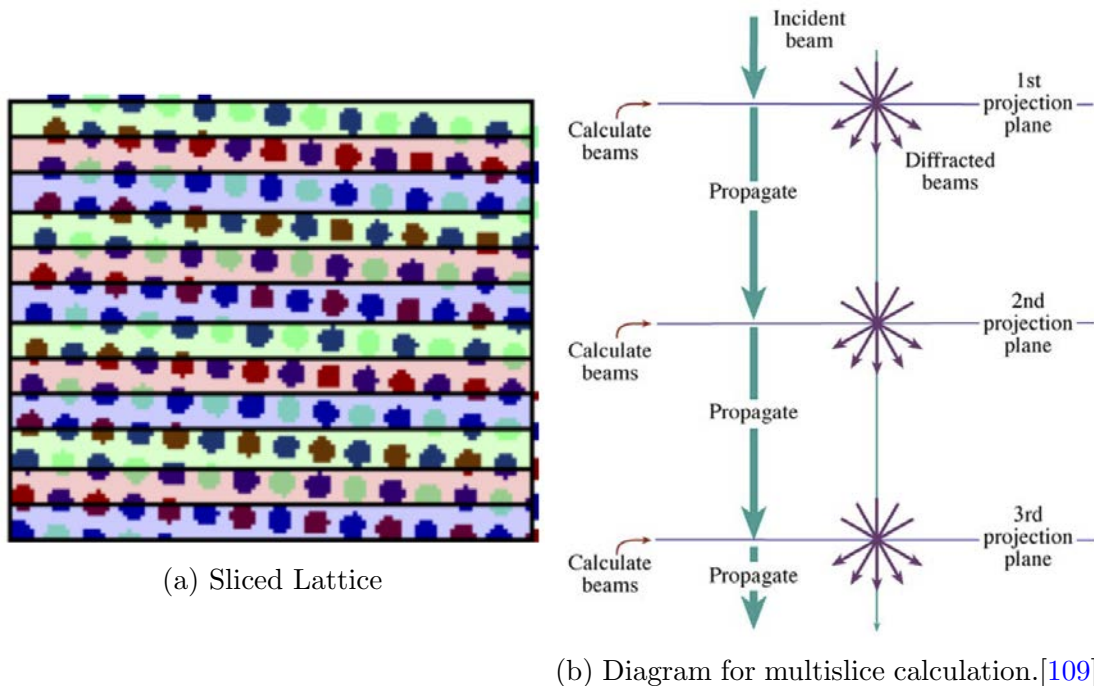
Figure 2.19

The principle of multislice simulation is to section the atomic model of interest into many small slices. The slicing direction is perpendicular to the incident beam direction. The wave function simulating the electron source is firstly projected onto the position of the atomic model in the first slice. The phase and the amplitude of interaction from each of these atoms is then calculated. The result of the beam projection from interaction with the layer of atom in the first slice would then be used as a starting point of calculating the interaction between the beam and atoms in the next slice. The reason for performing multislice calculations is to emulate the effect of electrons that may be scattered by the atoms in different layers more than once.

In my study, three magic size clusters we come across are 561, 923, and 2057. For each of these three magic sizes, there are three possible high symmetry structures that were

taken into considered, cuboctahedron, ino-decahedron, and icosahedron. We performed multislice simulation on sizes 561 and 2057 clusters. The previously published simulation results for Au_{923} clusters were also used[35]. The atomic models use are generic unrelaxed models of the three candidate structures. Each of these models were sent for image simulation calculation at all possible orientation according to the symmetry of the structure. Multislice image simulation at different orientations reveals different patterns for the nanoclusters, which is later used for comparison with experimental images to assign the individual images to a specific structure. Simulated STEM image atlas' for the icosahedron, ino-decahedron and cuboctahedron of Au_{561} and Au_{2057} are attached in the appendix.
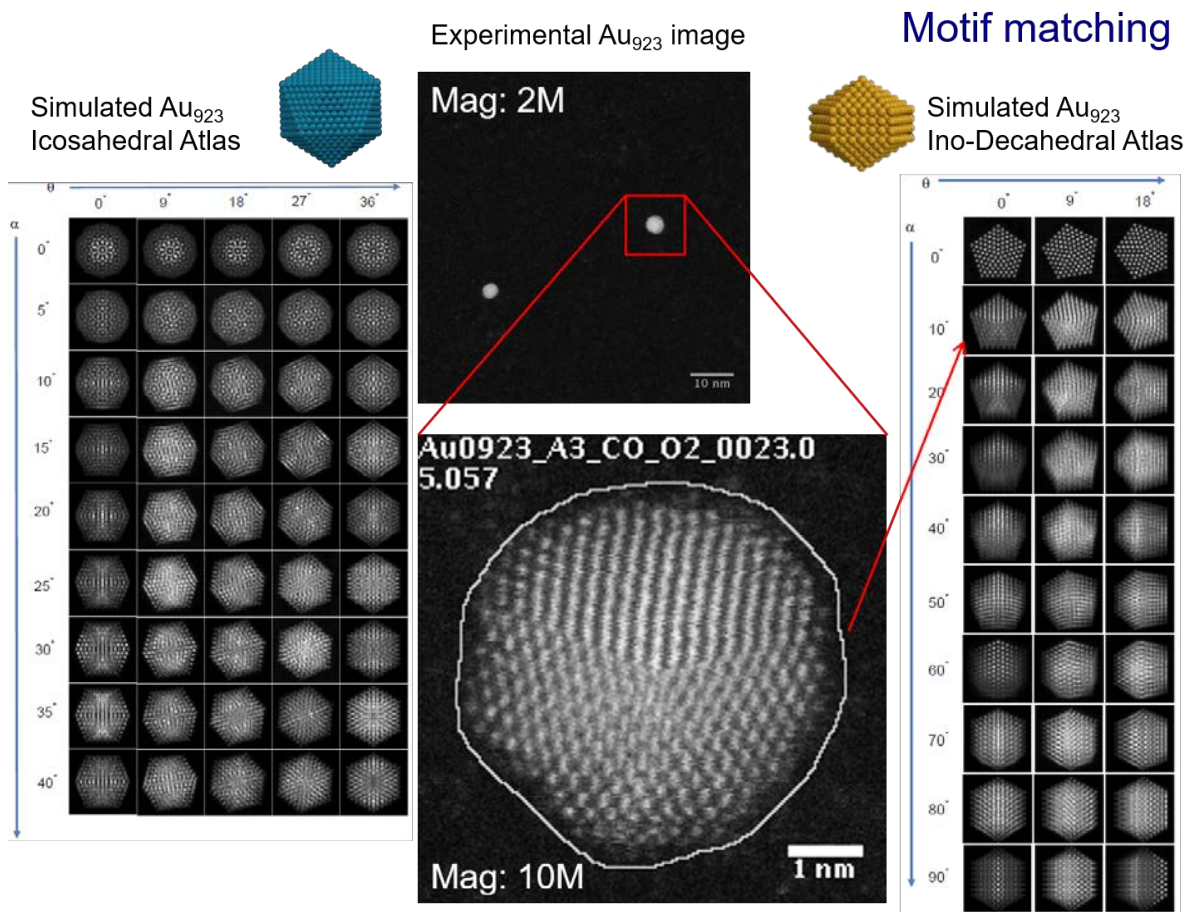
Figure 2.20: Demonstrate of motif matching of an experimental STEM image with simulated STEM image atlas.

2.5 Vapour-phase chemical reaction facility

Figure 2.21: Vapour-phase chemical reaction facility. Photo credit to Christopher M. Brown, Johnson Matthey Technology Centre.

To observe how chemical reactions affect the morphology of clusters, samples need to be treated in a carefully controlled environment so that the concentration of reactant, temperature and pressure are regulated, or at least monitored. The facility is provided by and located in Johnson Matthey Technology Centre and all the gas/vapout-phase chemical reactions were conducted by Mr. Christopher M. Brown. This reaction facility has the ability to send gases of controlled flow rate through a glassy tube (4mm width) located in a mesh cylinder as shown in the picture. A quartz wool plug is stuffed inside the tube as a support to the catalyst that sits on top of it. In our experiment, the sample is a commercially used TEM grid with size-selected metal clusters deposited on it. Types of gas that can be sent into the tube are helium, hydrogen, oxygen, and in the case of CO oxidation reaction, a mixture of $CO:O_2=1:21$ is used. All the gases flow rates are controlled separately by regulators. Liquid phase reactants can be vaporised when gases flowed into the glassy tube as well; A bottle (blue lid on the top right corner in Fig.2.21)

is used for storing 1M 1-Pentyne solution. The gas flow can be heated up to follow a certain temperature ramp.
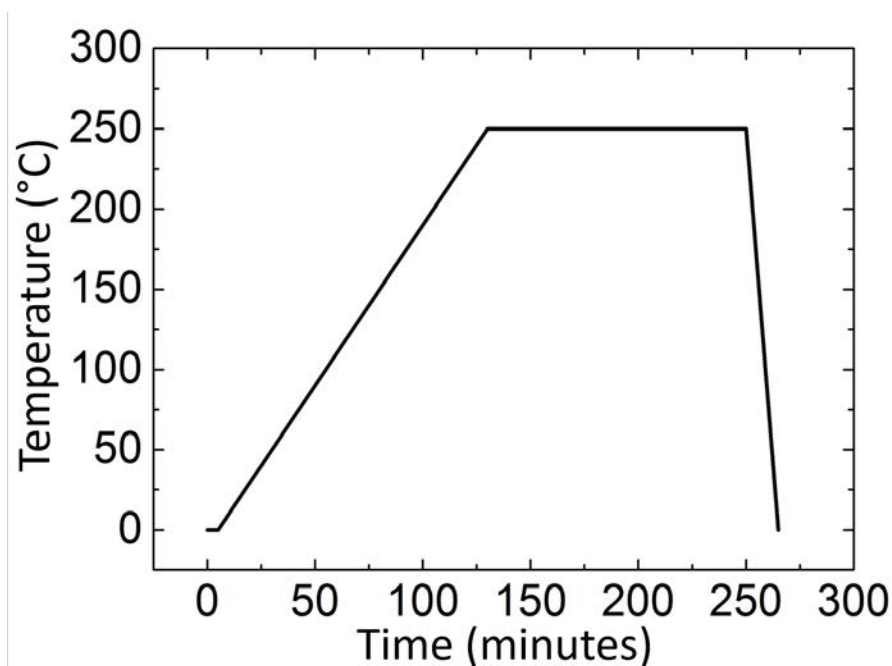
Figure 2.22: Graph showing temperature ramp curve used for all reactions and treatment in this study.

In all our experiments, the temperature program was started by using helium gas to flash the whole facility for 5 minutes, then the temperature was risen at 2°C per minute from room temperature to 250°C with a final dwell time of 120 minutes. At the end of the temperature program, cool helium gas was flowed through the system for 15 minutes to bring the temperature down. The pressure and temperature inside the glass tube can be measured and recorded throughout the experiment. The temperature program is plotted in Fig.2.22 for easier understanding.

CHARACTERISATION AND DYNAMICS OF COLLOIDAL GOLD NANOCLUSTERS PROBED BY STEM

Fig.3.4 is used in the paper with our collaborators. Malola, S.; Lehtovaara, L.; Knoppe, S.; Hu, K. J.; Palmer, R. E.; Brgi, T.; Hkkinen, H. *Au$_{40}$(SR)$_{24}$ Cluster as a Chiral Dimer of 8-Electron Superatoms: Structure and Optical Properties. J. Am. Chem. Soc. 2012, 134 (48), 19560*

3.1   Characterisation of MP-Au$_{40}$

3.1.1   Atom counting of MP-Au$_{40}$ nanoparticles

To determine how many gold atoms there are in a monomer of monolayer-protected Au$_{40}$ clusters we can take advantage of the incoherency nature of the HAADF-STEM signals which the strength of signal is proportional to the atomic number (Z) of the sample. We address the method we used as Atom counting which is based on measuring of the HAADF-STEM intensity of clusters in images and subtract the contribution of background signal calculated through measuring the area around the target cluster at the same time.[37] We make use of the size-selected (SS) cluster source we have to prepare bare Au$_{55}$ clusters as a mass standard for measuring MP-Au$_{40}$ clusters. In order to max-

imally reduce the error of electron optics between different sessions, we deposit both MP-Au$_{40}$ and SS-Au$_{55}$ clusters in different areas on the same electron microscopy grid. HAADF-STEM images of two different areas where different clusters are shown in Fig.3.1.
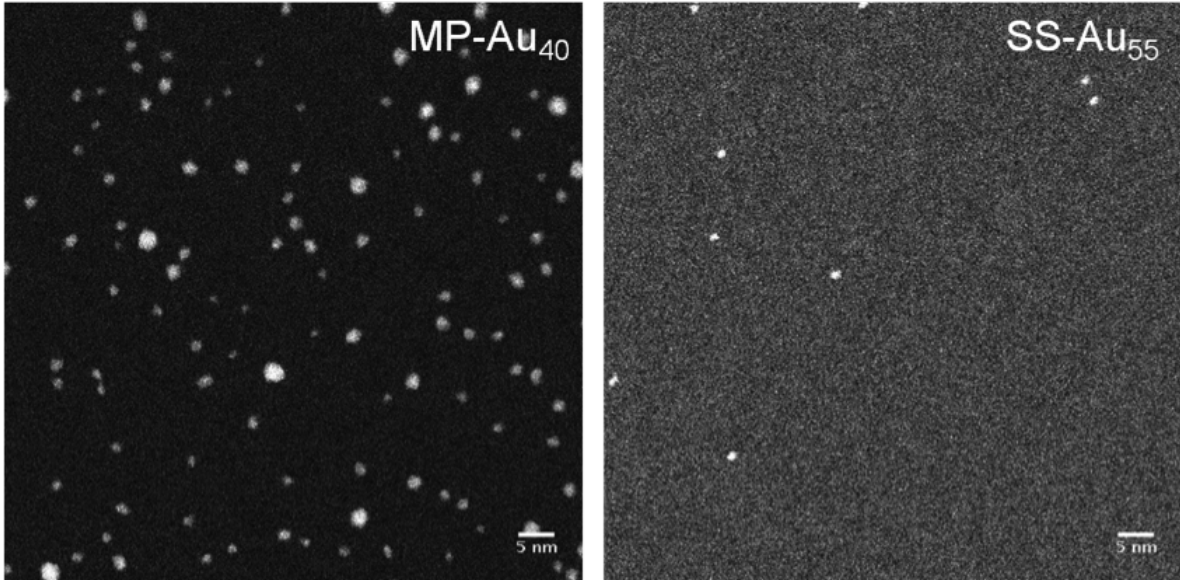
Figure 3.1: HAADF-STEM images of Monolayer-protected Au$_{40}$ and Size-selected Au$_{55}$ at low magnification (5M). Image for MP-Au$_{40}$ clusters at the left hand side show that they distribute on the surface with a higher density and bigger clusters from aggregation can be seen. At the right hand side, SS-Au$_{55}$ cluster appears to have little aggregations.

Fig.3.1 of SS-Au$_{55}$ shows that they are evenly deposited on the TEM grid with lower density compared with images of MP-Au$_{40}$. We observed little aggregation of two or more SS-Au$_{55}$ clusters. We then turn to the image of MP-Au$_{40}$ clusters, MP-Au$_{40}$ clusters are seen to distribute on the TEM grid with a higher concentration. Aggregations occur quite often. We see clearly wider distribution of clusters sizes on carbon film. As the result, we expect to get wider distribution of mass in later analysis as well.

Statistical analysis of HAADF-STEM intensities of 953 clusters was performed with diameter of clusters no bigger than 1.8 nm. The intensities of MP-Au$_{40}$ and SS-Au$_{55}$ are only mutually comparable to each other when the data is extracted from the same session. But we can use Au$_{55}$ as a standard, to merged statistical data from different sessions together.[37] In other words, we average results from two different sessions with the weight of contribution considered.
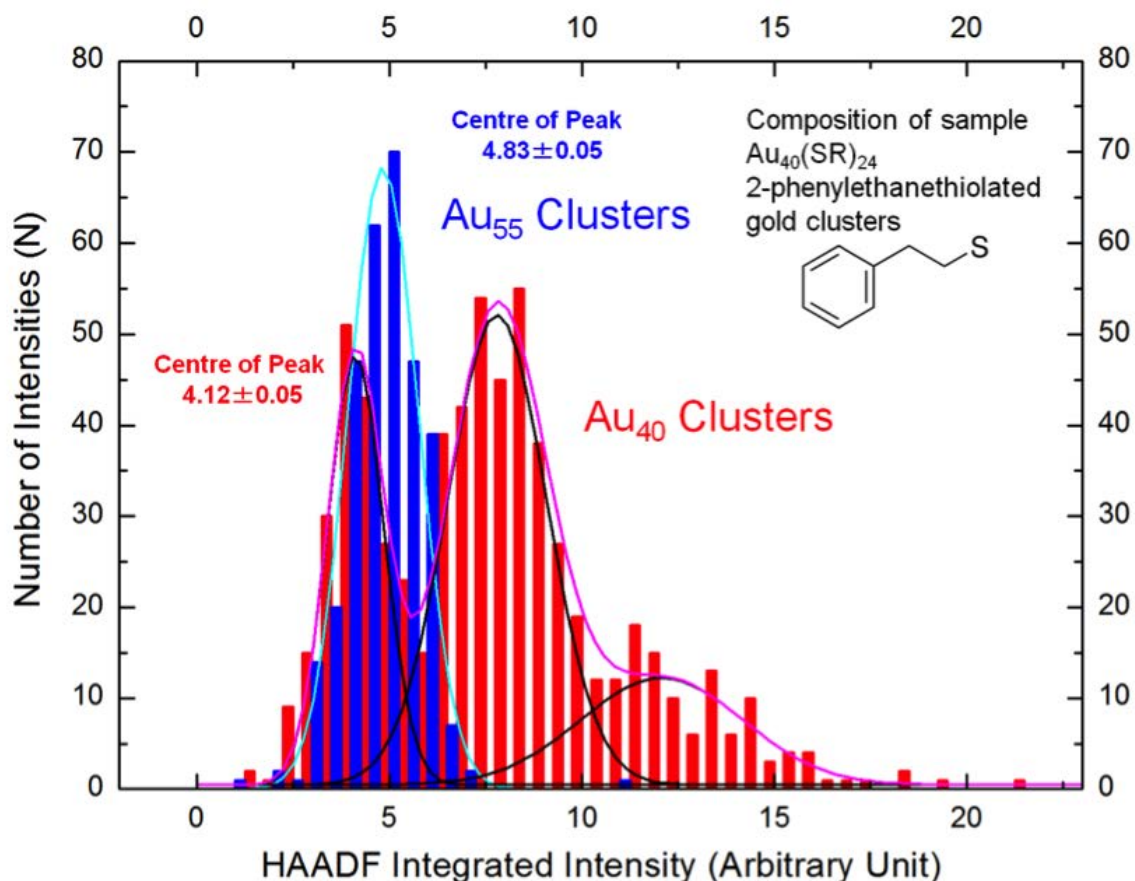
Figure 3.2: Histogram of Integrated HAADF intensities of MP-Au$_{40}$ and SS-Au$_{55}$. HAADF integrated intensities as a function of number of clusters.

Fig.3.2 shows the distribution of HAADF integrated intensity for SS-Au$_{55}$ clusters is a single peak, centred at 4.83 (arbitrary unit). The intensity represents the collection of atomic numbers (Z) in a cluster[23]. A single peak indicates that SS-Au$_{55}$ clusters are uniformly distributed in size. On the other hand, statistical result for MP-Au$_{40}$ clusters shows features of multiple peaks. We use curve fitting software to help us deconvolute overlapping peaks. After the deconvolution, we resolve three peaks. The first one, centred at HAADF integrated intensity 4.12 (arbitrary unit), is covered by the one peak of the SS-Au$_{55}$. The second one, centred at 7.80 (arbitrary unit), leans against the blue peak of SS-Au$_{55}$. The second peak has a shoulder near it at the higher intensity region, in which the third peak is located. The third peak is centred at 12.1 and its frequency on the graph is smaller, because we avoid taking intensities from clusters that are obviously not monomers in size during analysis. The position of the second and third peak are

85

integer multiples of the first peak. This suggests the second and third peaks are dimers and trimers respectively, aggregates from the monomer in the first peak.

To compare the weight of monolayer-protected and bare clusters, we use SS-Au$_{55}$ clusters as mass standard to measure the number of atoms in the MP-Au$_{40}$ clusters.[37] Though the atoms in ligands are usually lighter and much dimmer compared with gold atoms in the images, their contribution to the intensity of HAADF-STEM images is not negligible. We need to count in the contributions of these atoms using the following equation of describing the ratio of intensity between N$_A$ of A atoms and N$_B$ of B atoms.

$$\frac{I_A}{I_B} = \frac{N_A}{N_B}(\frac{Z_A}{Z_B})^n \tag{3.1}$$

As we are using the gold clusters as the mass standard, we can use the HAADF-STEM intensity of a gold atom as our unit of intensities. To estimate the effective intensity of ligands, we can transform the equation above into the equivalent number (E) of gold atoms, if there are three kinds of atom contained in the ligands of ours. They are sulfur, carbon and hydrogen. then

$$E = N_S(\frac{Z_S}{Z_{Au}})^n + N_C(\frac{Z_C}{Z_{Au}})^n + N_H(\frac{Z_H}{Z_{Au}})^n \tag{3.2}$$

Z is the atomic number of considered atom. The number n is the dependency between intensity and camera length. The value of n is 1.46±0.18 for the microscope we used here. And other values we put for 2-Phenylethanethiol (C$_8$H$_9$S) are, N$_S$=1, N$_C$=8, N$_H$=9, Z$_{Au}$=79, Z$_S$=16, Z$_C$=6, and Z$_H$=1. After considering the contribution of ligands, the MP-Au$_{40}$ clusters are found to have 39.8±1.89 gold atoms. Therefore, we conclude that the number of gold atoms contained in MP-Au$_{40}$ clusters are 40±2 Au atoms.

3.1.2 Real-space observation of Monolayer-Protected Au$_{40}$ Clusters

Fig.3.3 shows HAADF-STEM images of MP-Au$_{40}$ clusters at high magnification. The bright features in figures are contributed by gold atoms. The atoms in ligands (S, C, and H atoms) cannot be seen, due to their much smaller atomic number compared with gold. In over 500 images taken, less than 1% of images show structures clearly, others appear to have little symmetry, though we can confirm the Au atomic columns and the separations between columns. This indicates that at this size in room temperature, the structure of MP-Au$_{40}$ remain crystal-like, instead of being droplet-like structure, suggested by the previous research.[13, 43]
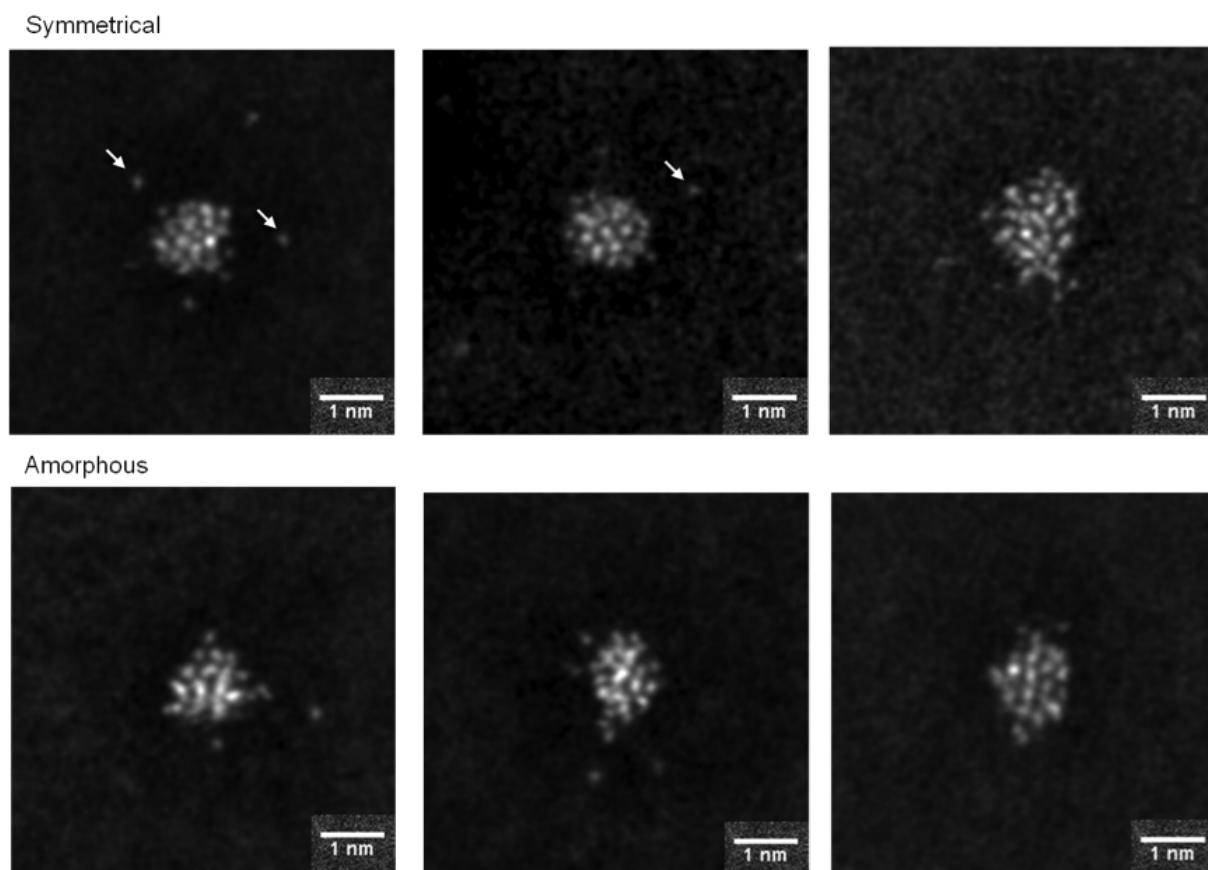
Figure 3.3: Representative series of MP-Au$_{40}$ clusters at high magnification (20M). Top three: clusters with symmetrical structures. Bottom three: clusters with amorphous structures.

Structural details often change between two successive images that are taken within

a second. The reason could be combined effects of intrinsic thermal fluctuation and the momentum transferred by high-energy electron beams. Due to this reason, the structure of MP-Au_{40} cannot be determined reliably under constant reconstruction and rearrangement. However, we can manage to optimise the experimental conditions so that the shape of sample clusters would be retained during STEM imaging.[24] In some images, single Au atoms away from the clusters can be seen (As indicated by arrows). They sometimes diffuse on the carbon film over repeat scanning.

To quantitatively investigate the shape of MP-Au_{40} clusters, we measure the aspect ratio (the ratio of major axis divided by minor axis) of clusters observed in the high-resolution HAADF-STEM images. We employ the Fit Ellipse module with ImageJ software package to perform the measurement. [24] Before the measurement is made, we perform noise removal on the images. And in some of the images, single atoms could be seen around clusters. These atoms might come off from clusters. The integrity of clusters might be damaged and thus the result of measurement would not be representative. Therefore we do not measure aspect ratio from clusters that have single atoms around them in the images.

We show here a scatter chart of the aspect ratio (X-axis), HAADF-STEM integrated intensity (Y-axis) and the histogram of these two measurements of MP-Au_{40} clusters. On the left hand side of the chart is a vertically presented histogram of HAADF-STEM integrated intensity. The result shows that both monomers and dimer are taken for aspect ratio measuring, according to two obvious peaks we saw in the histogram.

The purpose of including data of HAADF-STEM integrated intensity when we are measuring the aspect ratios is to provide us an indication of what type of clusters are chosen by us. During the STEM imaging for aspect ratio, we avoid clusters that are obviously too big to be monomers, but inevitably other type of clusters might be included as well. With this HAADF histogram, we can exclude aspect ratio of clusters outside the credible weight of monomers. We did this by performing Gaussian curve fitting on HAADF histogram. Then, we take these fitted parameters to rule out clusters that are

outside the region of (peak centre)(standard deviation) before we take following aspect ratio measurement.
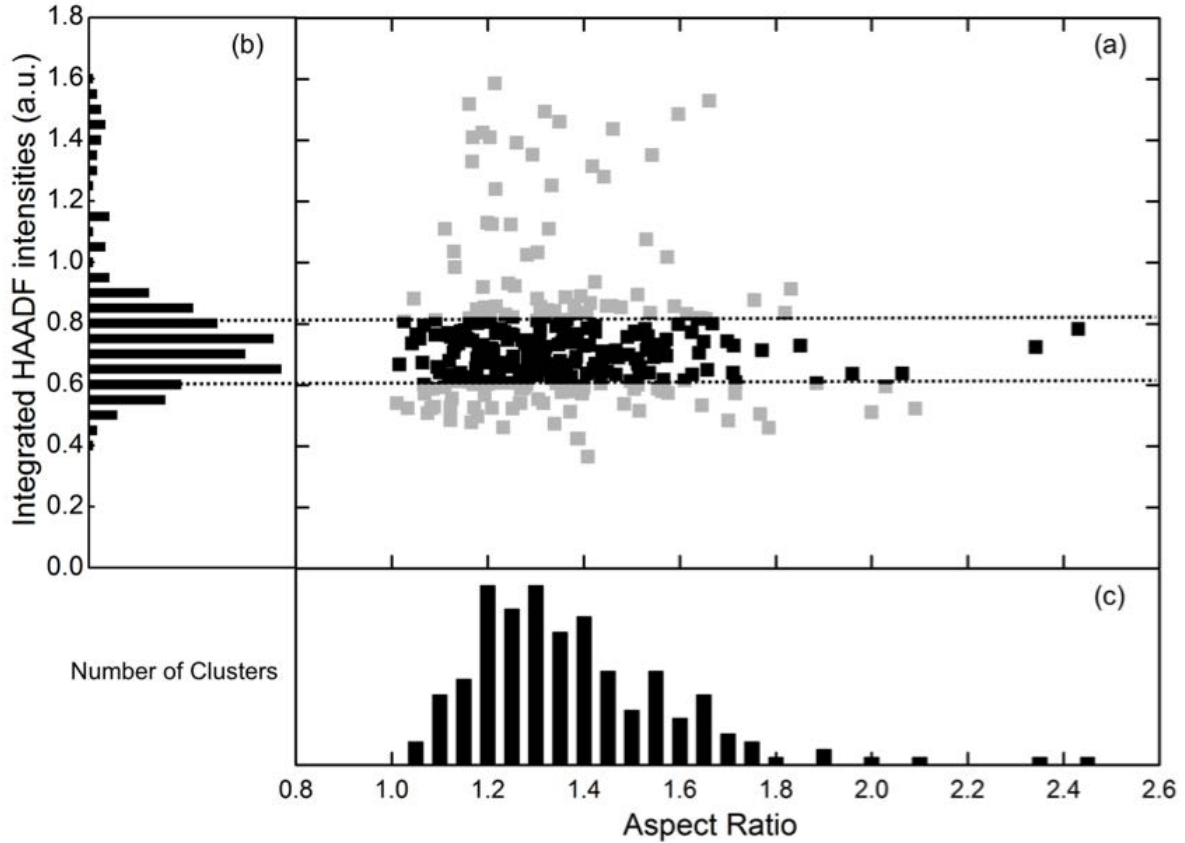
Figure 3.4: Result of aspect ratio measurement for MP-Au$_{40}$ clusters by STEM. (a) Statistical distribution of HAADF intensities as a function of measured aspect ratio. (b) Corresponding histogram of HAADF-STEM intensities. (c) Histogram of aspect ratios of MP-Au$_{40}$ monomers, obtained by excluding all particles outside the HAADF intensities range marked by the dotted lines.

Fig.3.4 (c) shows the statistical result of aspect ratio (AR) of 183 MP-Au$_{40}$ clusters, after excluding monomers that do not fall into the region of (peak centre)(standard deviation). The histogram ranges from 1.05 to 1.80 with several data points above 1.90, which is believed to be ignorable because they are away and separated from the main distribution. The place where the histogram of aspect ratio reaches a maximum is not close to 1.0. This indicates MP-Au$_{40}$ clusters do not have spherical shape. Otherwise we will expect the peak value of aspect ratio to center near 1.0.

MP-Au$_{40}$ cluster might have interaction with the carbon film on the grid. If MP-Au$_{40}$

clusters are mostly lying on the surface or even randomly orientated, we should expect the histogram of aspect ratio to reach highest value at the end of its distribution. From previous researches, results show ligands could interact quite strongly with the surface or other ligands. The carbon chain which is hydrophobic could bond and lie on the surface or stand up with an angle to the surface when there are enough of them.[110, 111] We suspect that these effect caused by ligands on the cluster surface make MP-Au_{40} tend to stand up with a angle on the amorphous carbon surface, neither stand up vertically nor completely lying on the surface. Therefore, the distribution of the AR becomes less important, what is crucial is instead the maximum value of aspect ratio distribution can reach. As the result, we conclude the aspect ratio for MP-Au_{40} in our experiment is 1.8.
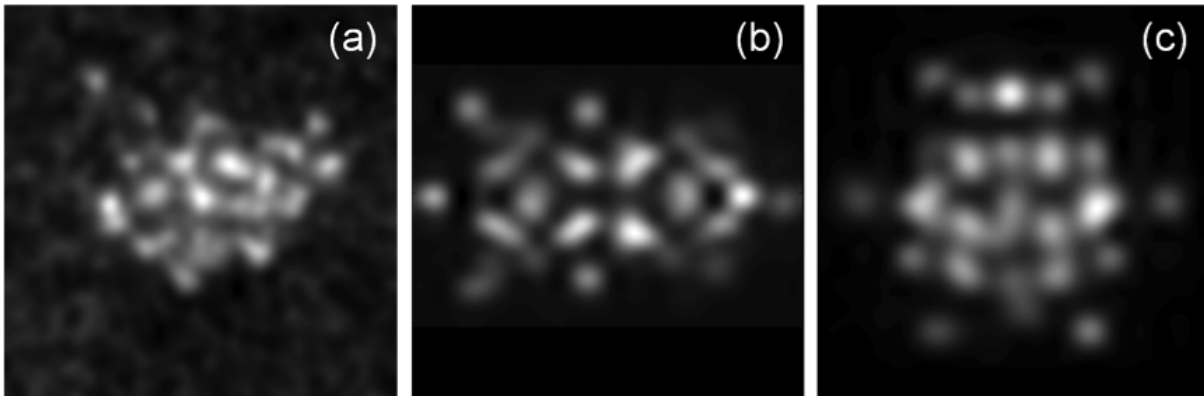
Figure 3.5: Represent images for (a) Experimental image for MP-Au_{40}. (b),(c) Simulated images of prolate model of Au_{26} bi-icosahedron core (b) and Au_{28} core tetrahedron atomic model (c).

In previous study, monolayer-protected Au_{38} clusters are expected to be formed of two Au13 icosahedrons clusters with a few long and short stable forming divided and protected motif. [112] It is predicted to have elongated shape of AR to be 1.58.[24] Two possible atomic models for MP-Au_{40} are calculated using density functional theory (DFT) by a collaborator. [112] One is a tetrahedral cluster with a 28 atoms core and 12 short Au-SR staples and this model has maximum aspect ratio of 1.17. The other model for MP-Au_{40} is formed of two Au_{13} icosahedrons, 4 long staples (-SR-(Au-SR)2-), and 6 short staples (-SR-Au-SR-). The difference for this model compared with the one for MP-Au_{38} is that two icosahedrons Au_{13} in the core did not share any atoms like in the atomic

model for MP-Au$_{38}$. Instead, two icosahedrons only connect to each other by overlapping one of their edges. Due to this, the shape of MP-Au$_{40}$ cluster is longer than MP-Au$_{38}$. The aspect ratio for the model is 1.82 which is a very good match of our measurement. Moreover, potential energy of tetrahedral model is significantly higher that prolonged model which makes it less stable in the experiment.

3.1.3 Dynamical behaviour of Monolayer-Protected Au$_{40}$ clusters

Constantly atomic rearrangement and reconstruction of clusters during STEM imaging has been observed. [113] This could be due to intrinsic thermal fluctuations and high energy electron beam shining on the clusters. [113] In particular, the electron beam plays a dual role as both the probe of STEM scanning and a main source of fluctuation. In order to observe the effect of electron beam acting on clusters, we conduct experiments of rapid image taking over prolong time under different electron beam intensity which is a main independent variable in our experiment.
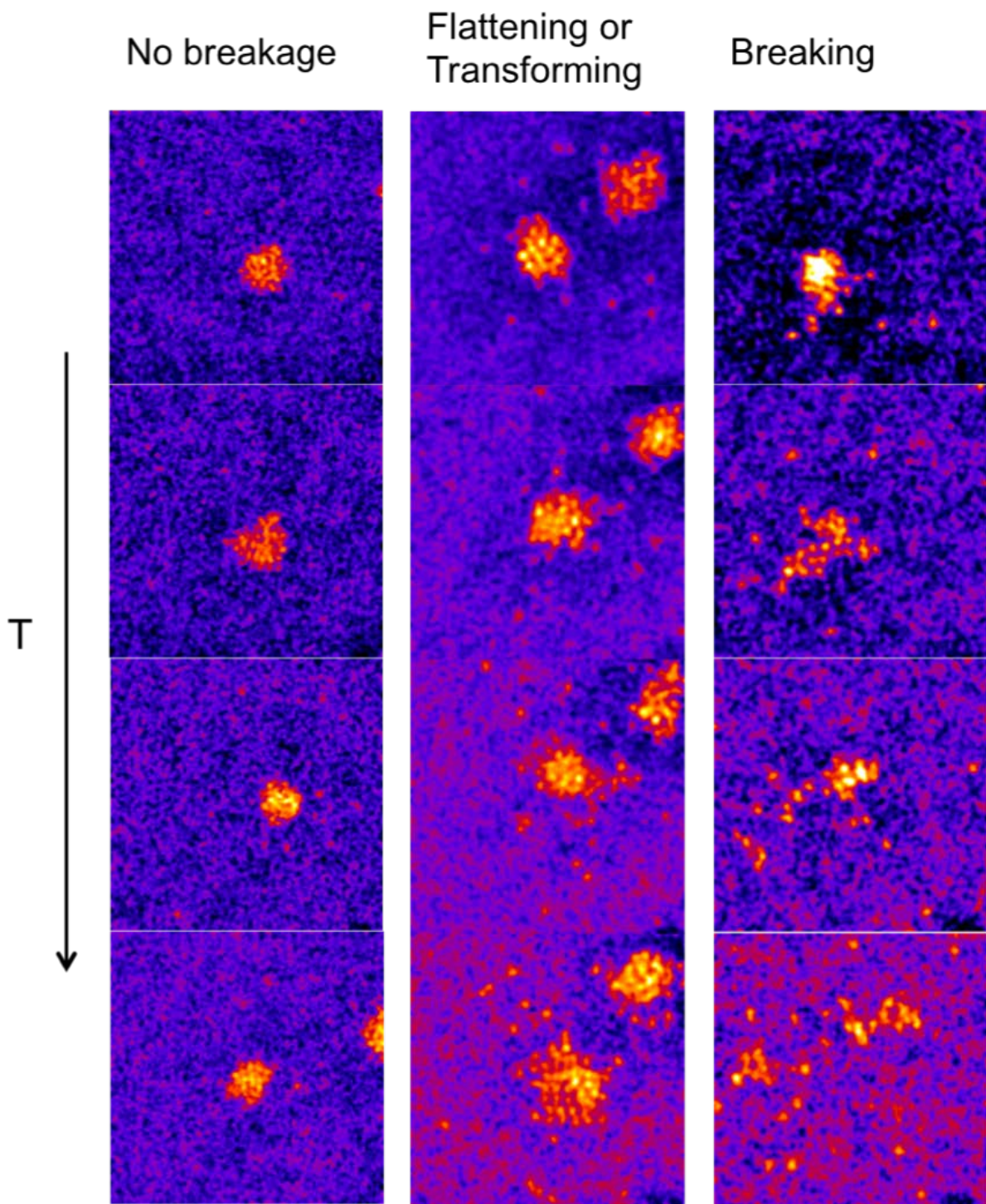
Figure 3.6: Representative images of different scenario clusters may take under prolonged electron beam irradiation. In the graph, four successive images from each set of film that is showing the behaviours of a cluster is presented.

We conduct experiments on both MP-Au$_{40}$ and SS-Au$_{55}$ clusters under three different electron beam intensities. The behaviours clusters undergo largely fall into three different

categories as following. See Fig.3.6. First, clusters may have some minor morphological changes or flipping, but they did not change significantly in structure nor give off single atoms from them. Second, clusters may change drastically in structure and considerably amount of single atoms fall from the clusters. Third, under an intensive electron beam, clusters vibrate rapidly and eventually break into small pieces of single atoms. In order to quantitatively describe the relation between rate of atom losing from clusters and beam intensity, we measure the initial and final weight of the clusters using atom counting method and then divide the difference of them by the length of the experiment to get the rate of atom losing.
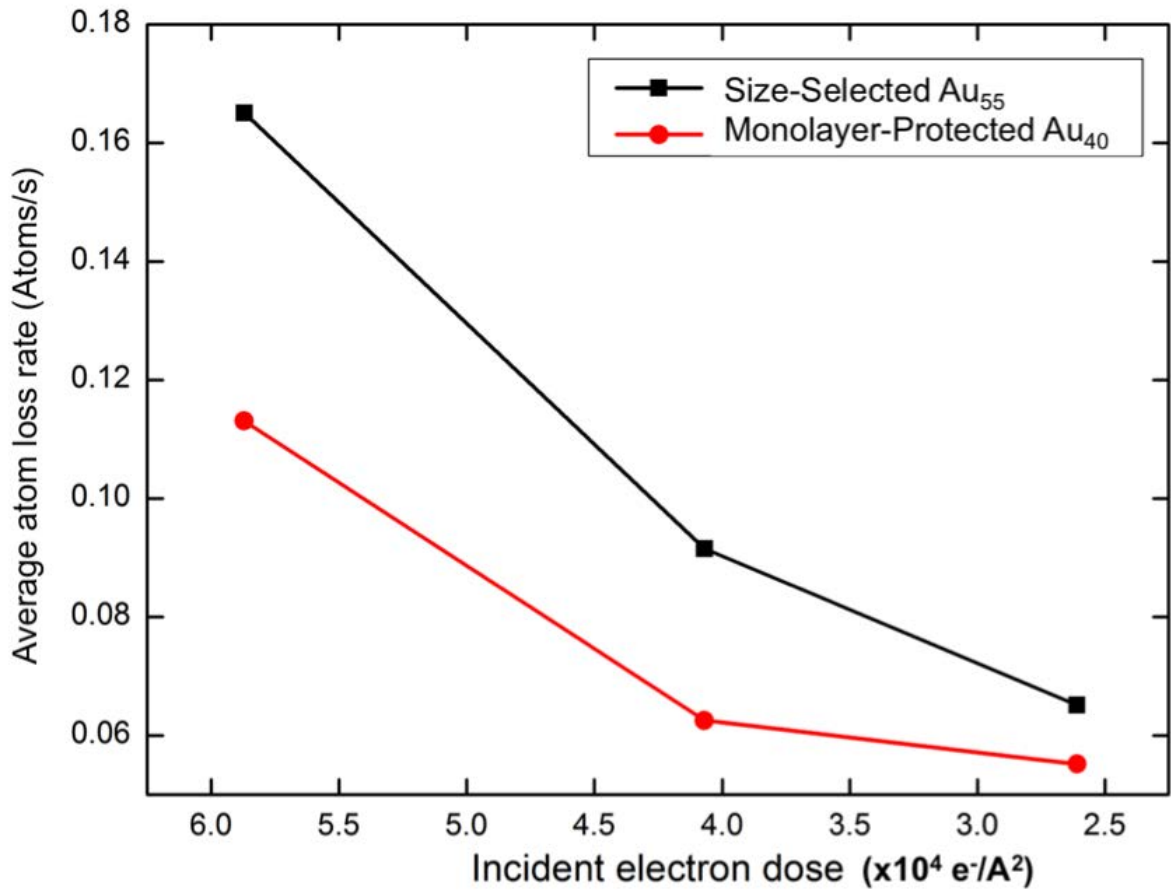
Figure 3.7: Average atom loss rate as a function of incident electron doses for MP-Au_{40} and SS-Au_{55} clusters. The average atom-losing rate of SS-Au_{55} is consistently higher than MP-Au_{40} clusters.

Fig.3.7 shows the relation between rate of atom losing and incident electron beam intensity. Previous research has shown that the fluctuation induced by electron beam

can be intensity dependent. [113] This explains the rate of both clusters drop with the decreasing of beam intensity. We know also from previous studies that the clusters with a larger size tend to be more stable, [14] but we notice that the losing rate of SS-Au$_{55}$ is consistently higher than MP-Au$_{40}$ clusters. This implies monolayer-protected Au$_{40}$ clusters are more stable than bare Au$_{55}$ clusters. It is challenging to compare the factors that could affect the stability of MP-Au$_{40}$ and SS-Au$_{55}$, because they are different in size, structure, and with or without ligands on the surface of them. But we know from previous research[34] about the clusters instability under prolonged electron beam scanning that indicated ligands protected clusters are more likely to retain their crystal structure compared with bare gold clusters of similar size. In that study, the precise weight of clusters is not mentioned or monitored and obvious single atoms falling off from clusters is not noticed. From another theoretical study about dynamic of bare Copper clusters growth, result suggest that the binding energy of clusters size 40 can only be as stable or less stable comparing with clusters size 55. [114] Moreover, researches indicates ligand protected gold clusters can form a layer of Au-ligand oligomers to protect the core inside from chemical reactions. From these previous results and the fact that MP-Au$_{40}$ is more stable than SS-Au$_{55}$ under electron beam in our experiment, we suspect that ligands could enhance the overall stability of gold clusters through involving the structural formation or directly protecting the inner core from losing atoms.

3.2 Characterisation of PVA-stabilized Au nanoparticles

3.2.1 Overview

PVA-protected Au nanoparticles were synthesised by colloidal methods and stabilised on titania. The effect of different temperatures (-75 to 75 °C) and mixing ratio of H$_2$O/EtOH solvent (0, 50, and 100) on the efficiency of the catalytically oxidising glycerol was in-

vestigated. It was discovered that the Au nanoparticles synthesised in H_2O at $1\,^\circ C$ are highly active compared with generic Au/TiO_2 catalyst. In order to find the reason of this effect, we employ TEM technique to survey a wide area of the Au/TiO_2 catalyst in order to acquire the size distribution of gold nanoparticles under different temperature and solvent mixing ratios.

3.2.2 Experimental section

The samples were prepared by our collaborator Scott et al[115], through the reduction of chloroauric acid ($HAuCl_4 \cdot H_2O$ 1.24×10^{-4} M) with $NaBH_4$ (0.1 M) solution in different mixing ratios of $H_2O/EtOH$ solvent. The temperature of the solution was another independent variable. We imaged samples, that are abbreviated to A1 and B1, with the JEOL-2100F under TEM mode at 200 kV accelerating voltage. Sample A1 was prepared in 100% water at $1\,^\circ C$ and sample B1 was prepared in 50% $H_2O/EtOH$ solution at -30 $^\circ C$ Powder catalysts prepared were dissolved in ethanol using sonication. The solution ($40\mu L$) was then drop cast with a pipette onto a commercially available holey carbon film that supported with a 300-mesh copper grid.

3.2.3 Size-distribution of Au/TiO$_2$ system
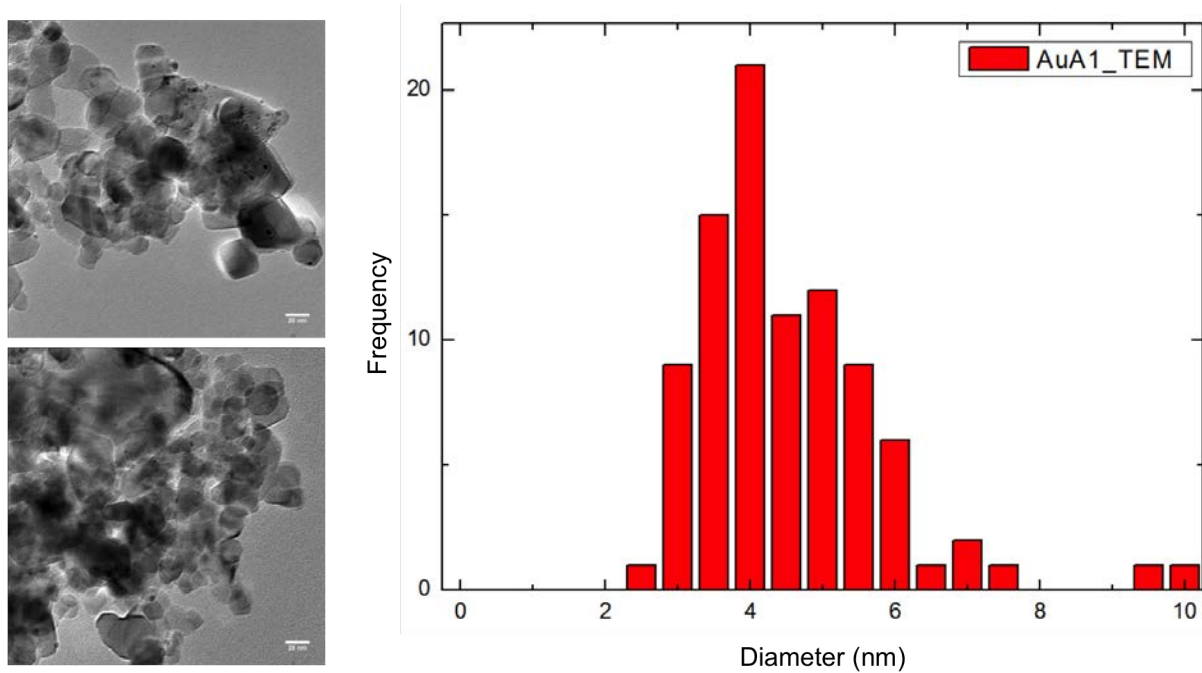
(a)
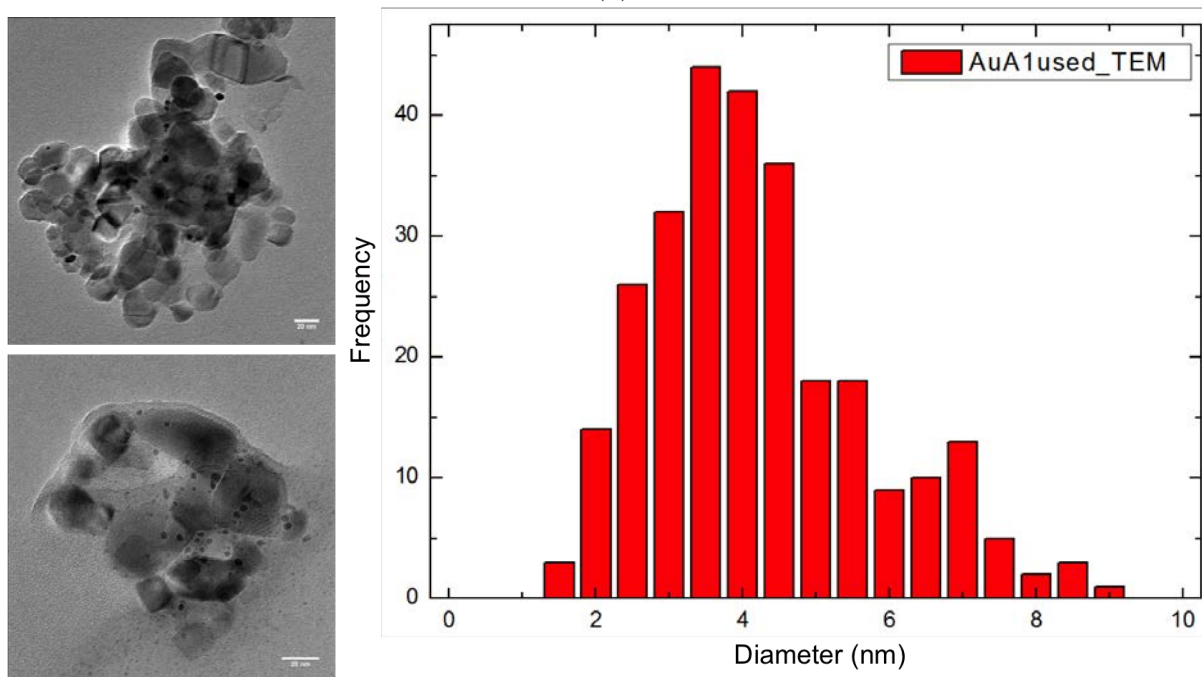
(b)

Figure 3.8

The representative TEM image of sample A1 and the size distribution derived from these images are shown in Fig.3.8. The result of catalyst as prepared with 100% H$_2$O at 1 °C is

shown in Fig.3.8 (a) and the result for the same catalyst after tested in glycerol oxidation reaction is shown in Fig.3.8 (b). In both unused and used catalyst, powder TiO_2 particles with various sizes, aggregate with neighbouring particles but did not completely coalesce with each other. Au nanoparticles attached to the support can be seen in the images. The diameter of the gold nanoparticles was acquired through measuring the area of the particle and then deriving the diameter by assuming these particles are circular in shape. The unused catalyst A1 was imaged and its size distribution statistics are presented in Fig.3.8 (a). The size distribution in Fig.3.8 (a) is a single broad and asymmetry peak (tailing to the larger cluster size direction) with the highest frequency at 4 nm and FWHM 2.5 nm. The size distribution of the same catalyst after being subjected to glycerol oxidation is presented in Fig.3.8 (b). The size distribution became broader than it was before reaction, in both larger and smaller clusters size direction. The distribution maintained its asymmetry manner with the highest frequency reduced slightly to 3.5 nm.
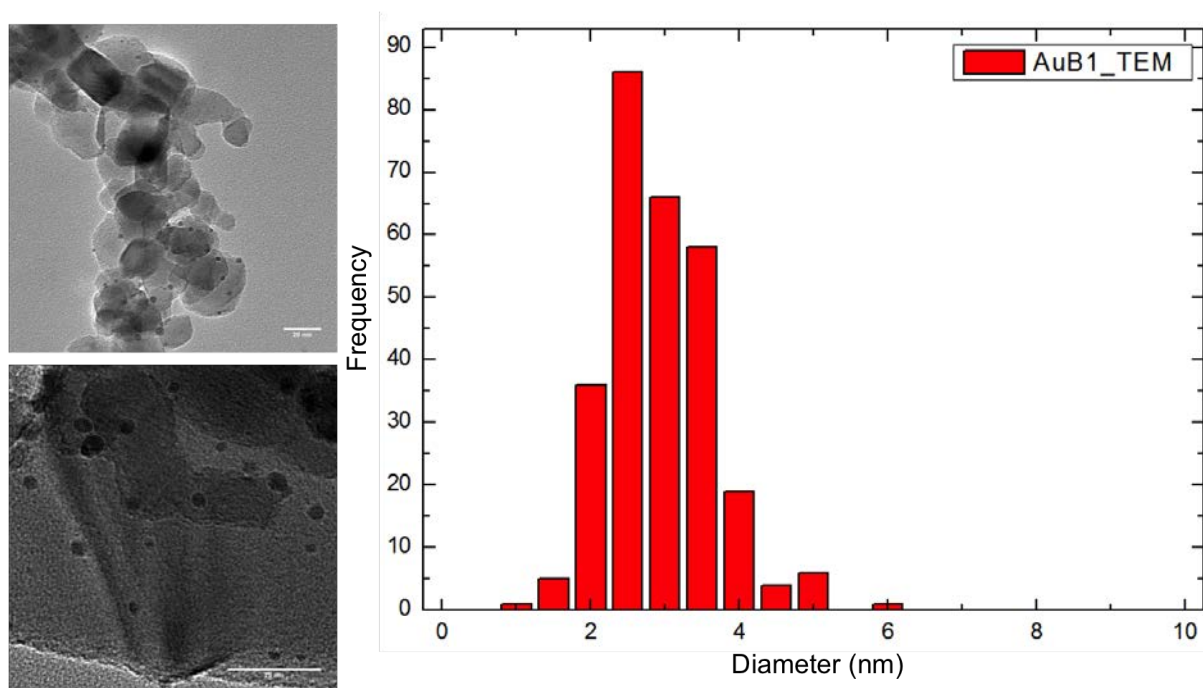
Figure 3.9

Sample B1 was prepared with different conditions from sample A1. It was prepared in 50% H_2O/EtOH solvent ratio at -30 °C . The representative images and size distribution

for unused sample B1 was presented in Fig.3.9. The size distribution of B1 has its highest frequency at 2.5 nm with FWHM of 1.5 nm.

The samples in group A represented preparation in pure water solvent and group B catalysts were prepared in 50% H_2O/EtOH solvent. The number following after A and B represent different temperatures used during synthesis. It was found that Au nanoparticles on B1 were smaller and their distribution narrower than on A1. In catalytic reaction, A1 and B1 were the most active catalyst from their group of preparation conditions. The A1 was the most active catalyst amongst all catalysts prepared. Although sample A1 have larger size than nanoparticles on B1, the existence of ultrasmall Au_2 to Au_5 clusters on A1 catalyst were found by HAADF sTEM observation[115], which could explain the high activity on A1.

3.2.4 Conclusion

TEM imaging and size statistics were carried out on PVA stablised Au nanoparticles with TiO_2 support, prepared under different ratios of H_2O/EtOH and temperature. Characterisation showed the particle size to be 4±2.5 nm on sample A1 and 2.5±1.5 nm on sample B1. Although the size distribution on A1 is larger than on B1, A1 has better catalytic ability compared with B1, however, it may be that the presence of ultrasmall Au_2 to Au_5 particles are crucial to the enhanced catalytic ability of A1[115].

CHAPTER 4

RIPENING MODES OF MASS-SELECTED GOLD NANOCLUSTERS DUE TO CO OXIDATION

Most of the text in this chapter is used in my publication (with me as first author, accepted in Nov 2015) Hu, K.-J.; Plant, S. R.; Ellis, P. R.; Brown, C. M.; Bishop, P. T.; Palmer, R. E. *Atomic Resolution Observation of a Size-Dependent Change in the Ripening Modes of Mass-Selected Au Nanoclusters Involved in CO Oxidation J. Am. Chem. Soc. 2015, jacs.5b08720*

4.1 Overview

Identifying the ripening modes of supported metal nanoparticles used in heterogenous catalysis can provide important insights into the mechanisms that lead to sintering. We report the observation of a cross-over from Smoluchowski to Ostwald ripening, under realistic reaction conditions, for monomodal populations of precisely-defined gold particles in the nanometer size range, with decreasing particle size. We study the effects of the CO oxidation reaction on the size distributions and atomic structures of mass-selected $Au_{561\pm13}$, $Au_{923\pm20}$ and $Au_{2057\pm45}$ clusters supported on amorphous carbon films. Under identical conditions, $Au_{561\pm13}$ and $Au_{923\pm20}$ clusters are found to exhibit Ostwald ripening, whereas $Au_{2057\pm45}$ ripens through cluster diffusion and coalescence only (Smoluchowski ripening). The Ostwald ripening is not activated by thermal annealing or heating in O_2

alone.

4.2 Introduction to ripening of metal nanoclusters

The inhibition of sintering remains a central challenge for heterogenous catalysis using ultrafine metal particles.[116, 117] Sintering leads to the coarsening of the particles, and hence the irreversible deactivation of their catalytic activity as the average particle size increases over time.[118] This places limitations on the efficiency and longevity of supported metal particle catalysts. The size and morphology of small catalyst particles is integral to their activity, as these parameters determine the number of active sites (e.g. facet and edge sites), and other size-dependent electronic effects and quantum effects.[119] Particle ripening is commonly ascribed to one of two modes: *Ostwald ripening*,[77, 79] in which large particles grow at the expense of smaller particles through the migration of single atoms or small atomic clusters, and *Smoluchowski ripening*,[78] in which whole particles are free to diffuse and coalesce with neighbouring particles. Nanoparticle ripening modes have been investigated *in situ* with environmental TEM[94, 93, 120, 121], however, the challenge is to replicate realistic reaction conditions whilst also de-coupling the effects of any damage induced through exposure to the electron beam. In general, the imaging of small clusters at the atomic level, even *in vacuo*, remains challenging.[122, 119] It has long been known that supported metal clusters exhibit size-dependent catalytic properties,[123] although it has only been recently that catalytically-active, size-selected $Pt_N(N = 22, 68)$ clusters on oxide supports have been used to provide evidence of Ostwald ripening suppression in truly monomodal populations.[124] Particle size has long been associated with catalyst sintering kinetics,[125] but detailed studies of truly monodisperse nanoparticles at atomic resolution has proved elusive.

Using amorphous carbon supports in the present work, we begin with stable populations of monodisperse, mass-selected particles centred at the magic number sizes of Au_N (N = 561, 923, 2057). Au nanoparticles of this size range are found to be active in

catalysing CO oxidation.[126, 127, 62, 66, 128, 65, 119], at low-temperatures (≥ 273 K) in particular.[127] Indeed, heterogenous catalysis using Au nanoparticles or clusters (<5 nm in size) has been studied extensively on a variety of supports (e.g. oxides, carbons, polymers), both for gas- and liquid-phase reactions.[62, 129, 67, 126, 130] Au on carbon presents a versatile selective oxidation catalyst for a number of reactions.[131] Although generally the catalytic activity of Au/C is considered to be low for CO oxidation below ambient temperature, an important example is CO oxidation at RT using highly dipersed (2-5 nm) Au particles supported on activated carbon fibres.[132] Commonly, Au particles catalysing CO oxidation at low temperature are supported on transition metal oxides, however, HAADF-STEM studies reveal that Au particles in the size range relevant to the present work (2-3 nm) exhibit semicoherent interfacial expitaxy,[133, 134] meaning that the morphology of the particles is, broadly, quasi-hemispehrical, rather than quasi-spherical, as for free-standing clusters.

The interest in magic numbers stems from theoretical treatments that indicate abrupt variations in the adsorption energies, e.g. for oxygen and CO, on Au clusters at magic number sizes.[75, 135] Low co-ordinated atoms at edge and corner sites may play a role in the catalytic activity of gold clusters and nanoparticles[136] and, for small clusters mimicking corner sites of larger (2-5 nm) particles, gold is predicted to be more catalytically active towards CO oxidation than other transition and noble metals.[137] Au can effectively catalyze the reaction even for few-atom particles.[136, 63] The study of Au catalysts by UHV-STM, for instance Au on titania,[99] has elucidated the sintering kinetics, suggesting that sintering is reaction-induced. There is much still to explore experimentally using accurately mass-selected clusters as model systems to complement the theory. Indeed, there is renewed interest in predictions of the relative stabilities for the geometric, magic-number high-symmetry isomers (I_h, D_{5h}, O_h) of Au nanoclusters with sizes up 3.5 nm,[72] prompted in particular by the recent experimental demonstration of atomic structure control for Au$_{923}$ in the cluster beam source.[138]

Here, by using monomodal populations of atomically-precise particles in the nanometer

size range, we reveal the cross-over between Ostwald and Smoluchowski ripening modes, as a function of particle size, and under realistic reaction conditions. We investigate the effect of CO oxidation reaction conditions (0.15±0.1 bar, 250 °C) on the size and atomic structures of mass-selected $Au_{561\pm13}$, $Au_{923\pm20}$ and $Au_{2057\pm45}$ clusters supported on amorphous carbon films. We find that $Au_{561\pm13}$ and $Au_{923\pm20}$ clusters exhibit Ostwald ripening, whereas $Au_{2057\pm45}$ ripens through coalescence and diffusion only. Indeed, what we show may account for the perceived preferential disappearance of certain particle sizes during sintering.[120] Furthermore, we determine for $Au_{923\pm20}$ that Ostwald ripening is activated by the introduction of CO oxidation, and not by thermal annealing (0.35 bar, 250 °C) nor the presence of O_2 alone (0.14 bar ($Au_{923\pm20}$) and 0.12 bar ($Au_{2057\pm45}$) at 250 °C).

4.3 Experimental section

Gold nanoclusters were produced with a magnetron-sputtering gas-condensation cluster beam source.[102] An inline lateral time-of-flight mass filter is used to select cluster of a specific size, offering a mass resolution of $M/\Delta M \approx 23$ based on calibration with Ar^+. The mass-selected gold clusters are focussed into the deposition chamber under high vacuum conditions (10^{-7}–10^{-6} mbar), with each size deposited onto separate amorphous carbon films suspended on molybdenum TEM grids at a soft landing energy of 0.5 eV/atom. In this approach, Au clusters with 561±13, 923±20, and 2057±45 were soft landed on the substrate.[85] Related cluster generation parameters: condensation length, 250 mm; magnetron sputtering power, 10 W DC; condensation gas flow rates, 200 sccm (Ar) and 150 sccm (He); condensation pressures, 2.05, 0.77, 0.86 mbar for Au_{561}, Au_{923}, Au_{2057}, respectively. After deposition, the Au clusters were imaged in HAADF-STEM, exposed to treatment conditions, and then imaged again. Samples were stored in a vacuum desiccator between measurements. The total time for which the Au clusters were exposed to the atmospheric conditions during transfer between storage and instruments was <30

minutes. We find that, prior to treatment, the clusters maintained their high selective mass whilst stored in a vacuum desiccator at room temperature. Gas-phase reactions and treatments were conducted as previously reported.[139] Each TEM grid that carries Au clusters sits on a quartz wool plug in the middle of a quartz tube (length 360mm, inner diameter 4 mm). For all treatments, the temperature was increased at a rate of $2\,°C\,min^{-1}$ from room temperature to $250\,°C$ and held at $250\,°C$ for 2 hours. For thermal treatment, pure He gas was used at an initial pressure of 0.32 bar, rising to 0.35 bar at $250\,°C$. For treatment with O_2, a mixture of 20.9 % O_2 + 79.1 % He was used, with the pressure initially at 0.10 bar rising to 0.14 bar ($Au_{923\pm20}$) and 0.12 bar ($Au_{2057\pm45}$) at $250\,°C$. For the full CO oxidation reaction, premixed CO and O_2 gases were diluted in pure He, resulting in a mixture of 1 % CO + 20.9 % O_2 + 78.1 % He. The pressure was 0.11 bar (ambient temp.) rising to 0.16 and 0.14 bar ($250\,°C$) for $Au_{923\pm20}$ and $Au_{2057\pm45}$, respectively. After the temperature ramp cycle, pure He at room temperature was used to cool down the system for 15 min. Atomic resolution imaging was conducted with a JEOL 2100F STEM equipped with a spherical aberration probe corrector (CEOS GmbH) at a convergence angle of 20 mrad and a high-angle annular dark field (HAADF) detector. The microscope operates at 200 kV and the collecting angle on HAADF detector was between 62 mrad (inner) and 164 mrad (outer). In total, 4025 nanoclusters were imaged at atomic resolution (6 Mx magnification or higher) in order to measure diameters from the images and assign the atomic structures. Additionally, a total of 3162 clusters were imaged at 2Mx for measurement of the integrated HAADF intensities. In order to be able to assign the atomic structure for each cluster imaged, multi-slice HAADF-STEM image simulations were generated $Au_{561\pm13}$, $Au_{923\pm20}$, and $Au_{2057\pm45}$ using the QSTEM package. This atlas covers a full range of possible orientations for a given high-symmetry structure. By comparing experimental images with image simulations atlases, the structure of each cluster can be assigned. In image simulation, the following parameters were used: spherical aberration C_S= 1 μm; defocus C_1=-19 Å; acceleration voltage, probe convergence angle, and inner & outer collecting angles on HAADF detector are as described for the

experiment conditions.

Our aim is to preserve the free-space properties (size and structure) at the point of deposition onto a support. Of course, morphology is substrate-dependent.[88], and carbon supports offer advantages in this regard: the weak interactions between carbon and small metal particles has long been established,[140] and thus the supported particles retain the quasi-sphericity of their free space structures under soft-landing conditions (energy per cluster, 0.5 eV). Yet the clusters are not freely mobile on amorphous carbon:[42, 90] they are sufficiently stable on the surface to remain monodisperse at room temperature, in common with the behaviour observed on graphene[138] and graphene oxide.[141] This differs from the case of graphite, for which both Ag and Au clusters diffuse across the atomically-flat terraces at RT,[82, 142] unless energetically pinned,[85, 86] in which case, depending on size and binding energy, the clusters may resist lateral diffusion up to several hundred degrees above RT, undergoing Ostwald ripening above a threshold temperature.[87] Size-selected clusters pinned in this manner have been shown to resist sintering under realistic reaction conditions.[143] An additional virtue of using carbon as the support is that the atomic number is sufficiently low to offer high contrast imaging in HAADF-STEM, as the relative intensity (I_R) of gold to carbon in the image follows the relationship, $I_R = I_{Au}/I_C = (N_{Au}/N_C)(Z_{Au}/Z_C)^\alpha$, where N represents the number of atoms and $\alpha = 1.46 \pm 0.18$ is an instrument-specific parameter, which has been calibrated previously at an inner collection angle of 62 mrad. Given also that $I_{Au} \propto N_{Au}$, the relative masses of the particles can be determined quantitatively. Thus, the diameters of the particles can be measured directly from the HAADF-STEM images taken at atomic resolution, whilst the HAADF-STEM intensity distributions at lower magnification yield the relative particle masses within a given population.

4.4 Result and Discussion

4.4.1 Size distribution of different ripening mode

Populations of mass-selected clusters exhibit very narrow particle size distributions that are approximately Gaussian (see as examples Fig.4.1 b,d and Fig.4.2 a,c,i). This is advantageous given that Granqvist and Buhrman posited that the ripening mode could be identified simply by the weighting (skewness) of the particle size distribution.[78] Historically, modeling researches done to investigate the shape of size distribution of nanoclusters after physical vapour deposition.[80, 77, 81, 78, 79] It was found, via different machanisim of ripening, the distribution would develop to different tailing directions. With diffusion and coalescence, the distribution would be tailing toward larger size. It can be described as equation.

$$\Delta n = f(R)\Delta(\ln R), \tag{4.1}$$

where

$$f_{Smoluchowski}(R) = \frac{1}{(2\pi)^{\frac{1}{2}}\ln\sigma}\exp\{-\frac{1}{2}[\frac{\ln(R/\bar{R})}{\ln\sigma}]^2\}. \tag{4.2}$$

On the contrary, with Ostwald ripening, distribution is tailing toward smaller size. Its size can be discribed as

$$f_{Ostwald}(R) = \frac{4}{9}\rho^2(\frac{3}{3+\rho})^{\frac{7}{3}}(\frac{1.5}{1.5-\rho})^{\frac{11}{3}}\exp(-\frac{1.5}{1.5-\rho}), \rho < 1.5 \tag{4.3}$$

and

$$\rho = \frac{R}{\bar{R}} \tag{4.4}$$

However, the challenge to verify the Granqvist-Buhrman phenomenon experimentally has been two-fold: to track the change in the particle size distribution given that supported nanoparticles tend to exhibit an inherent broad, log-normal distribution from the outset, and to perform the analysis at the single particle level whilst amassing meaningful statistics. Mass-selected clusters can provide a valuable insight into the ripening process[124],

as there are no clusters smaller than the original, pre-determined size to be consumed in favour of other sizes. Clusters that result from ripening are therefore highly distinguishable from the original clusters. Furthermore, a monomodal population of clusters implies the same cohesive energy for all particles, and therefore the same energy required to liberate atoms and undergo fragmentation for all particles within the sample population.

4.4.2   Ripening of Au nanoclusters in control experiments
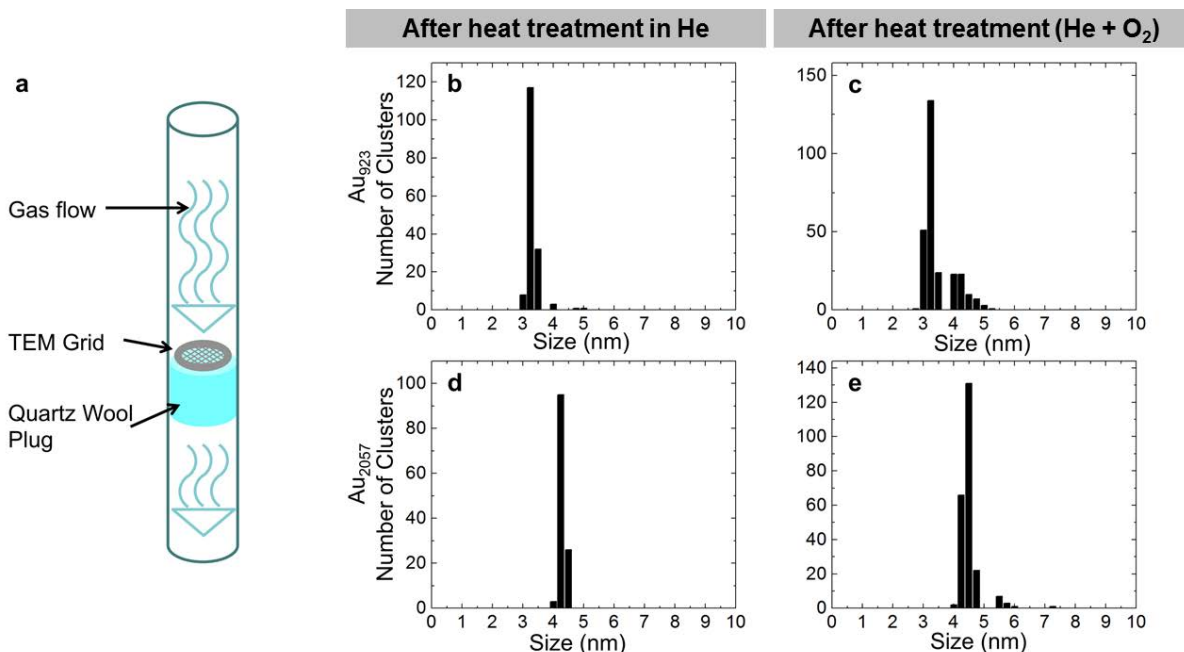
Figure 4.1: (a) Schematic diagram illustrating the gas-flow reaction setup for the treatment of mass-selected Au nanoclusters supported on amorphous carbon. (b-e) Histograms showing the size distributions for (b,c) $Au_{923\pm20}$ and (d,e) $Au_{2057\pm45}$ following (b, d) heat treatment in a pure He atmosphere (0.35 bar at 250 °C) and (c,e) after the introduction of O_2 (concentration by volume: 20.9 % O_2, 79.1 % He), with the pressure initially at 0.10 bar rising to 0.14 bar ($Au_{923\pm20}$) and 0.12 bar ($Au_{2057\pm45}$) at 250 °C.

In order to gain insights into the ripening mechanisms, we first seek to determine the effects due to separate thermal and O_2 treatments on the particle size distributions of $Au_{923\pm20}$ and $Au_{2057\pm45}$. Fig.4.1 (a) shows a schematic representation of the gas-flow reaction setup for the treatment of mass-selected Au nanoclusters supported on amorphous carbon used for these treatments. Fig.4.1 (b) and (d) reveal the results of the thermal treatment

(250 °C) of $Au_{923\pm20}$ and $Au_{2057\pm45}$, during which the particles were protected under an inert, dynamic atmosphere of pure He. There is no shift in, nor broadening of, the discrete particle size distributions at the initial particle size, although there is some evidence of aggregation for $Au_{923\pm20}$ given the presence of a proportion of larger particles, although it is limited. By comparison, the introduction of O_2 into the dynamic atmosphere for a separate set of $Au_{923\pm20}$ and $Au_{2057\pm45}$ samples induces a more pronounced change in the particles' size distributions (Fig.4.1(c) and (e)), which, as it appears to be quantized, is consistent with enhancement of the rate of dimerization, which is more pronounced for $Au_{923\pm20}$ than for $Au_{2057\pm45}$. Thus, this behaviour of whole particle migration and coalescence observed due to O_2 treatment is commensurate with Smoluchowski ripening. It is worth considering the factors that drive first surface diffusion then ripening of the particles: ambient temperature and the exothermicity of reaction. These factors then compete with the binding of the particles to defects, which governs the mean diffusion lengths. Of course, the role of molecular oxygen at elevated temperatures can be two-fold: the molecule can dissociate at active sites on the catalyst particle, and it can bind to surface defects to further attenuate interactions between particles and the support, and thus enhancing the rate of cluster diffusion in the presence of oxygen.

4.4.3 Ripening of Au nanoclusters in CO oxidation reaction
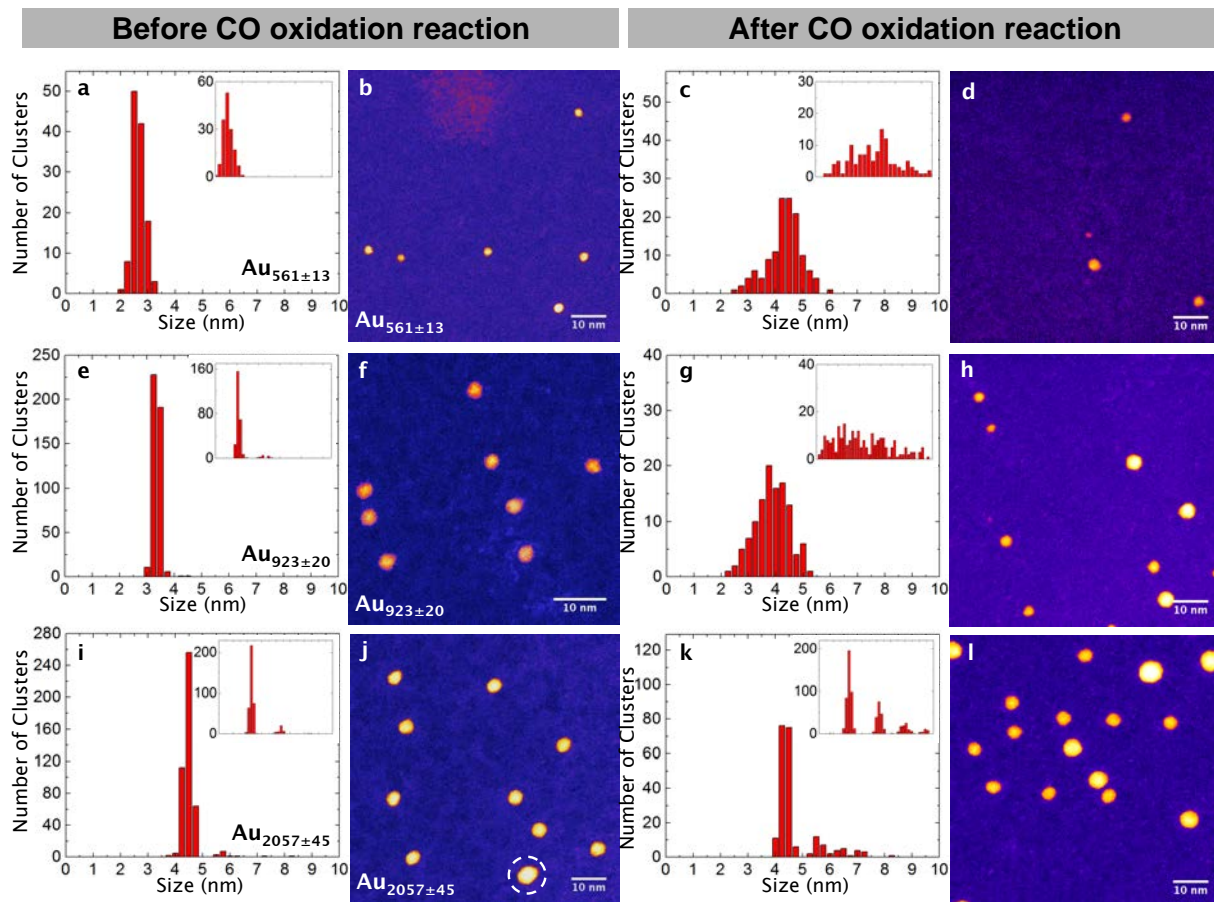
Figure 4.2: Histograms of the particle size distributions for mass-selected $Au_{561\pm13}$, $Au_{923\pm20}$ and $Au_{2057\pm45}$ nanoclusters both before (a,e,i) and after (c,g,k) exposure to the CO oxidation reaction conditions. The integrated HAADF-STEM intensity distributions are shown in the inset. The distributions are accompanied by representative HAADF-STEM images before (b,f,j) and after (d,h,l) the reaction. Conditions of the CO oxidation reaction: 0.15 ± 0.1 bar, 250 °C (ramp rate of 2 °C min^{-1} from RT and dwell for 2 hours). Gas mixture by volume: 1 % CO + 20.9 % O_2 + 78.1 % He.

Next, the behaviour due to O_2 treatment is contrasted with the effects of the CO oxidation reaction. The panel shown in Fig.4.2 illustrates the transformation in the particle sizes for $Au_{561\pm13}$, $Au_{923\pm20}$ and $Au_{2057\pm45}$. The corresponding and representative HAADF-STEM images (Fig.4.2(b, f, j)) taken before reaction, reveal the randomly distributed, monodispersed particles, the general morphology of which is quasispherical, as expected. Specifically, Fig.4.2 (a, e, i) presents the original particle size distributions for each of these mass-selected Au clusters, with the integrated HAADF intensity distributions shown in-

set. The diameter distribution for mass-selected $Au_{561\pm13}$ (Fig.4.2 (a)) exhibits a mean diameter of 2.63 nm with a full-width half-maximum (FWHM) of 0.44 nm, which then transforms to a broad continuous distribution ranging between $\sim$2.5 nm and 6 nm following CO oxidation. A broadened, continuous distribution shifted to larger sizes, with almost no overlap of the original distribution, indicates Ostwald ripening. The trend is confirmed through the integrated HAADF intensity which is proportional to number of atoms within each cluster, shown in inset of Fig.4.1 (c), revealing a very scattered distribution. Similarly, the original diameter distribution for $Au_{923\pm20}$ is narrow with a peak centred at 3.36 nm and a FWHM of 0.14 nm (3.36$\pm$0.14 nm). However, after the reaction, the distribution becomes very broad, ranging from *circa* 2 nm to 5.5 nm (see Fig.4.2 (g)), which is also suggestive of Ostwald ripening, given that the distribution again shifts to larger sizes as compared to the original peak position. That is to say, the presence of clusters smaller than the original size indicates fragmentation accompanied by the growth of larger clusters.

A comparison of the insets in Fig.4.2 (c) and (g) demonstrates that the number of atoms within each cluster changes from being centred at a specific mass to a broad mass range. Notably, for $Au_{923\pm20}$, no clusters were found to be <3 nm before reaction, whereas after the reaction, there are considerable quantities of clusters that are found to be smaller than the original particle size.

The effects of CO oxidation on $Au_{2057\pm45}$, shown in Fig.4.2 (k), are in stark contrast with those for $Au_{561\pm13}$ and $Au_{923\pm20}$. The size distribution of $Au_{2057\pm45}$ clusters before reaction in Fig.4.2 (i) has a very sharp peak centred at 4.41$\pm$0.17 nm. A small number of clusters are found to be 5.70$\pm$0.15 nm nm in diameter, which we attribute to spontaneous dimerization. Indeed, we note the presence of a dimer (denoted with a dashed circle) in the corresponding HAADF-STEM image shown in Fig.4.2 (j), a feature that can occur either at source due to the deposition of a small fraction of doubly charged (2m/2z) particles, or through coalescence of co-incident and proximate particles at the substrate. Fig.4.2 (k) shows that, after the CO oxidation reaction, the size distribution of $Au_{2057\pm45}$

is different from that observed for both $Au_{561\pm13}$ and $Au_{923\pm20}$ after reaction, in that no clusters smaller than the initial size are observed and also aggregation is evident from the emergence of features larger than ∼5.5 nm. However, these new features distributed in a discreet manner, instead of forming one broad, continuous distribution across a wide range of sizes as in Fig.4.2 (c) and Fig.4.2 (g). The Gaussian fitting of these features reveals peaks at 4.37±0.17, 5.56±0.17 and 6.39±0.22 nm (Fig.4.3 (k)), which we attribute to monomers, dimers and trimers, respectively. The trend is echoed, if not more pronounced, in the histogram of the integrated HAADF intensity, shown in the inset of Fig.4.3 (e), revealing discrete peaks at regular intervals, directly corresponding to the quantization in terms of the number of atoms per particle. At 5.56 nm and 6.69 nm, the diameters of the dimers and trimers are 1.25 and 1.45 times the diameter of the original monomer, respectively. This supports a quasi-spherical model for these clusters, given that the volume increases with the cube of the radius. The results are consistent with the diffusion and coalescence of whole clusters, such that Smoluchowski ripening for the mode of particle coarsening in this case. It is worth noting that reactivity starts to decrease when the diameter exceeds 4 nm.[126, 127, 62, 66, 128, 65, 119]

Previous studies have indicated that the ripening process can be triggered by CO oxidation, as in the present work.[144, 99] Among them, control experiments were conducted to show that Ostwald ripening, under some controlled conditions, can only be seen when the Au clusters are exposed to a mixture of CO and oxygen, and that the presence of CO[99] alone would not activate the Ostwald ripening process. Similarly, in our control experiments (Fig.4.1) mass-selected $Au_{923\pm20}$ was treated in pure helium and oxygen helium mixture (identical gas flow component to full CO oxidation reaction, merely replaced CO with more helium) under identical temperature program and no Ostwald ripening process was observed. Several studies have shown that Au clusters at ∼3.5 nm in diameter have the highest throughput in CO combustion.[144, 66, 62] A mechanism has been proposed that involves each CO combustion event releasing as much as 2.9 eV [99, 145, 146, 147], in which the liberated energy can induce hot electrons to acti-

vate fragmentation,[148, 147, 146] on top of the heating provided by the system. There is also evidence showing the possibility of atomic migration between clusters mediated by CO through the formation of volatile gold complexes.[126, 149, 64] Furthermore, a thorough modelling study reveals the possibility of promoting Ostwald ripening by CO-metal complexation by lowering the surface energy, and thus increasing the probability of disintegration.[150]

4.4.4 Structural variation in CO oxidation reaction
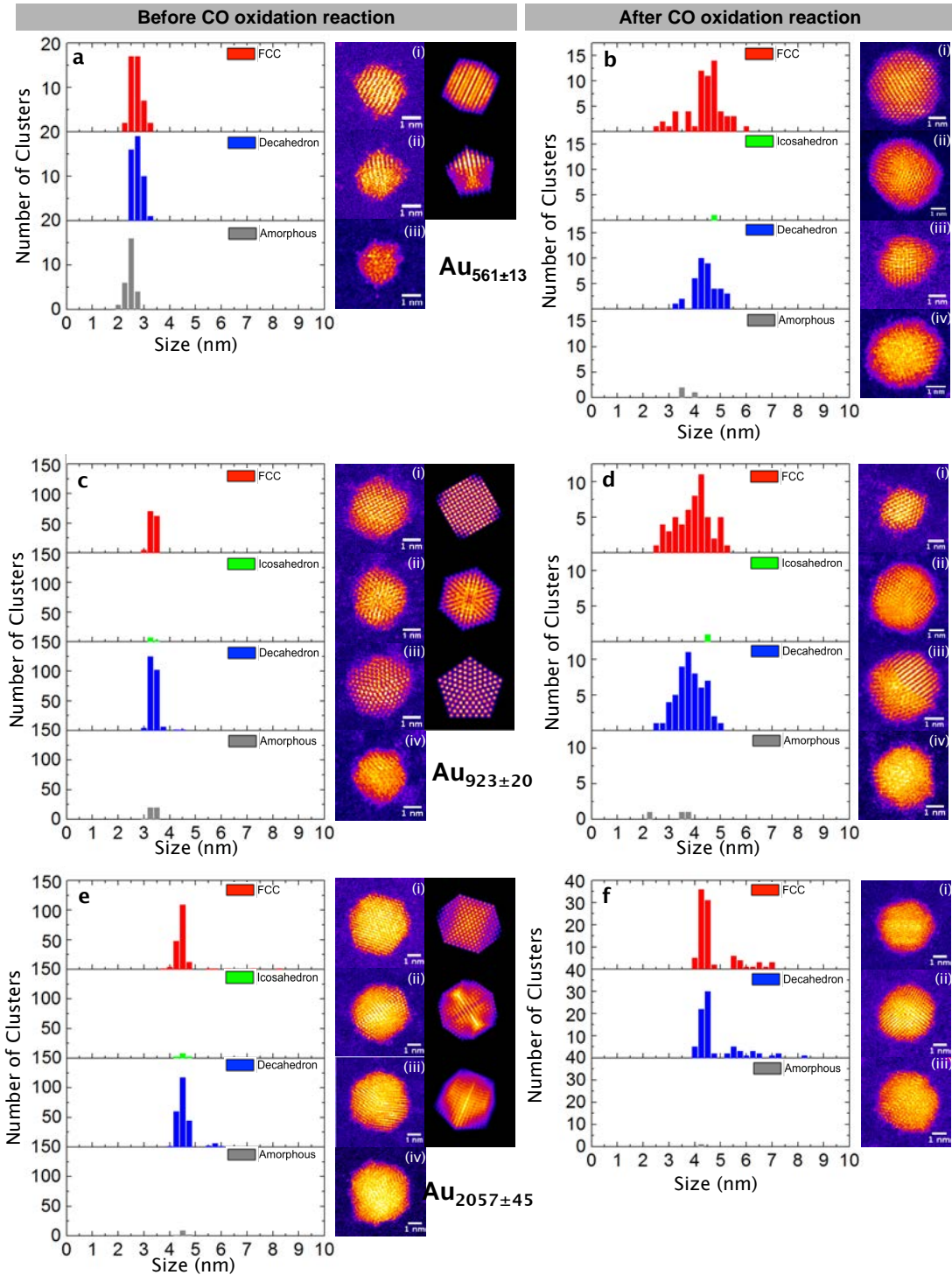
Figure 4.3: Histograms showing the size distributions as a function of the atomic structures for mass-selected $Au_{561\pm13}$, $Au_{923\pm20}$ and $Au_{2057\pm45}$ nanoclusters, both before (a,c,e) and after (b,d,f) exposure to the CO oxidation reaction conditions. Representative atomic resolution HAADF-STEM images are shown alongside (labelled i-iv, as appropriate), accompanied by multislice image simulations for the sizes Au_N ($N = 561, 923, 2057$).

To further investigate the morphological transformations of the clusters due to the CO oxidation reaction, we examined the particles in HAADF-STEM at atomic resolution. This technique allows the full three-dimensional atomic structure of the particles to be resolved.[23] The magic-number gold clusters exhibit motifs that correspond to one of three high-symmetry, ordered structures, namely icosahedral (I_h), decahedral (D_h) and face-centred cubic (FCC). We are able to assign the particles according to their structural motifs by reference to a simulation atlas, one for each particle size of Au_{561}, Au_{923} and Au_{2057}, each of which contains a series of multi-slice HAADF-STEM simulations generated over a full range of viewing orientations. (see appendix for simulated image atlas.) We note that the particles may exhibit inherent surface reconstructions, an example being partially reconstructed decahedron observed for Au_{923} previously,[138, 35] as well as the mobility of surface adatoms under the electron beam,[113] both of which are examples of deviations from the ideal case. Additionally, we often find there are a number of particles within a sample population that cannot be assigned to the ordered structures considered, and therefore we assign these particles as being amorphous or unidentified.

Fig.4.3 shows the particle size distributions 'fractionated' according to atomic structure, both before and after the CO oxidation reaction. These diameter distributions therefore provide quantitative analyses of the high symmetry structures as a function of particle size. It is worth remarking that the proportions of I_h isomers in all sample populations are low ($\leq$ 3 %). Also, only the $Au_{561\pm13}$ sample population (Fig.4.3(a)) exhibits any significant proportion of amorphous structures (22 %), and the number of amorphous particles observed for that sample population actually diminishes to $\sim$2 % following CO oxidation (Fig.4.3b). Indeed, it is clear from the distributions shown in Fig.4.3 that the CO oxidation reaction does not cause amorphisation of the particles. This is entirely consistent with experimental evidence that I_h is metastable with respect to D_h and FCC.[138, 35, 151]

For $Au_{923\pm20}$, atomic resolution images taken after reaction (Fig.4.3(d)) reveal particles smaller than the original cluster size, as well as significantly enlarged clusters that are

the result of Ostwald ripening. All particles are observed to maintain high symmetry configurations, and possess a quasi-spherical morphology. The proportion of decahedral to FCC structures was approximately 2:1 before reaction (Fig.4.2 (c)) and became 1:1 after exposure to the CO oxidation reaction conditions (Fig.4.2 (g)).

The proportions of D_h and FCC isomers of Au_{2057} that are monodisperse after reaction remain largely unchanged; however, we must also consider the atomic structure of clusters that aggregate to form dimers, trimers and tetramers. If the isomers in a collision event are different, there is an ensuing competition then to adopt the most energetically favourable structure, although given that the relative surface energy of FCC and D_h structure are predicted to be similar in the size range 2000-6000 atoms[152], the resulting statistical proportions of the isomers are expected to be approximately equivalent. In addition, structureal contagion process was found to be very efficient when two clusters were making contact. At 300 K, after the interface formed between two clusters, the interface would be pushed toward the less stable clusters through neck joining bridge bewtween them. The structural tranformation could be completed before completion of the totoal coalesce of two clusters.[153] We find that, overall, the ratio of FCC to D_h isomers before the reaction is in the approximate ratio of 3:4, whereas there is a slightly higher proportion 11:10 (FCC 68 clusters, D_h 61 cluster, in monomer range) of FCC to D_h isomers is observed after reaction. In the size region of the monomer, the proportion of FCC increases after reaction directly corresponding to a reduction in D_h isomers. We note that there were almost no I_h isomers and amorphous particles observed for $Au_{2057\pm45}$, both before and after the CO oxidation reaction.

Overall, the most intriguing thing we have observed is that the extensive Ostwald ripening of $Au_{561\pm13}$ and $Au_{923\pm20}$ does not occur for $Au_{2057\pm45}$ under identical temperature and reaction conditions. Moreover, Ostwald ripening is not the mechanism for particle coarsening in the absence of 1% of CO, as the control experiments for $Au_{923\pm20}$ showed, but instead ripening proceeds by diffusion and coalescence. It is therefore reasonable to suggest that ripening is driven by the energy provided due to the exothermicity of the CO

oxidation. Given that catalytic activity also varies as a function of cluster size, the energy liberated can also vary. For instance, a cluster of diameter 3.5 nm (close to $Au_{923\pm20}$) is more active than that of 4.5 nm in diamater (close to $Au_{2057\pm45}$).[144] Surface free energy also rises with increasing cluster size.[154] At size $Au_{2057\pm45}$, the energy gained is not enough to drive atoms to detach from the clusters, so Ostwald ripening is prevented and only Smoluchowski ripening is possible. Although originating from different cluster sizes before ripening under exposure to the reaction conditions, it can be seen that for $Au_{561\pm13}$ and $Au_{923\pm20}$, both cases result in a broad distribution between 2.75 nm and 5.75 nm. Given the conclusion that these clusters undergo Ostwald ripening, once the cluster has grown to the limit that Ostwald ripening should cease, clusters would not be able to grow bigger, but should instead reach a ceiling at this size.[155, 45, 44, 154, 156] Further growth would depend on the cluster diffusion around this ceiling size of 5.75 nm, which would depend on the mean free path. We also suggest that clusters of size around 6 nm ($Au_{2057\pm45}$ dimer) are not highly mobile under the reaction conditions we provided, for which this conclusion relies on our assumption that the mobility of the $Au_{2057\pm45}$ monomer is responsible for the formation of dimer and trimer, whilst the formation of the tetramer would arise largely due to the mobility of the dimer through two-body collisions.

4.5   Conclusion

In conclusion, the evolution of the sizes and atomic structures of mass-selected $Au_{561\pm13}$, $Au_{923\pm20}$, and $Au_{2057\pm45}$ clusters were investigated, both before and after they were subjected to realistic catalytic CO combustion conditions. $Au_{561\pm13}$ and $Au_{923\pm20}$ were found to undergo Ostwald ripening, whereas $Au_{2057\pm45}$, Smoluchowski ripening was observed instead. We suggest that the emergence of a cross-over in ripening modes occurs due to the inability of the energy provided by the exothermicity of the CO being to reach the activation energy threshold for Ostwald ripening for the largest mass-selected cluster size examined here.

CHAPTER 5

STRUCTURE OF GOLD & PALLADIUM CLUSTERS BEFORE AND AFTER 1-PENTYNE HYDROGENATION

This chapter is closely based on my publication (with me as the first author), in particularly in section 5.1 to 5.4, and part of the content in 5.6.1. Hu, K.-J.; Plant, S. R.; Ellis, P. R.; Brown, C. M.; Bishop, P. T.; Palmer, R. E. *The Effects of 1-Pentyne Hydrogenation on the Atomic Structures of Size-Selected Au N and Pd N (N = 923 and 2057) Nanoclusters Phys. Chem. Chem. Phys. 2014, 16 (48), 26631* Content in 5.5 to 5.6 presenting study of 1-pentyne hydrogenation on Pd nanocluster, base on unpublished results.

5.1   Overview

This chapter concerns the effects of the vapour-phase hydrogenation of 1-pentyne on the atomic structures of size-selected Au and Pd nanoclusters supported on amorphous carbon films. We use aberration-corrected high-angle annular dark field (HAADF) scanning transmission electron microscopy (STEM) to image populations of the nanoclusters at atomic resolution, both before and after the reaction, and assign their atomic structures by comparison with multi-slice image simulations over a full range of cluster orientations. Gold nanoclusters consisting of 923 ± 20 and 2057 ± 45 atoms are found to be robust, exhibiting high structural stability. However, a significant portion of $Pd_{923\pm20}$ and $Pd_{2057\pm45}$

116

nanoclusters that appear amorphous prior to treatment are found to exhibit high symmetry structures post-reaction, which maybe interpreted as the effects of hydrogen induced melting point lowering and heat generated from reduction reaction. Most intriguingly, while $Pd_{2057\pm45}$ transformed significantly from amorphous to high symmetry structures, $Pd_{923\pm20}$ remains amorphous structure after identical heat treatment in hydrogen atmosphere, which might be attributed to greater internal stress with the growth of amorphous structure.

5.2 Introduction of Au nanocluster in 1-pentyne hydrogenation

It has long been established that the catalytic properties of supported metal particles vary as a function of size.[157] The use of size-selected metal nanoclusters as model catalysts[158, 159, 160, 161, 162, 163] is one of the routes that has enabled catalytic activity to be accurately related to particle size. However, it is not just the size, but the full atomic structure which can regulate the performance of a catalyst, since catalytic activity can, in some cases, be correlated with specific reactive sites at the catalyst particle surface.[137] Indeed, it has been demonstrated that controlling particle shape may enable improved selectivity.[159] As a result, it is vital to gain an understanding of the effects upon the structure of such model catalysts arising from exposure to realistic reaction conditions, in order to achieve more robust catalyst design with improved performance. A number of techniques have been used to monitor nanocluster or nanoparticle catalysts subject to reaction conditions, including, for instance, in-situ TEM,[93, 120, 121] electron tomography[164] and in-situ STM.[99] Aberration-corrected HAADF-STEM has previously been used to identify catalytically-active Au nanoclusters on oxide supports,[63] and the catalytic activity of size-selected Au nanoclusters on oxides is well-established.[67] For instance, amongst size-selected Au nanoclusters, Au_{55} has been highlighted as a high performance catalyst with pronounced oxidation resistance.[71] HAADF-STEM imaging

117

of size-selected Au nanoclusters on amorphous carbon has enabled the elucidation of their three-dimensional atomic structures.[23] Nanoclusters of a specific size can exhibit a range of atomic structures that differ significantly from the bulk, and multi-slice image simulations have facilitated the identification of structures from HAADF-STEM images for size-selected Au_{20},[36] Au_{55},[32] Au_{309}[23] and $Au_{923\pm20}$,[35, 138, 165] regardless of cluster orientation on the substrate. Given the recent demonstration of atomic structure control during the formation of size-selected $Au_{923\pm20}$,[138] there is now a great potential to study the catalytic properties of such nanoclusters not only as a function of their size, but also atomic configuration, under realistic reaction conditions. Aging of the catalyst as a result of thermally- or chemically-driven restructuring[166, 40, 43] is important for both the catalytic activity and stability. It is therefore crucial to be able to identify changes in the structure and composition of such catalytic particles both *before* and *after* exposure to realistic reaction conditions, in order to achieve catalysts with optimised efficiency, selectivity and sustained performance.

In the first half of this chapter, we report the atomic structures of size-selected Au and Pd nanoclusters (containing 923 and 2057 atoms) supported on amorphous carbon films, both before and after exposure to the thermal treatment and 1-pentyne hydrogenation reaction. Observations made *ex situ* using aberration-corrected HAADF-STEM provide direct geometric information about these nanoclusters. Multi-slice HAADF-STEM image simulations are compared with experimental images to identify the atomic structures of the observed clusters, regardless of their orientation on the substrate. Our results show that the Au nanoclusters of both sizes are very stable under the reaction conditions, remaining largely unchanged after pure thermal treatment and after full exposure to the chemical reaction conditions. In comparison to Au clusters, although some variation in structure between repeating experiments due to the slight difference in generation and treating conditions, Pd clusters that was initially being highly amorphous prior to chemical reaction, have the tendency to transform to high symmetry structures after 1-pentyne hydrogenation, which would be discussed in the second half of this chapter.

5.3   Experimental Section

Gold and palladium nanoclusters were generated using a magnetron sputtering gas condensation cluster beam source.[167, 102] A lateral time-of-flight mass filter[103] connected to the source permits accurate size selection prior to deposition of the nanoclusters in high vacuum conditions (10^{-7}–10^{-6} mbar). Based on calibration with Ar^+, the nominal mass resolutions employed were M/Δ M $\approx$ 18 and M/Δ M $\approx$ 23 for Pd and Au nanoclusters, respectively, resulting in nanoclusters that consist of 923±26 and 2057±57 atoms for Pd, and 923±20 and 2057±45 atoms for Au. The size-selected nanoclusters were deposited (at energies in the range 0.4–0.9 eV/atom) directly onto amorphous carbon films supported on molybdenum TEM grids. Following deposition, the supported Au nanoclusters were brought into air (ambient conditions) and then transferred to a vacuum desiccator for storage, both before and after imaging and treatment. Transfer of the supported Au nanoclusters from the vacuum desiccator to the microscope (in ambient conditions) was performed within ~20 minutes. The Pd nanoclusters were stored in a desiccator at ambient temperature and pressure for 100 days prior to initial imaging, and the reaction exposure was conducted within a further 10 days. Imaging was then performed 20 days after the reaction. The samples were transferred in ambient conditions for imaging and treatment. For 1-pentyne hydrogenation treatment, each of the TEM grids was transferred into a quartz tube (length 360 mm, inner diameter 4 mm) and held at the centre of the tube by means of a quartz wool plug. A flow of pure He gas (279 ml/min) was used to provide an inert atmosphere when investigating the effects of the thermal annealing. For the hydrogenation reaction, the carrier gas consisted of 40 % H_2/60 % He (flow rate of 247 ml/min). In the reaction, this carrier gas was used to vaporise a reagent solution comprising 1 M 1-pentyne plus 1-M 2-methylpentane (used in such reactions as an internal standard for gas chromatography[168]) dissolved in n-hexane. The temperature was increased at a rate of 2 °C/min from room temperature to 250 °C and then maintained at constant temperature for 2 hours. At the end of the treatment, the carrier gas was switched to pure He, and the sample was allowed to cool for 30 minutes. Atomic resolution

imaging was carried out using a JEOL 2100F STEM operating at 200 keV and equipped with a spherical aberration probe corrector (CEOS GmbH) and high-angle annular dark field (HAADF) detector. The inner and outer collection angles of the HAADF detector were 62 and 164 mrad, respectively.[24] Imaging was performed so as to avoid beam damage to the atomic structures of the nanoclusters (see supporting information). Following imaging, high symmetry nanocluster structures were identifed by comparing experimental images with an atlas of multi-slice image simulations over a full range of orientations in three dimensions. Simulations of $Au_{2057\pm45}$, Pd_{923} and Pd_{2057} were generated using the QSTEM package.[169] The previously published simulation atlas was used in the case of $Au_{923\pm20}$.[35]

5.4 Results of Au clusters in 1-pentyne Hydrogenation

5.4.1 High symmetry structures Au magic clusters
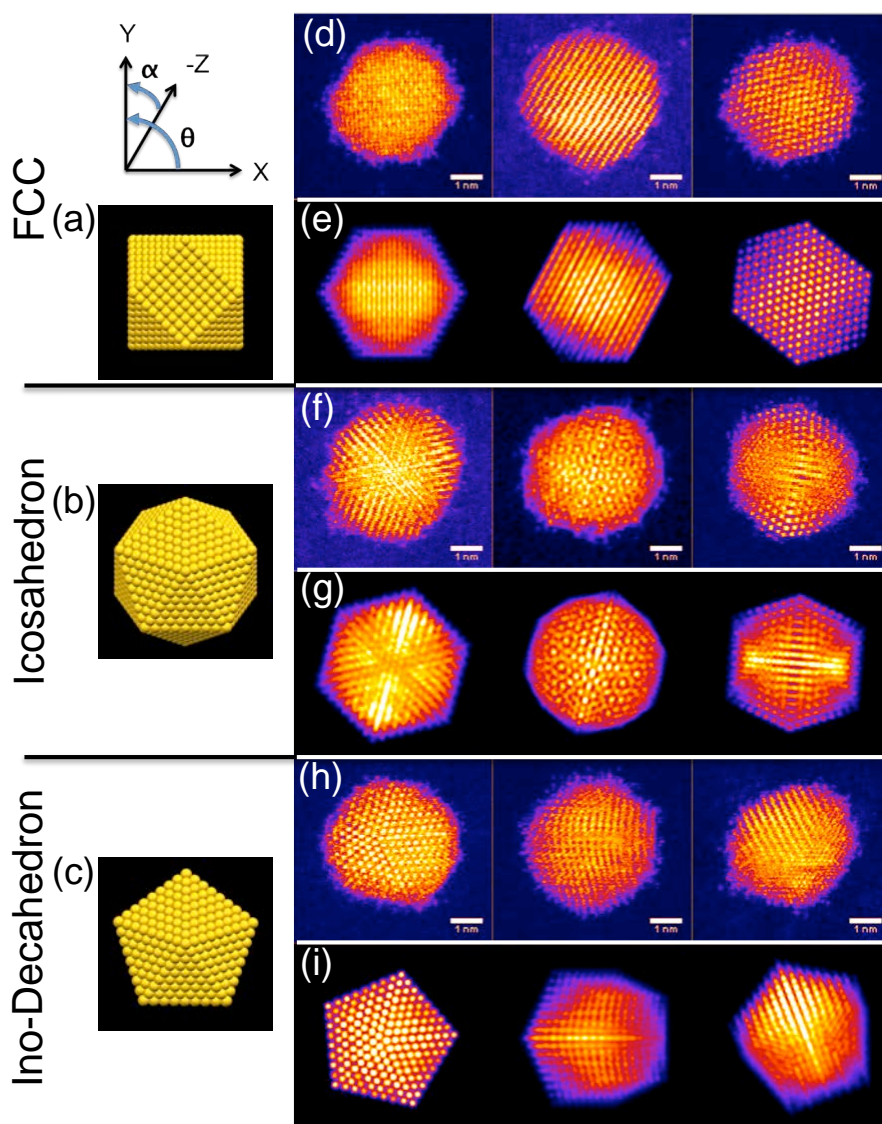
Figure 5.1: Models of the atomic structure for the (a) cuboctahedral, (b) icosahedral, and (c) Ino-Decahedral isomers of Au_{2057}, viewed at $\theta=0°$, $\alpha=0°$, as defined by the axes shown. Typical HAADF-STEM images of $Au_{2057\pm45}$ nanoclusters (top) with corresponding multi-slice image simulations (below) for: (d, e) the face-centered cubic (FCC) polyhedron, (simulation orientation in row (e) from left to right are along $\theta=45°$, $\alpha=45°$, and $\theta=0°$, $\alpha=30°$, and the 110 axis) (f, g) the icosahedron (I_h) (simulation orientation in row (g) from left to right are normal to (111) facet, along the 5-fold axis, and along the 2-fold axis) , and (h, i) the Ino-decahedron (D_h) (simulation orientation in row (i) from left to right are along 5-fold axis, at $\theta=0°$, $\alpha=50°$, and at $\theta=0°$, $\alpha=30°$).

The high symmetry isomers of the nanoclusters observed in this study display structural motifs that are characteristic of the icosahedron (I_h), Ino-decahedron (D_h) and face-centred cubic (FCC) polyhedron, just as for size-selected $Au_{923\pm20}$ nanoclusters studied previously.[35, 138, 165] Fig.5.1 shows typical HAADF-STEM images and corresponding multi-slice image simulations of an illustrative set of high symmetry $Au_{2057\pm45}$ isomers. There is always a proportion of nanoclusters within a sample population that cannot be assigned uniquely to a high symmetry structure, while some nanoclusters appear to be completely amorphous, and we designate such structures as being amorphous or unidentified (A/U). In the present study, the D_h-$Au_{923\pm20}$ and D_h-$Au_{2057\pm45}$ nanoclusters are found to be the most abundant; recent experimental investigations of $Au_{923\pm20}$ suggest that D_h-$Au_{923\pm20}$ is a low energy structure in this size regime, whereas I_h-$Au_{923\pm20}$ in particular is metastable.[35, 138]

Several factors might induce changes in the structure of nanoclusters in the continuous flow vapour-phase reaction. For example, thermal annealing alone can be an important driving force in triggering the structural transformation of nanoparticles.[40, 43, 61] In order to de-couple any effects of (merely) elevated temperatures from the full reaction conditions, thermal annealing was first conducted on $Au_{923\pm20}$ and $Au_{2057\pm45}$ nanoclusters. Since recent work shows that the relative proportions of isomers within a sample population can be controlled by tuning the formation parameters for the generation of $Au_{923\pm20}$,[138] samples were produced using identical formation conditions in the cluster beam source (parameters are detailed in the figure captions).

5.4.2 Size distribution of $Au_{923\pm20}$ and $Au_{2057\pm45}$ clusters and structural variation in control experiments
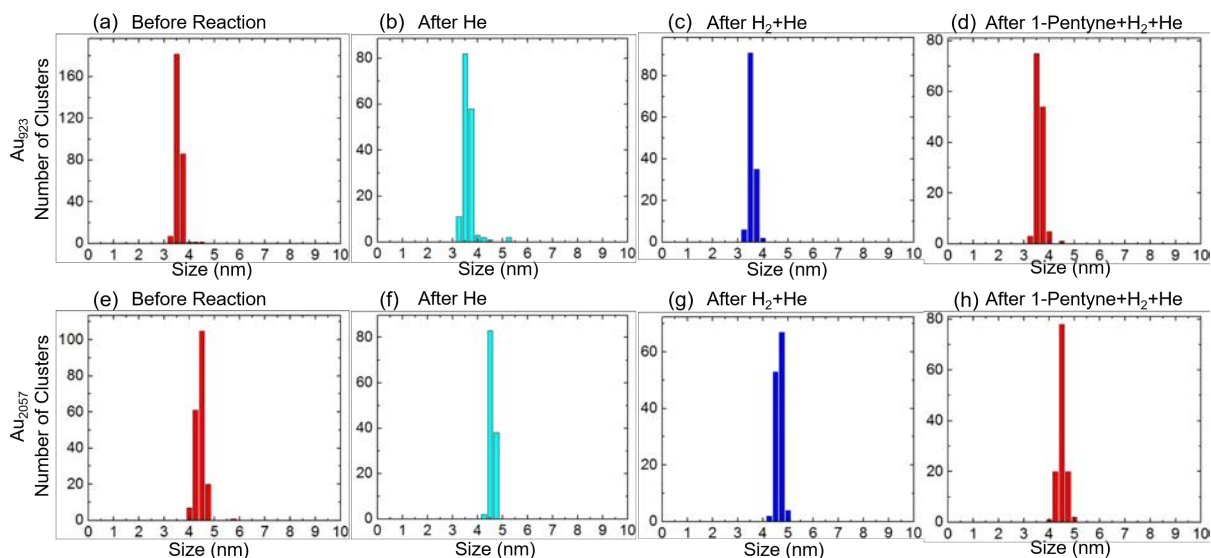
Figure 5.2: Charts showing the size distribution of $Au_{923\pm20}$ (a-d) and $Au_{2057\pm45}$ (e-h) before and thermal treatment in different atmosphere or with reactant. (a, e) as prepared before any treatment at RT, (b, f) after thermal treatment under a gas flow of pure He (279 ml/min), and (c, g) after thermal treatment under a gas flow of 40% H_2 + 60 % He (247 ml/min). (d, h) after thermal treatment with 1 M 1-pentyne in hexane vaporised by a carrier gas flow of 40% H_2 + 60 % He (247 ml/min). Thermal treatment was conducted at 523 K for 2 hours (ramp rate of $2\,°C$/min from RT). Related cluster formation parameters: condensation length, 250 mm; magnetron sputtering power, 10 W DC; condensation pressure, 0.60 mbar ($Au_{923\pm20}$) and 0.67 mbar ($Au_{2057\pm45}$); deposition energy, 0.5 eV/atom; condensation gas flows, rate 200 sccm (Ar) and 150 sccm (He).

The result of size distribution is shown in Fig.5.2 of size-selected $Au_{923\pm20}$ and $Au_{2057\pm45}$ before and after various different reactions. The centre of peak distribution for $Au_{923\pm20}$ (Fig.5.2 (a)) and $Au_{2057\pm45}$ (Fig.5.2 (e)) before reactions were at 3.5 and 4.5 nm respectively. The width of the distribution in both size-selected clusters were both very sharp and there were no aggregated features other than monomers. Further, in the control experiments of treating with helium (b, f), hydrogen-helium mixture (c, g) and after full 1-pentyne hydrogenation reactions (d, h), all of the results show that the size distribution is almost identical to the original condition as they were prepared from cluster beam source. There were neither new features emerging nor shifting or broadening of peaks. This suggests that gold nanoclusters in various treatments and reactions listed here did

not undergo any aggregation nor cluster disintegration. As a result, when we discuss the analytically result of proportion of structures, all histogram would be done with regards to monomers.

Figure 5.3: Charts showing the relative proportions of $Au_{923\pm20}$ isomers (a) before thermal treatment, (b) after storage in vacuum at RT, (c) after thermal treatment under a gas flow of pure He (279 ml/min), and (d) after thermal treatment under a gas flow of 40% H_2 + 60 % He (247 ml/min). Thermal treatment was conducted at 523 K for 2 hours (ramp rate of 2 °C/min from RT). Related cluster formation parameters: condensation length, 250 mm; magnetron sputtering power, 10 W DC; condensation pressure, 0.60 mbar; deposition energy, 0.5 eV/atom; condensation gas flows, rate 200 sccm (Ar) and 150 sccm (He).

Fig.5.3 shows a comparison of the proportions of $Au_{923\pm20}$ isomers, before and after thermal annealing at 523 K for 2 hours in different atmospheres. The results for $Au_{2057\pm45}$

nanoclusters are very similar to those shown in Fig.5.3. Fig.5.3 (a) presents charts showing the combined results for all 3 samples of $Au_{923\pm20}$ nanoclusters prior to thermal annealing. In general, the error bars shown on the bar charts are related to the Poisson error. However, the error bars shown on the bar chart in Fig.5.3 (a) derive from the standard error for the 3 samples. Fig.5.3 (b) shows the proportions of $Au_{923\pm20}$ isomers following storage in a vacuum desiccator, where the sample has been imaged within 14 days of preparation, while Fig.5.3 (c) and (d) show the result of heating in a pure He gas flow, and in a gas flow of 40% H_2/ 60% He, respectively. Although some slight variations in isomers distributions can be observed, there are no significant changes in the $Au_{923\pm20}$ (or $Au_{2057\pm45}$) isomers as a result of subjecting them to these conditions.

The results may be explained by considering the temperatures required to induce melting in gold nanoparticles as a function of particle size. Thermal annealing in an inert atmosphere can be interpreted as a rapid process of bringing nanoclusters into a state of thermal equilibrium, where no reactants are involved. According to previous studies,[40] the I_h-to-D_h structural transformation can occur for particles in the size range from 3 nm to 14 nm without having to reach melting point. For instance, the gap between transition temperature and melting point is predicted to be $\sim$100 K for a Au particle size of 4 nm, based on the extrapolation from experimental data.[40] The transformation from more stable FCC or decahedral to icosahedral structures requires temperatures above the melting point, followed by rapid cooling (freezing) of the nanoparticle.[40, 61] The melting point of gold nanoparticles is highly sensitive to size. Although the melting point of gold nanoparticles at $\sim$2.6 nm in size is close to 500 K, an increase in size to 3 (or 4) nm causes the melting point to rise to $\sim$750 K (or $\sim$900 K).[43] This is consistent with the observations presented in Fig.5.3. Given the size of $Au_{923\pm20}$ is $\sim$3 nm and $Au_{2057\pm45}$ $\sim$4 nm, the temperature of 523 K employed does not approach sufficiently close to the the melting point of the nanoparticles to induce an I_h-to-D_h structural transition, so even the least stable nanocluster isomer can survive the treatment.
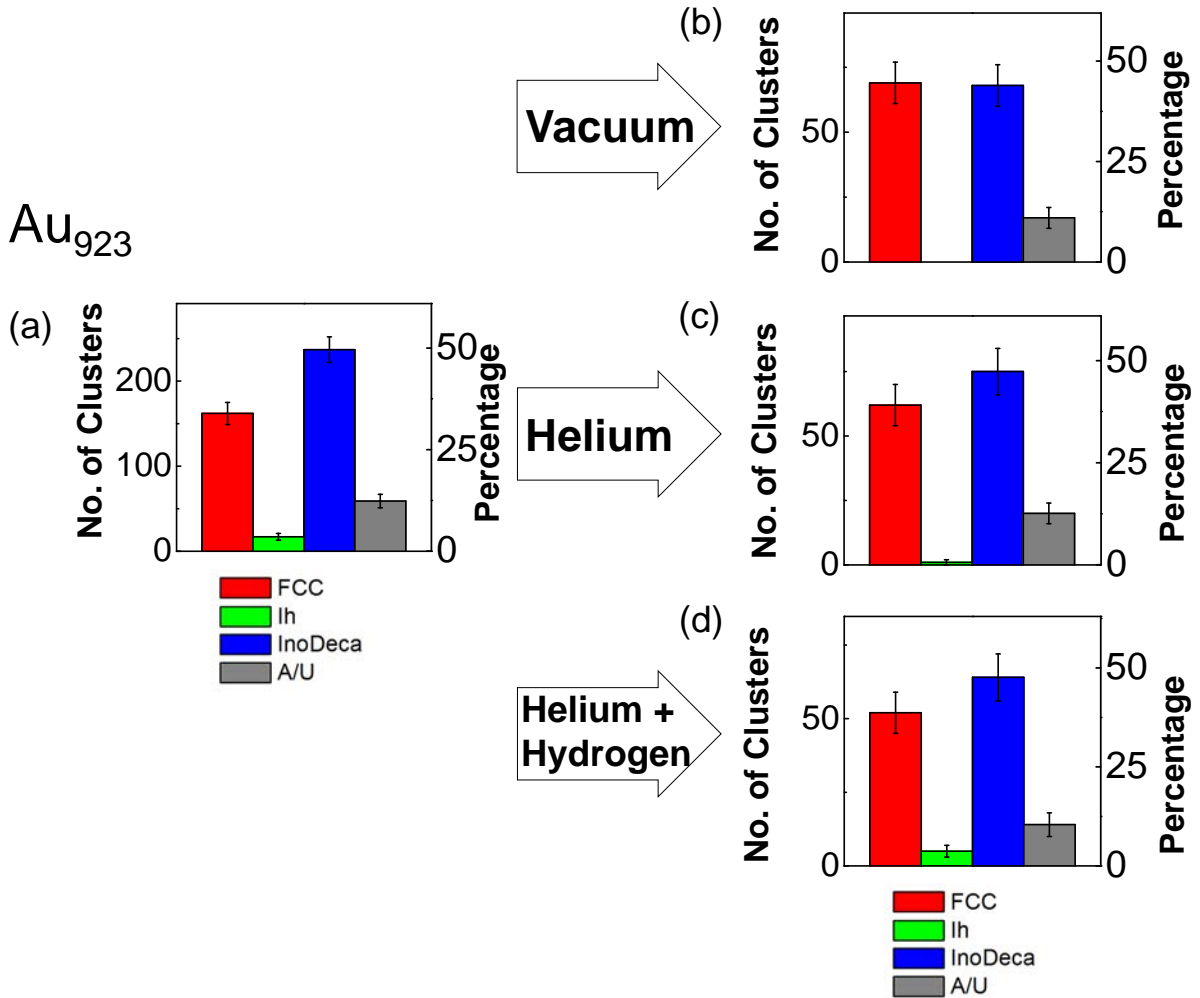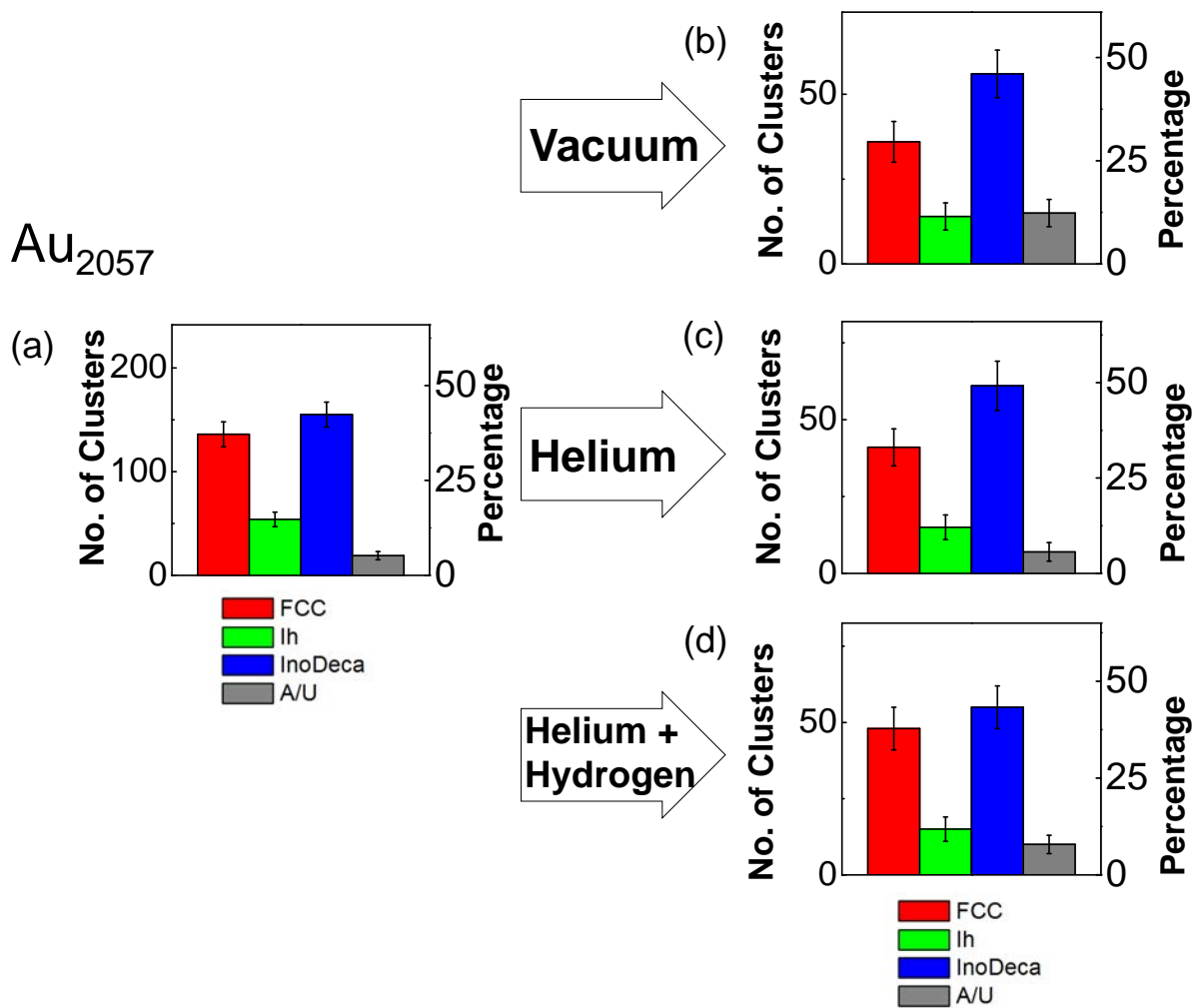
Figure 5.4: Charts showing the proportions of Au2057 isomers (a) before thermal treatment, (b) after storage in vacuum at RT, (c) after thermal treatment under a gas flow of pure He (279 ml/min), and (d) after thermal treatment under a gas flow of 40% H2 + 60% He (247 ml/min). Thermal treatment was conducted at 523 K for 2 hours (ramp rate of 2C/min from RT). Related cluster formation parameters: condensation length, 250 mm; magnetron sputtering power, 10 W DC; condensation pressure, 0.67 mbar; deposition energy, 0.5 eV/atom; condensation gas flows, rate 200 sccm (Ar) and 150 sccm (He).

5.4.3 Structural variation of $Au_{923\pm20}$ and $Au_{2057\pm45}$ clusters in 1-pentyne hydrogenation
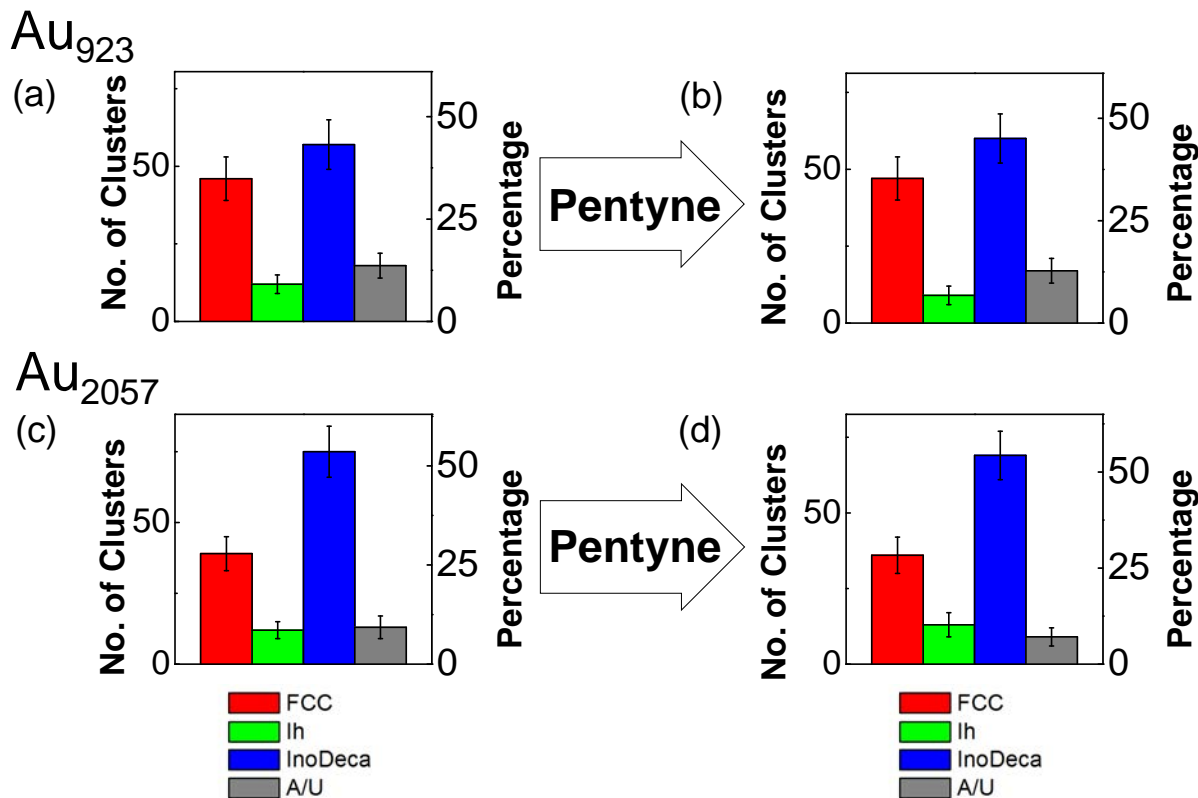
Figure 5.5: (a, b) Charts showing the relative proportions of $Au_{923\pm20}$ isomers (a) before and (b) after exposure to the reaction conditions for vapour-phase 1-pentyne hydrogenation. (c, d) Charts showing the relative proportions of $Au_{2057\pm45}$ isomers (c) before and (d) after exposure to the same conditions. The reaction was conducted at 523 K for 2 hours (ramp rate of $2\,°C/min$ from RT) with 1 M 1-pentyne in hexane vaporised by a carrier gas of 40 % H_2 and 60 % He (flow rate 247 ml/min). The cluster formation parameters were: condensation length, 250 mm; magnetron sputtering power, 10 W DC; condensation pressure, 0.60 mbar ($Au_{923\pm20}$) and 0.67 mbar ($Au_{2057\pm45}$); deposition energy, 0.5 eV/atom; condensation gas flows, 200 sccm (Ar) and 150 sccm (He).

Fig.5.5 shows the proportions of size-selected $Au_{923\pm20}$ and $Au_{2057\pm45}$ nanocluster isomers, both before and after full vapour-phase 1-pentyne hydrogenation reaction conditions. As shown in Fig.5.5 (a, b), with 9% I_h, 43% D_h and 35% FCC before the reaction, $Au_{923\pm20}$ clusters displayed similar stability to $Au_{2057\pm45}$: the relative proportions of $Au_{923\pm20}$ isomers after treatment are 7% I_h, 45% D_h and 35% FCC. Such variations in isomer proportions fall within the (Poissonian) error. As shown in Fig.5.5 (c) the proportions of

as-deposited $Au_{2057\pm45}$ isomers before the reaction are 9% I_h, 54% D_h and 28% FCC. The isomer proportions were found to be almost identical post reaction (see Fig.5.5 (d)).

Although there is evidence for the chemisorption of 1-pentyne at the surface of bulk gold,[170] there are a limited number of investigations on the catalysis of 1-pentyne hydrogenation using gold. However, the hydrogenation of alkynes involving oxide-supported gold nanoparticles [171, 172] suggests that, although there is higher selectivity to semi-hydrogenation with Au, gold catalysts are considerably less active than Pd.[173, 172] For instance, TiO_2-supported gold nanoclusters of average size 4.7 nm are reported to show poor adsorption of alkyne or alkene species, suggesting there may be a weaker interaction between gold and 1-pentyne (as compared with Pd).

5.5 Introduction to 1-pentyne hydrogenation in Pd nanoclusters

Palladium has been known as an effective catalyst for alkyne hydrogenation reactions. Size-selected Pd_N nanoclusters (N = 55–400) supported on graphite have already been studied under such conditions for methane oxidation [143] and 1-pentyne hydrogenation.[168] The largest nanoclusters in this size range (especially Pd_{400}) exhibited very high selectivity to the hydrogenation of 1-pentyne in the vapour phase, thus motivating the study of still larger nanocluster sizes. The selective hydrogenation of alkynes is relevant to Pd catalysts.[174, 175, 176, 168, 177] The vapour-phase 1-pentyne hydrogenation reaction over Pd supported on θ-Al_2O_3 reveals incorporation of carbon into the catalyst to provide a Pd-C phase believed to be active for selective hydrogenation,[175] and indeed, the incorporation of carbon and hydrogen into the surface has been shown to control hydrogenation events at the surface.[176] However, Pd catalysts can also become deactivated and degraded by such processes.[178]

Structure of palladium nanoparticles were experimentally investigated previously.[41] In theoretically investigation confirmed that the amorphous structure could be a metastable

structure that is more stable than icosahedron under certain size and temperature (amorphous Pd_{55} is entropically more favourable than I_h).[53] The structure transformation is related to both configuration energy difference and the temperature the nanoclusters experiencing. Evidence showed that structure transformation toward more stable structure could occur near melting temperature. However, structural transformation of the other direction requires temperature to climb above the melting point.[40] It is also found that for palladium nanocluster, such reverse structural transformation could proceed through a solid-liquid coexistence state, which could make transformation happen more readily.[57] Further, incorporating of hydrogen into palladium nanoclusters were significantly lowering the melting point on top of the melting point suppression of a given size of nanoclusters.[58, 59]

5.6 Results of Pd clusters in 1-pentyne Hydrogenation

5.6.1 Results of 1-Pentyne hydrogenation on Pd magic number clusters
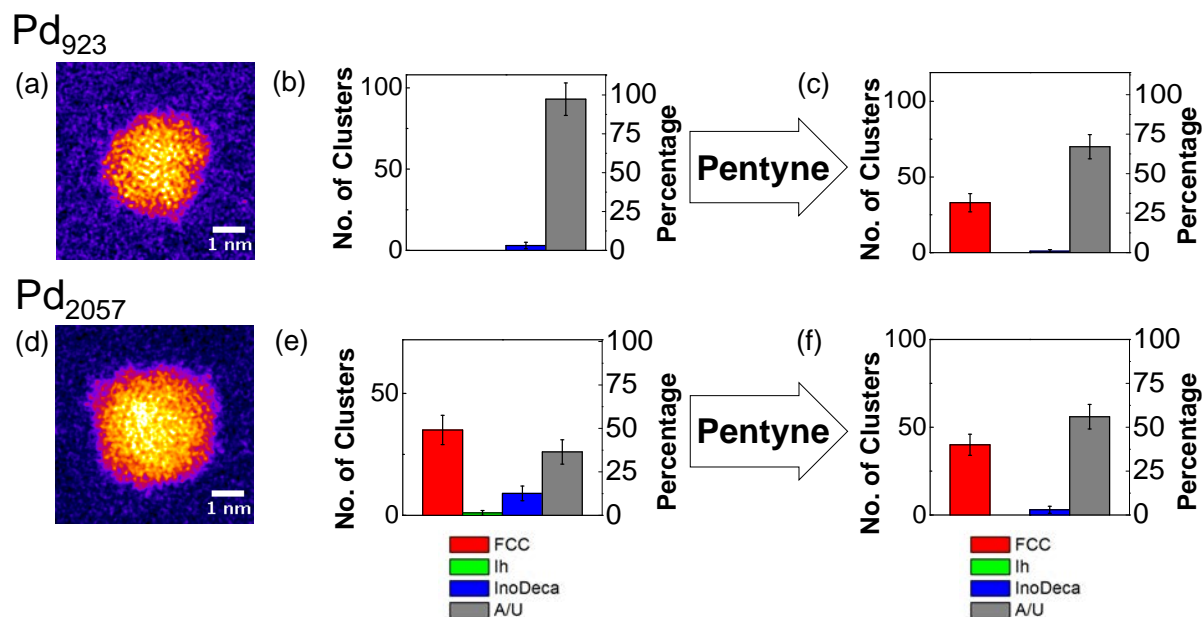
Pd$_{923}$

Pd$_{2057}$

Figure 5.6: (a, d) are the representative images for (a) Pd$_{923\pm26}$, and (d) Pd$_{2057\pm57}$ clusters. (b, c) Charts showing the relative proportions of Pd$_{923\pm26}$ (b) before and (c) after vapour-phase 1-pentyne hydrogenation treatment. (e, f) Charts showing the relative proportions of Pd$_{2057\pm57}$ both (e) before and (f) after the same treatment. The conditions for the treatments were identical to those for the Au nanolcusters shown in Fig.5.2. Related cluster formation parameters: condensation length, 172 mm; magnetron sputtering power, 10 W DC; condensation pressure, 0.18 mbar (Pd$_{923\pm26}$) and 0.28 mbar (Pd$_{2057\pm57}$); deposition energy, 0.9 eV/atom (Pd$_{923\pm26}$) and 0.4 eV/atom (Pd$_{2057\pm57}$); condensation gas flows, 100 sccm (Ar) and 110 sccm (He).

Fig.5.6 shows the variation in the proportions of Pd$_{2057}$ and Pd$_{923}$ nanocluster isomers as a result of exposure to 1-pentyne hydrogenation reaction conditions, which were exactly the same as the case of the Au nanoclusters. Example images of the amorphous Pd$_{923}$ and Pd$_{2057}$ nanoclusters observed are shown in Fig.5.6 (a) and (d), respectively. Fig.5.6 (b) reveals that the vast majority (97 %) of Pd$_{923}$ nanoclusters initially exhibit an amorphous appearance; the only nanoclusters with an identifiable high symmetry structure (3 %) are

found to be D_h. After the reaction, as shown in Fig.5.6 (c), a large proportion (33 %)) of the nanoclusters could be assigned to a high symmetry structure, dominated by FCC (32 %), leaving 1 % as D_h. For Pd_{2057}, the proportion of amorphous nanoclusters pre-reaction is much lower at 37 %, and the majority of nanoclusters are FCC (see Fig.5.6 (e)). Both before and after reaction (Fig.5.6 (e, f)), more than three-quarters of the identified high symmetry isomers are assigned to be FCC. In this set of experiment, we were focussed on monomers. As a result, the effect of ripening and structural analysis on aggregated clusters are omitted. Further experiments were conducted for analysis of structure of clusters with regards to the size in the following section.

5.6.2 Comparison of Pd clusters in control experiments and 1-pentyne hydrogenation
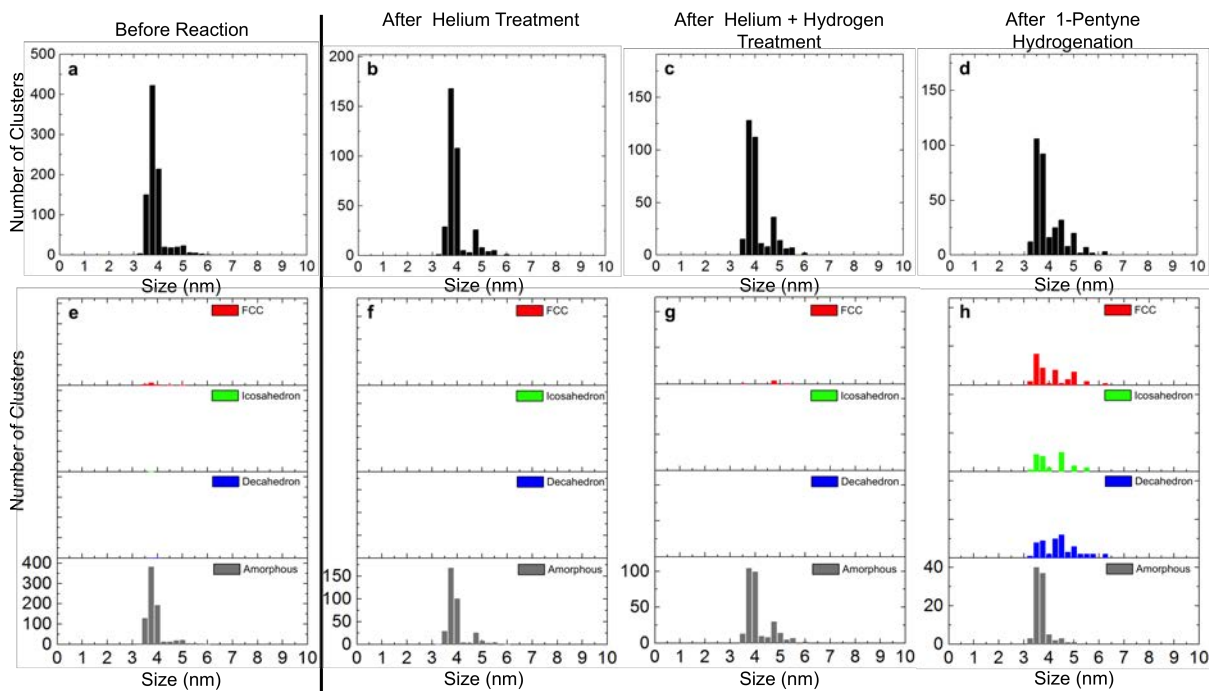
Figure 5.7: Charts showing the size distribution (a-d) and structural analysis with regards to size of clusters (e-h) of $Pd_{923\pm20}$ (a, e) before, after helium treatment (b, f), after helium hydrogen mixture (c, g) and after vapour-phase 1-pentyne hydrogenation treatment (d, h). The conditions for the thermal treatments were kept at 523 K for 2 hours (ramp rate of $2\,^\circ$C/min from RT to $\sim 250\,^\circ$C), under the atmosphere for helium treatment with gas flow of He (279 ml/min), for helium-hydrogen mixture with 40 % H_2 and 60 % He and the overall flow rate is 247 ml/min. For 1-pentyne hydrogenation, 1 M 1-pentyne in hexane was vaporised by carrier gas with flow rate identical as helium-hydrogen mixture. Independent pressure gauge and temperature sensor measured are $17.9\sim250.2\,^\circ$C ;$0.30\sim0.34$ bar(Helium treatment), $18.8\sim249.8\,^\circ$C ;$0.20\sim0.23$ bar(Helium/Hydrogen treatment), and $19.9\sim250.2\,^\circ$C ;$0.32\sim0.35$ bar(full 1-pentyne hydrogenation). Related cluster formation parameters: condensation length, 250 mm; magnetron sputtering power, 10 W DC; condensation pressure, $0.19\sim0.21$ mbar; deposition energy, 0.5 eV/atom; condensation gas flows, 100 sccm (Ar) and 110 sccm (He).

In Fig.5.7 showing size distributions of $Pd_{923\pm20}$ nanoclusters before treatments (Fig.5.7 (a) and (e)) and after treatment in different atmosphere. In addition to overall size distribution shown on top (a-d), another histogram comprised of a series of four rows of histograms below each size distribution graph shows the number of clusters being assigned to different structure with regards to their size(e-h). In Fig.5.7 (a), the size distribution

before reaction is a single sharp peak at 3.77±0.19 nm and the structural analysis in Fig.5.7 (e) shows that almost all the clusters produced from cluster source beam are amorphous, only minute amount of cluster appears to be FCC and icosahedron. Further, when some clusters of size larger than the first peak are found in the histogram before reaction, a shoulder is seen which means some degree of aggregation has happened on $Pd_{923\pm20}$ cluster as they were prepared. Next, results from heat treatment in helium (b, f) and hydrogen-helium mixture (c, g) show that in both treatments, more aggregation arises while the majority of the clusters are still amorphous structure. Both first peaks in (b, c) reflect original size distribution as clusters were prepared and the feature emerged from aggregation located at 4.78±0.16 nm. There is no obvious structural transformation in heat treatment in helium and helium hydrogen mixture. However, after full 1-penytne hydrogenation reaction, considerable amount of clusters were found to transform to high symmetry structure (in the monomer region the ratio between different structure, FCC:I_h:D_h:Amorphous is 3:2:2:9) in Fig.5.7 (h). In Fig.5.7 (d), the size of clusters distributed in a discrete manner. The clusters remain as monomer can be distincted from aggregated clusters readily. It led us to notice that in Fig.5.7 (h), the aggregated clusters have high symmetry structure rather than remaining as amorphous. Notably, for all $Pd_{923\pm20}$ clusters, no matter what substance they were subjected to, or what degree of aggregation or transformation they had been through, no clusters were found to become smaller than their initial size, which indicates no disintegration has happened on $Pd_{923\pm20}$ even in reaction.

The size of the monomer peak has not been changed or attenuated to a broader distribution after heat treatment in helium and helium-hydrogen reduction mixture. No clusters of diameter smaller than the initial size were observed while new peak emerged on the larger size located at roughly 1.26 times of the size of monomer. This shared similarity which have been discussed in previous chapter about the ripening of size-selected clusters only went through Smoluchowski mode that clusters grow via coalescence and aggregation. The mathematical model that expressed the shape of size distribution of Smoluchowski

ripening was discussed by Granqvist et al.[78] In that study, size distribution of coalescence growth was predicted to be log-normal distribution and this prediction would also adapt to Smoluchowski ripening of size-selected clusters.[88] Under Smoluchowski ripening distribution, coalescence growth size-selected clusters would form discrete peaks, since they start with monomer and are only being able to grow as joining of monomers, not all sizes of clusters were accessible. Next, considering the amorphous structure, it was observed previously in characterising of Pd nanoparticles larger than 1 nm[41]. Being the dominating structure of the $Pd_{923\pm20}$ clusters on our sample, their configuration energy, however, were seldom investigated. This might be due to the difficulty of defining the structure of amorphous nanoclusters in calculation studies as well as experiments. Amorphisation process was investigated for various noble and quasi-noble metals[53]. In theoretical investigation, amorphisation occurs from stuffing one more atoms to the five-fold symmetry apex on icosahedron. It is also found that this amorphisation process involves co-ordinate numbers changing on surface and inner atoms. As a result, elements that have sticky potential would be able to create a local minima for amorphous structure, hence amorphous structure could be preserved while cluster is forming. This study on Ih_{55} clusters showed that it is energetically more favourite over icosahedron when temperature goes above 600 K. As it can be identified from our result, though amorphous structure is often considered as metastable, they were still stable when simply heating them in helium atmosphere which indicates that there is a considerable energy barrier existing between amorphous and high symmetry structures.
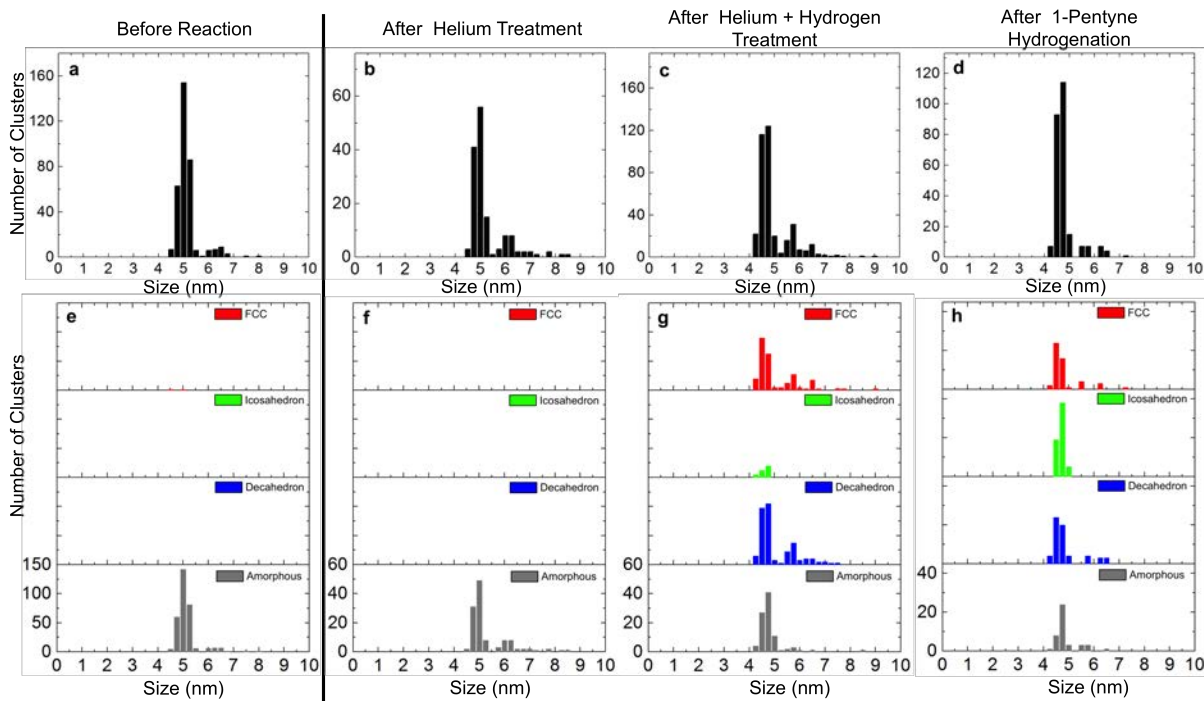
Figure 5.8: Charts show the size distribution (a-d) and structural analysis with regards to size of clusters (e-h) of $Pd_{2057\pm45}$ (a, e) before, after helium treatment (b, f), after helium hydrogen mixture (c, g) and after vapour-phase 1-pentyne hydrogenation treatment (d, h). The conditions for the thermal treatments were kept at 523 K for 2 hours (ramp rate of 2 °C/min from RT to $\sim$ 250 °C), under the atmosphere for helium treatment with gas flow of He (279 ml/min), for helium-hydrogen mixture with 40 % H_2 and 60 % He and the overall flow rate of 247 ml/min. For 1-pentyne hydrogenation, 1 M 1-pentyne in hexane was vaporised by carrier gas with flow rate identical as helium-hydrogen mixture. Independent pressure gauge and temperature sensor measured are 22.2$\sim$246.7 °C ;0.33$\sim$0.37 bar(Helium treatment), 19.4$\sim$247.8 °C ;0.22$\sim$0.25 bar(Helium/Hydrogen treatment), and 19.4$\sim$246.2 °C ;0.34$\sim$0.36 bar(full 1-pentyne hydrogenation). Related cluster formation parameters: condensation length, 250 mm; magnetron sputtering power, 10 W DC; condensation pressure, 0.19$\sim$0.21 mbar; deposition energy, 0.5 eV/atom; condensation gas flows, 100 sccm (Ar) and 110 sccm (He).

Fig.5.8 shows size distribution (a-d) and structural analysis (e-h) of $Pd_{2057\pm45}$ before reaction, in different atmosphere, and in full 1-pentyne hydrogenation reaction. It can be seen that size distribution is comprised of a monomer peak (centre at 5.02±0.20 nm) and aggregated feature (centre at 6.34±0.29 nm) for $Pd_{2057\pm45}$ before reaction. The distribution remains the same manner after heat treatment in helium, with slightly more obvious dimer feature at 6.3 nm. The structural analysis in both untreated (e) and heat treated (f) clusters showed that the majority of clusters stay as amorphous structure. However,

after helium-hydrogen mixture treatment in temperature cycle, significant amount of clusters transformed to FCC and decahedral structure. The ratio of composition of different structures within monomer size region, expressing in FCC:I_h:D_h:Amorphous is 8:2:10:9 in Fig.5.8 (g). In other words, more than two third of the clusters transformed to high symmetry structure. Among those that have high symmetry structures, decahedral and FCC structure were the majority, leaving very small amount of clusters to be icosahedral. On the contrary, icosahedral is the highest proportion after 1-pentyne hydrogenation (Fig.5.8 (h)), accounting for more than 80% of the monomer that transformed from amorphous to high symmetry structures. For $Pd_{2057\pm45}$ cluster undergoing helium-hydrogen mixture in Fig.5.8 (g), an aggregated cluster from monomers is most likely to be either FCC or decahedral structure; very few clusters remains amorphous after aggregation and none of them transform into icosahedral. Finally, there is no disintegrated $Pd_{2057\pm45}$ found after treatments, which is similar to what have been shown for $Pd_{923\pm20}$.

For $Pd_{2057\pm45}$ nanoclusters, well-defined and discrete monomer and dimer peaks before and after helium treatment with no clusters seen to reduce in size indicates that the ripening mechanism is Smoluchowski mode (Coalescence growth with no clusters disintegration). The surviving of amorphous structure after heating treatment in helium suggests again that local minima in configuration energy is stable enough to accommodates amorphous structure for $Pd_{2057\pm45}$ and $Pd_{923\pm20}$, before they get enough energy to transform to high symmetry structure. Next, after treatments, some degrees of Smoluchowski ripening could be identified through observing the emerged peaks and their positions. Assuming the total coalescence clusters remain spherical,[179] diameter of a dimer (joined by two monomers) would be 1.26 times of the diameter of a monomer and a trimer would be 1.45 times. Through curve fitting in size distribution of treated samples, it is found that 2nd and 3rd peak were 1.23 (5.70±0.17 nm) and 1.40 (6.46±0.16 nm) times of the monomer peak (4.60±0.19 nm) after hydrogen treatment, and it is 1.21 (5.63±0.07 nm) and 1.36 (6.36±0.07 nm) times of monomer peak (4.65±0.16 nm) after 1-pentyne hydrogenation reaction. Further, though structural transformation from amorphous to high symmetry

structure were observed on both hydrogen and 1-pentyne hydrogenation treatments, subtle differences were noticed. After treated with hydrogen, only a few clusters transformed to icosahedral, whereas after full 1-pentyne hydrogenation, large amount of icosahedral clusters were observed. In previous study, gold nanoclusters of ~4.5 nm initially dominated by icosahedron transformed to decahedron when annealed to 1173 K in ultrahigh vacuum. The majority of the clusters transformed to decahedron from metastable icosahedral leaving the population of icosahedral clusters almost eliminated. In further annealing to higher temperature, proportion of decahedral nanoclusters dropped and transformed to icosahedron again. It is concluded in this study that metastable icosahedral tend to transform to more stable higher symmetry decahedron, until clusters underwent thawed-frozen process above the melting point.[40] However, the melting point for bulk Pd is 1828 K and even existing with the melting-point depression, nanoparticles as small as Pd_{147} was calculated to melt at 1400 K. How could the treatments with merely 523 K of annealing melt Pd nanoclusters? It is intriguing that the melting point of palladium nanoclusters was found to become significant lower when they were incorporated with hydrogen.[58, 59] Depending on the number of hydrogen atoms incorporated into Pd_{147} nanoclusters, at 1 to 1 mixture in calculation, the melting point can reduce from 1400 K to 300 K. For Pd_{55} clusters, ten hydrogen incorporated into nanoclusters could reduce their melting temperature by 250 K. Furthermore, the participation of 1-pentyne might provide extra heat from hydrogenation reaction that would rise the temperature of palladium clusters actually experienced. Finally, nearly no icosahedral and amorphous structures were seen after the hydrogen and 1-pentyne hydrogenation reaction. It is noteworthy for icosahedral after 1-pentyne hydrogenation, even there is a great number of icosahedral clusters, none of them were dimers or trimers. The larger the size of clusters is, the larger the configuration energy difference between icosahedron and other high symmetry structure became FCC and decahedron, which have nearly overlapped configuration energy curve[57, 45, 44]. When aggregation between two clusters occurs, the newly coalescences clusters tend to follow the structure of lower configuration energy.[41]

Among this set of three identical treatments on different sizes of palladium clusters, structure of both sizes of Pd nanoclusters undergoing helium treatments remain amorphous, indicating that heat bath with inert gas of $250\,°C$ was not capable of triggering the transformation. It was also found that after hydrogen heat cycle on $Pd_{2057\pm45}$, considerable amorphous clusters transformed to high symmetry clusters. However, the identical treatment on smaller $Pd_{923\pm20}$ does not affect the structure of clusters; almost all clusters remain amorphous. It is known that the smaller the nanoclusters were, the more effective melting-point depression effect would be for gold[43] and palladium[180]. Structural transformation from metastable icosahedral structure to decahedral or fcc tend to occur on smaller nanoclusters before larger ones as well.[40] The possible explanation might come from the surface and internal strain of quenched Pd nanoclusters. Surface strain of nanoparticles that stretches interatomic distance would affect configuration energy and determine the accessible structure for a given size. FCC, resemble to the packing order in bulk material has least strain between atoms, thus being a most stable packing structure. Decahedron is joined by five tetrahedron and each of them sharing two faces with their neighbours. These five tetrahedron would not be able to join together unless they stretch longer to overcome the geometric difference between decahedron and five tetrahedrons. As the result, the further away from the centre, the more strain there will be between atoms. However, due to the strain, decahedron is not considered to be a stable structure, unless truncations are introduced to reveal [100] surface which modified it to become ino-decahedron structure. Icosahedron is joined by 20 tetrahedrons and each tetrahedron was sharing three faces to other tetrahedrons. Its configuration energy would also be raised by interatomic strain in the outer shells and there is no compatible truncation to compensate for the energy. Hence, icosahedron was considered to be the least stable structure among these three.[41] Structures of nanoclusters were found to sustain strain in experiment.[181] Due to this surface strain, it is also found that the larger the nanoclusters is, the larger the surface strain will be, hence making the configuration energy less favorable.[57] The structural transition mechanism is not entirely clear; however, there were evidence show-

ing the transition can proceed through surface rearrangement[182] or surface melting.[57] When the clusters generated through quenching were locking the clusters at metastable structure, presumably there is a larger straining force the clusters was trying to overcome, which might make the larger metastable cluster even less stable. Classically an example for this kind of quasi-stable high internal stress condition would be Rupent's drop. Moreover, there is also evidence showing, with the presence of hydrogen integrating into Pd nanoclusters, interatomic distance would dilate by 1.38%[174] and hence would become easier to undergo structural transition.[57]

In the first set of experiment, $Pd_{923\pm26}$ and $Pd_{2057\pm57}$ were prepared and sent under reactive environment for 1-pentyne hydrogenation after 100 days of storage in the ambient environment. Control experiments of heat treatment in helium and hydrogen-helium mixture were conducted later in another set of experiment together with repetition of full 1-pentyne hydrogenation reaction for $Pd_{923\pm20}$ and $Pd_{2057\pm45}$. The cluster generation parameter were kept as close as possible to a certain set of parameter. Pd_{923} clusters in both set of experiment almost all appeared to be amorphous structure. The generation parameters were kept the same for condensation gas flowing rate 100 sccm (Ar), 110 sccm (He) and magnetron sputtering power 10 W DC. 0.9 eV/atom for $Pd_{923\pm26}$ in Fig.5.6 and 0.5 eV/atom for all samples in Fig.5.7. The condensation length for $Pd_{923\pm26}$ in Fig.5.6 is 172 mm and in Fig.5.7 is 250 mm. Condensation pressure for $Pd_{923\pm26}$ in Fig.5.6 is 0.19 mbar and in Fig.5.7 it was between 0.19 to 0.21 mbar for three samples prepared. Structural population for $Pd_{2057\pm57}$ in first set of experiments was majority FCC structure (50%), small proportion of D_h and one-third to be amorphous. However, in repeated experiments $Pd_{2057\pm45}$ were found to be nearly all amorphous structure. The generation parameter were largely kept the same, except for condensation length (250 mm in Fig.5.8, 172 mm in Fig.5.6) and condensation pressures (0.28 mbar in Fig.5.6, 0.43∼0.45 mbar in Fig.5.8). These might be the reason that there is some clusters of high symmetry structure cluster in the Fig.5.6 while there is almost only amorphous in Fig.5.8. Though the systematic understanding of how generation parameter affecting population

of the Pd nanoclsuters is not entirely clear, it was found that for Au nanocluster, condensation length and magnetron sputtering power would significantly affect the population of high symmetry structures.[138] The interpretation of this shift in structural population is that the average concentration of atomic vapour that affected by sputtering power and condensation length would allow different lengths of time for the growing clusters to reach selected size. It is also found that the structural population of clusters can also be influenced quite sensitively by pressure in the condensation chamber.[151]

5.6.3 Pd$_{2057\pm45}$ nanoclusters heat treatment in air
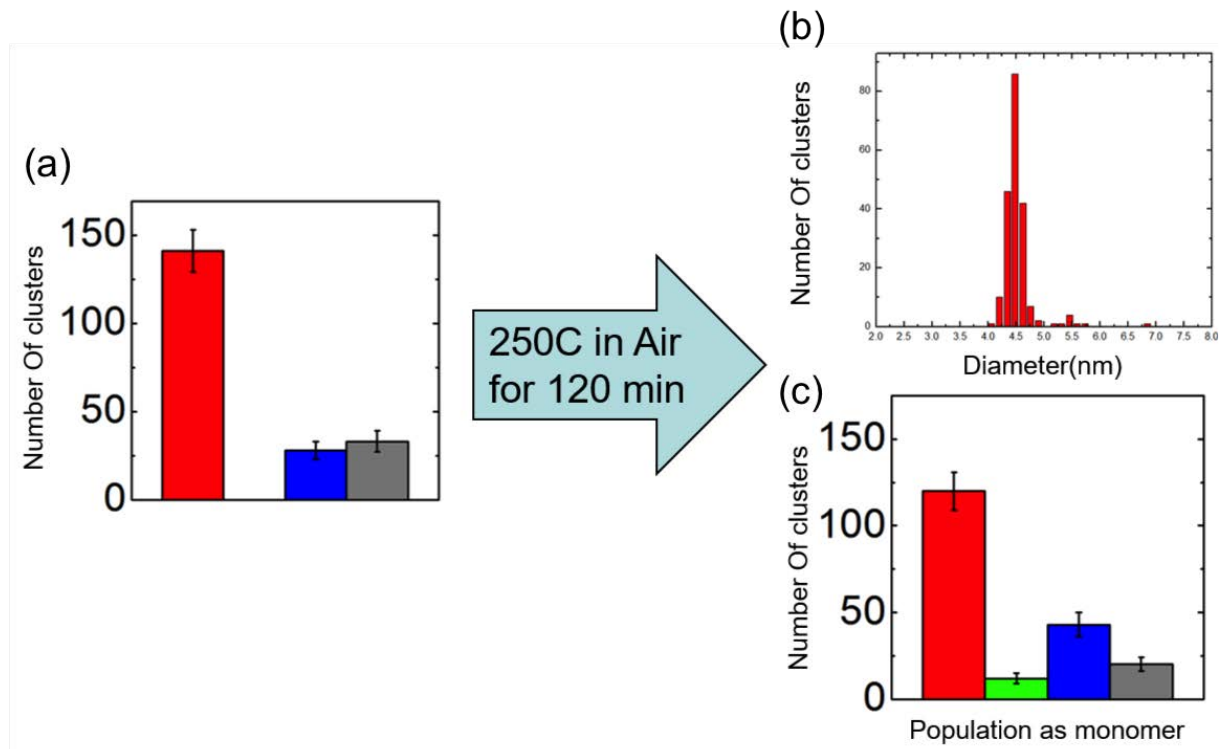
Figure 5.9: Charts showing the relative proportions of Pd$_{2057\pm45}$ (a) before and (c) after heat treatment in ambient condition. (b) shows the size distribution that corresponds to (c). Heat treatment is done under ambient conditions. Temperature rise from RT to 250 °C in 14 min then dwell at 250 °C for 120 min. After treatment, it takes 45 min to cool down to RT. Related cluster formation parameters: condensation length, 250 mm; magnetron sputtering power, 10 W DC; condensation pressure, 0.39 mbar; deposition energy, 0.5 eV/atom; condensation gas flows, 100 sccm (Ar) and 110 sccm (He).

Fig.5.9 shows the composition of different structures of $Pd_{2057\pm45}$ nanoclusters before and after annealing in ambient conditions. This experiment was conducted to investigate the degree of spontaneous oxidation of Pd clusters when they were exposed to atmosphere. $Pd_{2057\pm45}$ was prepared in high vacuum ($2.0x10^{-6}$ mbar) at room temperature. The initial imaging which the result was shown in Fig.5.9 (a), was conducted on the same day after the sample has been made. The sample was transferred directly from cluster beam source in high vacuum to STEM column. The time used for transferring in air was less than 5 minutes. As the clusters have just been made, FCC was dominated the structure as shown in Fig.5.9 (a). The ratio between FCC:D_h:Amorphous is 6:1:1. The sample was then treated in ambient condition in the heat program that reached and dwelled at $250\,^{\circ}$C for 2 hours. After the sample cooled down, the post-treatment imaging was done immediately with the transferring time less than 5 minutes. Results of size distribution of $Pd_{2057\pm45}$ clusters showed the clusters did not suffer from serious ripening in Fig.5.9 (b). Clusters did not aggregate into larger ones nor disintegrate into smaller pieces. Though a minute dimer peak was seen, clusters largely remain monomer. Fig.5.9 (c) showed the population of different monomer clusters after annealed in air. There is slightly decrease in proportion of FCC structure and increase in D_h, and emerging of tiny amount of I_h clusters were observed. But it remains large proportion of high symmetry structures.

Pd is known to oxidise spontaneously upon contact with oxygen,[183, 175, 184, 185] but the oxidation depth on Pd single crystals is temperature dependent.[186] On the Pd(111) surface, PdO first forms as an amorphous layer, gradually increasing in crystallinity at elevated temperatures. When the temperature reaches 500 K, amorphous PdO layers coalescence to form a PdO(110) ad-layer with thickness of 3.5 ML at saturation.[187] However, there were also contradicting evidence showing that after exposing Pd in air flow of oxygen partial pressure of $3x10^2$ mbar(50% higher than atmosphere) at 373 K, the oxidation depth on Pd surface is 1 ML.[183] Inconsistency between different experiments might due to the reason that the strength of oxidation resistance on nanoclusters depend significantly on crystal surfaces. Among various low and high Millar index surfaces which

were investigated, low index (100), (111), and (110) were more stable than other surfaces when clean and with oxygen atom absorbed. Among these three low index surfaces, (110) was constantly being less stable than the other two directions under various oxygen partial pressure tested. (100) surface with 0.8 ML of oxygen adsorption is the most stable among all surfaces and coverage throughout this investigation. Compared with low index surfaces, high index surface were less stable and tend to be more extensively oxidised deeply to form PdO.[188, 189] With carefully tuning of clusters generation parameter, population of different structure generated from cluster beam source is controllable.[138] Sample can be prepared from cluster beam source with amorphous-rich or high-symmetry structure rich clusters. In previous study, we suspect that the restoration from amorphous to high symmetry structures after full 1-pentyne hydrogenation was due to the removal of oxidised layer around the Pd nanoclusters.[139] However, in a more comprehensive experiment being conducted recently, it is shown that though both $Pd_{2057\pm45}$ and $Pd_{923\pm20}$ clusters that initially were highly amorphous, transformed to high symmetry structures in full 1-pentyne hydrogenation. Nevertheless, amorphous $Pd_{923\pm20}$ cluster did not undergo any transformation in hydrogen treatment, which indicates that either the treating condition was not able to trigger structural transformation or there was no oxidised layer on the surface of Pd nanocluster for hydrogen to reduced further. Both possibilities suggest that, instead of obscuring by oxide layer, the structure of the whole palladium nanoclusters were amorphous. Furthermore, the structure of high symmetry $Pd_{2057\pm45}$ clusters did not show serious amorphisation in ambient condition in a heat cycle that reached the same temperature (250 °C) as other treatments. This indicates limited degree of oxidation occur on the surface of $Pd_{2057\pm45}$ clusters. More precisely, during the transferring process that takes five minutes in air of Pd clusters from cluster beam source to STEM column, the oxidation on the surface has been saturated. Further oxidation in air at 250 °C did not increase the proportion of amorphous nanoclusters seen. (3.5 layers of oxidation layer is not enough to cover Pd_{923} has 7 layers and Pd_{2057} has 9 layers.) However, due to the set-up of instrument, in situ treatments cannot be achieved, the fact that some degree of

oxidation has occurred on Pd cluster prior to initial imaging is inevitable.

The ability to produce oxidised and oxidation-resistant Pd catalysts selectively may be advantageous,[190] particularly as there is some debate as to whether Pd or PdO is the more active catalyst. An example concerns the comparative activities of alumina-supported palladium for the combustion of methane,[191, 192, 193] for which early reports are conflicting. It is generally believed that methane oxidation proceeds rapidly through the chemisorption of oxygen onto PdO for alumina-supported Pd catalyst at atmospheric pressure.[193] Such chemisorption would cease on the Pd catalyst surface above 650 °C, which is the decomposition temperature of PdO, and hence the catalysed methane combustion stops. [192, 193] Furthermore, in a more recent study conducted on a polycrystalline Pd plate in an ultrahigh vacuum system, the reaction rate of methane production drops drastically when the system goes beyond the decomposition temperature of PdO.[194]

5.7 Conclusion

It has been shown that during cluster generation, by carefully controlling the generation parameters, some degree of control in structural population can be achieved.[138] The parameter of structural population control on Pd nanoclusters is not entirely clear. Nevertheless, Pd nanoclusters that were rich in amorphous and nanoclusters that were rich in high symmetry structure were managed to be prepared and treated. Though being aware of the knowledge of spontaneous oxidation that occurred on Pd single crystal and supported clusters, the amorphous structure that was observed could not account solely account to the obscured oxidised surface. Because it is shown in our experiment that FCC and D_h structures rich sample largely remain in high symmetry structure after oxidation under ambient condition in 250 °C . On the contrary, after being subjected to reducing hydrogen atmosphere, amorphous $Pd_{2057\pm45}$ nanoclusters which were imaged as highly amorphous prior to treatment became high symmetry structures after treat-

ment, while $Pd_{923\pm20}$ remains mostly amorphous. This may imply that the structural transformation is due to the reconstruction of the entire cluster instead of the structural restoring on the surface. Finally, both Pd_{923} and Pd_{2057} clusters in our experiments, after full 1-pentyne hydrogenation reactions, amorphous clusters tended to transform to high symmetry structures. In the most recent set of experiments, icosahedral clusters were seen after the reactions; this suggested the interplay of heat release and hydrogen incorporating from 1-pentyne hydrogenation might promote the actual temperature exerting on the Pd nanoclusters. Hence, for those clusters which were at least partly melting could have the chance to become icosahedron after quenching.

CHAPTER 6

CONCLUSIONS

In this Thesis monolayer-protected and size-selected bare metal clusters were investigated with STEM focus on their structures, structural response to chemical reaction, and ripening modes.

The chemically synthesised monolayer-protected Au_{40} clusters were found to contain 40 ± 2 gold atoms via the atom counting method using size-selected Au_{55} clusters as mass standards. The aspect ratio of MP-Au_{40} clusters was 1.8, based on the largest aspect ratios observed in the images, with dimers or larger particles excluded according to their integrated HAADF intensity.

The vapour-phase 1-pentyne hydrogenation reaction (up to $250\,^{\circ}\mathrm{C}$) was conducted on to size-selected Au_x and Pd_x clusters (x = 923 and 2057). It is found that the reaction hardly affects the structure of the gold nanoclusters, whereas amorphous Pd clusters transform toward high symmetry structures. Furthermore, in control experiments on Pd clusters, heat treatment of $250\,^{\circ}\mathrm{C}$ in helium was not capable of transforming amorphous Pd clusters. It seems that the extra heat generated by the chemical reaction and hydrogen might participate driving the structural transformation of Pd.

Gas-phase CO oxidation over Au_x (x = 561, 923 and 2057) clusters was found to induce cluster ripening, with a mode of ripening which depended on the size of cluster. Clusters smaller than 923 atoms were found to demonstrate Ostwald ripening, in which cluster atom unbind and diffuse to other clusters nearby. On the contrary, Au_{2057} clusters

was found to undergo Smulochowski ripening, in which clusters diffuse and coalesce with other clusters as intact clusters. Solid evidence was found, through size distributions and integrated HAADF intensities, that, after CO oxidation reaction Au_{2057} monomers aggregated in a discrete manner. The size distribution was strongly peaked at monomers, dimers, trimers etc.. In the control experiments for both Au_{923} and Au_{2057}, where clusters were heated in helium or oxygen, the clusters did not exhibit Ostwald ripening, regardless of the size. We conclude that the heat generated by the CO oxidation reaction driving the Ostwald ripening process. The observed size dependence might be related to an enhanced CO oxidation rate in the smaller, Au_{923} clusters.

APPENDIX I

MACRO SCRIPT

CLUSTER DIAMETER MEASUREMENT

This script is written in ImageJ macro script. It is used to measure the diameter of clusters captured in images.

```
1  //Initial a Table for organised data
2  title1 = "["+"Size_Statistic"+"]";
3  run("New...␣", "name="+title1+"␣type=Table");
4  print(title1,"\\Headings:Cluster.No.\tArea\tMajor\tMinor\
       tDiameter");
5
6  //Loop Head
7  while (getTitle()!="") {
8  //Clear previous results
9  run("Clear␣Results");
10
11 //Get the Title and printing name for following output files.
       Trimed between chracter "X" and "."
12 readin=getTitle();
13 StartingIndex=indexOf(readin,"X");
14 EndingIndex=indexOf(readin,".");
15 printingname=substring(readin, StartingIndex+1, EndingIndex);
16
17 //Get image width
18 getVoxelSize(width, height, depth, unit);
19
20 //Duplicate and do FFT filtering on original image
21 run("Duplicate...", "title=WorkingCopy.dm3");
22 resetMinAndMax();
23 run("Bandpass␣Filter...", "filter␣large=512␣filter␣small=2␣
       suppress=None␣tolerance=5␣autoscale␣saturate");
24 setFont("SansSerif", 12, "bold");
25 setColor(255,255,255);
26
27 //Jump to duplicate image and Run Median filter, then get whole
       image statistic
28 selectWindow("WorkingCopy.dm3");
29
30 //run("Bandpass Filter...", "filter␣large=512 filter␣small=20
       suppress=None tolerance=5 autoscale saturate");
```

```
31  //This is a step for getting rough contour for clusters.
32  run("Median...", "radius=5");
33  getRawStatistics(nPixels, mean, min, max, std, histogram);
34
35  //BubbleSorting to find the peak centre of this image
36  //initialCondition
37  MaxNumCache=0;
38  MaxCache=histogram[0];
39  //bubbleSorting
40  for(i=0;i<255;i++){
41      if(histogram[i]>MaxCache){
42          MaxNumCache=i;
43          MaxCache=histogram[i];
44      }
45  }
46  CentreOfPeak=min+((max-min)*(MaxNumCache+0.5)/256);
47
48  //Decide the Threshold lower limit at X(decided differently on
        different cases) standard deviation
49  setThreshold(CentreOfPeak+(2*std),max);
50
51  //Make duplicated image binary and do particle measurement
52  run("Make Binary");
53  run("Set Measurements...", "  area centroid bounding fit
        redirect=None decimal=3");
54  run("Analyze Particles...", "size=0-Infinity circularity
        =0.60-1.00 show=Nothing display");//"Exclude" can be added to
         exclude particles on the edges.
55  n=nResults;
56
57  //Draw the contuor on the original image by the fitting on the
        duplicate image, one by one.
58  //setTool("wand");
59  for(i=0;i<=n-1;i++){
60  selectWindow("WorkingCopy.dm3");
61  X=getResult("X", i)*(1/width);
62  Y=getResult("Y", i)*(1/width);
63  doWand(X,Y);
64  selectWindow(readin);
65  run("Restore Selection");
66
67      do {
68
69      getRawStatistics(nPixels_1, mean_1, min_, max_, std_,
            histogram_);
70      run("Enlarge...", "enlarge=2 pixel");
```

```
71    getRawStatistics(nPixels_2, mean_2, min_, max_, std_,
         histogram_);
72    run("Enlarge...", "enlarge=2_pixel");
73    getRawStatistics(nPixels_3, mean_3, min_, max_, std_,
         histogram_);
74
75    run("Enlarge...", "enlarge=-2_pixel");
76
77    //Cluster intensity inside Circle 1, using space between
         circle 1 and 2 as bacjground
78    Value1=(mean_1-(nPixels_2*mean_2-nPixels_1*mean_1)/(nPixels_2-
         nPixels_1))*nPixels_1;
79    //Cluster intensity inside Circle 2, using space between
         circle 2 and 3 as background
80    Value2=(mean_2-(nPixels_3*mean_3-nPixels_2*mean_2)/(nPixels_3-
         nPixels_2))*nPixels_2;
81
82    background1=((mean_2*nPixels_2)-(mean_1*nPixels_1))/(nPixels_2
         -nPixels_1);
83
84    background2=((mean_3*nPixels_3)-(mean_2*nPixels_2))/(nPixels_3
         -nPixels_2);
85
86    //print(title1,"Cluster"+i+"."+j+"\t"+background);
87
88    } while (abs((Value2-Value1)/Value2)>0.15);
89    //} while (abs(background2-background1)>22500);
90
91 run("Measure");
92
93 setForegroundColor(255, 255, 255);
94 run("Draw");
95 run("Select_None");
96 }
97
98 //close duplicate image
99 selectWindow("WorkingCopy.dm3");
100 close();
101
102 //Do the actual image cropping on the original image, output
       size info to table, save the cropped cluster image, including
       their diameter(calculated from their Area measurement)
103 for(i=0;i<=n-1;i++){
104 X=getResult("X", i)*(1/width);
105 Y=getResult("Y", i)*(1/width);
106 //DuplicatingWidth=40*(floor(maxOf(getResult("Width", i),
```

```
         getResult("Height", i))*(1/width)/40)+2);
107  DuplicatingWidth=40*(floor(((getResult("Width", n+i)+getResult("
         Height", n+i))/2)*(1/width)/40)+2);
108  makeRectangle(X-(DuplicatingWidth*0.5), Y-(DuplicatingWidth*0.5)
         , DuplicatingWidth, DuplicatingWidth);
109  run("Duplicate...", "title="+printingname+"."+i);
110  //Meant to reset Max and Min for Duplicated small images.
111  //resetMinAndMax();
112  drawString(printingname+"."+i,0,13);
113  run("Scale Bar...", "width=1 height=5 font=10 color=White
         background=None location=[Lower Right] bold");
114
115  AreaResult=getResult("Area", n+i);
116  MajorAxir=getResult("Major", n+i);
117  MinorAxir=getResult("Minor", n+i);
118  // Work out diameter from Area measurement
119  // d2s is digital to string function
120  ClusterDiameter=d2s(sqrt(4*AreaResult/PI),3);
121
122  drawString(ClusterDiameter,0,26);
123
124  print(title1,printingname+"."+i+"\t"+AreaResult+"\t"+MajorAxir+"
         \t"+MinorAxir+"\t"+ClusterDiameter);
125
126  saveAs("PNG", "/Users/Ray/Desktop/PNGtemp/"+ClusterDiameter+"."+
         printingname+"."+i);
127  //saveAs("PNG", "C:\\PNGtemp\\"+ClusterDiameter+"."+printingname
         +"."+i);
128  close();//close cropped window
129  }
130
131  close();//close image window
132
133  }
134
135  selectWindow("Size Statistic");
136  saveAs("XLS", "/Users/Ray/Desktop/PNGtemp/"+printingname);
137  close();
```

ATOM COUNTING MEASUREMENT

This script is written in ImageJ macro script language. It is used to measure the integrated HAADF intensity of nanocluster in the images.

```
1  //Table Title
2  //Initial a Table for organised data
```

```
 3 title1 = "["+"HAADF_Statistic"+"]";
 4 run("New...", "name="+title1+"_type=Table");
 5 print(title1,"\\Headings:Cluster.No.\tClusterInt\tBackground");
 6
 7 //Loop Head
 8 while (getTitle()!="") {
 9
10 run("Clear_Results");
11
12 //Get Original Title
13 readin=getTitle();
14 StartingIndex=indexOf(readin,"X");
15 EndingIndex=indexOf(readin,".");
16 printingname=substring(readin, StartingIndex+1, EndingIndex);
17
18 //Descaled
19 run("Set_Scale...", "distance=0_known=0_pixel=1_unit=pixel");
20
21 //Duplicate and for Median Filter
22 run("Duplicate...", "title=MedianFilter.dm3");
23 selectWindow("MedianFilter.dm3");
24 run("Median...", "radius=100");
25
26 //Substract Origianl image with Median filtered Slop
27 imageCalculator("Subtract_create", readin,"MedianFilter.dm3");
28
29 //Close Median Slop Window
30 selectWindow("MedianFilter.dm3");
31 close();
32
33 //Duplicate and for FFT Filter
34
35 selectWindow("Result_of_"+readin);
36 run("Bandpass_Filter...", "filter_large=1024_filter_small=30_
      suppress=None_tolerance=5_autoscale_saturate");
37
38 //Get Statistic and Put on Threshold Filter
39   //initialCondition
40   getRawStatistics(nPixels, mean, min, max, std, histogram);
41   MaxNumCache=0;
42   MaxCache=histogram[0];
43   //bubbleSorting
44 for(i=0;i<255;i++){
45   if(histogram[i]>MaxCache){
46     MaxNumCache=i;
47     MaxCache=histogram[i];
```

```
48    }
49 }
50
51 //Use Centre of Peak found to set the threshold
52 CentreOfPeak=min+((max−min)∗(MaxNumCache+0.5)/256);
53 setThreshold(CentreOfPeak+(2∗std),max);
54 run("Make Binary");
55 run("Remove Outliers...", "radius=10 threshold=254 which=Dark");
56 run("Set Measurements...", "  area centroid bounding fit
      redirect=None decimal=3");
57 run("Analyze Particles...", "size=0−Infinity circularity
      =0.70−1.00 show=Nothing display exclude");
58 n=nResults;
59
60 close();//close Binary window
61
62 //Go back to Original image
63 selectWindow(readin);
64
65 //Atom count loop stopping criterion
66 LoopStopValue=0.1;
67
68 //Atom Count Loop(for)
69 for(i=0;i<=n−1;i++){
70    AC_radius=(0.5∗maxOf(getResult("Major", i),getResult("Minor",
      i)))+10;
71    X=getResult("X", i);
72    Y=getResult("Y", i);
73
74    //Initial Circle
75    makeOval(X−AC_radius, Y−AC_radius, 2∗AC_radius, 2∗AC_radius);
76
77      do {
78
79      getRawStatistics(nPixels_1, mean_1, min_, max_, std_,
          histogram_);
80      run("Enlarge...", "enlarge=3 pixel");
81      getRawStatistics(nPixels_2, mean_2, min_, max_, std_,
          histogram_);
82      run("Enlarge...", "enlarge=3 pixel");
83      getRawStatistics(nPixels_3, mean_3, min_, max_, std_,
          histogram_);
84
85      run("Enlarge...", "enlarge=−3 pixel");
86
87      Value1=(mean_1−(nPixels_2∗mean_2−nPixels_1∗mean_1)/(
```

```
          nPixels_2-nPixels_1))*nPixels_1;
88      Value2=(mean_2-(nPixels_3*mean_3-nPixels_2*mean_2)/(
          nPixels_3-nPixels_2))*nPixels_2;
89
90      } while (abs((Value2-Value1)/Value2)>LoopStopValue);
91
92    //Inner Circle
93    getRawStatistics(nPixels1, mean1, min1, max1, std1, histogram1
        );
94
95    //Outer Circle
96    run("Enlarge...", "enlarge=3 pixel");
97    getRawStatistics(nPixels2, mean2, min2, max2, std2, histogram2
        );
98    run("Select None");
99
100   //Total intensity of whole Large Area
101   TA2=nPixels2*mean2;
102
103   //Total intensity of Small Area
104   TA1=nPixels1*mean1;
105
106   //Total carbon intensity
107   Carbon_Anulus_Intensity= TA2-TA1;
108
109   //number of carbon pixels
110   nPixC= nPixels2-nPixels1;
111
112   //background intensity per pixel
113   Background_Pixel_Intensity=Carbon_Anulus_Intensity/nPixC;
114
115   //total intensity (inner circle) minus background
116   Cluster_Intensity= TA1-(Background_Pixel_Intensity*nPixels1);
117   Cluster_Pixel_Intensity = Cluster_Intensity / nPixels1;
118
119   print(title1, printingname+"."+i+"\t"+Cluster_Intensity+"\t"+
        Background_Pixel_Intensity);
120
121 }//for loop end
122
123 //Draw Record
124 setForegroundColor(255, 255, 255);//set Drawing colour
125 setFont("SansSerif", 24, "bold");//set String Font
126
127 for(i=0;i<=n-1;i++){
128   AC_radius=(0.5*maxOf(getResult("Major", i),getResult("Minor",
```

```
            i ) ) )+5;
129   X=getResult ( ”X” ,  i ) ;
130   Y=getResult ( ”Y” ,  i ) ;
131
132   //Initial Circle
133   makeOval (X−AC_radius ,  Y−AC_radius ,  2∗AC_radius ,  2∗AC_radius ) ;
134
135     do {
136
137     getRawStatistics ( nPixels_1 ,  mean_1 ,  min_ ,  max_ ,  std_ ,
            histogram_ ) ;
138     run ( ”Enlarge . . . ” ,  ”enlarge=3_pixel ” ) ;
139     getRawStatistics ( nPixels_2 ,  mean_2 ,  min_ ,  max_ ,  std_ ,
            histogram_ ) ;
140     run ( ”Enlarge . . . ” ,  ”enlarge=3_pixel ” ) ;
141     getRawStatistics ( nPixels_3 ,  mean_3 ,  min_ ,  max_ ,  std_ ,
            histogram_ ) ;
142
143     run ( ”Enlarge . . . ” ,  ”enlarge=−3_pixel ” ) ;
144
145     Value1=(mean_1−(nPixels_2∗mean_2−nPixels_1∗mean_1 )/(
            nPixels_2−nPixels_1 ) )∗nPixels_1 ;
146     Value2=(mean_2−(nPixels_3∗mean_3−nPixels_2∗mean_2 )/(
            nPixels_3−nPixels_2 ) )∗nPixels_2 ;
147
148     } while ( abs ( ( Value2−Value1 )/Value2)>LoopStopValue ) ;
149
150   //Inner Circle
151   run ( ”Draw” ) ;
152
153   //Outer Circle
154   run ( ”Enlarge . . . ” ,  ”enlarge=3_pixel ” ) ;
155   run ( ”Draw” ) ;
156   run ( ” Select _None” ) ;
157
158   //Draw Number
159   drawString ( i+1 , X−AC_radius ,  Y−AC_radius ) ;
160
161   run ( ” Select _None” ) ;
162
163 }//for loop end
164
165 saveAs ( ”PNG” ,  ”/Users/Ray/Desktop/PNGtemp/”+printingname ) ;
166 //saveAs(”PNG”, ”C:\\PNGtemp\\”+printingname+”.”+i ) ;
167
168 close ( ) ;//close Measured and Marked window
```

```
169
170 } //While Loop End
```

AUTOMATE SCRIPT QSTEM MULTISLICE IMAGE STEM SIMULATION ON BLUE-
BEAR

    This program is written in C language. This program is assisting the user to generate
calculation parameter for QSTEM simulation in BlueBEAR cluster computer. It converts
the calculating angle from Cartesian coordinate to Eularian angle.

```
 1 #include <stdio.h>
 2 #include <stdlib.h>
 3 #include <errno.h>
 4 #include <wchar.h>
 5 #include <math.h>
 6
 7 float *rotate(float Xrot, float Yrot, float Zrot, int
      NumOfCoords, float *Coords)
 8 {
 9 int i;
10 float cx,cy,cz,sx,sy,sz;
11 static float *tempCoords;
12
13 tempCoords=malloc(sizeof(float[3])*NumOfCoords);
14
15 cx=cos(Xrot);cy=cos(Yrot);cz=cos(Zrot);
16 sx=sin(Xrot);sy=sin(Yrot);sz=sin(Zrot);
17
18 for(i=0;i<NumOfCoords;i++){
19
20    *(tempCoords+3*i)  =(cy*cz)*(*(Coords+3*i))   +(cz*sy*sx-cx*sz)
         *(*(Coords+3*i+1))  +(sx*sz+cx*sy*cz)*(*(Coords+3*i+2));
21    *(tempCoords+3*i+1) =(cy*sz)*(*(Coords+3*i))   +(cx*cz+sx*sy*sz
         )*(*(Coords+3*i+1))  +(cx*sy*sz-sx*cz)*(*(Coords+3*i+2));
22    *(tempCoords+3*i+2) =-(sy)*(*(Coords+3*i))      +(sx*cy)*(*(
         Coords+3*i+1))     +(cx*cy)*(*(Coords+3*i+2));
23
24    }
25
26 return tempCoords;
27 }
28
29 float *eularconvert(float theta_input_eularconv, float
      alpha_input_eularconv)
30 {
```

```
31 static float XYZrot_output[3]={0,0,0};
32 float tiltX,tiltY;
33
34 XYZrot_output[1]=asin(−sin(alpha_input_eularconv/180*M_PI)*sin(
      theta_input_eularconv/180*M_PI));
35
36 tiltX=cos(alpha_input_eularconv/180*M_PI)/cos(XYZrot_output[1]);
37 if(tiltX==1 || tiltX==−1){  XYZrot_output[0]=0; }
38 else{       XYZrot_output[0]=acos(cos(alpha_input_eularconv/180*
      M_PI)/cos(XYZrot_output[1])); }
39
40 tiltY=cos(theta_input_eularconv/180*M_PI)/cos(XYZrot_output[1]);
41 if(tiltY==1 || tiltY==−1){  XYZrot_output[2]=0; }
42 else{       XYZrot_output[2]=acos(cos(theta_input_eularconv/180*
      M_PI)/cos(XYZrot_output[1])); }
43
44 /*
45 XYZrot_output[0]=13;
46 XYZrot_output[1]=29;
47 XYZrot_output[2]=37;
48 */
49
50 return XYZrot_output;
51 }
52
53 float *bubsort_Coord( float *Coord, int NumOfCoords)
54 {
55 static float extremum[6]={1,2,3,4,5,6};
56 int i;
57 /*Initialize*/
58 extremum[0]=*(Coord);
59 extremum[2]=*(Coord+1);
60 extremum[4]=*(Coord+2);
61 extremum[1]=*(Coord);
62 extremum[3]=*(Coord+1);
63 extremum[5]=*(Coord+2);
64
65 /*Biggests*/
66 for(i=0;i<NumOfCoords;i++){
67   extremum[0]=*(Coord+3*i)>extremum[0]?*(Coord+3*i):extremum[0];
68   extremum[2]=*(Coord+3*i+1)>extremum[2]?*(Coord+3*i+1):extremum
         [2];
69   extremum[4]=*(Coord+3*i+2)>extremum[4]?*(Coord+3*i+2):extremum
         [4];
70
71 /*Smallests*/
```

```
72    extremum[1]=*(Coord+3*i)<extremum[1]?*(Coord+3*i):extremum[1];
73    extremum[3]=*(Coord+3*i+1)<extremum[3]?*(Coord+3*i+1):extremum
          [3];
74    extremum[5]=*(Coord+3*i+2)<extremum[5]?*(Coord+3*i+2):extremum
          [5];
75    }
76
77 return extremum;
78 }
79
80 /* ————————————————————————————MAIN Program Starts
       HERE———————————————————————— */
81
82 int main(int argc,char *argv[])
83 {
84 int NumOfAtoms;
85 int i,j,dummy=0;
86
87 float dimensions[3];
88 float *oBox;
89 float *rBox;
90 float oBox_ar
       [][3]={{0,0,0},{1,0,0},{0,1,0},{0,0,1},{1,1,0},{1,0,1},{0,1,1},{1,1,1}
91 float *oCoord,*rCoord;
92 float *extremum_acceptor;
93 float extremum_box[6]={0,0,0,0,0,0};
94 float extremum_main[6]={0,0,0,0,0,0};
95 float Spacing;
96 float theta_input_main,alpha_input_main;
97 float *XYZrot_main;
98 char nullchar[255];
99
100 FILE *in_stream;
101
102 /* File stream opening*/
103 if ((in_stream=fopen(argv[1],"r"))==NULL) {
104   perror("Error_when_opening_file");
105   exit(EXIT_FAILURE);
106   }
107
108 /* Coordicates and Rotation Parameters Load in */
109 fscanf(in_stream,"%d\n",&NumOfAtoms);
110
111 oCoord=malloc(sizeof(float[3])*NumOfAtoms);
112 rCoord=malloc(sizeof(float[3])*NumOfAtoms);
```

```
113 extremum_acceptor=malloc(sizeof(float)*6);
114 XYZrot_main=malloc(sizeof(float)*3);
115 rBox=malloc(sizeof(float[3])*8);
116 oBox=oBox_ar;
117
118 /*   for(j=0;j<1;j++) fgets(nullchar,255,in_stream);*/
119 fscanf(in_stream,"%f\n",&dimensions[0]);
120 /*   for(j=0;j<3;j++) fgets(nullchar,255,in_stream);*/
121 fscanf(in_stream,"%f\n",&dimensions[1]);
122 /*   for(j=0;j<3;j++) fgets(nullchar,255,in_stream);*/
123 fscanf(in_stream,"%f\n",&dimensions[2]);
124 /*   for(j=0;j<4;j++) fgets(nullchar,255,in_stream);*/
125
126    dummy=0;
127 while(1){
128            if(fscanf(in_stream,"%f_%f_%f\n",(oCoord+3*dummy),(
                   oCoord+3*dummy+1),(oCoord+3*dummy+2))==EOF)
129        break;
130            else{
131 /*       printf("%f %f %f\n",*(oCoord+3*dummy),*(oCoord+3*dummy),*(
         oCoord+3*dummy+2));*/
132      dummy++;
133            }
134    }
135
136
137 theta_input_main=atof(argv[2]);
138 alpha_input_main=atof(argv[3]);
139 Spacing=atof(argv[4]);
140
141 /* Preload Box and Atom coordicates with dimensions */
142 for(i=0;i<8;i++){
143    *(oBox+3*i)=*(oBox+3*i)*dimensions[0];
144    *(oBox+3*i+1)=*(oBox+3*i+1)*dimensions[1];
145    *(oBox+3*i+2)=*(oBox+3*i+2)*dimensions[2];
146    }
147
148 for(i=0;i<NumOfAtoms;i++){
149    *(oCoord+3*i)=*(oCoord+3*i)*dimensions[0];
150    *(oCoord+3*i+1)=*(oCoord+3*i+1)*dimensions[1];
151    *(oCoord+3*i+2)=*(oCoord+3*i+2)*dimensions[2];
152    }
153
154 /* Conversion from Eularian rotation coordination to XYZ
        rotation */
155 XYZrot_main=eularconvert(theta_input_main,alpha_input_main);
```

```
156
157 /* Bubble Sorting for the extremums */
158 rBox=rotate(*(XYZrot_main+0),*(XYZrot_main+1),*(XYZrot_main+2),(
       int)8,oBox);
159 extremum_acceptor=bubsort_Coord(rBox,(int)8);
160 for(i=0;i<6;i++) extremum_box[i]=*(extremum_acceptor+i);
161
162 rCoord=rotate(*(XYZrot_main+0),*(XYZrot_main+1),*(XYZrot_main+2)
       ,NumOfAtoms,oCoord);
163 extremum_acceptor=bubsort_Coord(rCoord,NumOfAtoms);
164 for(i=0;i<6;i++) extremum_main[i]=*(extremum_acceptor+i);
165
166 /* Testing Scripts */
167
168 if(argv[5]!=NULL) {
169    if(strcmp(argv[5],"c")==0) {
170
171     printf("Coordinate file name %s\n",argv[1]);
172     printf("Num of Atoms = %d\n",NumOfAtoms);
173 printf("Dimensions X->%f ; Y->%f ;  Z->%f\n",dimensions[0],
       dimensions[1],dimensions[2]);
174 printf("Rotation Parameters theta->%f ; alpha->%f\n",
       theta_input_main,alpha_input_main);
175 printf("Rotation converted into Xrot->%f ; Yrot->%f ; Zrot->%f\
       n",*(XYZrot_main+0)/M_PI*180,*(XYZrot_main+1)/M_PI*180,*(
       XYZrot_main+2)/M_PI*180);
176 printf("\n");
177 for(i=0;i<8;i++)
178             printf("Orig Box Num %d = X->%f ; Y->%f ;  Z->%f\n",i
                 ,*(oBox+3*i),*(oBox+3*i+1),*(oBox+3*i+2));
179 for(i=0;i<8;i++)
180    printf("Rota Box Num %d = X->%f ; Y->%f ;  Z->%f\n",i,*(rBox
         +3*i),*(rBox+3*i+1),*(rBox+3*i+2));
181 printf("\n");
182 for(i=0;i<NumOfAtoms;i++)
183    printf("Orig atom Num %d = X->%f ; Y->%f ;  Z->%f \n",i,*(
         oCoord+3*i),*(oCoord+3*i+1),*(oCoord+3*i+2));
184 for(i=0;i<NumOfAtoms;i++)
185             printf("Rota atom Num %d = X->%f ; Y->%f ;  Z->%f \n",i
                 ,*(rCoord+3*i),*(rCoord+3*i+1),*(rCoord+3*i+2));
186 printf("Extremums Main %f %f %f %f %f %f\n",extremum_main[0],
       extremum_main[1],extremum_main[2],extremum_main[3],
       extremum_main[4],extremum_main[5]);
187 printf("Extremums Box %f %f %f %f %f %f\n",extremum_box[0],
       extremum_box[1],extremum_box[2],extremum_box[3],extremum_box
       [4],extremum_box[5]);
```

```
188
189    }
190
191 }
192
193 /* Final outputs of extremem values in X and Y direction */
194 printf("Xmax->_%f_Xmin->_%f\n",(extremum_main[0]-extremum_box
        [1]),(extremum_main[1]-extremum_box[1]));
195 printf("Ymax->_%f_Ymin->_%f\n",(extremum_main[2]-extremum_box
        [3]),(extremum_main[3]-extremum_box[3]));
196 printf("Spaced\n_Xrot_Yrot_Zrot\n_Xmax_Xmin_Ymax_Ymin\n");
197 printf("%f_%f_%f\n",*(XYZrot_main+0),*(XYZrot_main+1),*(
        XYZrot_main+2));
198 printf("%f_%f_%f_%f\n",((extremum_main[0]+extremum_main[1])/2-
        extremum_box[1]+Spacing/2),((extremum_main[0]+extremum_main
        [1])/2-extremum_box[1]-Spacing/2),((extremum_main[2]+
        extremum_main[3])/2-extremum_box[3]+Spacing/2),((
        extremum_main[2]+extremum_main[3])/2-extremum_box[3]-Spacing
        /2));
199
200 /* Ending Part */
201 free(oCoord);
202 free(rCoord);
203 free(rBox);
204 fclose(in_stream);
205 return 0;
206 }
```

APPENDIX II

STEM SIMULATED ATLAS

STEM simulated image atlas for Au_{561} and Au_{2057} are presented here. Simulate image atlas of Au_{923} used in this study is in previous publication[35].
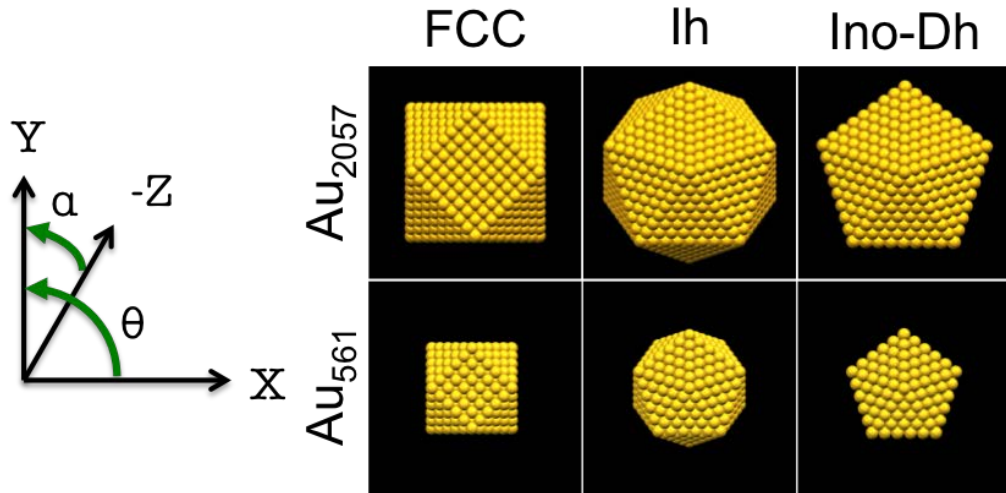
Figure 6.1: Coordinates for simulation Atlas

Au$_{561}$ Icosahedron
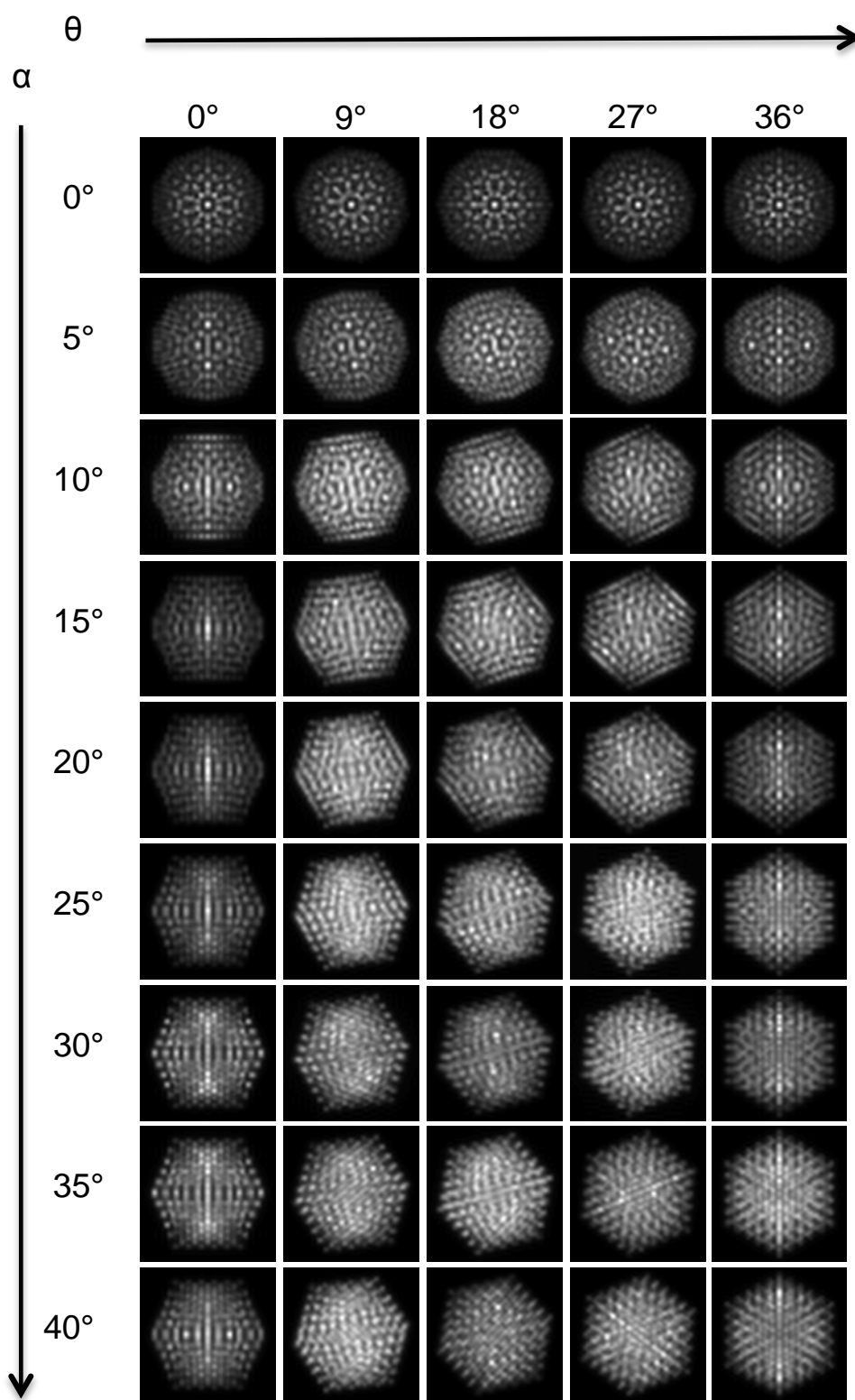
Figure 6.2: Au$_{561}$ Icosahedron
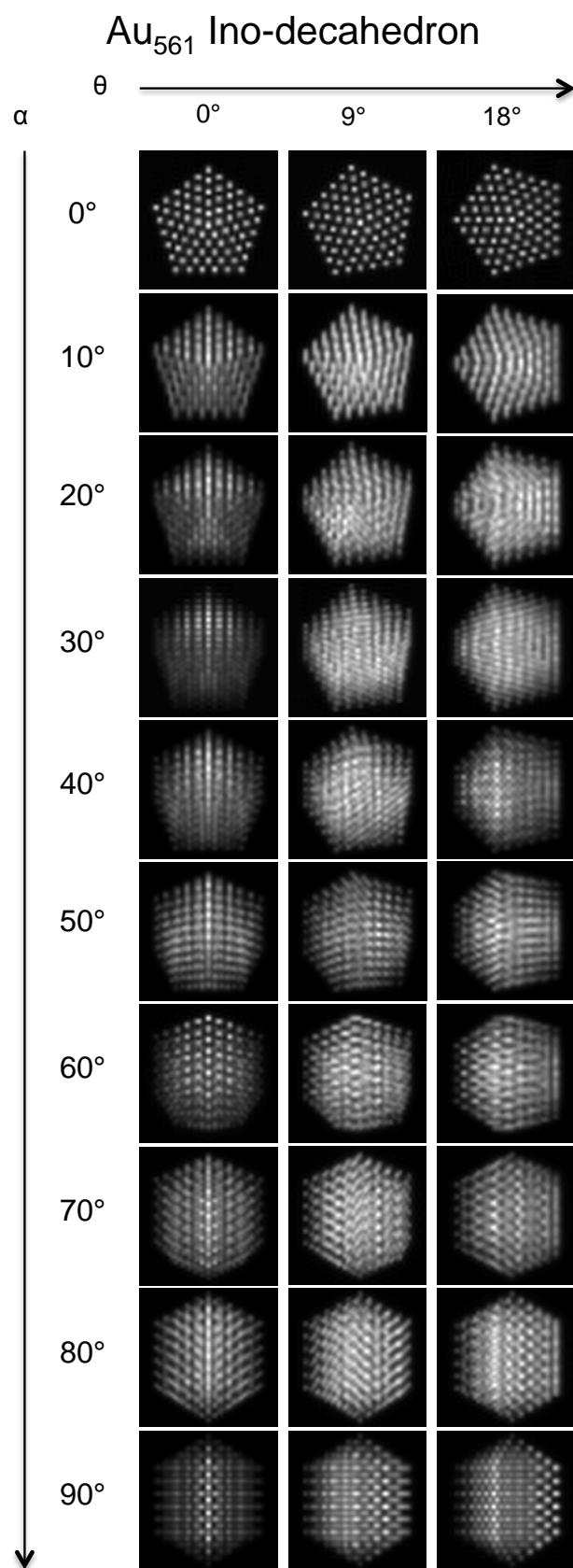
Figure 6.3: Au$_{561}$ Ino-Decahedron

Au$_{561}$ Cuboctahedron

θ

	0°	15°	30°	45°
α				
0°				
15°				
30°				
45°				
60°				
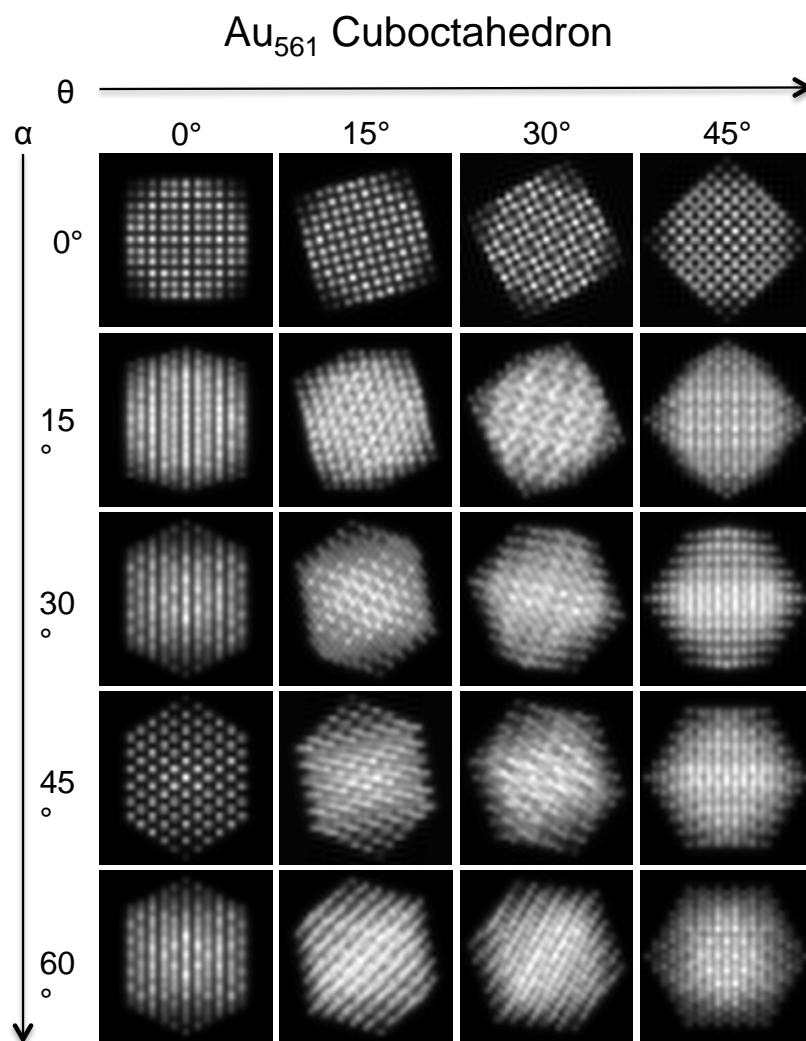
Figure 6.4: Au$_{561}$ Cuboctahedron

Au$_{2057}$ Icosahedron
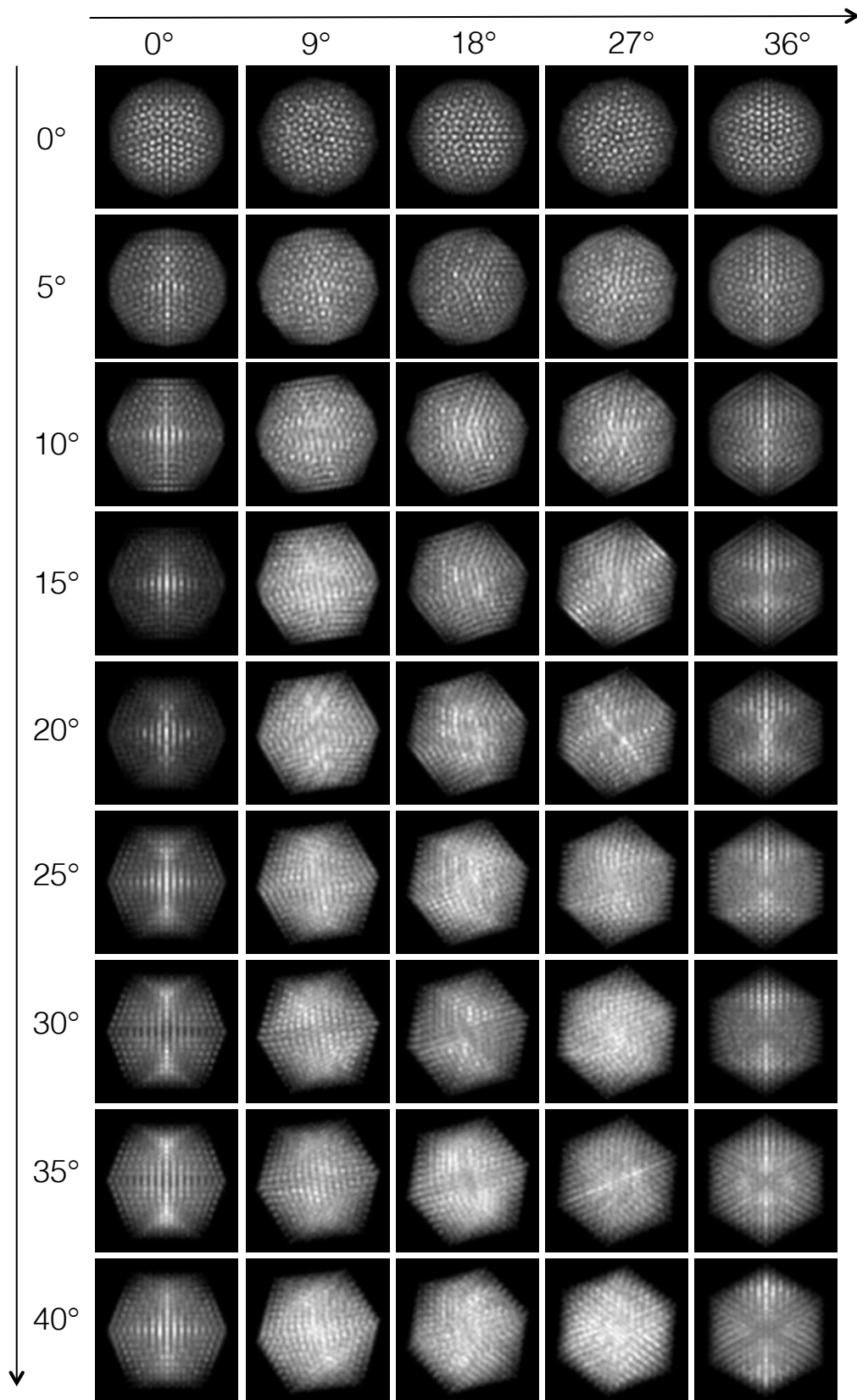
Figure 6.5: Au$_{2057}$ Icosahedron

Au$_{2057}$ Ino-Decahedron
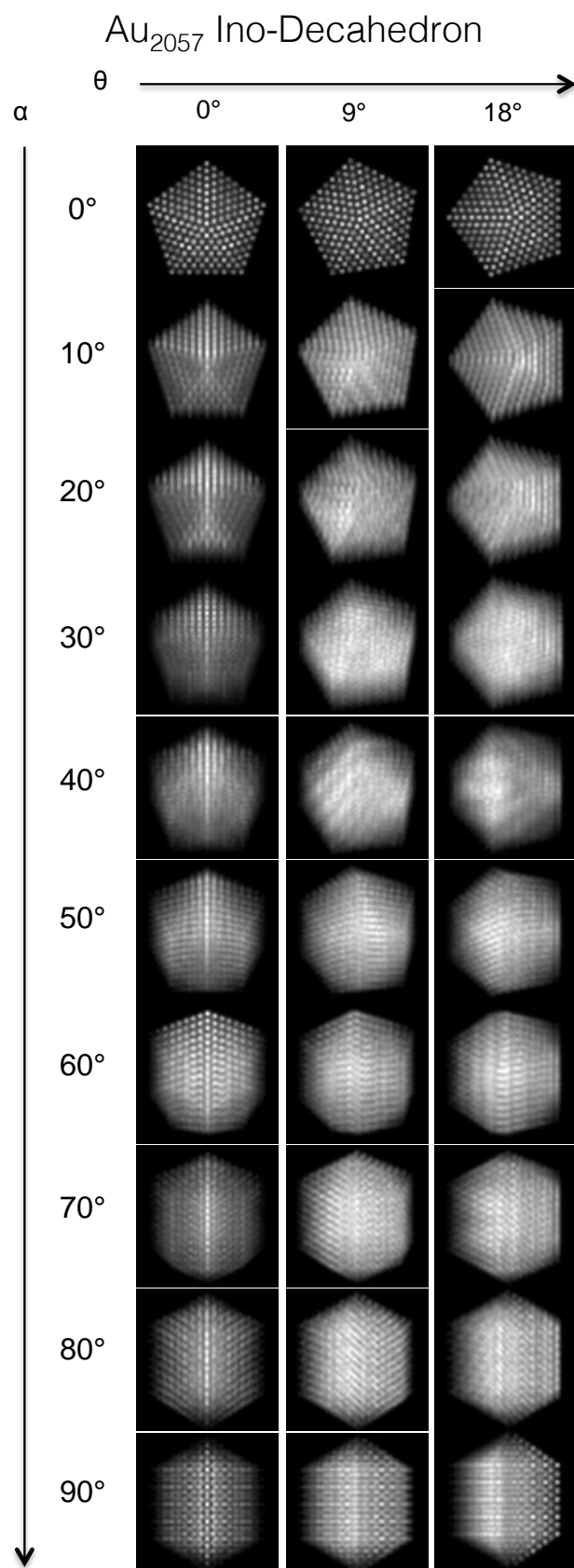
Figure 6.6: Au$_{2057}$ Ino-Decahedron
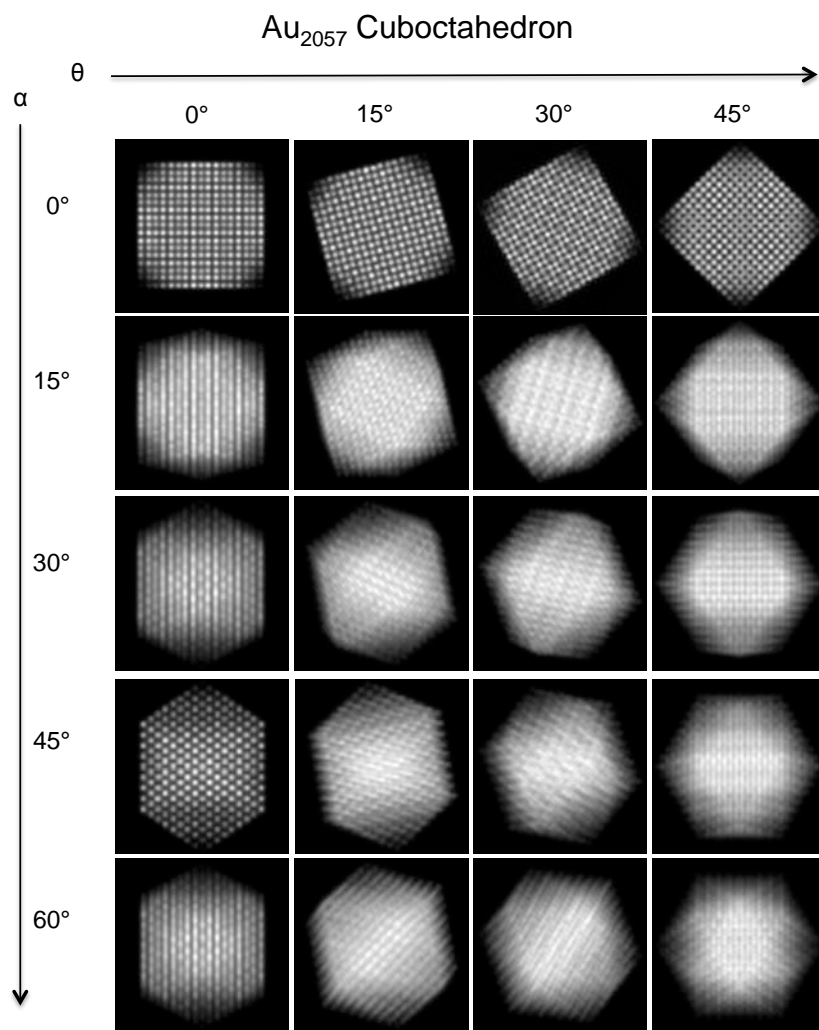
Figure 6.7: Au$_{2057}$ Cuboctahedron

Au$_{40}$(SR)$_{24}$ Cluster as a Chiral Dimer of 8-Electron Superatoms: Structure and Optical Properties

Sami Malola,[†] Lauri Lehtovaara,[†] Stefan Knoppe,[‡] Kuo-Juei Hu,[§] Richard E. Palmer,[§] Thomas Bürgi,[‡] and Hannu Häkkinen*,[†,⊥]

[†]Department of Chemistry, Nanoscience Center, University of Jyväskylä, FI-40014 Jyväskylä, Finland

[‡]Department of Physical Chemistry, University of Geneva, 1211 Geneva 4, Switzerland

[§]Nanoscale Physics Research Laboratory, School of Physics and Astronomy, University of Birmingham, Birmingham B15 2TT, U.K.

[⊥]Department of Physics, Nanoscience Center, University of Jyväskylä, FI-40014 Jyväskylä, Finland

S *Supporting Information*
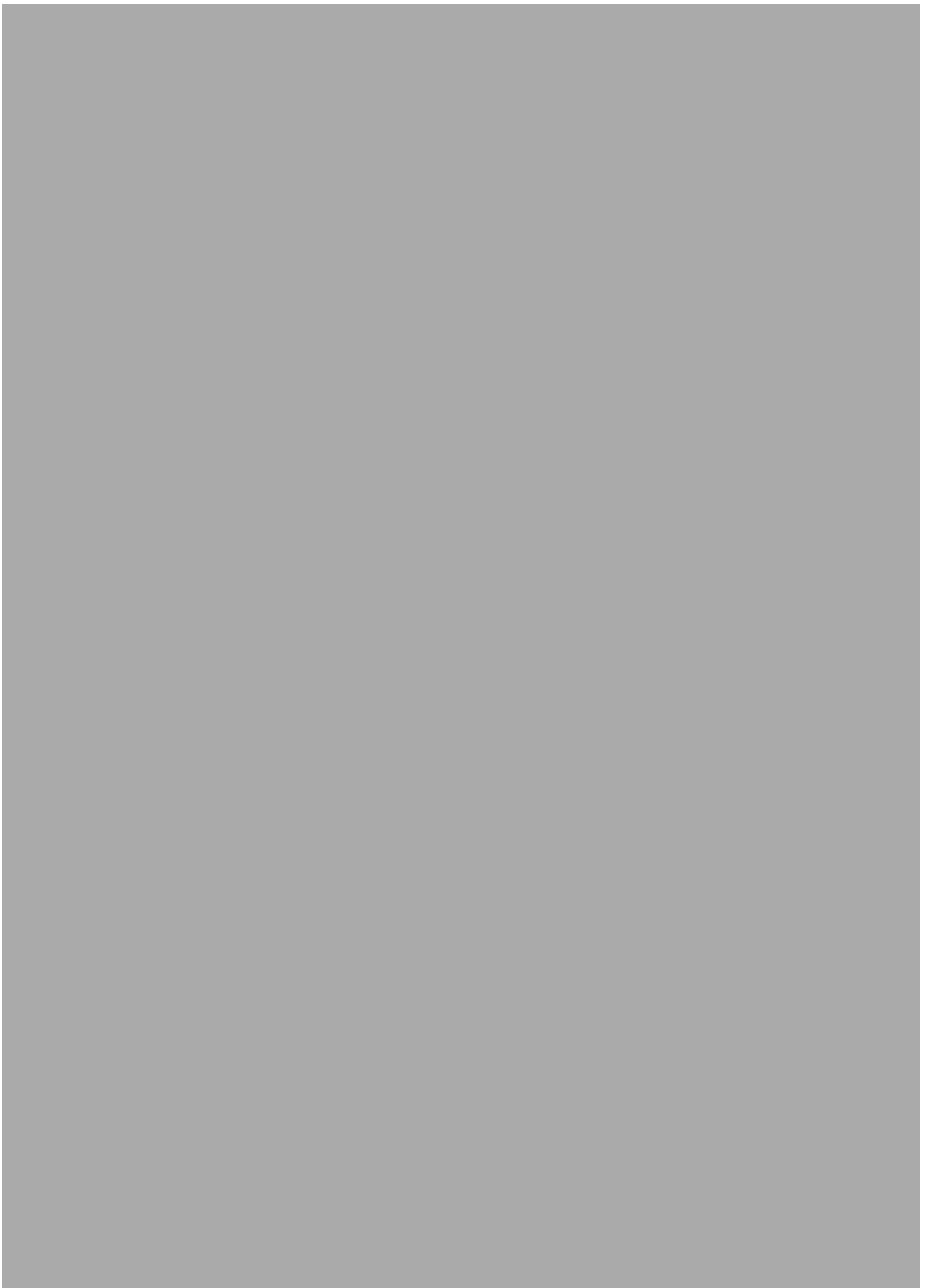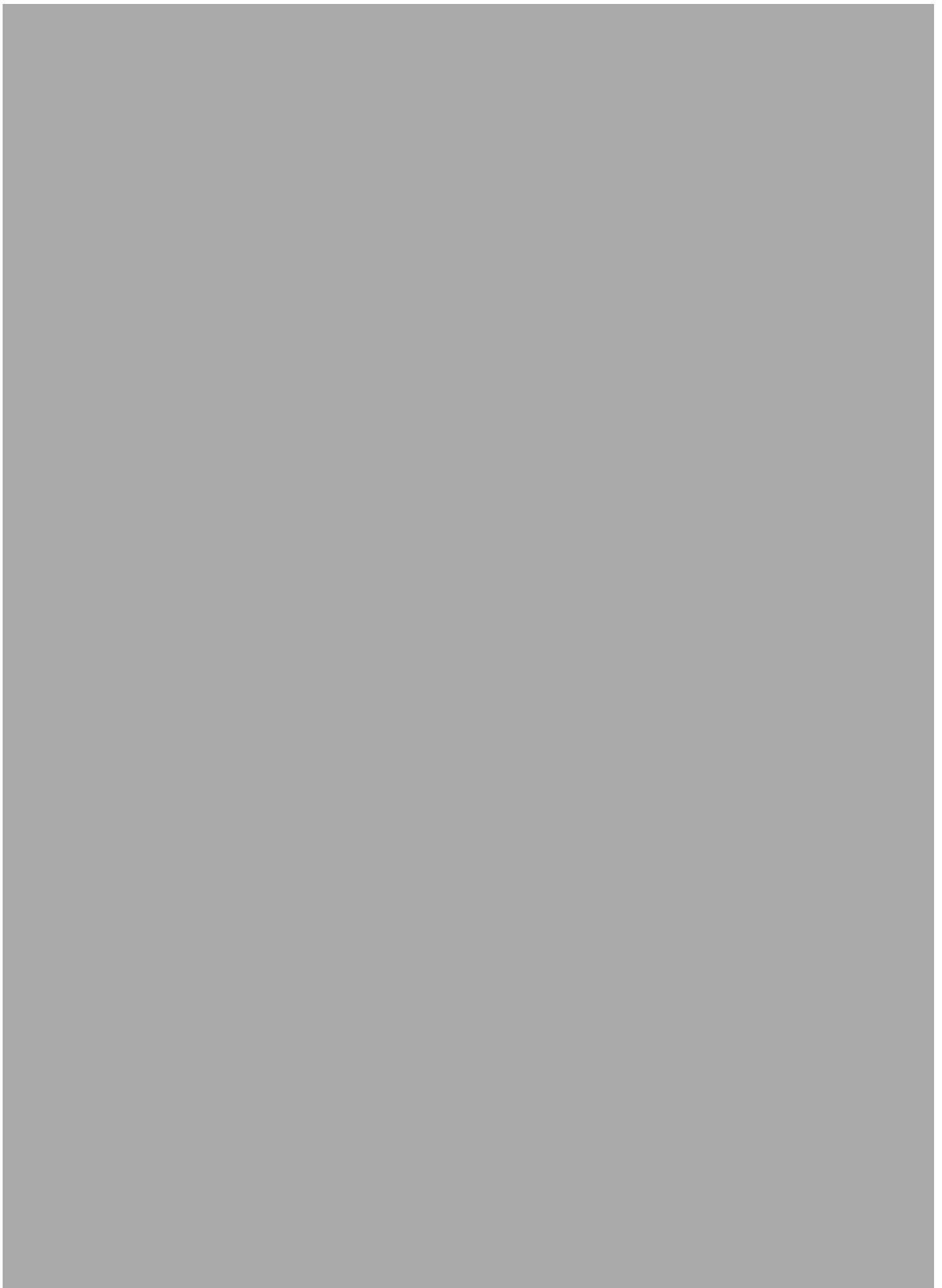
The effects of 1-pentyne hydrogenation on the atomic structures of size-selected Au$_N$ and Pd$_N$ (*N* = 923 and 2057) nanoclusters†

Kuo-Juei Hu,[a] Simon R. Plant,[a] Peter R. Ellis,[b] Christopher M. Brown,[b] Peter T. Bishop[b] and Richard E. Palmer*[a]

We report an investigation into the effects of the vapour-phase hydrogenation of 1-pentyne on the atomic structures of size-selected Au and Pd nanoclusters supported on amorphous carbon films. We use aberration-corrected high-angle annular dark field (HAADF) scanning transmission electron microscopy (STEM) to image populations of the nanoclusters at atomic resolution, both before and after the reaction, and we assign their atomic structures by comparison with multi-slice image simulations over a full range of cluster orientations. Gold nanoclusters consisting of 923 ± 20 and 2057 ± 45 atoms are found to be robust, exhibiting high structural stability. However, a significant portion of Pd$_{923\pm26}$ nanoclusters that appear amorphous prior to treatment are found to exhibit high symmetry structures post-reaction, which is interpreted as the reduction of oxidised Pd nanoclusters under the reaction conditions.

1 Introduction

It has long been established that the catalytic properties of supported metal particles vary as a function of size.[1] The use of size-selected metal nanoclusters as model catalysts[2–8] is one of the routes that has enabled catalytic activity to be accurately related to particle size. However, it is not just the size, but the full atomic structure which can regulate the performance of a catalyst, since catalytic activity can, in some cases, be correlated with specific reactive sites at the catalyst particle surface.[9] Indeed, it has been demonstrated that controlling particle shape may enable improved selectivity.[10] As a result, it is vital to gain an understanding of the effects upon the structure of such model catalysts arising from exposure to realistic reaction conditions, in order to achieve more robust catalyst design with improved performance. A number of techniques have been used to monitor nanocluster or nanoparticle catalysts subject to reaction conditions, including, for instance, *in situ* TEM,[11–13] electron tomography[14] and *in situ* STM.[15] Aberration-corrected HAADF-STEM has previously been used to identify catalytically-active Au nanoclusters on oxide supports,[16] and the catalytic

activity of size-selected Au nanoclusters on oxides is well-established.[17] For instance, amongst size-selected Au nanoclusters, Au$_{55}$ has been highlighted as a high performance catalyst with pronounced oxidation resistance.[18] HAADF-STEM imaging of size-selected Au nanoclusters on amorphous carbon has enabled the elucidation of their three-dimensional atomic structures.[19] Nanoclusters of a specific size can exhibit a range of atomic structures that differ significantly from the bulk, and multi-slice image simulations have facilitated the identification of structures from HAADF-STEM images for size-selected Au$_{20}$,[20] Au$_{55}$,[21] Au$_{309}$ (ref. 19) and Au$_{923}$,[22–24] regardless of cluster orientation on the substrate. Given the recent demonstration of atomic structure control during the formation of size-selected Au$_{923}$,[24] there is now a great potential to study the catalytic properties of such nano-clusters not only as a function of their size, but also atomic configuration, under realistic reaction conditions. Size-selected Pd$_N$ nanoclusters (*N* = 55–400) supported on graphite have already been studied under such conditions for methane oxidation[25] and 1-pentyne hydrogenation.[26] The largest nanoclusters in this size range (especially Pd$_{400}$) exhibited very high selectivity to the hydrogenation of 1-pentyne in the vapour phase, thus motivating the study of still larger nanocluster sizes.

The selective hydrogenation of alkynes is relevant to both Au[27–29] and Pd catalysts.[26,30–33] The vapour-phase 1-pentyne hydrogenation reaction over Pd supported on θ-Al$_2$O$_3$ reveals incorporation of carbon into the catalyst to provide a Pd–C phase believed to be active for selective hydrogenation,[31] and indeed, the incorporation of carbon and hydrogen into the

a Nanoscale Physics Research Laboratory, School of Physics and Astronomy, University of Birmingham, Birmingham, B15 2TT, UK.
  E-mail: R.E.Palmer@bham.ac.uk
b Johnson Matthey Technology Centre, Blounts Court Road, Sonning Common, Reading, RG4 9NH, UK.
† Electronic supplementary information (ESI) available. See DOI: 10.1039/c4cp02686a

This journal is © the Owner Societies 2014

Phys. Chem. Chem. Phys., 2014, **16**, 26631–26637 | **26631**

surface has been shown to control hydrogenation events at the surface.[32] However, Pd catalysts can also become deactivated and degraded by such processes.[34] Aging of the catalyst as a result of thermally- or chemically-driven restructuring[35–37] is important for both the catalytic activity and stability. It is therefore crucial to be able to identify changes in the structure and composition of such catalytic particles both *before* and *after* exposure to realistic reaction conditions, in order to achieve catalysts with optimised efficiency, selectivity and sustained performance.

Here, we report the atomic structures of size-selected Au and Pd nanoclusters (containing 923 and 2057 atoms) supported on amorphous carbon films, both before and after exposure to the thermal and chemical conditions for the 1-pentyne hydrogenation reaction. Observations made *ex situ* using aberration-corrected HAADF-STEM provide direct geometric information about these nanoclusters. Multi-slice HAADF-STEM image simulations are compared with experimental images to identify the atomic structures of the observed nanoclusters, over a full range of orientations on the substrate. Our results show that the Au nanoclusters of both sizes are very stable under the reaction conditions, remaining largely unchanged after pure thermal treatment and after full exposure to the chemical reaction conditions. However, a notable proportion of Pd_{923} nanoclusters, of which the vast majority (97%) appear amorphous before the reaction, are found to exhibit a face-centred cubic structure after treatment.

2 Experimental section

Gold and palladium nanoclusters were generated using a magnetron-sputtering gas-condensation cluster beam source.[38,39] A lateral time-of-flight mass filter[40] connected to the source permits accurate size selection prior to deposition of the nanoclusters in high vacuum conditions (10^{-7}–10^{-6} mbar). Based on calibration with Ar^+, the nominal mass resolutions employed were $M/\Delta M \approx 18$ and $M/\Delta M \approx 23$ for Pd and Au nanoclusters, respectively, resulting in nanoclusters that consist of 923 ± 26 and 2057 ± 57 atoms for Pd, and 923 ± 20 and 2057 ± 45 atoms for Au. The size-selected nanoclusters were deposited (at energies in the range 0.4–0.9 eV per atom) directly onto amorphous carbon films supported on molybdenum TEM grids. Following deposition, the supported Au nanoclusters were brought into air (ambient conditions) and then transferred into a vacuum desiccator for storage, both before and after imaging and treatment. Transfer of the supported Au nanoclusters from the vacuum desiccator to the microscope (in ambient conditions) was performed within ~20 minutes. The Pd nanoclusters were stored in a desiccator at ambient temperature and pressure for 100 days prior to initial imaging, and the reaction exposure was conducted within a further 10 days. Imaging was then performed 20 days after the reaction. The samples were transferred in ambient conditions for imaging and treatment. For 1-pentyne hydrogenation treatment, each of the TEM grids was transferred into a quartz tube (length 360 mm, inner diameter 4 mm) and held at the centre of the tube by means of a quartz wool plug. A flow of

pure He gas (279 ml min^{-1}) was used to provide an inert atmosphere when investigating the effects of the thermal annealing. For the hydrogenation reaction, the carrier gas consisted of 40% H_2/60% He (flow rate of 247 ml min^{-1}). In the reaction, this carrier gas was used to vaporise a reagent solution comprising 1 M 1-pentyne plus 1 M 2-methylpentane (used in such reactions as an internal standard for gas chromatography[26]) dissolved in *n*-hexane. The temperature was increased at a rate of 2 °C min^{-1} from room temperature to 250 °C and then maintained at constant temperature for 2 hours. At the end of the treatment, the carrier gas was switched to pure He, and the sample was allowed to cool for 30 minutes. Atomic resolution imaging was carried out using a JEOL 2100F STEM operating at 200 keV and equipped with a spherical aberration probe corrector (CEOS GmbH) and high-angle annular dark field (HAADF) detector. The inner and outer collection angles of the HAADF detector were 62 and 164 mrad, respectively.[41] Imaging was performed so as to avoid beam damage to the atomic structures of the nanoclusters (see ESI†). Following imaging, high symmetry nanocluster structures were identified by comparing experimental images with an atlas of multi-slice image simulations over a full range of orientations in three dimensions. Simulations of Au_{2057}, Pd_{923} and Pd_{2057} were generated using the QSTEM package.[42] The previously published simulation atlas was used in the case of Au_{923}.[22]

3 Results and discussion

The high symmetry isomers of the nanoclusters observed in this study display structural motifs that are characteristic of the icosahedron (Ih), Ino-decahedron (Dh) and face-centred cubic (FCC) polyhedron, just as for size-selected Au_{923} nanoclusters studied previously.[22–24] Fig. 1 shows typical HAADF-STEM images and corresponding multi-slice image simulations of an illustrative set of high symmetry Au_{2057} isomers. There is always a proportion of nanoclusters within a sample population that cannot be assigned uniquely to a high symmetry structure, while some nanoclusters appear to be completely amorphous, and we designate such structures as being amorphous or unidentified (A/U). In the present study, the Dh-Au_{923} and Dh-Au_{2057} nanoclusters are found to be the most abundant; recent experimental investigations of Au_{923} suggest that Dh-Au_{923} is a low energy structure in this size regime, whereas Ih-Au_{923} in particular is metastable.[22,24]

Several factors might induce changes in the structure of nanoclusters in the continuous flow vapour-phase reaction. For example, thermal annealing alone can be an important driving force in triggering the structural transformation of nanoparticles.[36,37,43] In order to de-couple any effects of (mere) elevated temperatures from the full reaction conditions, thermal annealing was first conducted on Au_{923} and Au_{2057} nanoclusters. Since recent work shows that the relative proportions of isomers within a sample population can be controlled by tuning the formation parameters for the generation of Au_{923},[24] samples were produced using identical formation conditions in the

26632 | *Phys. Chem. Chem. Phys.*, 2014, **16**, 26631–26637

This journal is © the Owner Societies 2014
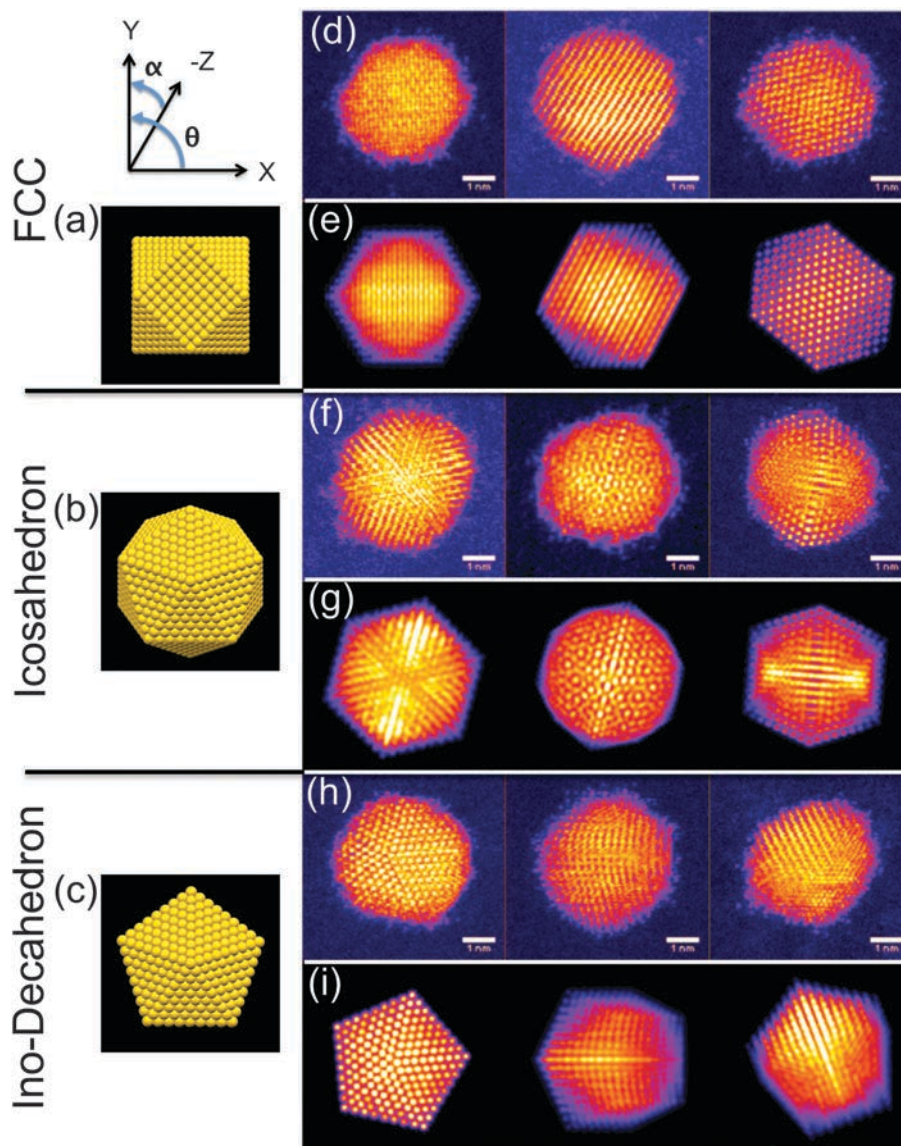
Fig. 1 Models of the atomic structures for the (a) face-centred cubic (cuboctahedron shown), (b) icosahedral, and (c) Ino-decahedral isomers of Au_{2057}, viewed at $\theta = 0°$, $\alpha = 0°$, as defined by the axes shown. Typical HAADF-STEM images of Au_{2057} nanoclusters (top) with corresponding multi-slice image simulations (below) for: (d, e) the face-centered cubic (FCC) polyhedron, (simulation orientations in row (e), from left to right, are along $\theta = 45°$, $\alpha = 45°$, and $\theta = 0°$, $\alpha = 30°$, and the 110 axis), (f, g) the icosahedron (Ih) (simulation orientations in row (g) from left to right are normal to (111) facet, along the 5-fold axis, and along the 2-fold axis), and (h, i) the Ino-decahedron (Dh) (simulation orientations in row (i) from left to right are along 5-fold axis, at $\theta = 0°$, $\alpha = 50°$, and at $\theta = 0°$, $\alpha = 30°$).

cluster beam source (parameters are detailed in the figure captions). Fig. 2 shows a comparison of the proportions of Au_{923} isomers, before and after thermal annealing at 523 K for 2 hours in different atmospheres. (The results for Au_{2057} nanoclusters are very similar to those shown in Fig. 2, and are provided in the ESI.†) Fig. 2(a) presents charts showing the combined results for all 3 samples of Au_{923} nanoclusters prior to thermal annealing. In general, the error bars shown on the bar charts are related to the Poisson error. However, the error bars shown on the bar chart in Fig. 2(a) derive from the standard error for the 3 samples. Fig. 2(b) shows the proportions of Au_{923} isomers following storage in a vacuum desiccator, where the sample has been imaged within 14 days of preparation, while Fig. 2(c) and (d) show the result of heating in a pure He

gas flow, and in a gas flow of 40% H_2/60% He, respectively. Although some slight variations in isomer distributions can be observed, there are no significant changes in the Au_{923} (or Au_{2057}) isomers as a result of subjecting them to these conditions.

The results may be explained by considering the temperatures required to induce melting in gold nanoparticles as a function of particle size. Thermal annealing in an inert atmosphere can be interpreted as a rapid process of bringing nanoclusters into a state of thermal equilibrium, where no reactants are involved. According to previous studies,[36] the Ih-to-Dh structural transformation can occur for particles in the size range from 3 nm to 14 nm without having to reach the melting point. For instance, the gap between transition temperature and melting point is predicted to be ~100 K for a Au particle size of 4 nm, based on
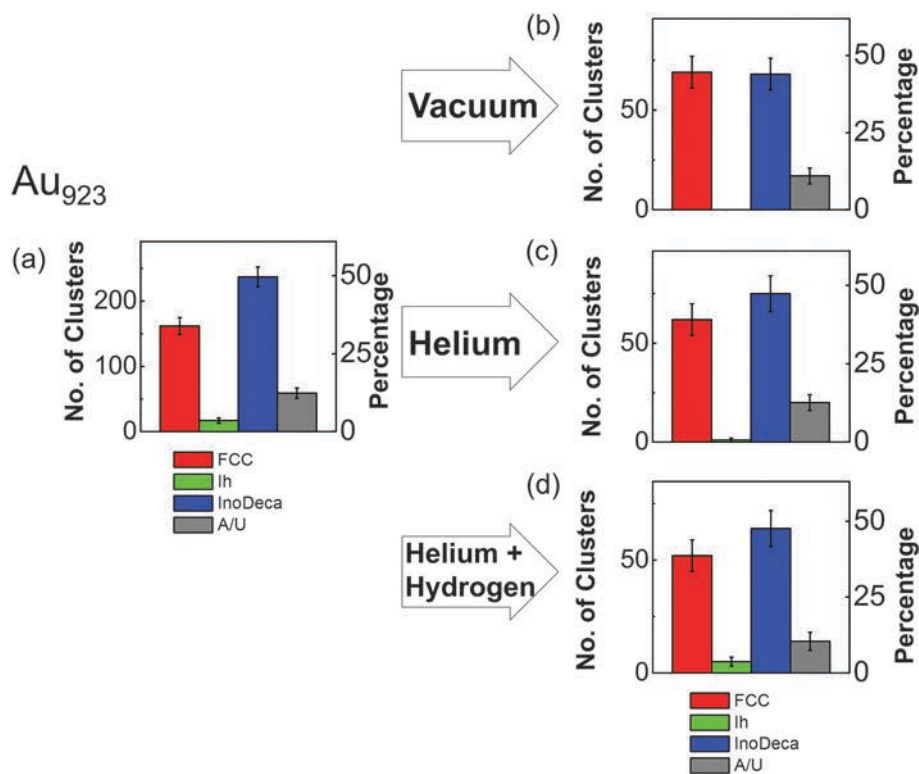
Fig. 2 Charts showing the relative proportions of Au$_{923}$ isomers (a) before thermal treatment, (b) after storage in vacuum at RT, (c) after thermal treatment under a gas flow of pure He (279 ml min^{-1}), and (d) after thermal treatment under a gas flow of 40% H$_2$ + 60% He (247 ml min^{-1}). Thermal treatment was conducted at 523 K for 2 hours (ramp rate of 2 °C min^{-1} from RT). Related cluster formation parameters: condensation length, 250 mm; magnetron sputtering power, 10 W DC; condensation pressure, 0.60 mbar; condensation gas flows, rate 200 sccm (Ar) and 150 sccm (He); deposition energy, 0.5 eV per atom.

the extrapolation from experimental data.[36] The transformation from more stable FCC or decahedral to icosahedral structures requires temperatures above the melting point, followed by rapid cooling (freezing) of the nanoparticle.[36,43] The melting point of gold nanoparticles is highly sensitive to size. Although the melting point of gold nanoparticles at ∼2.6 nm in size is close to 500 K, an increase in size to 3 (or 4) nm causes the melting point to rise to ∼750 K (or ∼900 K).[37] This is consistent with the observations presented in Fig. 2. Given that the size of Au$_{923}$ is ∼3 nm and Au$_{2057}$ ∼ 4 nm, the temperature of 523 K employed does not approach sufficiently close to the melting point of the nanoparticles to induce an Ih-to-Dh structural transition, so even the least stable nanocluster isomer can survive the treatment.

Fig. 3 shows the proportions of size-selected Au$_{923}$ and Au$_{2057}$ nanocluster isomers, both before and after exposure to the full vapour-phase 1-pentyne hydrogenation reaction conditions. As shown in Fig. 3(a) and (b), with 9% Ih, 43% Dh and 35% FCC before the reaction, Au$_{923}$ nanoclusters displayed similar stability to Au$_{2057}$: the relative proportions of Au$_{923}$ isomers after treatment are 7% Ih, 45% Dh and 35% FCC. Such variations in isomer proportions fall within the (Poissonian) error. As shown in Fig. 3(c) the proportions of as-deposited Au$_{2057}$ isomers before the reaction are 9% Ih, 54% Dh and 28% FCC. The isomer proportions were found to be almost identical post reaction (see Fig. 3(d)).

Although there is evidence for the chemisorption of 1-pentyne at the surface of bulk gold,[44] there are a limited number of

investigations on the catalysis of 1-pentyne hydrogenation using gold. However, the hydrogenation of alkynes involving oxide-supported gold nanoparticles[27,29] suggests that, although there is higher selectivity to semi-hydrogenation with Au, gold catalysts are considerably less active than Pd.[28,29] For instance, TiO$_2$-supported gold nanoclusters of average size 4.7 nm are reported to show poor adsorption of alkyne or alkene species, suggesting there may be a weaker interaction between gold and 1-pentyne (as compared with Pd).

Fig. 4 shows the variation in the proportions of Pd$_{2057}$ and Pd$_{923}$ nanocluster isomers as a result of exposure to the 1-pentyne hydrogenation reaction conditions, which were exactly the same as in the case of the Au nanoclusters. Example images of the amorphous Pd$_{923}$ and Pd$_{2057}$ nanoclusters observed are shown in Fig. 4(a) and (d), respectively. Fig. 4(b) reveals that the vast majority (97%) of Pd$_{923}$ nanoclusters initially exhibit an amorphous appearance; the only nanoclusters with an identifiable high symmetry structure (3%) are found to be Dh. After the reaction, as shown in Fig. 4(c), a large proportion (33%) of the nanoclusters could be assigned to a high symmetry structure, dominated by FCC (32%), leaving 1% as Dh. For Pd$_{2057}$, the proportion of amorphous nanoclusters pre-reaction is much lower at 37%, and almost a majority of the nanoclusters are FCC structures (see Fig. 4(e)). Both before and after reaction (Fig. 4(e) and (f)), more than three-quarters of the identified high symmetry isomers are assigned to be FCC.
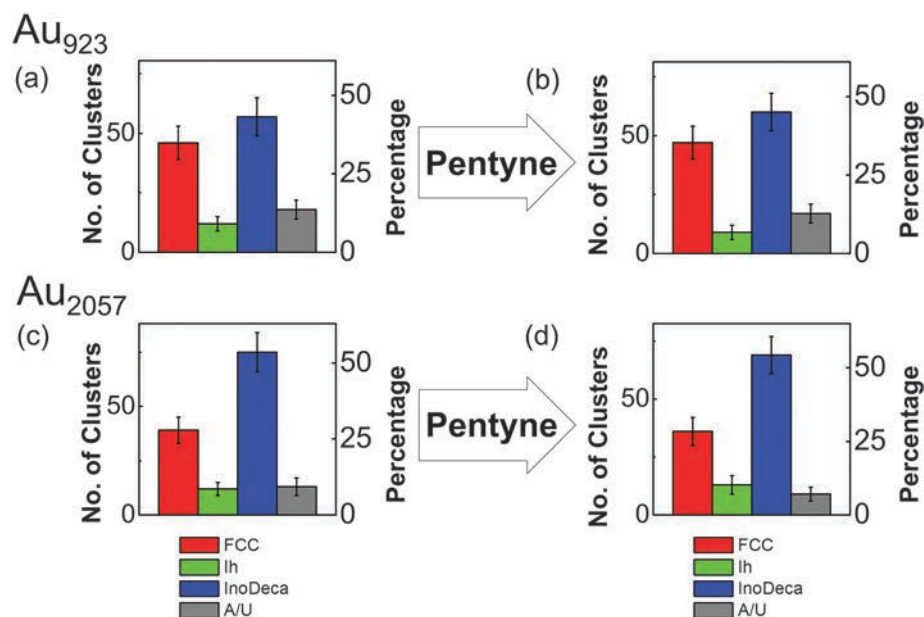
26634 | Phys. Chem. Chem. Phys., 2014, 16, 26631–26637

This journal is © the Owner Societies 2014

Fig. 3 (a, b) Charts showing the relative proportions of Au_{923} isomers (a) before and (b) after exposure to the reaction conditions for vapour-phase 1-pentyne hydrogenation. (c, d) Charts showing the relative proportions of Au_{2057} isomers (c) before and (d) after exposure to the same conditions. The reaction was conducted at 523 K for 2 hours (ramp rate of 2 °C min^{-1} from RT) with 1 M 1-pentyne in hexane vaporised by a carrier gas of 40% H_2 and 60% He (flow rate 247 ml min^{-1}). The cluster formation parameters were: condensation length, 250 mm; magnetron sputtering power, 10 W DC; condensation pressure, 0.60 mbar (Au_{923}) and 0.67 mbar (Au_{2057}); condensation gas flows, 200 sccm (Ar) and 150 sccm (He); deposition energy, 0.5 eV per atom.
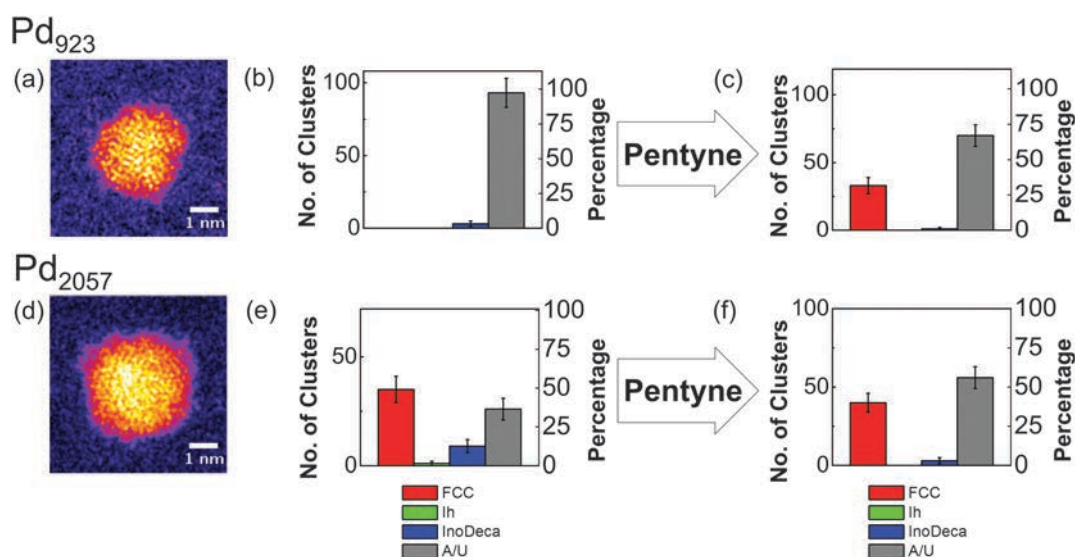
Fig. 4 (a, d) Example HAADF-STEM images of amorphous nanoclusters for (a) Pd_{923} and (d) Pd_{2057}, imaged prior to treatment. (b, c) Charts showing the relative proportions of Pd_{923} isomers (b) before and (c) after vapour-phase 1-pentyne hydrogenation treatment. (e, f) Charts showing the relative proportions of Pd_{2057} isomers both (e) before and (f) after the same treatment. The conditions for the treatments were identical to those for the Au nanoclusters shown in Fig. 3. Related cluster formation parameters: condensation length, 172 mm; magnetron sputtering power, 10 W DC; condensation pressure, 0.18 mbar (Pd_{923}) and 0.28 mbar (Pd_{2057}); condensation gas flows, 100 sccm (Ar) and 110 sccm (He); deposition energy, 0.9 eV per atom (Pd_{923}) and 0.4 eV per atom (Pd_{2057}).

Pd is known to oxidise spontaneously upon contact with oxygen,[31,45–47] but the oxidation depth on Pd single crystals is temperature dependent.[48] On the Pd(111) surface, PdO first forms as an amorphous layer, gradually increasing in crystallinity at elevated temperatures. When the temperature reaches 500 K, amorphous PdO layers coalescence to form a PdO(101) ad-layer with a thickness of 3.5 ML at saturation.[45,49] Oxygen can become incorporated into Pd nanoparticles in a number of ways, both at the surface and beneath, or through the formation of oxide shells.[50,51] For (oxide-supported) Pd nanoparticles with diameters of <5 nm, both oxidation and reduction by oxygen and hydrogen, respectively, proceed readily at room temperature.[52] For ZrO_2-supported PdO

Paper

nanoclusters with average size of 28 nm, shell-by-shell reduction in hydrogen has been observed and the clusters can be restored to Pd without fragmenting.[45] In the present case, the amorphous appearance of large proportions of both Pd_{2057} and, in particular, Pd_{923} nanoclusters, prior to the reaction, may therefore be attributable to surface oxidation in air, especially given storage conditions prior to imaging (desiccator, ambient temperature and pressure, 100 days). We note, however, that only 37% of Pd_{2057} nanoclusters observed before exposure to the reaction conditions appear to be amorphous, compared to 97% for Pd_{923} stored under identical conditions, which suggests that the Pd_{2057} nanoclusters exhibit a marked oxidation resistance as compared to Pd_{923}, a phenomenon that can be explored further in future work. It is possible that oxidised Pd nanoclusters can undergo reduction when exposed to the conditions of the 1-pentyne hydrogenation reaction, removing the oxide layer, and permitting the observation of (structural) motifs corresponding to high symmetry, ordered atomic structures in post-reaction HAADF-STEM imaging. As all Pd nanoclusters were stored under the same conditions both before and after the reaction, it implies that both Pd_{923} and Pd_{2057} nanoclusters are exhibiting a degree of oxidation resistance at room temperature and pressure post-reaction, at least for the high symmetry structural motifs observed. In particular, we note significant proportions of FCC structures for Pd_{2057} both before (49%) and after (40%) the reaction, as well as the emergence of FCC structures for Pd_{923} post-reaction. Indeed, the previous study of 1-pentyne hydrogenation with size-selected Pd nanoclusters suggested that there was no obvious change in the FCC-like structure of Pd_{400} following the reaction, although a full statistical analysis was not carried out. With regard to the present study, further investigation would be required to investigate fully the mechanisms involved and to verify whether the perceived oxidation resistance of the reduced Pd nanoclusters (post-reaction) arises due to changes to the intrinsic structure (to FCC), or results from deposits (due to surface adsorption) or carbonization (catalyst coking).

The ability to produce oxidised and oxidation-resistant Pd catalysts selectively may be advantageous,[53] particularly as there is some debate as to whether Pd or PdO is the more active catalyst. An example concerns the comparative activities of alumina-supported palladium for the combustion of methane,[54–56] for which early reports are conflicting. It is generally believed that methane oxidation proceeds rapidly through the chemisorption of oxygen onto PdO for alumina-supported Pd catalyst at atmospheric pressure.[56] Such chemisorption would cease on the Pd catalyst surface above 650 °C, which is the decomposition temperature of PdO, and hence the catalysed methane combustion stops.[55,56] Furthermore, in a more recent study conducted on a polycrystalline Pd plate in an ultrahigh vacuum system, the reaction rate of methane production drops drastically when the system goes beyond the decomposition temperature of PdO.[57]

4 Conclusions

We have reported an investigation into the effects of the 1-pentyne hydrogenation reaction, under realistic conditions, on the atomic structures of size-selected Au nanoclusters containing 923 ± 20 and 2057 ± 45 atoms, as well as Pd nanoclusters containing 923 ± 26 and 2057 ± 57 atoms. We find that both Au_{923} and Au_{2057} nanoclusters exhibit marked structural stability. The large majority of Pd_{923} nanoclusters were found to be amorphous in appearance before reaction, which may be attributable to surface oxidation. However, following exposure to the same reaction conditions, a significant proportion is found to exhibit high symmetry FCC structures, which may result from the reduction of the nanoclusters in hydrogen. Moreover, given the identical storage conditions before and after reaction, the observation of such structures implies a greater oxidation resistance post-reaction. We suggest that enhanced oxidation resistance may arise as a result of intrinsic structural changes or through protection of the surface due to carbonisation or surface absorption, but the exact origin would be the subject of further investigation. Au_{2057} nanoclusters, prepared under similar formation conditions to Au_{923}, are found to consist of a large proportion of FCC-like structures, both before and after the reaction, similar to Pd_{400} previously studied.

Acknowledgements

References

1 M. Che and C. O. Bennett, *Adv. Catal.*, 1989, **36**, 55–172.
2 S. Vajda, M. J. Pellin, J. P. Greeley, C. L. Marshall, L. A. Curtiss, G. A. Ballentine, J. W. Elam, S. Catillon-Mucherie, P. C. Redfern, F. Mehmood and P. Zapol, *Nat. Mater.*, 2009, **8**, 213–216.
3 S. Lee, L. M. Molina, M. J. López, J. A. Alonso, B. Hammer, B. Lee, S. Seifert, R. E. Winans, J. W. Elam, M. J. Pellin and S. Vajda, *Angew. Chem., Int. Ed.*, 2009, **48**, 1467–1471.
4 Y. Le, F. Mehmood, S. Lee, J. Greeley, B. Lee, S. Seifert, R. E. Winansl, W. Elám, R. J. Meyer, P. C. Redfern, D. Teschner, R. l. Schlögl, M. J. Pellin, L. A. Curtiss and S. Vajda, *Science*, 2010, **328**, 224–228.
5 C. Harding, V. Habibpour, S. Kunz, A. N.-S. Farnbacher, U. Heiz, B. Yoon and U. Landman, *J. Am. Chem. Soc.*, 2009, **131**, 538–548.
6 S. Kunz, K. Hartl, M. Nesselberger, F. F. Schweinberger, G. Kwon, M. Hanzlik, K. J. J. Mayrhofer, U. Heiz and M. Arenz, *Phys. Chem. Chem. Phys.*, 2010, **12**, 10288–10291.
7 G. Sitja, S. L. Moal, M. Marsault, G. Hamm, F. Leroy and C. R. Henry, *Nano Lett.*, 2013, **13**, 1977–1982.
8 F. J. Perez-Alonso, D. N. McCarthy, A. Nierhoff, P. Hernandez-Fernandez, C. Strebel, I. E. L. Stephens, J. H. Nielsen and I. Chorkendorff, *Angew. Chem., Int. Ed.*, 2012, **51**, 4641–4643.

26636 | *Phys. Chem. Chem. Phys.*, 2014, **16**, 26631–26637

This journal is © the Owner Societies 2014

9 H. Falsig, B. Hvolbæk, I. S. Kristensen, T. Jiang, T. Bligaard, C. H. Christensen and J. K. Nørskov, *Angew. Chem.*, 2008, **120**, 4913–4917.

10 I. Lee, F. Delbecq, R. Morales, M. A. Albiter and F. Zaera, *Nat. Mater.*, 2009, **8**, 132–138.

11 S. B. Simonsen, I. Chorkendorff, S. Dahl, M. Skoglundh, J. Sehested and S. Helveg, *J. Am. Chem. Soc.*, 2010, **132**, 7968–7975.

12 S. R. Challa, A. T. Delariva, T. W. Hansen, S. Helveg, J. Sehested, P. L. Hansen, F. Garzon and A. K. Datye, *J. Am. Chem. Soc.*, 2011, **133**, 20672–20675.

13 T. Uchiyama, H. Yoshida, Y. Kuwauchi, S. Ichikawa, S. Shimada, M. Haruta and S. Takeda, *Angew. Chem., Int. Ed.*, 2011, **50**, 10157–10160.

14 G. Prieto, J. Zečević, H. Friedrich, K. P. De Jong and P. E. De Jongh, *Nat. Mater.*, 2013, **12**, 34–39.

15 F. Yang, M. S. Chen and D. W. Goodman, *J. Phys. Chem. C*, 2009, **113**, 254–260.

16 A. A. Herzing, C. J. Kiely, A. F. Carley, P. Landon and G. J. Hutchings, *Science*, 2008, **321**, 1331–1335.

17 A. Sanchez, S. Abbet, U. Heiz, W. D. Schneider, H. Hakkinen, R. N. Barnett and U. Landman, *J. Phys. Chem. A*, 1999, **103**, 9573–9578.

18 H.-G. Boyen, G. Kastle, F. Weigl, B. Koslowski, C. Dietrich, P. Ziemann, J. P. Spatz, S. Riethmuller, C. Hartmann, M. Moller, G. Schmid, M. G. Garnier and P. Oelhafen, *Science*, 2002, **297**, 1533–1536.

19 Z. Y. Li, N. P. Young, M. Di Vece, S. Palomba, R. E. Palmer, A. L. Bleloch, B. C. Curley, R. L. Johnston, J. Jiang and J. Yuan, *Nature*, 2008, **451**, 46–48.

20 Z. W. Wang and R. E. Palmer, *Nanoscale*, 2012, **4**, 4947–4949.

21 Z. W. Wang and R. E. Palmer, *Nano Lett.*, 2012, **12**, 5510–5514.

22 Z. W. Wang and R. E. Palmer, *Phys. Rev. Lett.*, 2012, **108**, 245502.

23 S. R. Plant, L. Cao, F. Yin, Z. W. Wang and R. E. Palmer, *Nanoscale*, 2014, **6**, 1258–1263.

24 S. R. Plant, L. Cao and R. E. Palmer, *J. Am. Chem. Soc.*, 2014, **136**, 7559–7562.

25 F. Yin, S. Lee, A. Abdela, S. Vajda and R. E. Palmer, *J. Chem. Phys.*, 2011, **134**, 141101.

26 V. Habibpour, M. Y. Song, Z. W. Wang, J. Cookson, C. M. Brown, P. T. Bishop and R. E. Palmer, *J. Phys. Chem. C*, 2012, **116**, 26295–26299.

27 J. A. Lopez-Sanchez and D. Lennon, *Appl. Catal., A*, 2005, **291**, 230–237.

28 L. McEwan, M. Julius, S. Roberts and J. C. Q. Fletcher, *Gold Bull.*, 2010, **43**, 298–306.

29 Y. Segura, N. Lopez and J. Perezramirez, *J. Catal.*, 2007, **247**, 383–386.

30 M. W. Tew, M. Nachtegaal, M. Janousch, T. Huthwelker and J. A. van Bokhoven, *Phys. Chem. Chem. Phys.*, 2012, **14**, 5761–5768.

31 D. Teschner, E. Vass, M. Hävecker, S. Zafeiratos, P. Schnörch, H. Sauer, A. Knop-Gericke, R. Schlögl, M. Chamam, A. Wootsch, A. S. Canning, J. J. Gamman,

S. D. Jackson, J. McGregor and L. F. Gladden, *J. Catal.*, 2006, **242**, 26–37.

32 D. Teschner, J. Borsodi, A. Wootsch, Z. Révay, M. Hävecker, A. Knop-Gericke, S. D. Jackson and R. Schlögl, *Science*, 2008, **320**, 86–89.

33 M. W. Tew, H. Emerich and J. A. van Bokhoven, *J. Phys. Chem. C*, 2011, **115**, 8457–8465.

34 P. Albers, J. Pietsch and S. F. Parker, *J. Mol. Catal. A: Chem.*, 2001, **173**, 275–286.

35 Y. Li, H. Cheng, T. Yao, Z. Sun, W. Yan, Y. Jiang, Y. Xie, Y. Sun, Y. Huang, S. Liu, J. Zhang, Y. Xie, T. Hu, L. Yang, Z. Wu and S. Wei, *J. Am. Chem. Soc.*, 2012, **134**, 17997–18003.

36 K. Koga, T. Ikeshoji and K. Sugawara, *Phys. Rev. Lett.*, 2004, **92**, 2–5.

37 P. Buffat and J. P. Borel, *Phys. Rev. A: At., Mol., Opt. Phys.*, 1976, **13**, 2287.

38 I. M. Goldby, B. von Issendorff, L. Kuipers and R. E. Palmer, *Rev. Sci. Instrum.*, 1997, **68**, 3327–3334.

39 S. Pratontep, S. J. Carroll, C. Xirouchaki, M. Streun and R. E. Palmer, *Rev. Sci. Instrum.*, 2005, **76**, 045103.

40 B. von Issendorff and R. E. Palmer, *Rev. Sci. Instrum.*, 1999, **70**, 4497–4501.

41 Z. W. Wang, O. Toikkanen, B. M. Quinn and R. E. Palmer, *Small*, 2011, **7**, 1542–1545.

42 C. Koch, PhD thesis, Arizona Sate University, 2002.

43 C. Cleveland, W. Luedtke and U. Landman, *Phys. Rev. B: Condens. Matter Mater. Phys.*, 1999, **60**, 5065–5077.

44 H. Feilchenfeld and M. J. Weaver, *J. Phys. Chem.*, 1989, **93**, 4276–4282.

45 S. C. Su, J. N. Carstens and A. T. Bell, *J. Catal.*, 1998, **176**, 125–135.

46 E. Voogt, A. J. M. Mens, O. L. J. Gijzeman and J. W. Geus, *Catal. Today*, 1999, **47**, 321–323.

47 D. Zemlyanov, B. Klötzer and H. Gabasch, *Top. Catal.*, 2013, **56**, 885–895.

48 X. Guo, A. Hoffman and J. T. Yates, *J. Chem. Phys.*, 1989, **90**, 5787.

49 H. H. Kan and J. F. Weaver, *Surf. Sci.*, 2009, **603**, 2671–2682.

50 T. Schalow, B. Brandt, D. Starr, M. Laurin, S. Shaikhutdinov, S. Schauermann, J. Libuda and H.-J. Freund, *Angew. Chem., Int. Ed.*, 2006, **45**, 3693–3697.

51 I. Meusel, J. Hoffmann, J. Hartmann, M. Heemeier, M. Bäumer, J. Libuda and H.-J. Freund, *Catal. Lett.*, 2001, **71**, 5–13.

52 A. Baylet, P. Marécot, D. Duprez, P. Castellazzi, G. Groppi and P. Forzatti, *Phys. Chem. Chem. Phys.*, 2011, **13**, 4607–4613.

53 S. M. Lang, I. Fleischer, T. M. Bernhardt, R. N. Barnett and U. Landman, *J. Am. Chem. Soc.*, 2012, **134**, 20654–20659.

54 M. Lyubovsky and L. Pfefferle, *Catal. Today*, 1999, **47**, 29–44.

55 R. Burch and F. J. Urbano, *Appl. Catal., A*, 1995, **124**, 121–138.

56 R. J. Farrauto, M. C. Hobson, T. Kennelly and E. M. Waterman, *Appl. Catal., A*, 1992, **81**, 227–237.

57 G. Zhu, J. Han, D. Y. Zemlyanov and F. H. Ribeiro, *J. Phys. Chem. B*, 2005, **109**, 2331–2337.

Atomic Resolution Observation of a Size-Dependent Change in the Ripening Modes of Mass-Selected Au Nanoclusters Involved in CO Oxidation

Kuo-Juei Hu,[†] Simon R. Plant,[†] Peter R. Ellis,[‡] Christopher M. Brown,[‡] Peter T. Bishop,[‡] and Richard E. Palmer*,[†]

[†]Nanoscale Physics Research Laboratory, School of Physics and Astronomy, University of Birmingham, Birmingham, B15 2TT, U.K.
[‡]Johnson Matthey Technology Centre, Blounts Court Road, Sonning Common, Reading, RG4 9NH, U.K.

Ⓢ *Supporting Information*
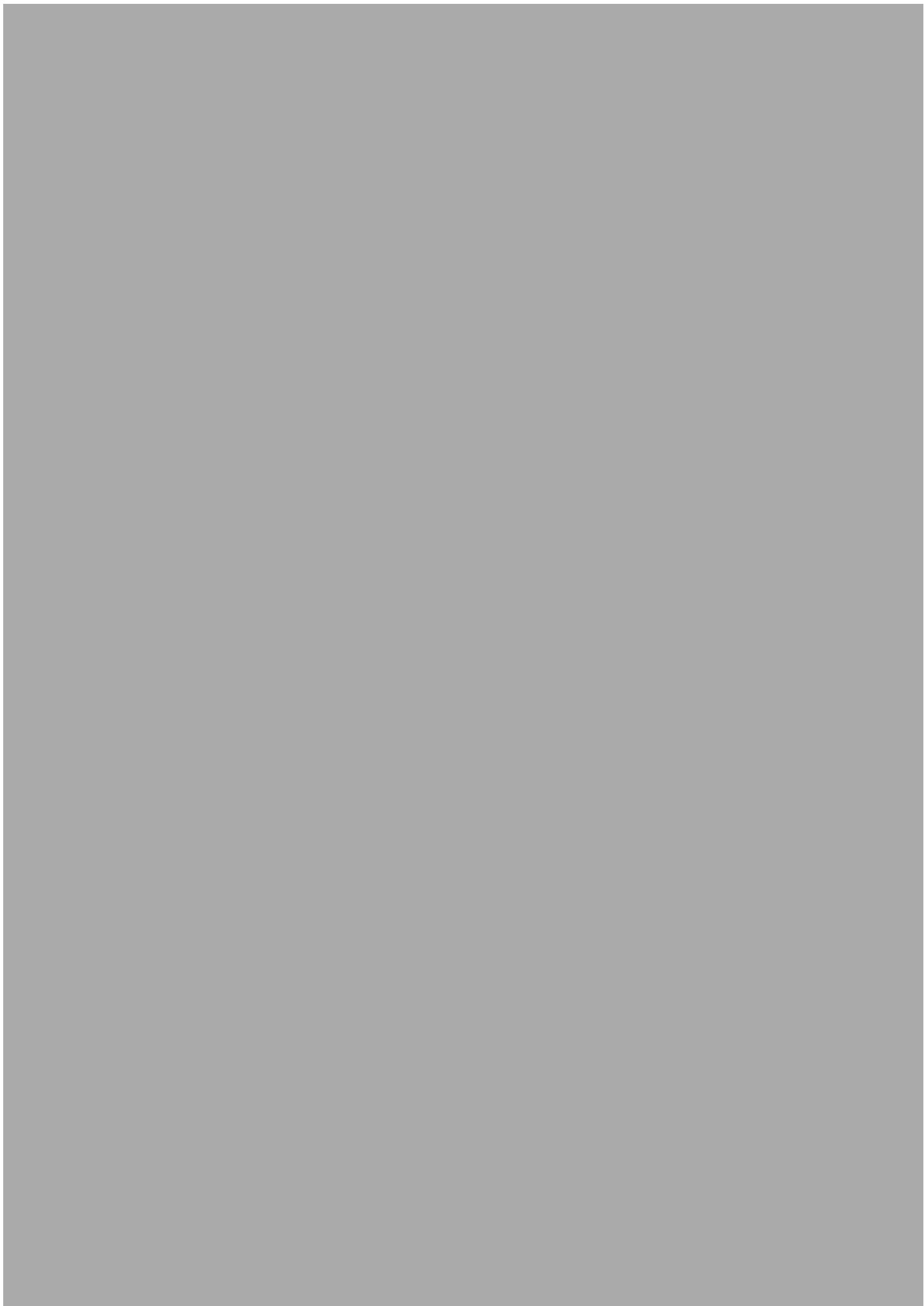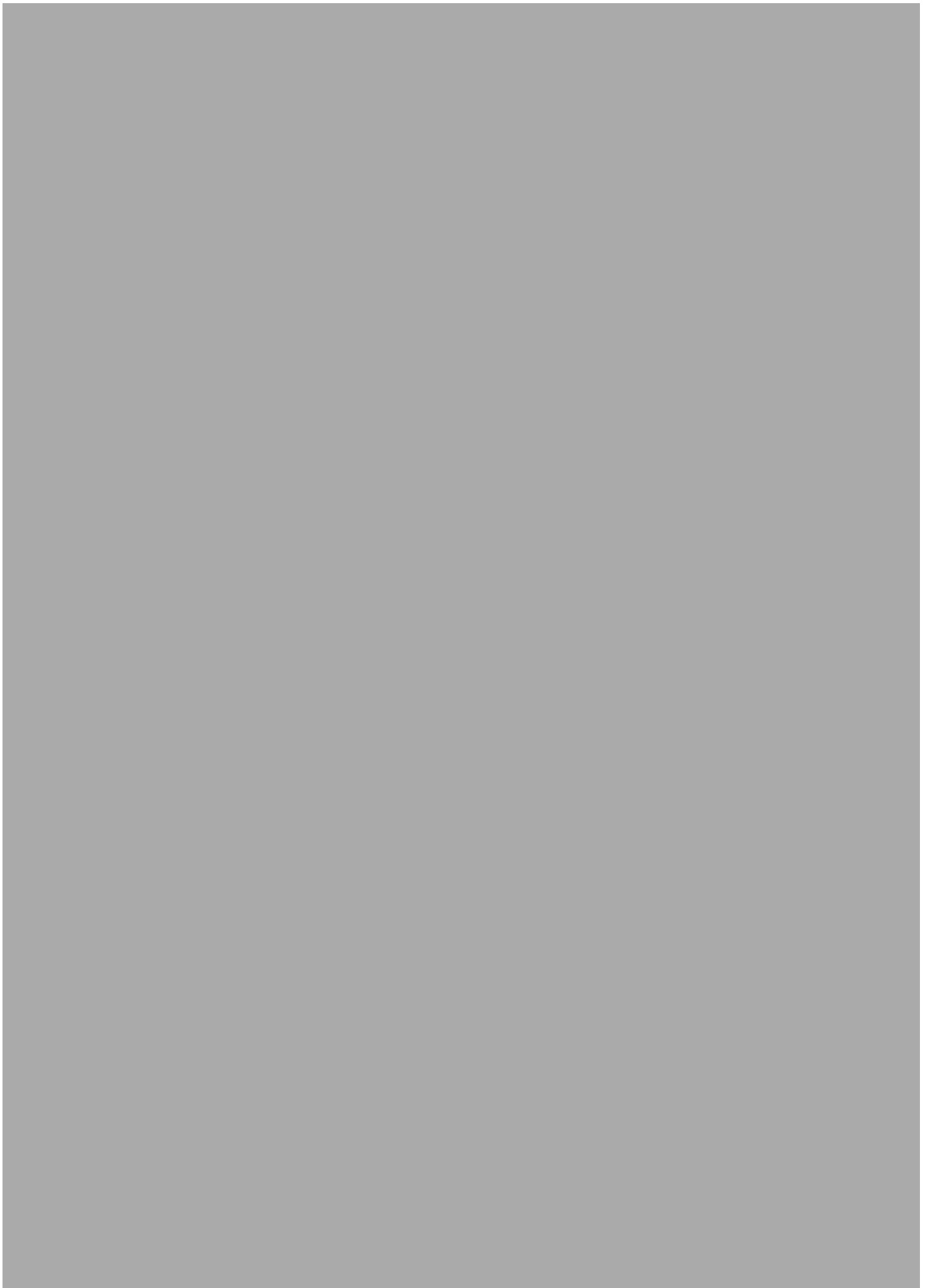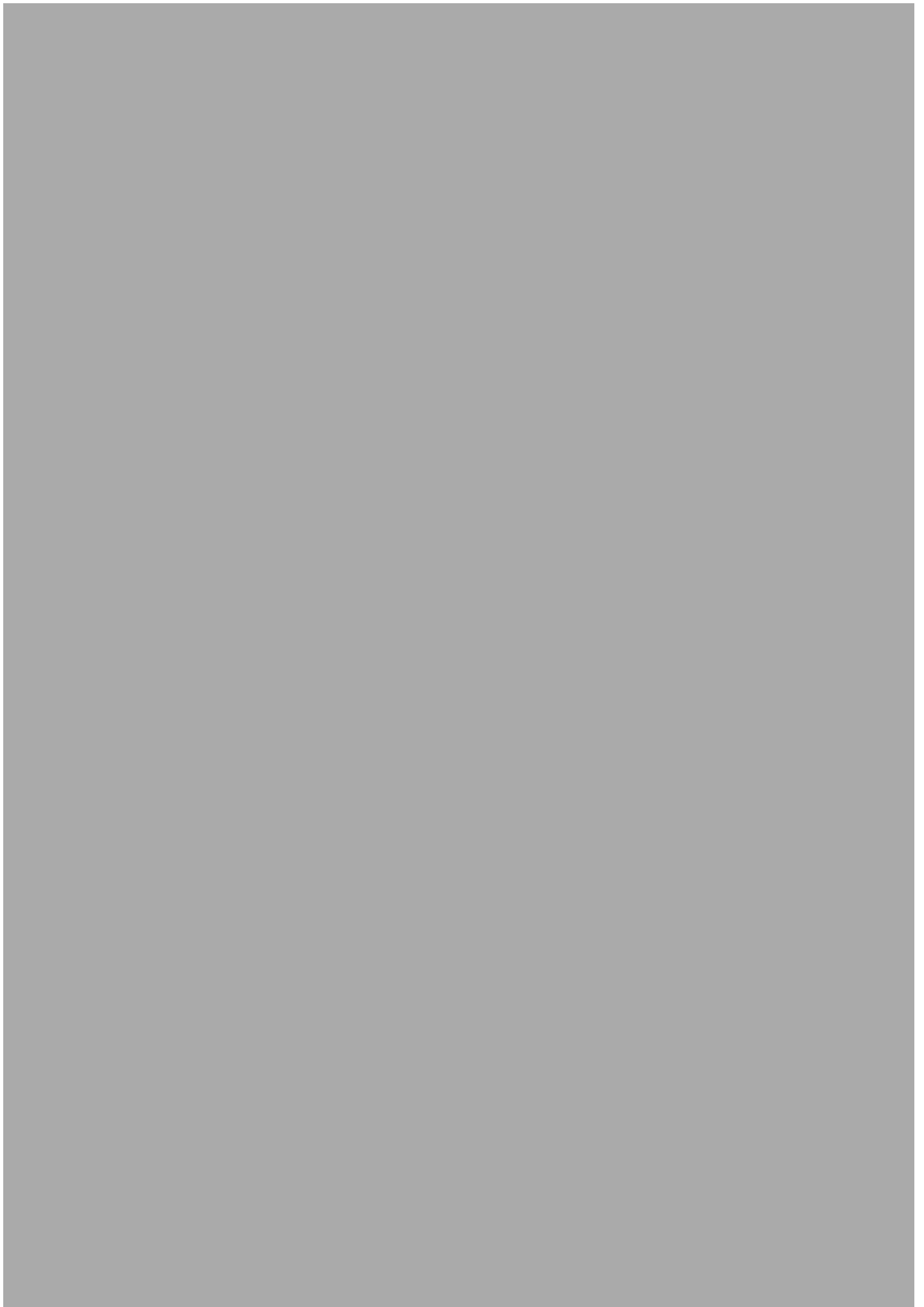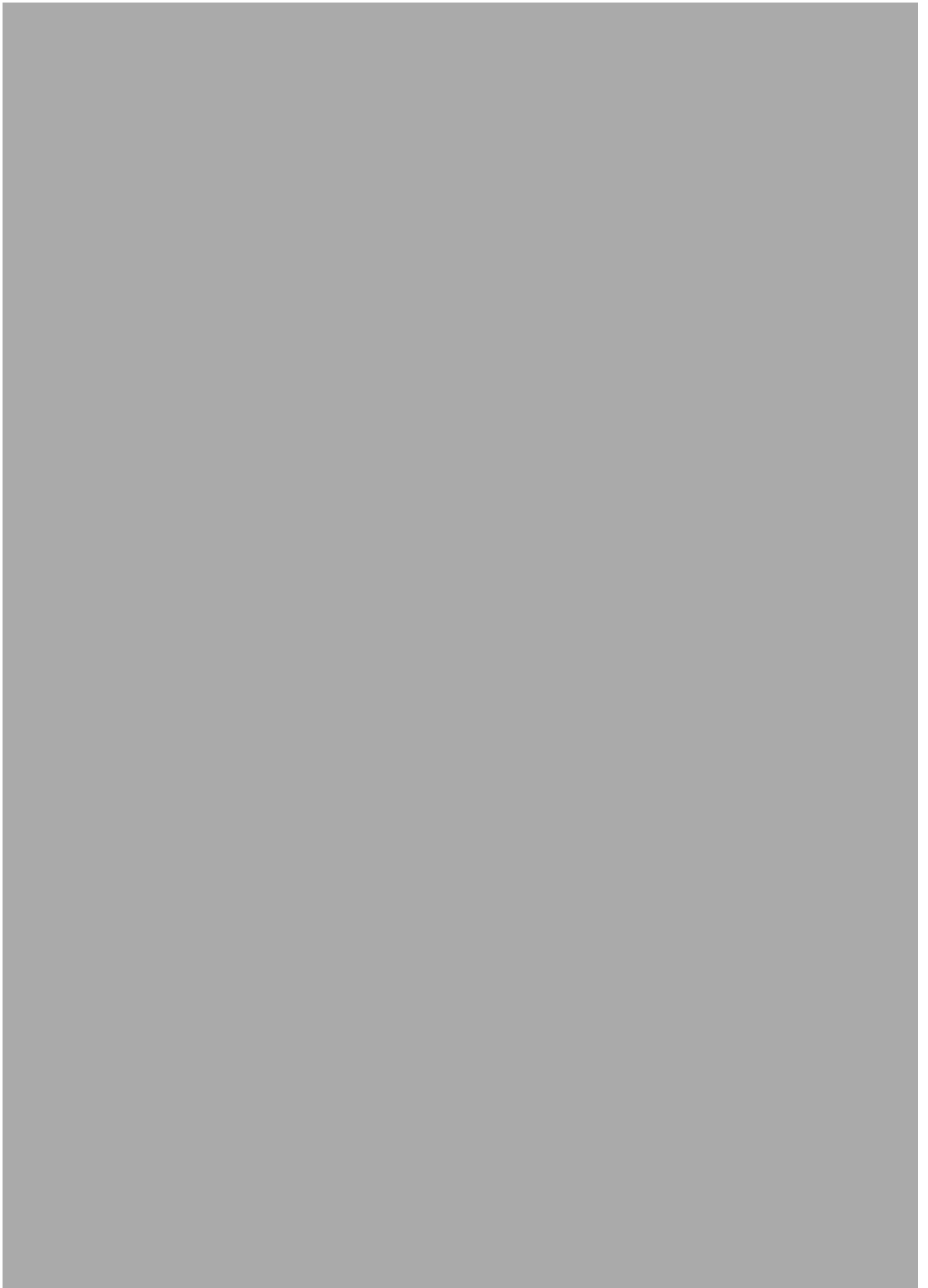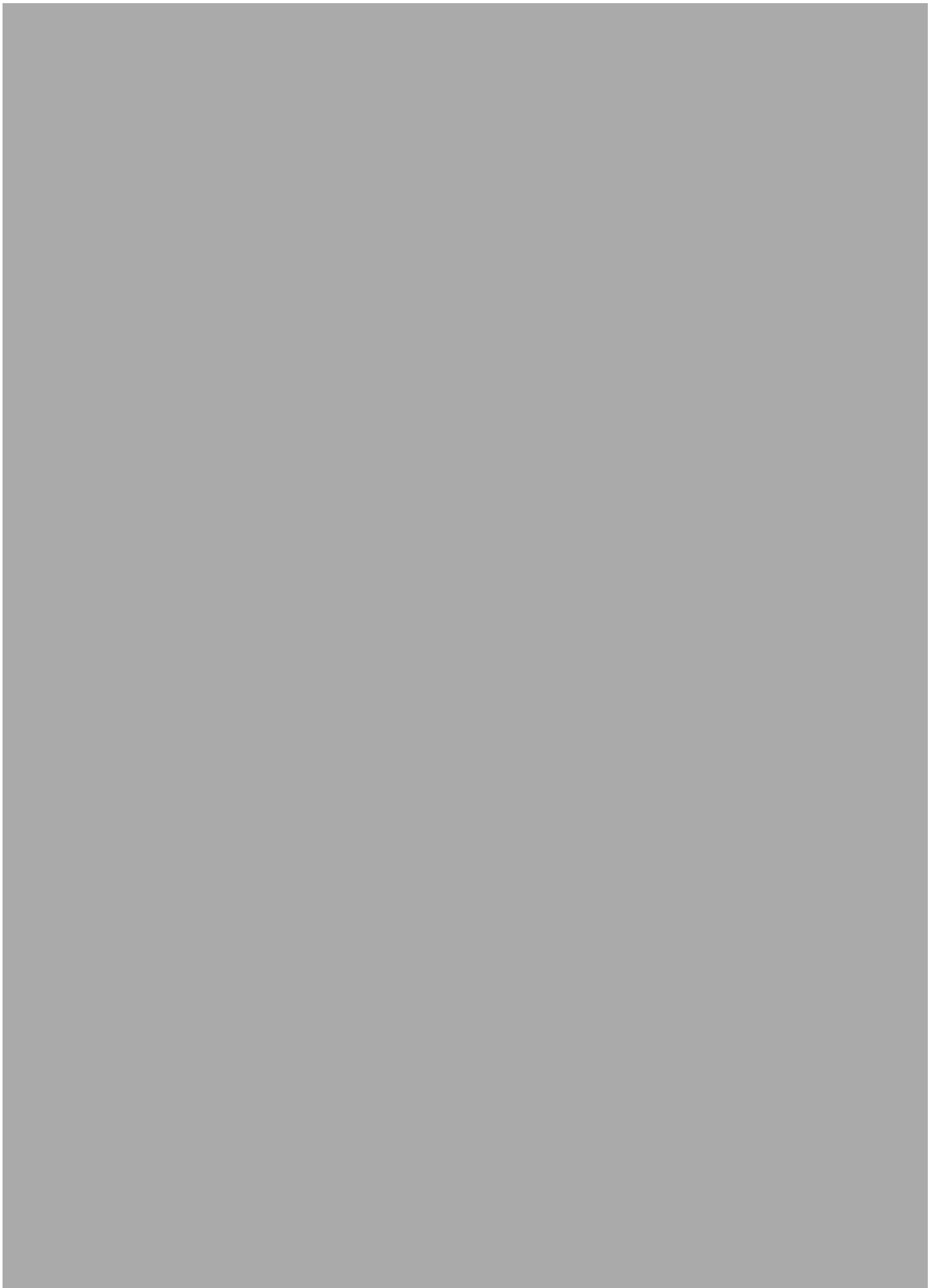
LIST OF REFERENCES

[1] W. de Heer. *The physics of simple metal clusters: experimental aspects and simple models. Rev. Mod. Phys.* 65(3):611, 1993. doi:10.1103/RevModPhys.65.611.

[2] W. D. Knight, K. Clemenger, W. a. De Heer, W. a. Saunders, M. Y. Chou, and M. L. Cohen. *Electronic shell structure and abundances of sodium clusters. Phys. Rev. Lett.* 52(24):2141, 1984. doi:10.1103/PhysRevLett.52.2141.

[3] I. Katakuse, T. Ichihara, Y. Fujita, T. Matsuo, T. Sakurai, and H. Matsuda. *Mass distributions of copper, silver and gold clusters and electronic shell structure. Int. J. Mass Spectrom. Ion Process.* 67(2):229, 1985. doi:10.1016/0168-1176(85)80021-5.

[4] W. Knight, W. a. De Heer, W. a. Saunders, K. Clemenger, M. Chou, and M. L. Cohen. *Alkali metal clusters and the jellium model. Chem. Phys. Lett.* 134(1):1, 1987. doi:10.1016/0009-2614(87)80002-7.

[5] J. L. Martins, R. Car, and J. Buttet. *Variational spherical model of small metallic particles. Surf. Sci.* 106(13):265, 1981. doi:http://dx.doi.org/10.1016/0039-6028(81)90210-7.

[6] M. Y. Chou, A. Cleland, and M. L. Cohen. *Total energies, abundances, and electronic shell structure of lithium, sodium, and potassium clusters. Solid State Commun.* 52(7):645, 1984. doi:10.1016/0038-1098(84)90725-7.

[7] W. Ekardt. *Dynamical polarizability of small metal particles: Self-consistent spherical jellium background model. Phys. Rev. Lett.* 52(21):1925, 1984.

[8] W. Ekardt. *Work function of small metal particles: Self-consistent spherical jellium-background model. Phys. Rev. B* 29(4):1558, 1984.

[9] R. Car and J. Martins. *Pseudo-potential spin-density-functional calculation of the electronic properties of small lithium and sodium clusters. Surf. Sci.* 106:280, 1981.

[10] K. Clemenger. *Ellipsoidal shell structure in free-electron metal clusters. Phys. Rev. B* 32(2):1359, 1985.

[11] K. Clemenger. *Spherical supershells in metal clusters and the transition to protocrystalline structure. Phys. Rev. B* 44(23):12991, 1991.

[12] T. Martin, T. Bergmann, H. Göhlich, and T. Lange. *Observation of electronic shells and shells of atoms in large Na clusters. Chem. Phys. Lett.* 172(3):209, 1990.

[13] T. Martin, T. Bergmann, H. Göhlich, and T. Lange. *Evidence for icosahedral shell structure in large magnesium clusters. Chem. Phys. Lett.* 176(3):343, 1991.

[14] T. P. Martin, U. Naher, H. Schaber, and U. Zimmermann. *Evidence for a size-dependent melting of sodium clusters. J. Chem. Phys.* 100(3):2322, 1994. doi:10.1063/1.466530.

[15] B. J. Winter, E. K. Parks, and S. J. Riley. *Copper clusters: The interplay between electronic and geometrical structure. J. Chem. Phys.* 94(12):8618, 1991. doi:10.1063/1.460046.

[16] G. Alameddin, J. Hunter, D. Cameron, and M. M. Kappes. *Electronic and Geometric Structure in Silver Clusters. Chem. Phys. Lett.* 192(1):122, 1992. doi:10.1016/0009-2614(92)85439-H.

[17] G. Estiu and M. Zerner. *Interplay between Geometric and Electronic Structure and the Magnetism of Small Pd Clusters. J. Phys. Chem.* 98:4793, 1994.

[18] G. Schmid. *The relevance of shape and size of Au55 clusters. Chem. Soc. Rev.* 37(9):1909, 2008. doi:10.1039/b713631p.

[19] P. D. Jadzinsky, G. Calero, C. J. Ackerson, D. a. Bushnell, and R. D. Kornberg. *Structure of a thiol monolayer-protected gold nanoparticle at 1.1 A resolution. Science* 318(5849):430, 2007. doi:10.1126/science.1148624.

[20] M. Walter, J. Akola, O. Lopez-Acevedo, P. D. Jadzinsky, G. Calero, C. J. Ackerson, R. L. Whetten, H. Grönbeck, and H. Häkkinen. *A unified view of ligand-protected gold clusters as superatom complexes. Proc. Natl. Acad. Sci. U. S. A.* 105(27):9157, 2008. doi:10.1073/pnas.0801001105.

[21] P. E. Batson, N. Dellby, and O. L. Krivanek. *Sub-ångstrom resolution using aberration corrected electron optics.* Nature 418(6898):617, 2002. doi:10.1038/nature00972.

[22] S. Van Aert, K. J. Batenburg, M. D. Rossell, R. Erni, and G. Van Tendeloo. *Three-dimensional atomic imaging of crystalline nanoparticles.* Nature 470(7334):374, 2011. doi:10.1038/nature09741.

[23] Z. Y. Li, N. P. Young, M. Di Vece, S. Palomba, R. E. Palmer, A. L. Bleloch, B. C. Curley, R. L. Johnston, J. Jiang, and J. Yuan. *Three-dimensional atomic-scale structure of size-selected gold nanoclusters.* Nature 451(7174):46, 2008. doi:10.1038/nature06470.

[24] Z. W. Wang, O. Toikkanen, B. M. Quinn, and R. E. Palmer. *Real-space observation of prolate monolayer-protected Au38 clusters using aberration-corrected scanning transmission electron microscopy.* Small 7(11):1542, 2011. doi:10.1002/smll.201002168.

[25] S. Knoppe, A. C. Dharmaratne, E. Schreiner, A. Dass, and T. Bürgi. *Ligand exchange reactions on Au(38) and Au(40) clusters: a combined circular dichroism and mass spectrometry study.* J. Am. Chem. Soc. 132(47):16783, 2010. doi:10.1021/ja104641x.

[26] M. Azubel, J. Koivisto, S. Malola, D. Bushnell, G. L. Hura, a. L. Koh, H. Tsunoyama, T. Tsukuda, M. Pettersson, H. Hakkinen, and R. D. Kornberg. *Electron microscopy of gold nanoparticles at atomic resolution.* Science (80-.). 345(6199):909, 2014. doi:10.1126/science.1251959.

[27] L. Wallenberg, J. Bovin, and G. Schmid. *On the crystal structure of small gold crystals and large gold clusters.* Surf. Sci. 156:256, 1985.

[28] L. Wallenberg, J. Bovin, A. K. Petford-Long, and D. J. Smith. *Atomic-resolution study of structural rearrangements in small platinum crystals*, 1986. doi:10.1016/0304-3991(86)90171-3.

[29] E. Pérez-Tijerina, S. Mejía-Rosales, H. Inada, and M. José-Yacamán. *Effect of temperature on AuPd nanoparticles produced by inert gas condensation.* J. Phys. Chem. C 114(15):6999, 2010. doi:10.1021/jp101003g.

[30] S. Iijima and T. Ichihashi. *Structural instability of ultrafine particles of metals.* Phys. Rev. Lett. 56(6):616, 1986.

[31] V. Gryaznov. *Real temperature of nanoparticles in electron microscope beams. Philos. Mag. ...* 63(5):275.279, 1991.

[32] Z. W. Wang and R. E. Palmer. *Experimental evidence for fluctuating, chiral-type Au55 clusters by direct atomic imaging. Nano Lett.* 12(11):5510, 2012. doi:10.1021/nl303429z.

[33] J. Bovin, R. Wallenberg, and D. Smith. *Imaging of atomic clouds outside the surfaces of gold crystals by electron microscopy. Nature* 317:47, 1985.

[34] M. J. Yacaman. *Structural instabilities in passivated gold nanoclusters induced by electron irradiation. J. Clust. Sci.* 13(2):189, 2002. doi:10.1023/A:1015543901226.

[35] Z. W. Wang and R. E. Palmer. *Determination of the Ground-State Atomic Structures of Size-Selected Au Nanoclusters by Electron-Beam-Induced Transformation. Phys. Rev. Lett.* 108(24):1, 2012. doi:10.1103/PhysRevLett.108.245502.

[36] Z. W. Wang and R. E. Palmer. *Direct atomic imaging and dynamical fluctuations of the tetrahedral Au20 cluster. Nanoscale* 4(16):4947, 2012. doi:10.1039/c2nr31071f.

[37] Z. W. Wang, O. Toikkanen, F. Yin, Z. Y. Li, B. M. Quinn, and R. E. Palmer. *Counting the atoms in supported, monolayer-protected gold clusters. J. Am. Chem. Soc.* 132(9):2854, 2010. doi:10.1021/ja909598g.

[38] T. Martin. *Shells of atoms. Phys. Rep.* 273:199, 1996.

[39] K. Koga and K. Sugawara. *Population statistics of gold nanoparticle morphologies: Direct determination by HREM observations. Surf. Sci.* 529(1-2):23, 2003. doi:10.1016/S0039-6028(03)00300-5.

[40] K. Koga, T. Ikeshoji, and K.-i. Sugawara. *Size- and Temperature-Dependent Structural Transitions in Gold Nanoparticles. Phys. Rev. Lett.* 92(11):2, 2004. doi:10.1103/PhysRevLett.92.115507.

[41] M. José-Yacamán. *High resolution TEM studies on palladium nanoparticles. J. Mol. Catal. A Chem.* 173(1-2):61, 2001. doi:10.1016/S1381-1169(01)00145-5.

[42] B. Pauwels, G. Van Tendeloo, W. Bouwen, L. Theil Kuhn, P. Lievens, H. Lei, and M. Hou. *Low-energy-deposited Au clusters investigated by high-resolution electron*

microscopy and molecular dynamics simulations. Phys. Rev. B 62(15):10383, 2000. doi:10.1103/PhysRevB.62.10383.

[43] P. Buffat and J. Borel. *Size effect on the melting temperature of gold particles. Phys. Rev. A* 13(6):2287, 1976.

[44] C. Mottet, J. Goniakowski, F. Baletto, R. Ferrando, and G. Treglia. *Modeling free and supported metallic nanoclusters: structure and dynamics. Phase Transitions* 77(May 2015):101, 2004. doi:10.1080/1411590310001622473.

[45] F. Baletto, R. Ferrando, A. Fortunelli, F. Montalenti, and C. Mottet. *Crossover among structural motifs in transition and noble-metal clusters. J. Chem. Phys.* 116(9):3856, 2002. doi:10.1063/1.1448484.

[46] D. Reinhard, B. Hall, P. Berthoud, S. Valkealahti, and R. Monot. *Size-Dependent Icosahedral-to-fcc Structure Change Confirmed in Unsupported Nanometer-Sized Copper Clusters. Phys. Rev. Lett.* 79(8):1459, 1997. doi:10.1103/PhysRevLett.79.1459.

[47] P. Berthoud, B. Hall, R. Monot, S. Valkealahti, and D. Reinhard. *Unsupported nanometer-sized copper clusters studied by electron diffraction and molecular dynamics. Phys. Rev. B* 58(8):4917, 1998. doi:10.1103/PhysRevB.58.4917.

[48] D. Reinhard, B. D. Hall, D. Ugarte, and R. Monot. *Size-independent fcc-to-icosahedral structural transition in unsupported silver clusters: An electron diffraction study of clusters produced by inert-gas aggregation. Phys. Rev. B* 55(12):7868, 1997. doi:10.1103/PhysRevB.55.7868.

[49] M. Pellarin, B. Baguenard, J. Vialle, J. Lermé, M. Broyer, J. Miller, and a. Perez. *Evidence for icosahedral atomic shell structure in nickel and cobalt clusters. Comparison with iron clusters. Chem. Phys. Lett.* 217(4):349, 1994. doi:10.1016/0009-2614(93)E1474-U.

[50] V. Habibpour, Z. W. Wang, R. E. Palmer, and U. Heiz. *Size-Selected Metal Clusters: New Models for Catalysis with Atomic Precision. ChemInform* 11:1164, 2012.

[51] I. Garzón, K. Michaelian, M. Beltrán, a. Posada-Amarillas, P. Ordejón, E. Artacho, D. Sánchez-Portal, and J. Soler. *Lowest Energy Structures of Gold Nanoclusters. Phys. Rev. Lett.* 81(8):1600, 1998. doi:10.1103/PhysRevLett.81.1600.

[52] I. L. Garzón, M. R. Beltrán, G. González, I. Gutíerrez-González, K. Michaelian, J. A. Reyes-Nava, and J. I. Rodríguez-Hernández. *Chirality, defects, and disorder in gold clusters. Eur. Phys. J. D* 24(1-3):105, 2003. doi:10.1140/epjd/e2003-00187-4.

[53] E. Aprà, F. Baletto, R. Ferrando, and a. Fortunelli. *Amorphization mechanism of icosahedral metal nanoclusters. Phys. Rev. Lett.* 93(6):10, 2004. doi:10.1103/PhysRevLett.93.065502.

[54] I. Garzón, J. Reyes-Nava, J. Rodríguez-Hernández, I. Sigal, M. Beltrán, and K. Michaelian. *Chirality in bare and passivated gold nanoclusters. Phys. Rev. B* 66(7):1, 2002. doi:10.1103/PhysRevB.66.073403.

[55] F. Baletto and R. Ferrando. *Structural properties of nanoclusters: Energetic, thermodynamic, and kinetic effects. Rev. Mod. Phys.* 77(1):371, 2005. doi:10.1103/RevModPhys.77.371.

[56] I. Garzón and a. Posada-Amarillas. *Structural and vibrational analysis of amorphous Au55 clusters. Phys. Rev. B. Condens. Matter* 54(16):11796, 1996.

[57] D. Schebarchov and S. Hendy. *Solid-liquid phase coexistence and structural transitions in palladium clusters. Phys. Rev. B* 73(12):121402, 2006. doi:10.1103/PhysRevB.73.121402.

[58] F. Calvo and a. Carré. *Structural transitions and stabilization of palladium nanoparticles upon hydrogenation. Nanotechnology* 17(5):1292, 2006. doi:10.1088/0957-4484/17/5/022.

[59] H. Grönbeck, D. Tománek, S. Kim, and a. Rosén. *Does hydrogen pre-melt palladium clusters? Chem. Phys. Lett.* 264(1-2):39, 1997. doi:10.1016/S0009-2614(96)01293-6.

[60] L. Miao, V. Bhethanabotla, and B. Joseph. *Melting of Pd clusters and nanowires: A comparison study using molecular dynamics simulation. Phys. Rev. B* 72(13):1, 2005. doi:10.1103/PhysRevB.72.134109.

[61] C. Cleveland, W. Luedtke, and U. Landman. *Melting of gold clusters. Phys. Rev. B* 60(7):5065, 1999. doi:10.1103/PhysRevB.60.5065.

[62] M. Haruta. *Size-and support-dependency in the catalysis of gold. Catal. Today* 861(96), 1997.

[63] A. a. Herzing, C. J. Kiely, A. F. Carley, P. Landon, and G. J. Hutchings. *Identification of active gold nanoclusters on iron oxide supports for CO oxidation*. Science 321(5894):1331, 2008. doi:10.1126/science.1159639.

[64] M. Arenz, U. Landman, and U. Heiz. *CO combustion on supported gold clusters*. ChemPhysChem 7(9):1871, 2006. doi:10.1002/cphc.200600029.

[65] M. Comotti, W.-C. Li, B. Spliethoff, and F. Schüth. *Support effect in high activity gold catalysts for CO oxidation*. J. Am. Chem. Soc. 128(3):917, 2006. doi:10.1021/ja0561441.

[66] M. Valden, X. Lai, and D. W. Goodman. *Onset of Catalytic Activity of Gold Clusters on Titania with the Appearance of Nonmetallic Properties*. Science (80-.). 281(5383):1647, 1998. doi:10.1126/science.281.5383.1647.

[67] A. Sanchez, S. Abbet, U. Heiz, W.-D. Schneider, H. Häkkinen, R. N. Barnett, and U. Landman. *When gold is not noble: Nanoscale gold catalysts*. J. Phys. Chem. 103(48):9573, 1999. doi:10.1021/jp9935992.

[68] D. M. Cox, R. Brickman, K. Creegan, and A. Kaldor. *Gold clusters: reactions and deuterium uptake*. Zeitschrift fr Phys. D Atoms, Mol. Clust. 19(1-4):353, 1991. doi:10.1007/BF01448327.

[69] D. M. Cox, R. O. Brickman, K. Creegan, and A. Kaldor. *Studies of the Chemical Properties of Size Selected Metal Clusters: Kinetics and Saturation*. MRS Proc. 206:43, 2011. doi:10.1557/PROC-206-43.

[70] J. Libuda and H. J. Freund. *Molecular beam experiments on model catalysts*. Surf. Sci. Rep. 57:157, 2005. doi:10.1016/j.surfrep.2005.03.002.

[71] G. Seifert, E. Eschrig, W. Bieger, D. Porezag, G. Seifert, J. Widany, F. Weich, D. Porezag, M. M. M. Bilek, D. R. Mckenzie, and D. G. Mcculloch. *Oxidation-Resistant Gold-55 Clusters*. Science (80-.). 10468(1990):1533, 2001.

[72] H. Li, L. Li, A. Pedersen, Y. Gao, N. Khetrapal, and X. C. Zeng. *Magic-Number Gold Nanoclusters with Diameters from 1 to 3.5 nm: Relative Stability and Catalytic Activity for CO Oxidation*. Nano Lett. 15:682, 2015.

[73] E. S. Science, K. W. Jacobsen, P. Stoltze, and J. K. Nørskov. *A semi-empirical effective medium theory for metals and alloys*. Surf. Sci. 366:394, 1996. doi:http://dx.doi.org/10.1016/0039-6028(96)00816-3.

[74] K. W. Jacobsen, J. K. Norskov, and M. J. Puska. *Interatomic interactions in the effective-medium theory.* Phys. Rev. B 35(14):7423, 1987. doi:10.1103/PhysRevB. 35.7423.

[75] a. H. Larsen, J. Kleis, K. S. Thygesen, J. K. Nørskov, and K. W. Jacobsen. *Electronic shell structure and chemisorption on gold nanoparticles.* Phys. Rev. B 84(24):1, 2011. doi:10.1103/PhysRevB.84.245429.

[76] S. Schauermann, J. Hoffmann, and V. Johánek. *The molecular origins of selectivity in methanol decomposition on Pd nanoparticles.* Catal. Letters 84(December):209, 2002.

[77] C. G. Granqvist and R. a. Buhrman. *Ultrafine metal particles.* J. Appl. Phys. 47(5):2200, 1976. doi:10.1063/1.322870.

[78] C. G. Granqvist and R. a. Buhrman. *Size distributions for supported metal catalysts : Coalescence growth versus ostwald ripening.* J. Catal. 42(3):477, 1976. doi:10.1016/ 0021-9517(76)90125-1.

[79] P. Wynblatt and N. Gjostein. *Supported metal crystallites.* Prog. Solid State Chem. 9:21, 1975. doi:10.1016/0079-6786(75)90013-8.

[80] a.D Brailsford, P. Wynblatt, a.D Brailsford, and P. Wynblatt. *The dependence of ostwald ripening kinetics on particle volume fraction.* Acta Met. 27(3):489, 1979. doi:10.1016/0001-6160(79)90041-5.

[81] I. M. Lifshitz and V. V. Slyozov. *The kinetics of precipitation from supersaturated solid solutions.* J. Phys. Chem. Solids 19(1-2):35, 1961. doi:10.1016/0022-3697(61) 90054-3.

[82] I. M. Goldby, L. Kuipers, B. Von Issendorff, and R. E. Palmer. *Diffusion and aggregation of size-selected silver clusters on a graphite surface.* Appl. Phys. Lett. 69(19):2819, 1996. doi:10.1063/1.116854.

[83] L. Kuipers and R. Palmer. *Influence of island mobility on island size distributions in surface growth.* Phys. Rev. B 53(12):R7646, 1996. doi:10.1103/PhysRevB.53.R7646.

[84] G. M. Francis, L. Kuipers, J. R. a. Cleaver, and R. E. Palmer. *Diffusion controlled growth of metallic nanoclusters at selected surface sites.* J. Appl. Phys. 79(6):2942, 1996. doi:10.1063/1.361290.

[85] S. J. Carroll, P. Weibel, B. V. Issendorff, L. Kuipers, and R. E. Palmer. *The impact of size-selected Ag clusters on graphite: an STM study. J. Phys. Condens. Matter* 8(41):L617, 1999. doi:10.1088/0953-8984/8/41/025.

[86] S. J. Carroll, S. Pratontep, M. Streun, R. E. Palmer, S. Hobday, and R. Smith. *Pinning of size-selected Ag clusters on graphite surfaces. J. Chem. Phys.* 113(18):7723, 2000. doi:10.1063/1.1322657.

[87] F. Yin, C. Xirouchaki, Q. Guo, and R. E. Palmer. *High-temperature stability of size-selected gold nanoclusters pinned on graphite. Adv. Mater.* 17(6):731, 2005. doi:10.1002/adma.200401095.

[88] Y. Fukamori, M. König, B. Yoon, B. Wang, F. Esch, U. Heiz, and U. Landman. *Fundamental insight into the substrate-dependent ripening of monodisperse Clusters. ChemCatChem* 5(11):3330, 2013. doi:10.1002/cctc.201300250.

[89] L. J. Lewis, P. Jensen, N. Combe, and J.-L. Barrat. *Diffusion of gold nanoclusters on graphite. Phys. Rev. B* 61(23):16084, 2000. doi:10.1103/PhysRevB.61.16084.

[90] E. Thune, E. Carpene, K. Sauthoff, M. Seibt, and P. Reinke. *Gold nanoclusters on amorphous carbon synthesized by ion-beam deposition. J. Appl. Phys.* 98:034304, 2005. doi:10.1063/1.1985977.

[91] R. Werner, M. Wanner, G. Schneider, and D. Gerthsen. *Island formation and dynamics of gold clusters on amorphous carbon films. Phys. Rev. B* 72(4):14, 2005. doi:10.1103/PhysRevB.72.045426.

[92] R. Popescu, R. Schneider, D. Gerthsen, A. Böttcher, D. Löffler, P. Weis, and M. M. Kappes. *Coarsening of mass-selected Au clusters on amorphous carbon at room temperature. Surf. Sci.* 603(20):3119, 2009. doi:10.1016/j.susc.2009.08.025.

[93] S. B. Simonsen, I. Chorkendorff, S. Dahl, M. Skoglundh, J. Sehested, and S. Helveg. *Direct observations of oxygen-induced platinum nanoparticle ripening studied by in situ TEM. J. Am. Chem. Soc.* 132(23):7968, 2010. doi:10.1021/ja910094r.

[94] S. B. Simonsen, I. Chorkendorff, S. Dahl, M. Skoglundh, J. Sehested, and S. Helveg. *Ostwald ripening in a Pt/SiO2 model catalyst studied by in situ TEM. J. Catal.* 281(1):147, 2011. doi:10.1016/j.jcat.2011.04.011.

[95] M. Kahlweit. *Ostwald ripening of precipitates. Adv. Colloid Interface Sci.* 5(1):1, 1975. doi:10.1016/0001-8686(75)85001-9.

[96] R. Finsy. *On the critical radius in Ostwald ripening. Langmuir* 20(7):2975, 2004. doi:10.1021/la035966d.

[97] M. Chen and L. D. Schmidt. *Morphology and sintering of Pt crystallites on amorphous SiO2*1. J. Catal.* 55(3):348, 1978. doi:10.1016/0021-9517(78)90222-1.

[98] A. T. N'Diaye, T. Gerber, C. Busse, J. Mysliveček, J. Coraux, and T. Michely. *A versatile fabrication method for cluster superlattices. New J. Phys.* 11(10):103045, 2009. doi:10.1088/1367-2630/11/10/103045.

[99] F. Yang, M. S. Chen, and D. W. Goodman. *Sintering of Au particles supported on TiO2 (110) during CO oxidation. J. Phys. Chem. C* 1(113):254, 2009.

[100] J. Thomas and C. Ducati. *Transmission electron microscopy.* 1979.

[101] L. Reimer. *Transmission Electron Microscpy: Physics and Image Formation.* Springer.

[102] S. Pratontep, S. J. Carroll, C. Xirouchaki, M. Streun, and R. E. Palmer. *Size-selected cluster beam source based on radio frequency magnetron plasma sputtering and gas condensation. Rev. Sci. Instrum.* 76(4):045103, 2005. doi:10.1063/1.1869332.

[103] B. von Issendorff and R. E. Palmer. *A new high transmission infinite range mass selector for cluster and nanoparticle beams. Rev. Sci. Instrum.* 70(12):4497, 1999. doi:10.1063/1.1150102.

[104] *JEM-2100 ELECTRON ELECTRON MANUAL* .

[105] *(CME Scanned Tip and Electron Image) Lab - http://newton.umsl.edu/stei_lab/.*

[106] *Astigmatism - Wikimedia Commons - https://commons.wikimedia.org/wiki/File:Astigmatism.s*

[107] Dr. Erni Rolf. *Aberration-Corrected Imaging in Transmission Electron Microscopy (World Scientific).*

[108] *Fiji ImageJ - http://fiji.sc/Fiji.*

[109] *Quantitative TEM/STEM Simulations -QSTEM - http://qstem.org/.*

[110] G. E. Poirier. *Coverage-Dependent Phases and Phase Stability of Decanethiol on Au(111). Langmuir* 15(4):1167, 1999. doi:10.1021/la981374x.

[111] R. Staub, M. Toerker, T. Fritz, T. Schmitz-Hübsch, F. Sellam, and K. Leo. *Scanning tunneling microscope investigations of organic heterostructures prepared by a combination of self-assembly and molecular beam epitaxy. Surf. Sci.* 445(2-3):368, 2000. doi:10.1016/S0039-6028(99)01083-3.

[112] O. Lopez-Acevedo, H. Tsunoyama, T. Tsukuda, H. Häkkinen, and C. M. Aikens. *Chirality and electronic structure of the thiolate-protected Au38 nanocluster. J. Am. Chem. Soc.* 132(23):8210, 2010. doi:10.1021/ja102934q.

[113] Z. W. Wang and R. E. Palmer. *Mass spectrometry and dynamics of gold adatoms observed on the surface of size-selected au nanoclusters. Nano Lett.* 12(1):91, 2012. doi:10.1021/nl2037112.

[114] M. Kabir, A. Mookerjee, and a. K. Bhattacharya. *Copper clusters: electronic effect dominates over geometric effect. Eur. Phys. J. D* 31(3):477, 2004. doi:10.1140/epjd/e2004-00142-y.

[115] S. M. Rogers, C. R. A. Catlow, C. E. Chan-Thaw, D. Gianolio, E. K. Gibson, A. L. Gould, N. Jian, A. J. Logsdail, R. E. Palmer, L. Prati, N. Dimitratos, A. Villa, and P. P. Wells. *Tailoring Gold Nanoparticle Characteristics and the Impact on Aqueous-Phase Oxidation of Glycerol. ACS Catal.* 5(7):4377, 2015. doi:10.1021/acscatal.5b00754.

[116] T. W. Hansen, A. T. DeLaRiva, S. R. Challa, and A. K. Datye. *Sintering of Catalytic Nanoparticles: Particle Migration or Ostwald Ripening? Acc. Chem. Res.* 46(8):1720, 2013. doi:10.1021/ar3002427.

[117] A. Cao, R. Lu, and G. Veser. *Stabilizing metal nanoparticles for heterogeneous catalysis. Phys. Chem. Chem. Phys.* 12(41):13499, 2010. doi:10.1039/c0cp00729c.

[118] C. H. Bartholomew. *Mechanisms of catalyst deactivation. Appl. Catal. A Gen.* 212(1-2):17, 2001. doi:10.1016/S0926-860X(00)00843-7.

[119] O. Lopez-Acevedo, K. A. Kacprzak, J. Akola, and H. Häkkinen. *Quantum size effects in ambient CO oxidation catalysed by ligand-protected gold clusters. Nat. Chem.* 2(4):329, 2010. doi:10.1038/nchem.589.

[120] S. R. Challa, A. T. Delariva, T. W. Hansen, S. Helveg, J. Sehested, P. L. Hansen, F. Garzon, and A. K. Datye. *Relating rates of catalyst sintering to the disappearance of individual nanoparticles during Ostwald ripening. J. Am. Chem. Soc.* 133(51):20672, 2011. doi:10.1021/ja208324n.

[121] T. Uchiyama, H. Yoshida, Y. Kuwauchi, S. Ichikawa, S. Shimada, M. Haruta, and S. Takeda. *Systematic morphology changes of gold nanoparticles supported on CeO2 during CO oxidation. Angew. Chem. Int. Ed. Engl.* 50(43):10157, 2011. doi:10.1002/anie.201102487.

[122] M. Azubel, J. Koivisto, S. Malola, D. Bushnell, G. L. Hura, a. L. Koh, H. Tsunoyama, T. Tsukuda, M. Pettersson, H. Hakkinen, and R. D. Kornberg. *Electron microscopy of gold nanoparticles at atomic resolution. Science (80-.).* 345(6199):909, 2014. doi:10.1126/science.1251959.

[123] J. F. Hamilton and R. C. Baetzold. *Catalysis by small metal clusters. Science* 205(4412):1213, 1979. doi:10.1126/science.205.4412.1213.

[124] K. Wettergren, F. F. Schweinberger, D. Deiana, C. J. Ridge, A. S. Crampton, M. D. Ro, T. W. Hansen, V. P. Zhdanov, U. Heiz, and C. Langhammer. *High Sintering Resistance of Size-Selected Platinum Cluster Catalysts by Suppressed Ostwald Ripening. Nano Lett.* 14:5803, 2014.

[125] C. T. Campbell, S. C. Parker, and D. E. Starr. *The effect of size-dependent nanoparticle energetics on catalyst sintering. Science* 298(5594):811, 2002. doi:10.1126/science.1075094.

[126] R. Meyer, C. Lemire, S. K. Shaikhutdinov, and H. J. Freund. *Surface chemistry of catalysis by gold. Gold Bull.* 37(1-2):72, 2004. doi:10.1007/BF03215519.

[127] M. Haruta. *Low-Temperature Oxidation of CO over Gold Supported on TiO2, α-Fe2O3, and Co3O4. J. Catal.* 144(1):175, 1993. doi:10.1006/jcat.1993.1322.

[128] N. Lopez, T. V. W. Janssens, B. S. Clausen, Y. Xu, M. Mavrikakis, T. Bligaard, and J. K. Nørskov. *On the origin of the catalytic activity of gold nanoparticles for low-temperature CO oxidation. J. Catal.* 223(1):232, 2004. doi:10.1016/j.jcat.2004.01.001.

[129] M. Haruta. *When gold is not noble: Catalysis by nanoparticles. Chem. Rec.* 3(2):75, 2003. doi:10.1002/tcr.10053.

[130] a. S. K. Hashmi and G. J. Hutchings. *Gold Catalysis. Angew. Chemie - Int. Ed.* 45(47):7896, 2006. doi:10.1002/anie.200602454.

[131] G. J. Hutchings, S. Carrettin, P. Landon, J. K. Edwards, D. Enache, D. W. Knight, Y.-J. Xu, and A. F. Carley. *New approaches to designing selective oxidation catalysts: Au/C a versatile catalyst. Top. Catal.* 38(4):223, 2006. doi:10.1007/s11244-006-0020-y.

[132] D. A. Bulushev, I. Yuranov, E. I. Suvorova, P. A. Buffat, and L. Kiwi-Minsker. *Highly dispersed gold on activated carbon fibers for low-temperature CO oxidation. J. Catal.* 224(1):8, 2004. doi:10.1016/j.jcat.2004.02.014.

[133] T. Akita, K. Tanaka, M. Kohyama, and M. Haruta. *HAADF-STEM observation of Au nanoparticles on TiO 2. Surf. Interface Anal.* 40(13):1760, 2008. doi:10.1002/sia.2999.

[134] Y. Han, R. Ferrando, and Z. Y. Li. *Atomic details of interfacial interaction in gold nanoparticles supported on MgO(001). J. Phys. Chem. Lett.* 5(1):131, 2014. doi:10.1021/jz4022975.

[135] J. Kleis, J. Greeley, N. A. Romero, V. A. Morozov, H. Falsig, A. H. Larsen, J. Lu, J. J. Mortensen, M. Duak, K. S. Thygesen, J. K. Nørskov, and K. W. Jacobsen. *Finite Size Effects in Chemical Bonding: From Small Clusters to Solids. Catal. Letters* 141(8):1067, 2011. doi:10.1007/s10562-011-0632-0.

[136] N. Lopez and J. K. Nørskov. *Catalytic CO Oxidation by a Gold Nanoparticle: A Density Functional Study. J. Am. Chem. Soc.* 124(38):11262, 2002. doi:10.1021/ja026998a.

[137] H. Falsig, B. Hvolbæk, I. S. Kristensen, T. Jiang, T. Bligaard, C. H. Christensen, and J. K. Nørskov. *Trends in the Catalytic CO Oxidation Activity of Nanoparticles. Angew. Chemie Int. Ed.* 47(26):4835, 2008. doi:10.1002/anie.200801479.

[138] S. R. Plant, L. Cao, and R. E. Palmer. *Atomic structure control of size-selected gold nanoclusters during formation. J. Am. Chem. Soc.* 136(21):7559, 2014. doi:10.1021/ja502769v.

[139] K.-J. Hu, S. R. Plant, P. R. Ellis, C. M. Brown, P. T. Bishop, and R. E. Palmer. *The effects of 1-pentyne hydrogenation on the atomic structures of size-selected Au N and Pd N (N = 923 and 2057) nanoclusters. Phys. Chem. Chem. Phys.* 16(48):26631, 2014. doi:10.1039/C4CP02686A.

[140] M. G. Mason. *Electronic structure of supported small metal clusters. Phys. Rev. B* 27(2):748, 1983. doi:10.1103/PhysRevB.27.748.

[141] K. P. Arkill, J. M. Mantell, S. R. Plant, P. Verkade, and R. E. Palmer. *Using size-selected gold clusters on graphene oxide films to aid cryo-transmission electron tomography alignment. Sci. Rep.* 5, 2015. doi:10.1038/srep09234.

[142] S. J. Carroll, R. E. Palmer, P. A. Mulheran, S. Hobday, and R. Smith. *Deposition and diffusion of size-selected (Ag400 +) clusters on a stepped graphite surface. Appl. Phys. A* 67(6):613, 1998.

[143] F. Yin, S. Lee, A. Abdela, S. Vajda, and R. E. Palmer. *Communication: Suppression of sintering of size-selected Pd clusters under realistic reaction conditions for catalysis. J. Chem. Phys.* 134(14):141101, 2011. doi:10.1063/1.3575195.

[144] M. Valden, S. Pak, X. Lai, and D. W. Goodman. *Structure sensitivity of CO oxidation over model Au/TiO2 2 catalysts. Catal. Letters* 56:7, 1998.

[145] Z.-P. Liu, X.-Q. Gong, J. Kohanoff, C. Sanchez, and P. Hu. *Catalytic role of metal oxides in gold-based catalysts: a first principles study of CO oxidation on TiO2 supported Au. Phys. Rev. Lett.* 91(26 Pt 1):266102, 2003. doi:10.1103/PhysRevLett.91.266102.

[146] X. Ji, A. Zuppero, J. M. Gidwani, and G. A. Somorjai. *Electron flow generated by gas phase exothermic catalytic reactions using a platinum-gallium nitride nanodiode. J. Am. Chem. Soc.* 127(16):5792, 2005. doi:10.1021/ja050945m.

[147] X. Z. Ji and G. A. Somorjai. *Continuous hot electron generation in Pt/TiO2, Pd/TiO2, and Pt/GaN catalytic nanodiodes from oxidation of carbon monoxide. J. Phys. Chem. B* 109(47):22530, 2005. doi:10.1021/jp054163r.

[148] X. Ji, A. Zuppero, J. M. Gidwani, and G. A. Somorjai. *The catalytic nanodiode: gas phase catalytic reaction generated electron flow using nanoscale platinum titanium oxide Schottky diodes. Nano Lett.* 5(4):753, 2005. doi:10.1021/nl050241a.

[149] E. a. Willneff, C. Kiannerd, and S. L. M. Schroeder. *Gas phase transport of gold with gold(III) oxide and carbon monoxide. Chem. Commun. (Camb).* (2):258, 2003. doi:10.1039/b210579a.

[150] R. Ouyang, J. X. Liu, and W. X. Li. *Atomistic theory of ostwald ripening and disintegration of supported metal particles under reaction conditions. J. Am. Chem. Soc.* 135(5):1760, 2013. doi:10.1021/ja3087054.

[151] D. M. Wells, G. Rossi, R. Ferrando, and R. E. Palmer. *Metastability of the atomic structures of size-selected gold nanoparticles. Nanoscale* 7(15):6498, 2015. doi:10.1039/C4NR05811A.

[152] B. C. Curley, R. L. Johnston, B. B, N. P. Young, Z. Li, M. D. Vece, R. E. Palmer, and A. Bleloch. *Combining Theory and Experiment to Characterise the Atomic Structures of Surface-deposited Au 309 Clusters. Methodology* (0):1, 2007.

[153] M. José-Yacamán, C. Gutierrez-Wing, M. Miki, D. Q. Yang, K. N. Piyakis, and E. Sacher. *Surface diffusion and coalescence of mobile metal nanoparticles. J. Phys. Chem. B* 109(19):9703, 2005. doi:10.1021/jp0509459.

[154] S. Xiong, W. Qi, Y. Cheng, B. Huang, M. Wang, and Y. Li. *Modeling size effects on the surface free energy of metallic nanoparticles and nanocavities. Phys. Chem. Chem. Phys.* 13(22):10648, 2011. doi:10.1039/c0cp02102d.

[155] D. Liu, J. S. Lian, and Q. Jiang. *Surface energy and electronic structures of Ag quasicrystal clusters. J. Phys. Chem. C* 113(4):1168, 2009. doi:10.1021/jp810220f.

[156] K. K. Nanda. *Bulk cohesive energy and surface tension from the size-dependent evaporation study of nanoparticles. Appl. Phys. Lett.* 87(2):3, 2005. doi:10.1063/1.1994958.

[157] M. Che and C. O. Bennett. *The Influence of Particle Size on the Catalytic Properties of Supported Metals. Adv. Catal.* 36:55, 1989. doi:10.1016/S0360-0564(08)60017-6.

[158] S. Vajda, M. J. Pellin, J. P. Greeley, C. L. Marshall, L. A. Curtiss, G. A. Ballentine, J. W. Elam, S. Catillon-Mucherie, P. C. Redfern, F. Mehmood, and P. Zapol. *Sub-nanometre platinum clusters as highly active and selective catalysts for the oxidative dehydrogenation of propane. Nat. Mater.* 8(3):213, 2009. doi:10.1038/nmat2384.

[159] S. Lee, L. M. Molina, M. J. López, J. A. Alonso, B. Hammer, B. Lee, S. Seifert, R. E. Winans, J. W. Elam, M. J. Pellin, and S. Vajda. *Selective propene epoxidation on immobilized au(6-10) clusters: the effect of hydrogen and water on activity and selectivity. Angew. Chem. Int. Ed. Engl.* 48(8):1467, 2009. doi:10.1002/anie.200804154.

[160] C. Harding, V. Habibpour, S. Kunz, A. N.-S. Farnbacher, U. Heiz, B. Yoon, and U. Landman. *Control and manipulation of gold nanocatalysis: effects of metal oxide support thickness and composition. J. Am. Chem. Soc.* 131(2):538, 2009. doi:10.1021/ja804893b.

[161] S. Kunz, K. Hartl, M. Nesselberger, F. F. Schweinberger, G. Kwon, M. Hanzlik, K. J. J. Mayrhofer, U. Heiz, and M. Arenz. *Size-selected clusters as heterogeneous model catalysts under applied reaction conditions. Phys. Chem. Chem. Phys.* 12(35):10288, 2010. doi:10.1039/c0cp00288g.

[162] G. Sitja, S. Moal, M. Marsault, and G. Hamm. *Transition from molecule to solid state: Reactivity of supported metal clusters. Nano Lett.* 13:1977, 2013.

[163] F. J. Perez-Alonso, D. N. McCarthy, A. Nierhoff, P. Hernandez-Fernandez, C. Strebel, I. E. L. Stephens, J. H. Nielsen, and I. Chorkendorff. *The effect of size on the oxygen electroreduction activity of mass-selected platinum nanoparticles. Angew. Chem. Int. Ed. Engl.* 51(19):4641, 2012. doi:10.1002/anie.201200586.

[164] G. Prieto, J. Zečević, H. Friedrich, K. P. de Jong, and P. E. de Jongh. *Towards stable catalysts by controlling collective properties of supported metal nanoparticles. Nat. Mater.* 12(1):34, 2013. doi:10.1038/nmat3471.

[165] S. R. Plant, L. Cao, F. Yin, Z. W. Wang, and R. E. Palmer. *Size-dependent propagation of Au nanoclusters through few-layer graphene. Nanoscale* 6(3):1258, 2014. doi:10.1039/c3nr04770a.

[166] Y. Li, H. Cheng, T. Yao, Z. Sun, W. Yan, Y. Jiang, Y. Xie, Y. Sun, Y. Huang, S. Liu, J. Zhang, Y. Xie, T. Hu, L. Yang, Z. Wu, and S. Wei. *Hexane-driven icosahedral to cuboctahedral structure transformation of gold nanoclusters. J. Am. Chem. Soc.* 134:17997, 2012. doi:10.1021/ja306923a.

[167] I. M. Goldby, B. von Issendorff, L. Kuipers, and R. E. Palmer. *Gas condensation source for production and deposition of size-selected metal clusters. Rev. Sci. Instrum.* 68(9):3327, 1997. doi:10.1063/1.1148292.

[168] V. Habibpour, M. Y. Song, Z. W. Wang, J. Cookson, C. M. Brown, P. T. Bishop, and R. E. Palmer. *Novel Powder-Supported Size-Selected Clusters for Heterogeneous Catalysis under Realistic Reaction Conditions. J. Phys. Chem. C* 116(50):26295, 2012. doi:10.1021/jp306263f.

[169] C. Koch. *DETERMINATION OF CORE STRUCTURE PERIODICITY AND POINT DEFECT by. Dissertation* (May), 2002.

[170] H. Feilchenfeld and M. Weaver. *Binding of alkynes to silver, gold, and underpotential deposited silver electrodes as deduced by surface-enhanced Raman spectroscopy. J. Phys. Chem.* 93(03):4276, 1989.

[171] J. A. Lopez-Sanchez and D. Lennon. *The use of titania- and iron oxide-supported gold catalysts for the hydrogenation of propyne. Appl. Catal. A Gen.* 291(1-2):230, 2005. doi:10.1016/j.apcata.2005.01.048.

[172] Y. Segura, N. Lopez, and J. Perezramirez. *Origin of the superior hydrogenation selectivity of gold nanoparticles in alkyne + alkene mixtures: Triple- versus double-bond activation. J. Catal.* 247(2):383, 2007. doi:10.1016/j.jcat.2007.02.019.

[173] L. McEwan, M. Julius, S. Roberts, and J. Fletcher. *A review of the use of gold catalysts in selective hydrogenation reactions. Gold Bull.* 43(4):298, 2010.

[174] M. W. Tew, M. Nachtegaal, M. Janousch, T. Huthwelker, and J. a. van Bokhoven. *The irreversible formation of palladium carbide during hydrogenation of 1-pentyne over silica-supported palladium nanoparticles: in situ Pd K and L3 edge XAS. Phys. Chem. Chem. Phys.* 14(16):5761, 2012. doi:10.1039/c2cp24068h.

[175] D. Teschner, E. Vass, M. Havecker, S. Zafeiratos, P. Schnorch, H. Sauer, a. Knopgericke, R. Schlogl, M. Chamam, and a. Wootsch. *Alkyne hydrogenation over Pd catalysts: A new paradigm. J. Catal.* 242(1):26, 2006. doi:10.1016/j.jcat.2006.05.030.

[176] D. Teschner, J. Borsodi, A. Wootsch, Z. Révay, M. Hävecker, A. Knop-Gericke, S. D. Jackson, and R. Schlögl. *The roles of subsurface carbon and hydrogen in palladium-catalyzed alkyne hydrogenation. Science* 320(5872):86, 2008. doi:10.1126/science.1155200.

[177] M. W. Tew, H. Emerich, and J. a. van Bokhoven. *Formation and Characterization of PdZn Alloy: A Very Selective Catalyst for Alkyne Semihydrogenation. J. Phys. Chem. C* 115(17):8457, 2011. doi:10.1021/jp1103164.

[178] P. Albers, J. Pietsch, and S. F. Parker. *Poisoning and deactivation of palladium catalysts. J. Mol. Catal. A Chem.* 173(1-2):275, 2001. doi:10.1016/S1381-1169(01)00154-6.

[179] P. Jensen. *Growth of nanostructures by cluster deposition: Experiments and simple models. Rev. Mod. Phys.* 71(5):1695, 1999. doi:10.1103/RevModPhys.71.1695.

[180] G. Guisbiers, G. Abudukelimu, and D. Hourlier. *Size-dependent catalytic and melting properties of platinum-palladium nanoparticles. Nanoscale Res. Lett.* 6(1):396, 2011. doi:10.1186/1556-276X-6-396.

[181] M. J. Walsh, K. Yoshida, A. Kuwabara, M. L. Pay, P. L. Gai, and E. D. Boyes. *On the structural origin of the catalytic properties of inherently strained ultrasmall decahedral gold nanoparticles. Nano Lett.* 12(4):2027, 2012. doi:10.1021/nl300067q.

[182] D. Wales and L. Munro. *Changes of morphology and capping of model transition metal clusters. J. Phys. Chem.* (1):2053, 1996.

[183] S. Su, J. Carstens, and A. Bell. *A Study of the Dynamics of Pd Oxidation and PdO Reduction by H 2 and CH 4. J. Catal.* 176:125, 1998.

[184] E. Voogt, a.J.M. Mens, O. Gijzeman, and J. Geus. *XPS analysis of the oxidation of palladium model catalysts. Catal. Today* 47(1-4):321, 1999. doi:10.1016/S0920-5861(98)00313-7.

[185] D. Zemlyanov, B. Klötzer, H. Gabasch, A. Smeltz, F. H. Ribeiro, S. Zafeiratos, D. Teschner, P. Schnörch, E. Vass, M. Hävecker, A. Knop-Gericke, and R. Schlögl. *Kinetics of palladium oxidation in the mbar pressure range: Ambient pressure XPS study. Top. Catal.* 56(11):885, 2013. doi:10.1007/s11244-013-0052-z.

[186] X. Guo, A. Hoffman, and J. T. Yates. *Adsorption kinetics and isotopic equilibration of oxygen adsorbed on the Pd(111) surface. J. Chem. Phys.* 90(10):5787, 1989. doi:10.1063/1.456386.

[187] H. H. Kan and J. F. Weaver. *Mechanism of PdO thin film formation during the oxidation of Pd(111). Surf. Sci.* 603(17):2671, 2009. doi:10.1016/j.susc.2009.06.023.

[188] C. Popa, T. Zhu, I. Tranca, P. Kaghazchi, T. Jacob, and E. J. M. Hensen. *Structure of palladium nanoparticles under oxidative conditions. Phys. Chem. Chem. Phys.* 17(3):2268, 2015. doi:10.1039/C4CP01761G.

[189] F. Mittendorfer, N. Seriani, O. Dubay, and G. Kresse. *Morphology of mesoscopic Rh and Pd nanoparticles under oxidizing conditions. Phys. Rev. B - Condens. Matter Mater. Phys.* 76(23):8, 2007. doi:10.1103/PhysRevB.76.233413.

[190] S. M. Lang, I. Fleischer, T. M. Bernhardt, R. N. Barnett, and U. Landman. *Pd6O4+: an oxidation resistant yet highly catalytically active nano-oxide cluster. J. Am. Chem. Soc.* 134(51):20654, 2012. doi:10.1021/ja308189w.

[191] M. Lyubovsky and L. Pfefferle. *Complete methane oxidation over Pd catalyst supported on alumina. Influence of temperature and oxygen pressure on the catalyst activity. Catal. Today* 47:29, 1999.

[192] R. Burch and F. Urbano. *Investigation of the active state of supported palladium catalysts in the combustion of methane. Appl. Catal. A Gen.* 124:121, 1995.

[193] R. Farrauto, M. Hobson, T. Kennelly, and E. Waterman. *Catalytic chemistry of supported palladium for combustion of methane. Appl. Catal. A Gen.* 81(2):227, 1992. doi:10.1016/0926-860X(92)80095-T.

[194] G. Zhu, J. Han, D. Y. Zemlyanov, and F. H. Ribeiro. *Temperature dependence of the kinetics for the complete oxidation of methane on palladium and palladium oxide. J. Phys. Chem. B* 109(6):2331, 2005. doi:10.1021/jp0488665.